Author:
Leontaritis, Alexandros

Title:
Stochastic models of magnetic gear performance using asymmetric analytical field solutions

Stochastic Models of Magnetic Gear Performance Using Asymmetric Analytical Field Solutions

Alexandros Leontaritis

A dissertation submitted to the University of Bristol in accordance with the requirements for award of the degree of Doctor of Philosophy in the Faculty of Engineering

Faculty of Engineering
University of Bristol
Queen's Building
University Walk
Bristol
BS8 1TR
United Kingdom

September 2021

Word Count: 28350

Abstract

Magnetic gears offer several advantages over mechanical transmissions, the root of which is the contactless transmission. However, across a broad range of research studies, their practical performance has not matched design predictions. In addition, a very small number of magnetic gears are employed in industrial applications. It has been reported that manufacturing error contributes to the discrepancy between modelled and experimentally realised performance. Efficient modelling techniques, which could be used to predict the expected performance range, would clearly be valuable. Geometric deviations due to manufacturing error are difficult to predict and inherently random. This thesis assesses the effect of geometric error on the performance of a Coaxial Magnetic Gear (CMG) using a novel computationally efficient asymmetric analytical model to conduct Monte-Carlo simulations. The analytical model is validated through the very close agreement achieved with respect to linear FEA results. Furthermore, a hybrid stochastic model is proposed, which can calibrate the analytical statistical data with a few non-linear FEA instances. The scaling of the probability distributions derived using the analytical model are shown to match the equivalent, but much more computationally onerous, non-linear FEA based solutions. Such a statistical assessment of the effects of the modulation ring geometric deviations on the performance of CMGs is shown to potentially be important regarding both the stall torque and the torque ripple. Consideration of the effects on torque ripple becomes more important in applications where a fault mitigation perspective is considered, and accurate slipping torque estimation is essential. It is expected that as CMGs become more widely adopted, such studies will become increasingly valuable.

Acknowledgements

I would like to thank the Engineering and Physical Sciences Research Council and the University of Bristol for funding and supporting this research. I would also make a special mention to the following people, who have provided invaluable support over the years.

- Dr Jason Yon: My gratitude for your support, guidance and encouragement over the years cannot be expressed in words. It has been a very enjoyable journey – Thank you.
- Professor Aydin Nassehi: Thank you for your insightfulness and for constantly challenging me.
- Professor Philip Mellor: Thank you for your guidance over the past four years.
- My colleagues in the Electrical Energy Management Group: Thank you for your friendship and encouragement.
- My family and friends: Thank you for everything.

Author’s Declaration

I declare that the work in this dissertation was carried out in accordance with the requirements of the University's Regulations and Code of Practice for Research Degree Programmes and that it has not been submitted for any other academic award. Except where indicated by specific reference in the text, the work is the candidate's own work. Work done in collaboration with, or with the assistance of, others, is indicated as such. Any views expressed in the dissertation are those of the author.

Signed:……

Name: Alexandros Leontaritis

Date: 03/01/2022

Memorandum

The accompanying dissertation titled “Stochastic Models of Magnetic Gear Performance Using Asymmetric Analytical Field Solutions” is reporting on work performed by the author within the Electrical Energy Management Group of the University of Bristol. The principal contributions claimed by the author are as follows:

- The development of an asymmetric analytical model for a CMG considering individual dimensional and positional asymmetries of the pole pieces in the modulation ring.
- The establishment of a methodology capable of assessing these effects efficiently through statistical means.
- The development of a hybrid modelling approach, overcoming the limitations of purely analytical modelling, while offering a significant increase in computational speed compared to FEA.
- The determination of how key design parameters influence the CMG’s performance susceptibility to effects from geometric deviations, in the context of stall torque and torque ripple.

Publications

A. Leontaritis, A. Nassehi and J. Yon, "Causes and effects of Geometric Deviation in Magnetic Gears," 2019 IEEE Workshop on Electrical Machines Design, Control and Diagnosis (WEMDCD), 2019, pp. 34-39, doi: 10.1109/WEMDCD.2019.8887776. [Appendix B]

A. Leontaritis, A. Nassehi and J. Yon, "Assessing the Effect of Geometric Error on the Performance of Magnetic Gears," 2019 IEEE International Electric Machines & Drives Conference (IEMDC), 2019, pp. 1951-1958, doi: 10.1109/IEMDC.2019.8785384. [Appendix C]

A. Leontaritis, A. Nassehi and J. M. Yon, "A Monte Carlo Analysis of the Effects of Geometric Deviations on the Performance of Magnetic Gears," in IEEE Transactions on Industry Applications, vol. 56, no. 5, pp. 4857-4869, Sept.-Oct. 2020, doi: 10.1109/TIA.2020.3008115. [Appendix D]

List of Abbreviations

2D	Two-dimensional
3D	Three-dimensional
CDF	Cumulative Distribution Function
CFRP	Carbon Fibre Reinforced Polymer
CMG	Coaxial Magnetic Gear
DoF	Degree of Freedom
DoM	Direction of Magnetisation
EV	Electric Vehicle
eVTOL	Electrified Vertical Take-off and Landing
FE	Finite Element
FEA	Finite Element Analysis
GR	Gear Ratio
HSR	High-Speed Rotor
KDE	Kernel Density Estimator
LBM	Laser Beam Machining
LCM	Lowest Common Multiple
LSR	Low-Speed Rotor
MG	Magnetic Gear
MGM	Magnetically Geared Machine
MISE	Mean Integrated Square Error
MST	Maxwell Stress Tensor
NdFeB	Neodymium Iron Boron
O&M	Operation and Maintenance
PDF	Probability Density Function
PM	Permanent Magnet
SmCo	Samarium-Cobalt

UDL	Uniformly Distributed Load
VRM	Variable Reluctance Machine
wire-EDM	Wire Electrical Discharge Machining

List of Symbols

$\vec{A}$	Magnetic vector potential
α_p	Pole arc to pole pitch ratio
B_r	Radial flux density
B_θ	Tangential flux density
B_z	Axial flux density
B_{rem}	Remanent magnetic flux density
β	Slot opening angle
c_f	Cogging torque factor
$\vec{E}$	Electric flux density
φ_0	Initial angular position of a rotor
H_θ	Tangential field intensity
H_k	Peak field intensity value of k^{th} harmonic
h	Kernel density estimator bandwidth
$\vec{J}$	Current density vector
k	Number of harmonics – Region variants
K	Maximum number of harmonics – Region variants
m	Number of harmonics – Region variants
M	Maximum number of harmonics – Region subdomains
$\vec{M}$	Magnetisation vector
μ_0	Permeability of free space
μ_r	Relative permeability
p	Number of pole pairs
p_{HSR}	Number of pole pairs of high-speed rotor
Q	Number of pole pieces

THD	Total Harmonic Distortion
T_{max}	Maximum torque over one HSR pole pair pitch
T_{min}	Maximum torque over one HSR pole pair pitch
T_{mean}	Maximum torque over one HSR pole pair pitch
T_{ripple}	Torque ripple coefficient
Ω_{HSR}	High-speed rotor rotational velocity
Ω_{M}	Modulation ring rotational velocity

Throughout this thesis the following symbols are used as Fourier coefficients or simplifications of expressions $C, D, E, F, G, M, O, S, U, V, W, X, Y$, and are defined accordingly.

Contents

List of Figures

List of Tables

CHAPTER 1
THE DEVELOPMENT OF MAGNETIC GEARING

1.1 Introduction

Since the beginning of the 21st century, there has been significant advancement in technologies utilising electrical energy. It is widely accepted that the gradual electrification of many engineering sectors will lead to great long-term societal benefits, such as significantly reducing the environmental footprint of those sectors and consequently, the global air pollution [1]–[4]. Electric machines, which are an important factor in this transition, have received increased research interest from both the academic and industrial sectors. There has been a continued effort to increase specific torque and power, which has made electrification increasingly viable in mass critical sectors. In parallel, new technologies have arisen which complement and offer opportunities for further innovations. Such a technology is Magnetic Gears (MGs).

Many engineering applications require a multiplication of either angular speed or torque, and there is a wide range of transmission systems which can be used for this purpose. Mechanical gears are a highly developed technology, which dominates the transmission sector. However, the mechanical contact between the gears creates some fundamental drawbacks, including friction-induced wear and vibrations, increased maintenance requirements and reduced reliability. In the

past few decades, MGs have received increased attention due to their contactless nature, low maintenance requirements, inherent overload protection and intrinsic capacity to form a highly integrated solution with electric machines [5]–[7].

1.1.1 History of Magnetic Gearing

The concept of contactless magnetic transmission is not a modern one, with numerous cases dating back more than a century. A particular example is the 1901 U.S Patent invention of Charles

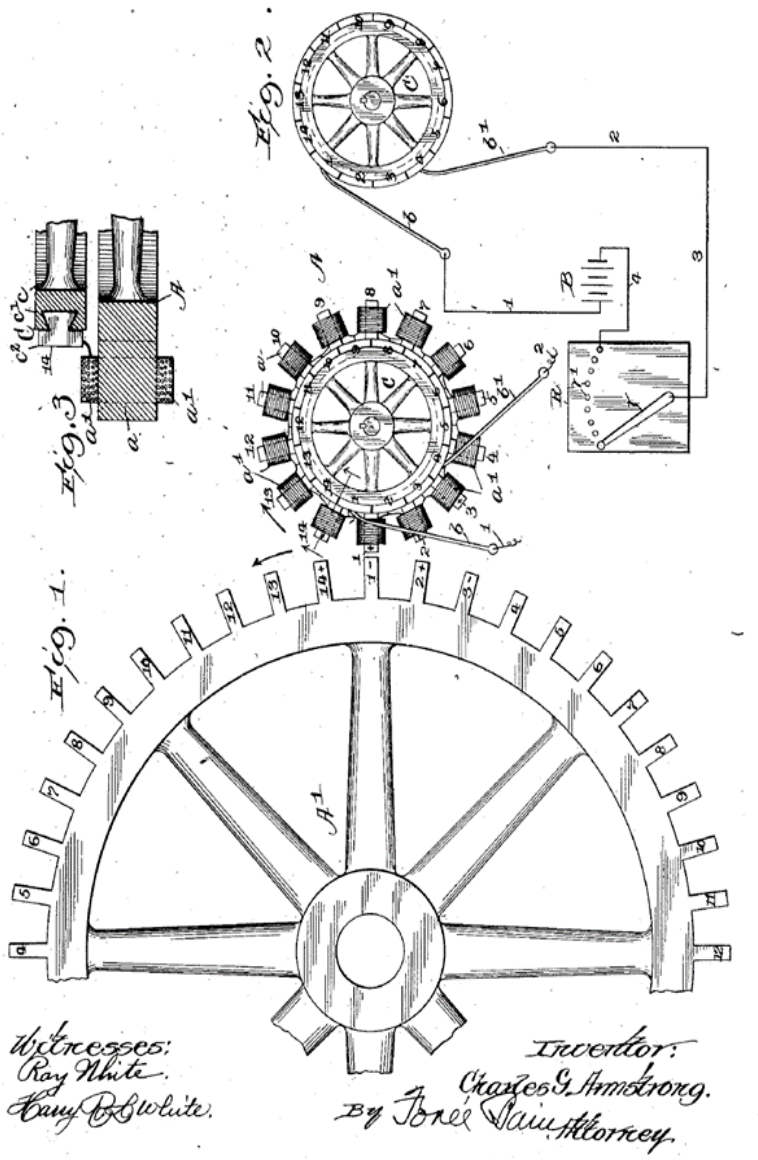

Figure 1-1 The first magnetically geared device, invented by Armstrong [8]

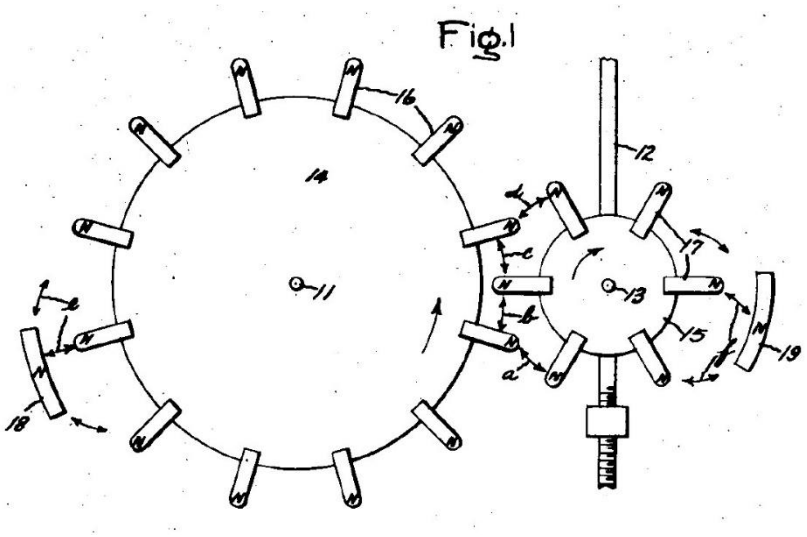

Figure 1-2 Faus's magnetic gear [9]

G. Armstrong [8]. The invention was based on two wheels and electromagnets (Figure 1-1). The driving wheel had its peripheral surface magnetically energised through a series of radial cores surrounded by coils, while the driven wheel was magnetically susceptible and placed in close proximity. The fundamental concept of this apparatus is very similar to a mechanical spur gear, where instead of the torque being transmitted mechanically (through shear force in the gear teeth) it is transmitted magnetically (through attraction forces between teeth). Harold T. Faus also proposed some MG topologies in his 1941 U.S Patent [9]. The first concept was again inspired by a mechanical spur gearbox (Figure 1-2), while the second was the equivalent of a worm gear. The proposed configurations featured teeth that were Permanent Magnets (PMs), however, they both had fundamental drawbacks. In the first instance, such designs suffer from very poor utilisation of their active material as, at any moment, very few magnets (or active parts) contribute to the torque transmission. This problem was also identified in several studies [10]–[13], where the researchers concluded that higher torque densities could only be achieved by engaging a larger number of magnetic poles. Furthermore, the available magnets at the time were very weak, with modern neodymium iron boron (NdFeB) magnets being around 6 times more energy dense than the

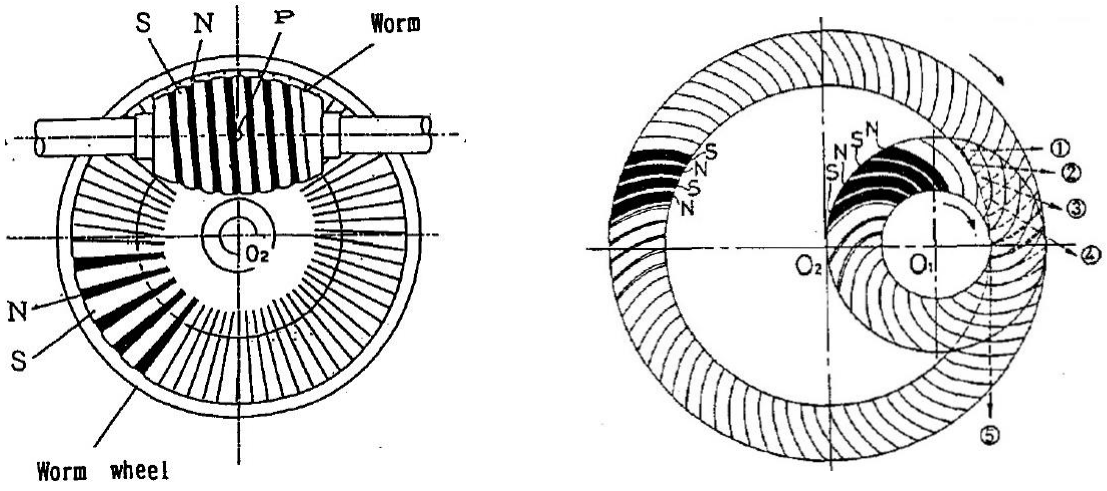

Figure 1-3 Kikuchi's and Tsurumoto's MGs: (a) Worm, (b) Involute [15], [16]

available ferrite ones [14]. The worm-type and an involute MG configurations were also explored by Kikuchi and Tsurumoto [15], [16] (Figure 1-3). However, these topologies exhibited very low torque density of less than 2 kNm/m^3, along with high complexity.

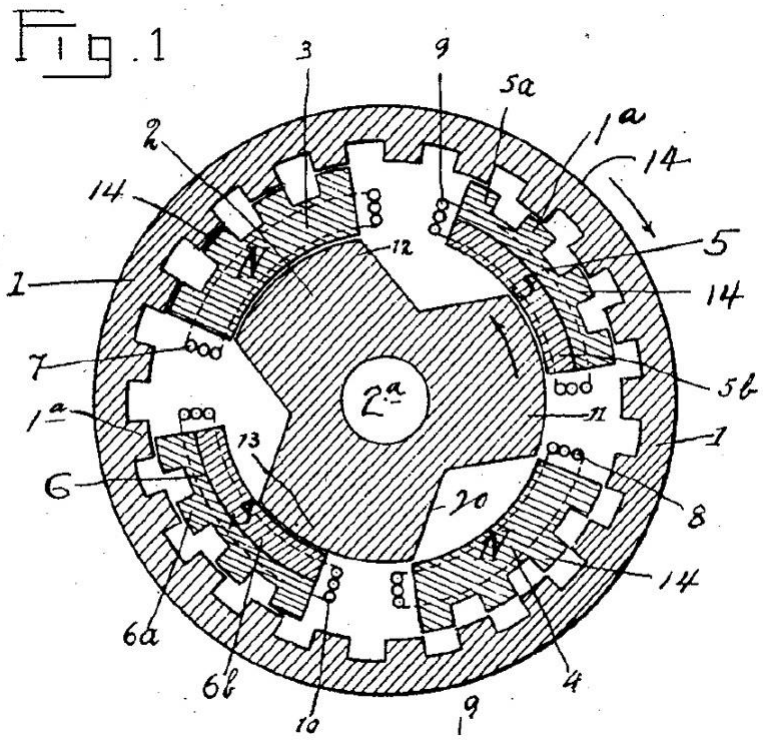

Figure 1-4 Neuland's magnetic gear [17]

Another interesting example is the 1916 U.S Patent invention from Neuland [17] (Figure 1-4). This was a reluctance-based MG consisting of two concentric rotors with salient steel poles. Coupling of the rotors was achieved without any mechanical contact using stationary electromagnets. Even though this configuration made much more efficient use of its active material, it was not developed further, nor was it used in industry. It is interesting to note however, that as a topology, it has similarities to modern MGs.

Martin proposed through his 1967 US Patent [18] an MG that even to the present day is very frequently used. It featured two concentric PM rotors and an assembly that would modulate the field of each one. Ackermann and Honds [19] also presented an MG with the same operating principles.

The discovery of rare-earth magnets such as NdFeB and samarium-cobalt (SmCo) led to further research of magnetic gearing, significantly improving and facilitating the development of several

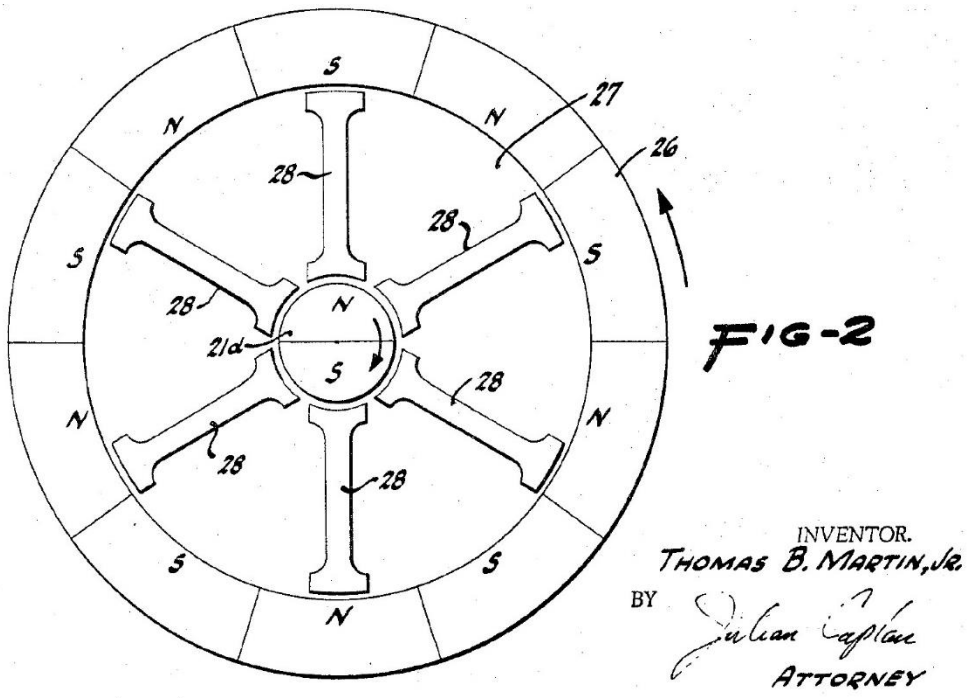

Figure 1-5 Martin's magnetic gear [18]

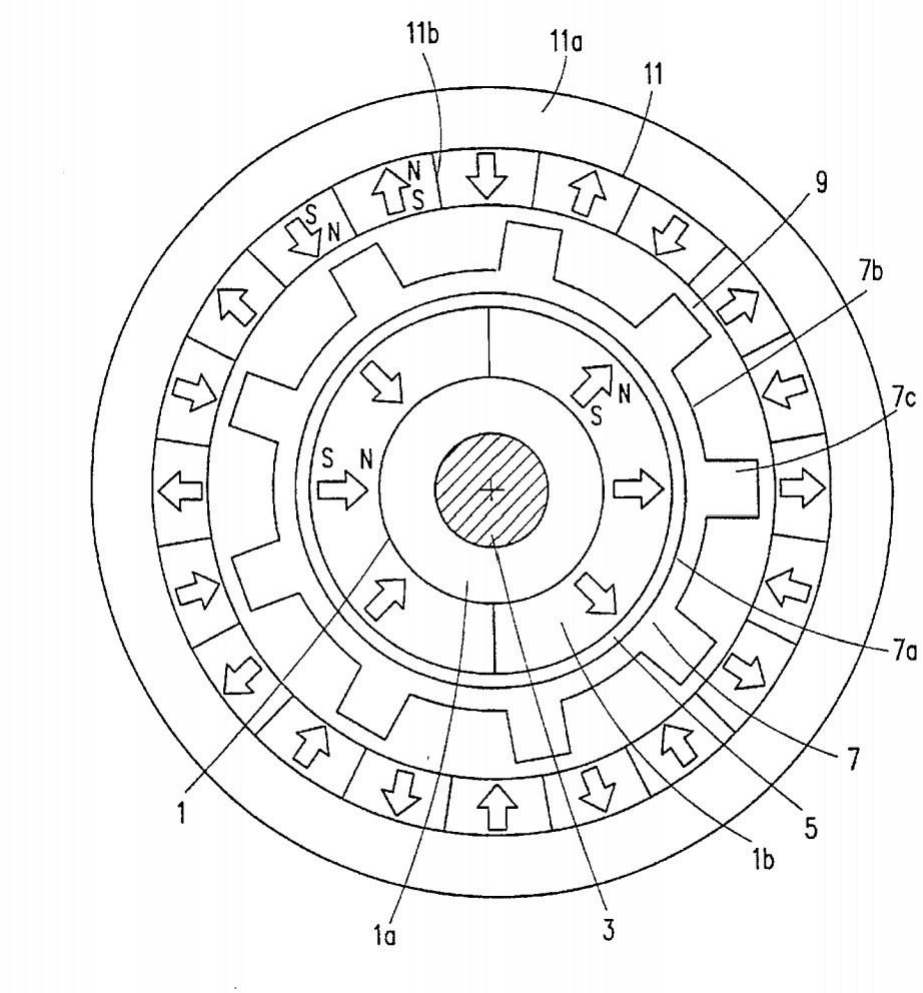

Figure 1-6 Ackermann's and Honds's magnetic gear [19]

novel forms. In recent years, MGs have been developed with torque densities high enough to potentially replace their mechanical counterparts [20].

1.1.2 Coaxial, Harmonic and Planetary Magnetic Gears

A very common topology is the Coaxial Magnetic Gear (CMG). CMGs (Figure 1-7 (a)) consist of two concentric PM rotors with a ring of ferromagnetic pole pieces placed between them, on the same axis. These ferromagnetic pole pieces are what provides the gearing effect by modulating the magnetic field to allow coupling of the rotors with different magnetisation patterns. Atallah et al [21] first described its operating principles in detail and demonstrated high achievable torque density of 100 kNm/m^3. This is comparable to torque densities of two- and three- stage helical

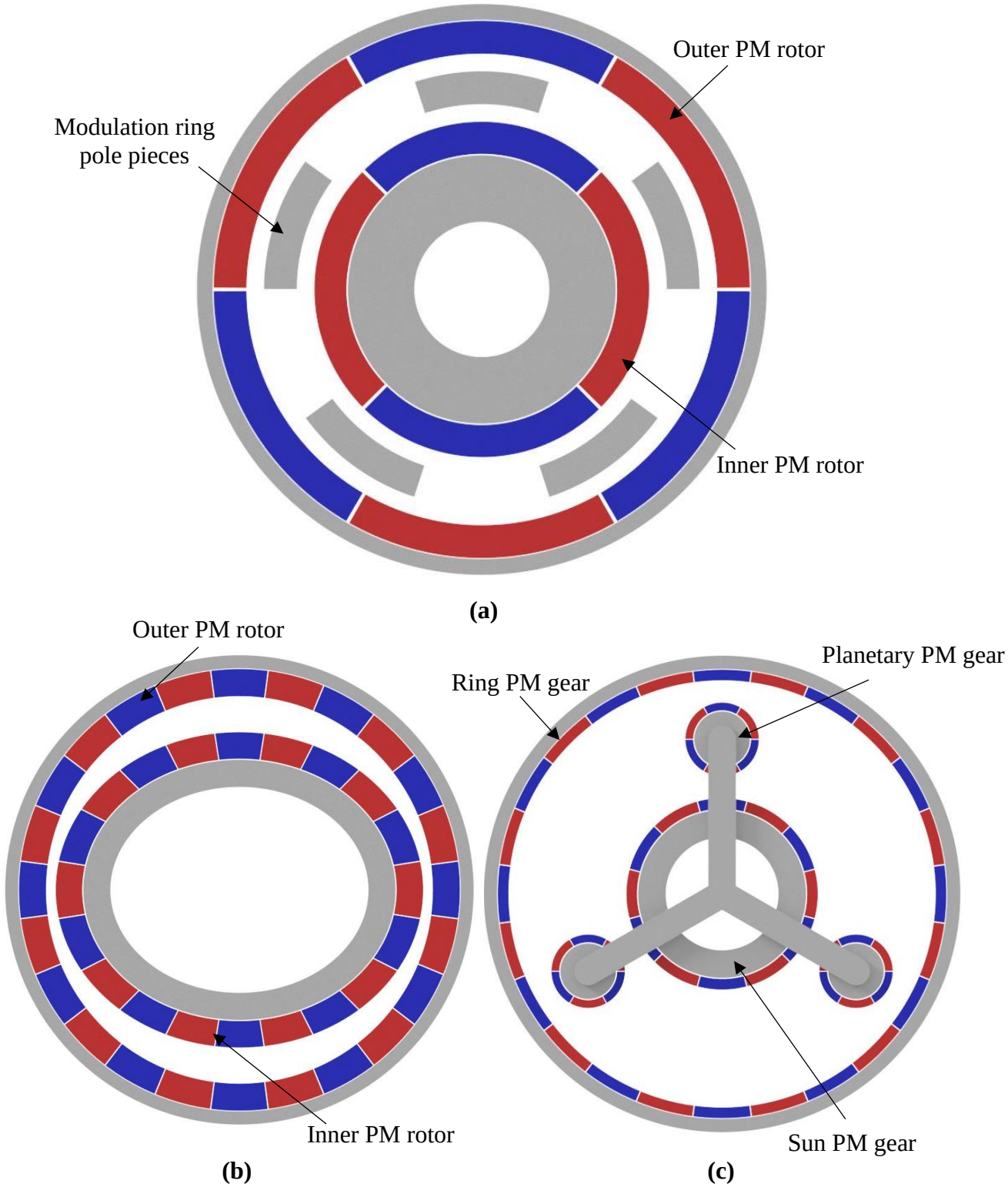

Figure 1-7 Modern MG topologies: (a) Coaxial, (b) Harmonic, (c) Planetary

Table 1 Torque density comparison for mechanical and magnetic gears [20]

Gear Type	Torque Density (kNm/m^3)
Mechanical spur gear	100-200
Mechanical helical gear	50-150
Magnetic spur gear	10-20
Coaxial magnetic gear	70-150
Harmonic magnetic gear	140-180
Planetary magnetic gear	100

gearboxes and shows the potential utility of CMGs. Since this development, CMGs have received substantial research attention, with torque densities achieved summarised in Table 1.

Another topology is the harmonic MG (Figure 1-7 (b)), first proposed in [22] and developed further in [23], [24]. The operating principle of a harmonic MG is very similar to the one of a mechanical harmonic gear, with a mechanism producing a sinusoidal time-varying air-gap. The advantages of this topology include higher achievable torque densities and high gear ratios [23]–[25], however, in common with their mechanical counterparts, mechanical complexity and structural challenges have hindered further research towards their practical realisation.

The planetary MG (Figure 1-7 (c)) is another topology that has received increased research attention in the last two decades [26]–[28]. Planetary MGs feature an almost identical configuration to their mechanical counterparts, consisting of a sun, ring and planetary gears. However, while they offer high torque densities and gearing ratios, compared to CMGs their mechanical challenges have been a limiting factor for further research [20].

1.1.3 Applications of Coaxial Magnetic Gears

The contactless nature and inherent overload protection of MGs result in some significant advantages when they are viewed in an application perspective. Magnetic gearing technology has

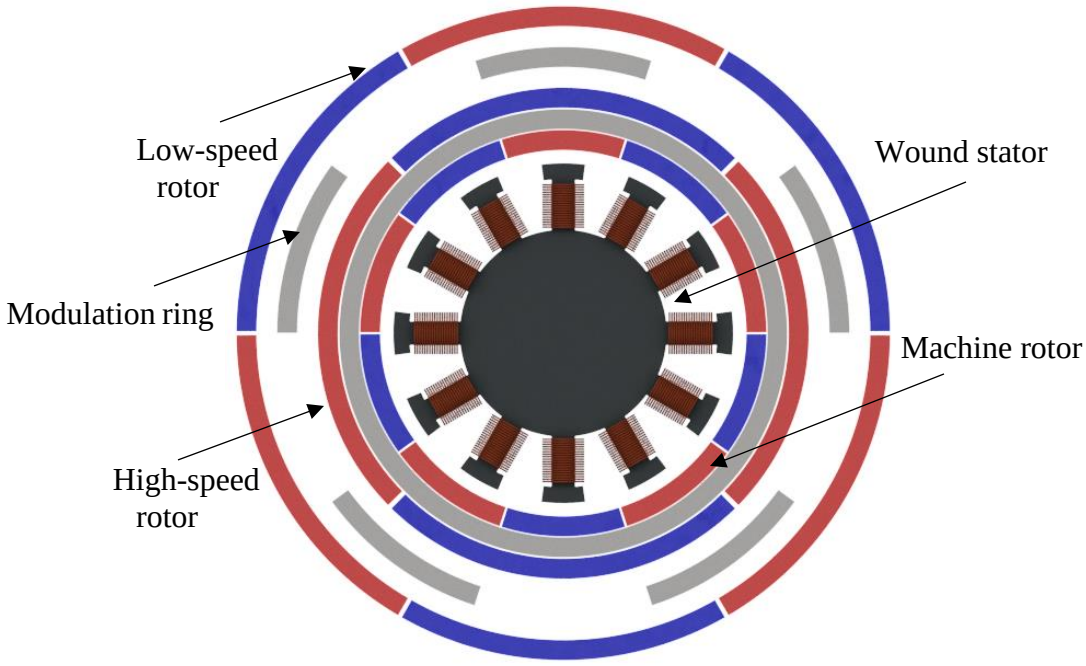

Figure 1-8 Magnetically Geared Machine (MGM)

therefore been suggested for applications in the aerospace, electric automotive, marine, robotics and energy generation industries, where size, reliability, efficiency and low Operation and Maintenance (O&M) requirements are key factors. In this thesis, only the CMG topology is investigated, as due to its promising performance characteristics, relative maturity and simpler structural configuration, it is considered the most likely to be implemented in real-world applications.

There are two possible approaches to using CMGs. The first is to simply replace a mechanical gearbox, where they are a separate component attached to the prime mover. However, the topology also facilitates close integration with an electric machine prime mover, forming a Magnetically Geared Machine (MGM). In an MGM either of the two rotors of a typical CMG has been coaxially integrated with a PM machine (Figure 1-8). The UK-based company Magnomatics [29] have taken

Figure 1-9 NASA's Revolutionary Vertical Lift Technologies (RVLT) Project [30]

this approach further by using a stationary PM array (effectively the inner rotor of a CMG) between the modulation ring and the wound stator [5].

In the aerospace sector multiple applications for CMGs have been suggested (Figure 1-9) [30]. In the emerging short-haul electric aircraft market, most vehicles use direct drive machines as mechanical gearing introduces significant penalties. These include their increased O&M requirements and the necessary primary and backup lubrication systems in order to mitigate overheating along with tooth wear and failures [31]. However, in such an application a direct drive orientation limits the capabilities of the propulsion system, since the propulsor and prime mover cannot be optimised independently. In particular, the propulsion efficiency of a propeller increases with decreasing tip speed, while the specific power of a PM machine increases as its rotational speed increases. NASA has therefore targeted the propulsion of these short-haul aircraft as a possible application for CMGs, as they can offer significant advantages, mainly through the optimisation of the overall efficiency of the propulsion system [31]. CMGs could either be used in electrified Vertical Take-off and Landing (eVTOL) vehicles or fixed-wing aircraft similar to the X-57 [31]–[35]. Apart from aircraft propulsion, CMGs have been investigated for flight control surface actuation. Potential jamming or failure of the electromechanical prime mover is a

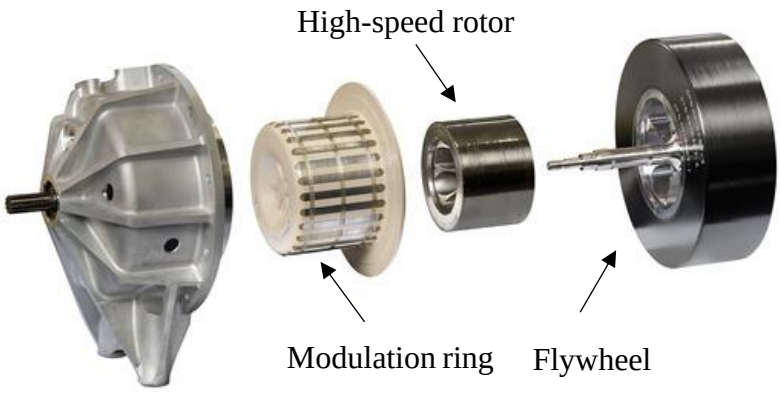

Figure 1-10 Ricardo's magnetically geared flywheel [38]

significant issue in such an application. In addition, due to the high gearing ratio between the actuator and the control surface, any shock loads on the control surface will be amplified on the actuator side. Their inherent torque limits mean CMGs can offer reliability advantages in this safety critical application. In [36], [37] the authors of the respective articles have suggested MGMs as a potential solution to this referred "shock" problem.

CMGs are also attractive options for automotive and other traction applications [38]. Ricardo has developed a flywheel energy storage system that employs a CMG. It is aimed at a range of vehicles such as cars, trucks and buses (Figure 1-10) [39], [40]. Here, a key advantage of magnetic gearing is that their configuration allows the whole system to be operated in vacuum, which eliminates aerodynamic drag on the flywheel surface. The mechanical alternative would require, vacuum pumps and management systems to be introduced to maintain this vacuum for long periods of time, thus increasing both the cost and the complexity of the system. Electric automotive vehicles (EVs) are also another example of where the magnetic gearing can be advantageous. In [41], [42], in-wheel MGMs are employed for EVs. Similar to other applications, in this case the MGMs help to minimise noise and O&M cost while improving reliability and physically isolating the input from the output.

(a) **(b)**

Figure 1-11 Magnomatics's magnetic gears in offshore wind (a) and tidal energy (b) generation applications [43], [44]

Apart from applications in the transportation sector, the advantages of MGs over traditional mechanical transmissions make them desirable for the energy generation industry as well (Figure 1-11) [43], [44]. Specifically, in this sector the O&M costs are among the highest concerns. In [7], [45] a CMG and an MGM (respectively) are proposed for wind power generation, in order to reduce O&M requirements and improve reliability along with minimising the acoustic noise. The inherent overload protection and maintenance-free aspects of MGs are even more important in tidal energy generation applications. Off-shore installations have significantly higher O&M costs while the harsh operating environment in which they exist, necessitates a high degree of system survivability [46]. CMGs and MGMs have been proposed as a technology to overcome these obstacles in tidal energy generation applications.

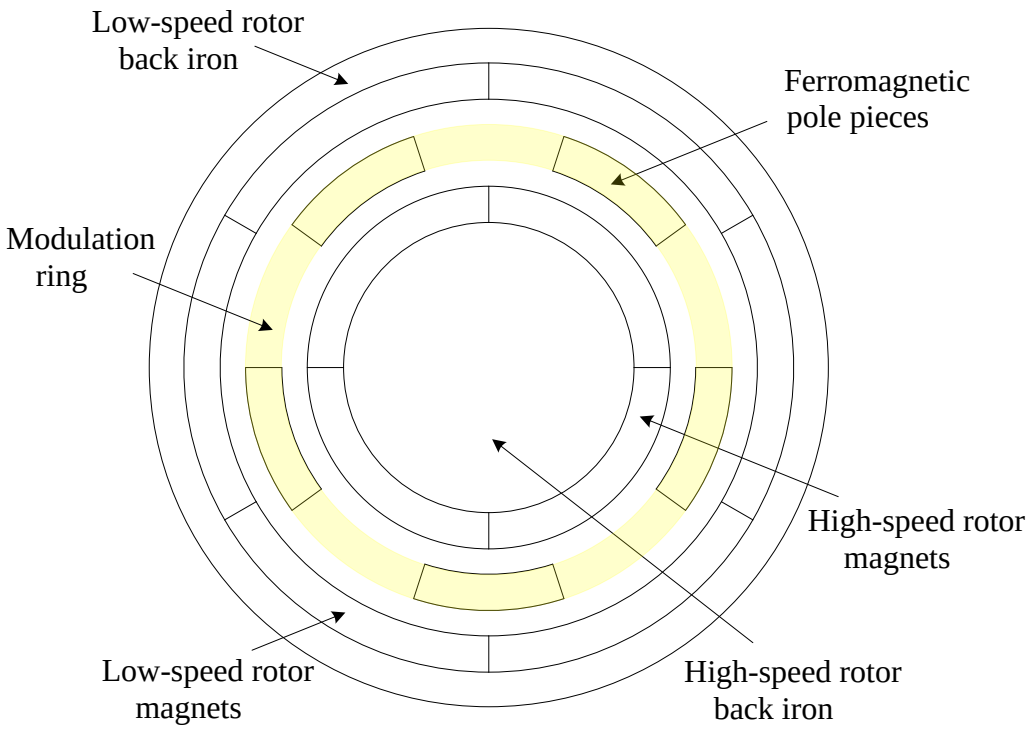

Figure 1-12 CMG component identification

1.2 Coaxial Magnetic Gear Operating Principles

In Section 1.1, the key advantages of CMGs are discussed, highlighting where and how this promising technology can be used to improve current engineering applications. This section provides a detailed explanation on the operating principles of a CMG.

A CMG (Figure 1-12) consists of three main components; two coaxial PM rotors and a ring of ferromagnetic pole pieces, known as the modulation ring. The fundamental operation of the CMG lies in this area of the modulation ring. Similar to mechanical gears, which require matching tooth pitch to transmit torque, MGs require matching field spatial harmonics. In a CMG the ferromagnetic pole pieces modulate the magnetic fields produced by each rotor, resulting in a space harmonic flux density distribution with an appropriate number of pole pairs to allow coupling with the other rotor.

Considering the High-Speed Rotor (HSR), the magnetic flux density distribution produced by a PM rotor at a radial distance *r* has been mathematically described in [47] and can be expressed using polar coordinates as in (1.2.1), (1.2.2).

$$B_r(r,\theta) = \sum_{m=1,3,5,\dots} b_{rm}(r)\ \cos(mp_{HSR}(\theta - \Omega_{HSR}t) + mp_{HSR}\theta_0) \tag{1.2.1}$$

$$B_\theta(r,\theta) = \sum_{m=1,3,5,\dots} b_{\theta m}(r)\ \sin(mp_{HSR}(\theta - \Omega_{HSR}t) + mp_{HSR}\theta_0) \tag{1.2.2}$$

where p_{HSR} and Ω_{HSR} are the number of pole pairs and rotational velocity of the HSR and b_{rm} and $b_{\theta m}$ are the Fourier coefficients for the radial and tangential component of the flux density, respectively. This mathematical description assumes B_z is zero, i.e., three-dimensional (3D) effects are negligible, including end effects.

The modulating function of the ferromagnetic pole pieces can be described as in (1.2.3), (1.2.4) [47].

$$\Lambda_r(r,\theta) = \lambda_{r0}(r) + \sum_{j=1,2,3,\dots} \lambda_{rj}(r)\cos(jQ(\theta - \Omega_M t)) \tag{1.2.3}$$

$$\Lambda_\theta(r,\theta) = \lambda_{\theta 0}(r) + \sum_{j=1,2,3,\dots} \lambda_{\theta j}(r)\cos(jQ(\theta - \Omega_M t)) \tag{1.2.4}$$

where Q and Ω_M are the number of pole pieces and the rotational velocity of the modulation ring and $\lambda_{r0}, \lambda_{rj}, \lambda_{\theta 0}$, and $\lambda_{\theta j}$ are the equivalent Fourier coefficients. Combining (1.2.1) with (1.2.3) and (1.2.2) with (1.2.4) the equations (1.2.5), (1.2.6) can be deduced.

$$
\begin{aligned}
B_r(r,\theta) = \ & \lambda_{r0} \sum_{m=1,3,5,\dots} b_{rm}(r)\cos(mp_{HSR}(\theta-\Omega_{HSR}t)+mp_{HSR}\theta_0) \\
& +\frac{1}{2}\sum_{m=1,3,5,\dots}\sum_{j=1,2,3,\dots}\lambda_{rj}(r)\, b_{rm}(r) \\
& \cos\left((mp_{HSR}+jQ)\left(\theta-\frac{(mp_{HSR}\Omega_{HSR}+jQ\Omega_M)}{(mp_{HSR}+jQ)}t\right)+mp_{HSR}\theta_0\right) \\
& +\frac{1}{2}\sum_{m=1,3,5,\dots}\sum_{j=1,2,3,\dots}\lambda_{rj}(r)\, b_{rm}(r) \\
& \cos\left((mp_{HSR}-jQ)\left(\theta-\frac{(mp_{HSR}\Omega_{HSR}-jQ\Omega_M)}{(mp_{HSR}-jQ)}t\right)+mp_{HSR}\theta_0\right)
\end{aligned}
\tag{1.2.5}
$$

$$
\begin{aligned}
B_\theta(r,\theta) = \ & \lambda_{\theta 0} \sum_{m=1,3,5,\dots} b_{\theta m}(r)\sin(mp_{HSR}(\theta-\Omega_{HSR}t)+mp_{HSR}\theta_0) \\
& +\frac{1}{2}\sum_{m=1,3,5,\dots}\sum_{j=1,2,3,\dots}\lambda_{\theta j}(r)\, b_{\theta m}(r) \\
& \sin\left((mp_{HSR}+jQ)\left(\theta-\frac{(mp_{HSR}\Omega_{HSR}+jQ\Omega_M)}{(mp_{HSR}+jQ)}t\right)+mp_{HSR}\theta_0\right) \\
& +\frac{1}{2}\sum_{m=1,3,5,\dots}\sum_{j=1,2,3,\dots}\lambda_{\theta j}(r)\, b_{\theta m}(r) \\
& \sin\left((mp_{HSR}-jQ)\left(\theta-\frac{(mp_{HSR}\Omega_{HSR}-jQ\Omega_M)}{(mp_{HSR}-jQ)}t\right)+mp_{HSR}\theta_0\right)
\end{aligned}
\tag{1.2.6}
$$

Therefore, according to (1.2.5), (1.2.6), the number of pole pairs of the modulated space harmonic flux density is described as:

$$
\begin{aligned}
& p_{modulated} = |mp_{HSR}+kQ| \\
& m = 1,3,5,\dots,\infty \\
& k = 0,\pm1,\pm3,\dots\pm\infty
\end{aligned}
\tag{1.2.7}
$$

while the rotational velocity of the flux density harmonics is given by

$$
\Omega_{modulated} = \frac{mp_{HSR}}{mp_{HSR}+kQ}\Omega_{HSR} + \frac{kQ}{mp_{HSR}+kQ}\Omega_M \tag{1.2.8}
$$

Equation (1.2.8) shows that for a gearing effect to occur, the number of pole pairs in the other rotor must equal those of an asynchronous space harmonic, viz. $k \neq 0$.

Similar to mechanical planetary gearboxes, two common operating modes exist, depending on which component is held stationary. The most common one is with a stationary modulation ring, i.e. $\Omega_M = 0$. With the highest asynchronous space harmonic represented by $m = 1$ and $k = -1$, the rotor poles [47] are expressed by (1.2.9) and the gear ratio by (1.2.10).

$$p_{LSR} = Q - p_{HSR} \tag{1.2.9}$$

$$GR = \frac{Q - p_{HSR}}{p_{HSR}} \tag{1.2.10}$$

where p_{LSR} is the pole pieces of the Low-Speed Rotor (LSR), i.e. outer rotor. The second operating mode has a stationary outer rotor with the modulation ring being used to transmit torque. While this orientation offers a higher gear ratio for the same gear specifications (1.2.11), it is considered a more complicated solution as further mechanical development is required in the modulation ring for it to output torque.

$$GR = \frac{Q}{p_{HSR}} \tag{1.2.11}$$

1.2.1 Harmonic Analysis

The operating principle of a CMG can be further understood by considering a simple harmonic analysis performed on a gear with the specifications outlined in Table 2. Figure 1-13 shows the harmonic content in the radial flux density distribution in the middle for both air-gaps. The effect of the modulation ring is observed in the new harmonics added to the flux distribution of each

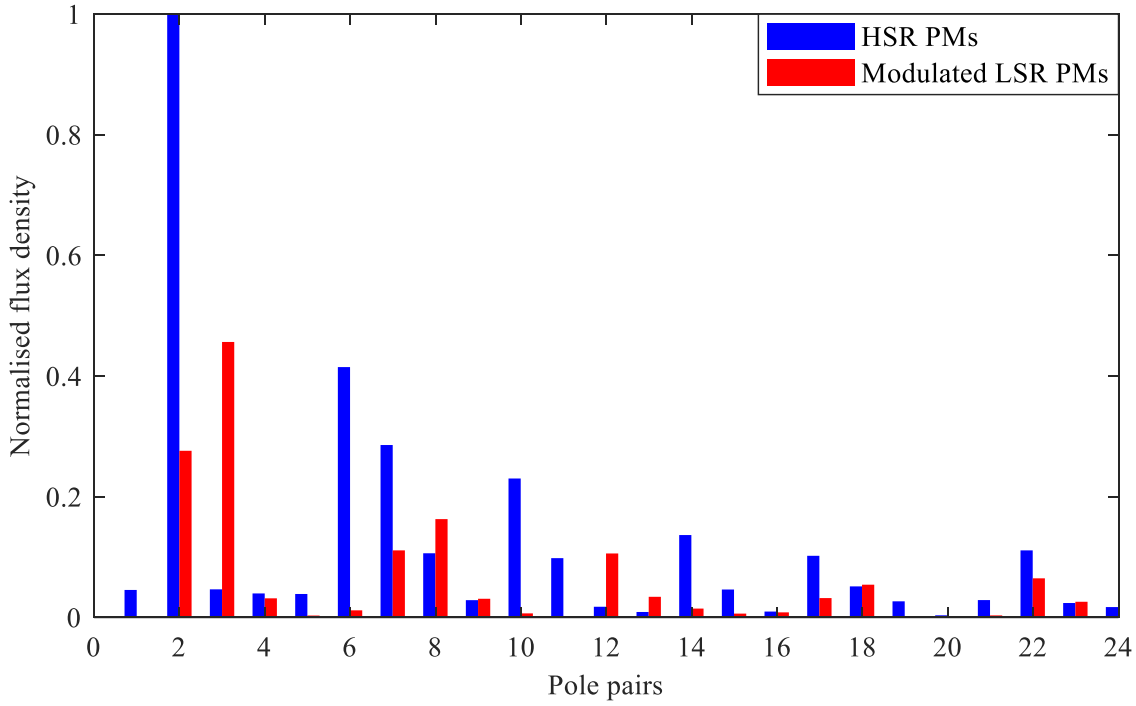

(a)

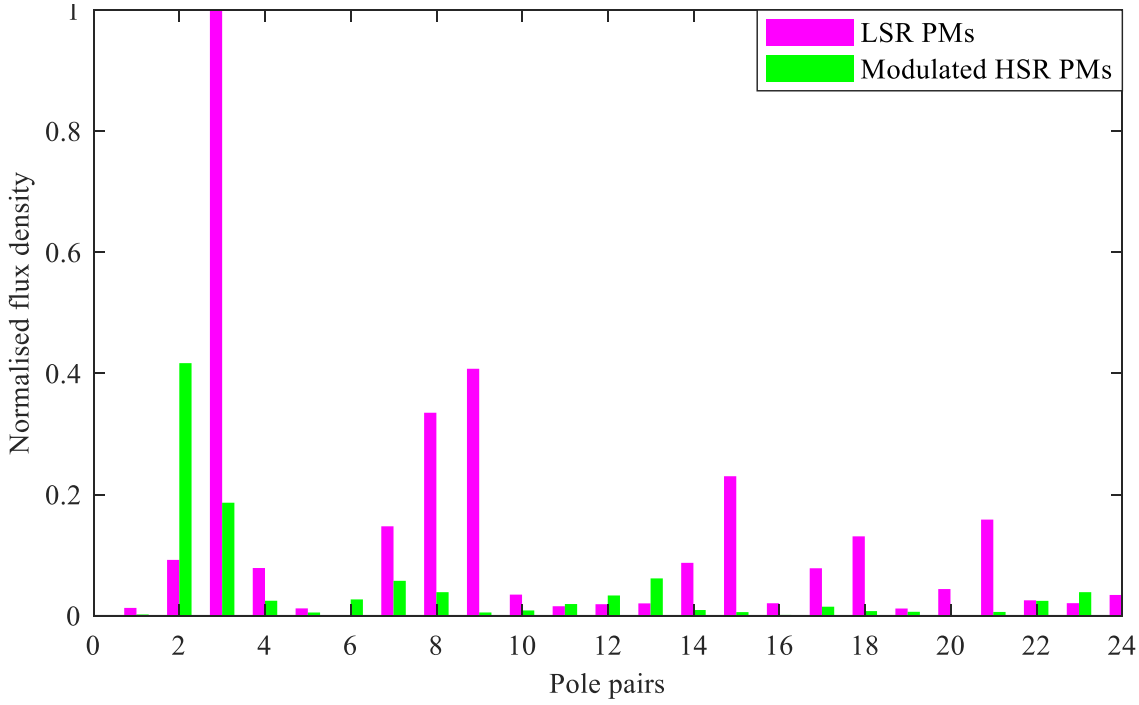

(b)

Figure 1-13 Harmonic content of radial flux density distribution in the middle of the air-gap (a) adjacent to the HSR and (b) adjacent to the LSR

Table 2 CMG Parameters – Harmonics Study

Variables	CMG 1
Number of pole pieces	5
Inner rotor poles	4
Outer rotor poles	6
Inner rotor OD (mm)	100 mm
Outer rotor OD (mm)	148 mm
PM length (mm)	10 mm
Pole pieces length (mm)	10 mm
Air-gap length (mm)	2 mm
Axial length (mm)	100 mm

rotor. In particular, in the air-gap adjacent to the HSR, the modulated LSR flux now has further spatial harmonics, the highest, asynchronous, of which is at 2 pole pairs. Similarly, in the air-gap adjacent to the LSR, the modulated HSR flux contains a new dominant harmonic at 3 pole pairs. These matching spatial harmonics are what allow the magnetic coupling to occur and therefore the CMG to operate and transmit torque.

1.2.2 Key Design Measures

A fundamental advantage of magnetic gears is their inherent overload protection, which is quantified by the maximum transmittable torque, i.e. the stall torque. The output torque of the gear depends on the relative angle between the two rotors, with respect to the modulation ring. Figure 1-14 presents the output torque of a sample CMG as a function of the HSR angle, with a stationary LSR and modulation ring. It is observed that the angular position of the stall torque is around 52°. If the loading torque exceeds the stall torque of the gear, the HSR and LSR will lose synchronism and effectively decouple, resulting in an average output torque equal to zero. The magnetic coupling can be recovered once the loading torque has reduced back within the gear's operating range. This can prevent "shock" load damage from occurring, however the vibrations

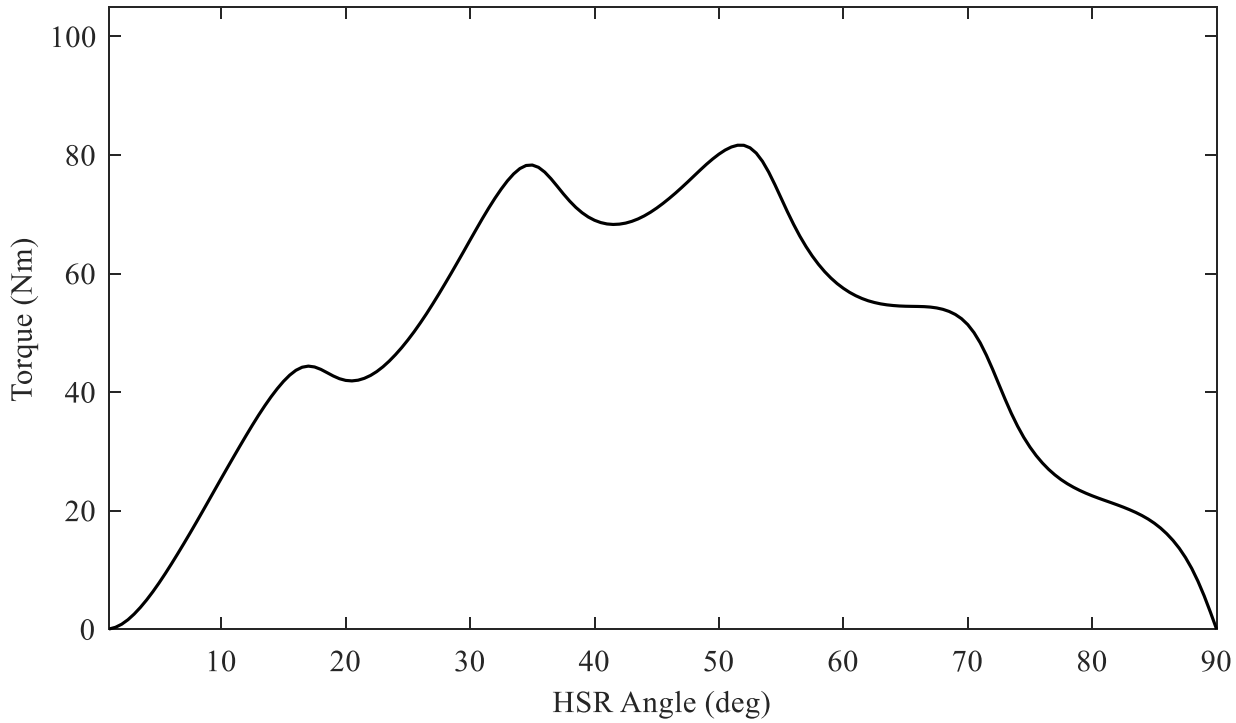

Figure 1-14 Sample CMG torque profile

generated during the stall can still damage the connected systems. Apart from stall prevention and recovery methods being employed, CMGs are typically operated at up to 70% – 80% their rated stall torque.

Another important measure is the torque ripple, which will induce noise and vibrations that will affect the performance of the gear. This could be critical in applications where smooth output torque is desired. In addition, the torque pulsations effectively increase the stall torque and therefore minimisation and accurate estimation of the torque ripple is necessary.

1.3 Introduction to the effects of geometric deviations

There is a substantial body of work in the literature focusing on improving the performance characteristics of a CMG [47]–[56]. Such research projects typically focus on optimising the gear with respect to a particular performance metric, with a significant percentage working towards

achieving higher torque densities. Finite Element Analysis (FEA) is the most commonly used method for the analysis of CMGs. However, numerous examples in the literature suggest that a discrepancy exists between FEA and experimental outcomes. Two-dimensional (2D) FEA is frequently used to model CMGs as it offers accessibility and gives a reasonable indication of performance. In studies using 2D FEA, large discrepancies have been reported in the calculation of stall torque, ranging from 20% to 40% [47], [51], [52]. These are attributed to some combination of 3D effects (particularly end-effects) and manufacturing error. Three-dimensional FEA can be employed to overcome the inherent limitations of 2D planar models but, is significantly more computationally intensive. This can include the modelling of end effects and can also allow the influence of supporting structures to be assessed. Even so, 3D FEA can still give a discrepancy of 4% to 10% [53]–[56]. In particular, in [56], 3D FEA is used with end-effects (active and structural parts). In this study a discrepancy of 9% is reported, which is attributed to 'manufacturing error'.

End effects are an important consideration in CMG analysis and have been extensively assessed, mainly through 3D FEA [52]–[56].Two main end effect phenomena are leakage and fringing and exist in all PM machines. However, the structure of a CMG is inherently prone to both phenomena. Specifically, the large equivalent air-gaps and the modulation ring saliency increases the gear's susceptibility to leakage and fringing, respectively [52]. In addition, the torque production in a CMG is a result of both attractive and repulsive magnetic forces. In [52] it is identified that in the areas where repulsive torque is produced, additional flux is forced is the axial direction by the opposing magnetic poles, an effect the authors of [52] define as escaping. However, it is also shown that similar to PM machines, knowledge of the aspect ratio could allow compensation to be applied to 2D results with very good correlation to those obtained using 3D

FEA. Nonetheless, end effects are an important factor in CMGs and caution must be taken when purely 2D modelling techniques are employed.

Any engineering product is far from being geometrically ‘perfect’. A degree of geometric deviation is inherently introduced during manufacturing, which will have an effect on the performance of the product. In spite of frequent mentions of ‘manufacturing error’ in the literature on magnetic gears, there is little to suggest that this has been studied in detail. In a CMG, geometric asymmetries will be identified in both the PM rotors as well as the modulation ring. Compared to the PM rotors, which are identical to those used in electric machines, the technology around the modulation ring is much less mature. Specifically, in order for the modulation ring to operate as explained in the previous section, its ferromagnetic pole pieces need to be supported by a non-magnetic and non-conductive material, to avoid altering the magnetic behaviour of the system and the generation of eddy-currents, respectively. In addition, the supporting structure is also required to be structurally sound and rigid to withstand the magnetic and mechanical forces that will be exerted on the pole pieces. Since standardised and well-controlled manufacturing processes for the modulation ring are yet to be developed, such geometric deviations in its construction may be significant. Therefore, the main centre of attention of this research is a performance assessment of a CMG having a modulation ring with geometrical asymmetries.

The study of those variations becomes a more significant challenge when large scale production is considered, where the range in expected performance is equally, if not, more important than the absolute value of a sample. In such an environment, statistical tools must be used to make accurate predictions of a sample’s performance, mainly through the use of modelling techniques. It is not practically feasible to conduct these studies through experimental means, as apart from the large number of CMG builds it would require, the effect of the errors in the modulation ring would need

to be isolated from the deviations in the rest of the gear. Models developed using FEA can be used to assess such a problem. However, due to the geometrical asymmetries, model simplifications cannot be used to decrease the computational time. In addition, it is necessary to use rigorous model meshing to properly capture the small geometric deviations. It therefore becomes apparent that as the computational time increases along with the large number of samples required for such statistical studies, the use of FEA becomes impractical. Analytical models can be a feasible alternative, as it is possible to achieve high accuracy with a much higher computational efficiency.

1.4 Summary

This chapter introduced magnetic gearing. A brief history of MGs was provided, from their inception over a century ago, to the modern topologies, including the CMG. CMGs, due to their inherent advantages over their mechanical counterparts, have been considered as promising alternatives in applications ranging from the aerospace to the energy generation sectors. A substantial body of work in the literature has investigated such devices. However, discrepancies between modelled and experimentally realised performance have often been reported, a degree of which is attributed to ‘manufacturing error’. Furthermore, calculated performance in research studies typically assumes exact geometry. Therefore, the effects of geometric imperfections have rarely been considered. Knowledge of those effects is even more important, when viewed from an application perspective, especially when mass production is considered. The use of statistical tools is necessary to accurately predict the range in expected performance. However, the use of FEA for these studies becomes impractical due to the high computational requirements of this method. This is an area in which analytical modelling could offer significant advantages.

1.5 Research Objectives and Thesis Structure

This thesis sets out to develop accurate and computationally efficient models capable of considering geometric asymmetries in the modulation ring of a CMG. A methodology will be established to allow the effect of geometric deviations to be statistically assessed.

1.5.1 Research Objectives

The principal objectives of this work are as follows:

- To develop an asymmetric analytical model for a CMG considering dimensional and positional asymmetries in the modulation ring.
- To establish a methodology capable of assessing the effect of geometric deviations through statistical means.
- To investigate how key modulation ring design parameters affect the sensitivity of gear performance to geometric deviations.

1.5.2 Thesis Structure

The remainder of the thesis is structured as follows:

Chapter 2 presents an overview of the potential sources of error in a CMG and provides estimates on their expected tolerances. A review of both magnetostatic and mechanical analytical modelling is also included.

Chapter 3 presents and explains the proposed asymmetric analytical model for a CMG, capable of assessing individual dimensional and positional deviations of the pole pieces. An assessment of this modelling approach is presented, with the limitations thoroughly discussed.

Chapter 4 details the statistical methodology. A hybrid stochastic modelling approach is also presented, overcoming key limitations of analytical modelling while still achieving high computational efficiency.

Chapter 5 reports on simulation studies performed to assess the influence of varying air-gap length and pole piece number on the effects of geometric deviations on stall torque. In addition, an assessment and discussion regarding the effects on torque ripple is also presented.

Chapter 6 summarises the findings and key outcomes and concludes the thesis by suggesting topics for future research.

CHAPTER 2
LITERATURE REVIEW AND OVERVIEW OF DEVIATIONS

2.1 Introduction

As outlined in Chapter 1, no engineering product is geometrically 'perfect'. CMGs have a number of different sources of error, which in this thesis are classified into two categories:

1. Errors related to the PM rotors,

2. Errors related to the modulation ring.

These errors will depend heavily on the particular structure of each gear as well as the manufacturing processes and materials that will be employed. Here, the term "manufacturing error" reported in the literature is expanded to the more generic, geometric deviations, which can include both manufacturing error and deflections of the structure under operation. This chapter reviews the most common CMG configurations and identifies their respective manufacturing processes along with the expected errors. The primary focus is on smaller CMGs similar to [31], rather than the larger ones typically employed in wind and marine energy generation applications. Furthermore, the methods available to assess the impact of these errors are also discussed and reviewed. Part of the work of this chapter was published in [57].

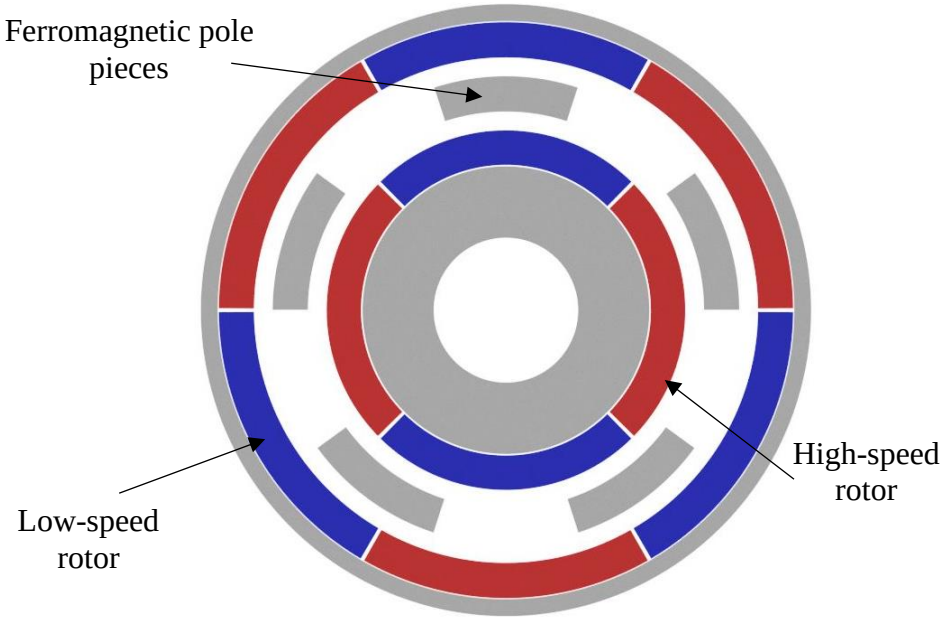

Figure 2-1 Simple CMG configuration

2.2 Review of Errors

A typical CMG configuration is presented in Figure 2-1. It features surface mounted PM rotors and a structurally simplified configuration regarding the modulation ring. In most analyses, the pole pieces are simply positioned correctly between the two rotors with little or no consideration of the necessary supporting features. In a real-world application, the complexity a CMG is understandably higher, a significant proportion of which is focused on the modulation ring. When considering PM rotors, two very mature topologies dominate the space – surface mounted and interior PMs. Surface mounted rotor topologies are also used in CMGs, and the technological maturity of PM machine rotors therefore maps well onto CMG rotors. PM rotor errors are explored in section 2.2.1. By contrast, due in part to the still limited industrial use of CMGs, the design of the modulation ring has not yet converged to a dominant topology. The absence of well-known practices for their design-and-manufacture and design-for-manufacture results in higher uncertainties regarding the ring's potential manufacturing processes and subsequent expected errors. This concern is explored in more detail in section 2.2.2.

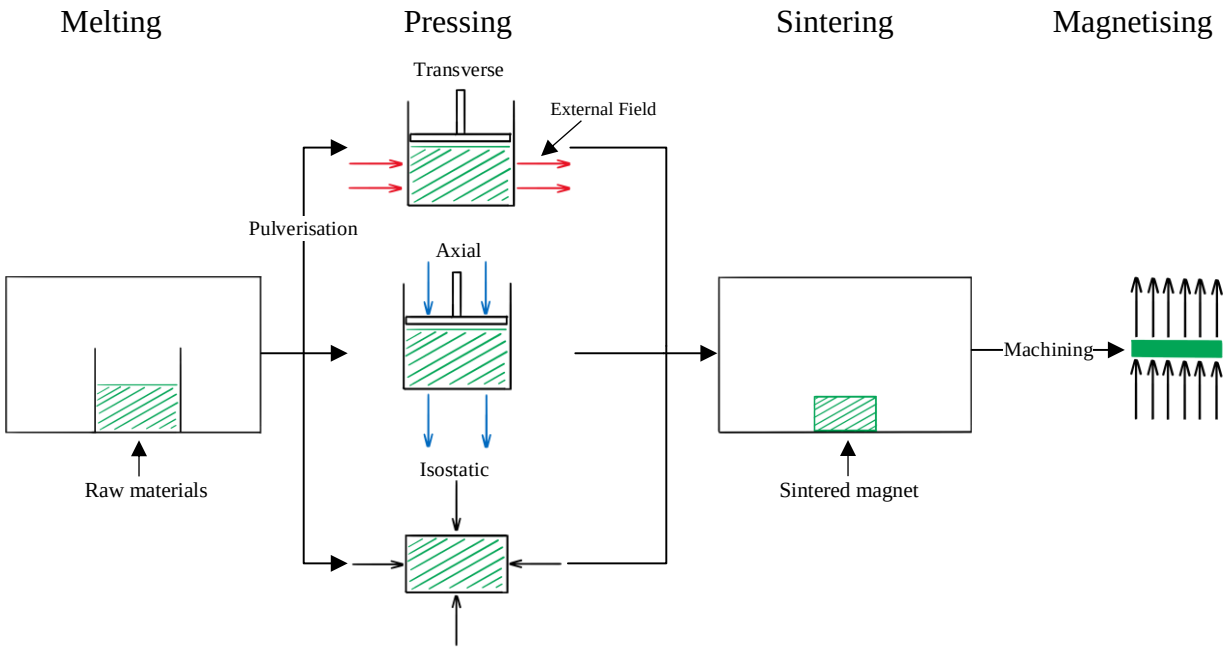

Figure 2-2 NdFeB PM manufacturing process

2.2.1 Error in the PM rotors

Irrespective of the rotor topology of the PMs (surface mounted vs interior) there are two primary contributors to the total error of a rotor. The first one is the manufacturing error in the PMs and the second is the positioning error of the PMs. PM manufacturing error may be geometric or a variation of the magnetic properties of the PMs, namely the residual magnetic flux (B_{rem}) and the Direction of Magnetisation (DoM).

High performance PMs, such as NdFeB magnets, are typically formed through a process known as Powder Metallurgy [58]. A simplified process diagram of this method is provided in Figure 2-2. Initially, suitable compositions of raw materials are melted in a vacuum induction furnace and the subsequent cured metal is pulverised into a fine powder with a particle diameter between 3 and 7 micrometres [58]. The following stage is pressing, where a solid is formed with a preferred magnetisation direction. There are several methods for this process with the most common ones being transverse, axial and isostatic pressing. In all these methods, shortly prior to

compaction, an external field is used to align the magnetic domains of the powder in the preferred magnetisation direction. The higher the homogeneity of this alignment is, the higher the performance of the resulting NdFeB magnet will be. The powder is then formed into a magnet in a sintering vacuum furnace, while having no external magnetic field and approximate dimensions. During this stage the volume of the magnet will also decrease by around 20% [58]. This preliminary magnet will then receive a shaping treatment that depends on the manufacturing volume. Some degree of machining is applied as the sintered magnets have rough surfaces and then they are typically finished through grinding or wire Electrical Discharge Machining (wire-EDM) for low volume manufacturing. Finally, a strong external magnetic field is applied to permanently magnetise the magnet and complete this manufacturing process.

Each of these stages in the manufacturing of a PM can contribute to the resulting error. The dimensional error of the PMs is usually low as the mentioned machining processes are highly accurate and precise. Further details are provided in Table 3. However, the same does not apply to the magnetic properties. Although the processes are well known and standardised, it is not possible to reduce this error to the degree of the dimensional one. The main reason is that multiple sources contribute to the generation of the error in the magnetic properties. For example, any discrepancies in the alignment during the pressing phase will result in higher error in both B_{rem} and DoM. Furthermore, the inherently imperfect alignment during the magnetisation phase will also contribute to this error. Therefore, the resulting magnetic error can be around ± 3 – 5 % and ± 5 – 10 % for B_{rem} and DoM, respectively [59]–[62]. It should also be mentioned that the residual flux depends on the temperature of the magnet and decreases by around 0.12 % per ^{o}C, for typical NdFeB magnets [62].

Table 3 Rotor Sources of Error and Expected Tolerances

Error Description		Manufacturing Processes	Expected Tolerance
Dimensional	Rotor Yoke	Turning	± 0.08 – 0.06 mm [64]–[66]
		Stamping	± 0.02 – 0.06 mm [64]–[66]
		Wire-EDM	± 0.01 – 0.125 mm [64]–[66]
		LBM	± 0.015 – 0.125 mm [64]–[66]
	Permanent Magnet	Grinding	± 0.125 mm [64], [66]
		Wire-EDM	± 0.01 – 0.125 mm [64]–[66]
	Glue Gap	N/A (Assembly)	± 0.05 mm [67]
Magnetic Properties	B_{rem}	External Magnetic Field	± 3 – 5 % [59]–[62]
		Temperature	– 0.12 % per ^{o}C [62]
	DoM	External Magnetic Field	± 5 – 10 % [59]–[62]

Positioning errors include manufacturing error in the rotor yoke and assembly error of the PMs. High accuracy is usually achieved in the manufacture of rotor yokes. For small scale production of laminated rotors, Laser Beam Machining (LBM) and wire-EDM are used to cut the laminations before bonding them either with adhesives or through welding [63]. In the design where a laminated rotor stack is not required, more conventional processes can be used, such as milling and turning. In mass production, laminations are typically stamped. In all cases, high levels of dimensional accuracy are achievable through these manufacturing techniques. Finally, the PMs are normally bonded to the rotor stack using adhesives and the corresponding glue gap will also introduce a degree of geometric deviation. Further details are provided in Table 3.

2.2.2 Error in the Modulation Ring

In order to better understand the sources of modulation ring geometric deviations an overview on the potential structural configurations is required. A wide variety of designs have been reported in the literature. Most topologies can incorporate laminated pole pieces. Modulation rings without

any laminations will have limited practical application as losses in the pole pieces would probably be excessively high. To facilitate the lamination of the pole pieces most topologies include a supporting structure, i.e., the ferromagnetic poles are not self-supporting.

2.2.2.1 Manufacture of the pole pieces

The manufacture of axially laminated pole pieces follows the same approach taken for the rotor yoke in section 2.2.1. In the case of wire-EDM manufacture, it is reported in [34] that even though cutting a pre-bonded stack can achieve high accuracy, separation between individual lamina can occur. The alternative approach, assembly of individual laminations after cutting, requires tooling and bonding processes (adhesion, welding) to be precise and well-defined to achieve consistent results. The author expects that the small cross section of many of the pole pieces reported in the literature could make this practically challenging in a prototyping, laboratory environment. Non-laminated pole pieces can be manufactured through more traditional processes, such as turning or

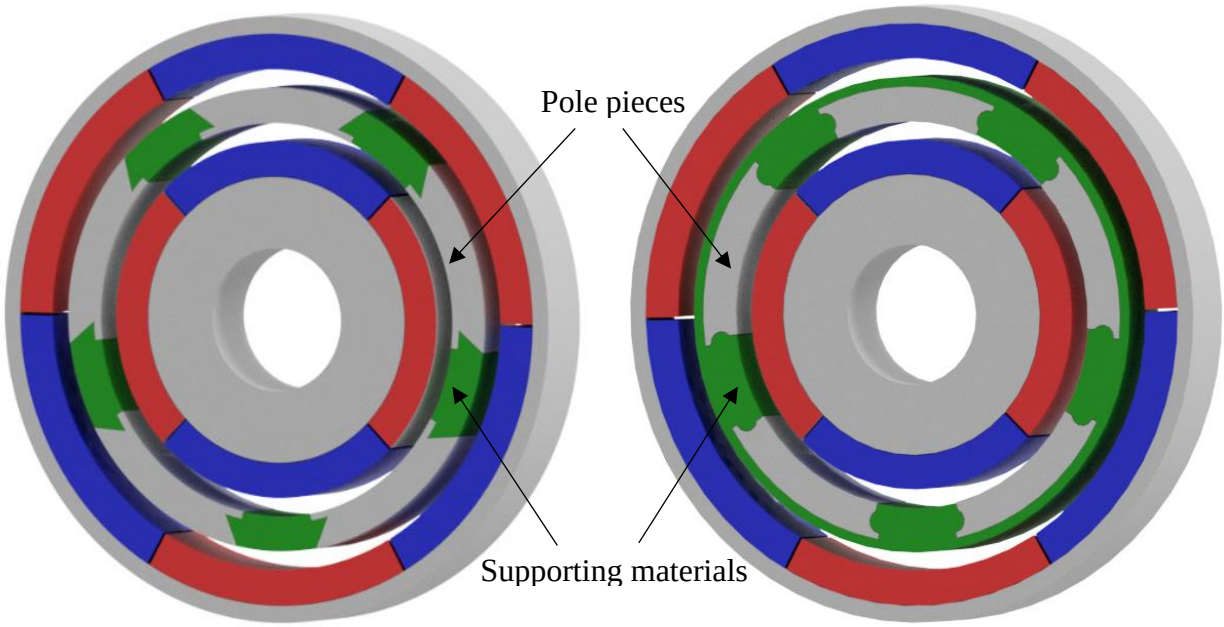

Figure 2-3 Modulation ring design with (a) mechanical interlocking features (b) encapsulated pole pieces

milling and can therefore also be assembled with relative ease. Further details on the expected dimensional errors of the pole pieces are provided in Table 4.

2.2.2.2 Manufacture of the supporting structure

A common CMG configuration is shown in Figure 2-3 (developed in [31]). The pole pieces are supported by a plastic 3D printed structure either through mechanical interlocking features (Figure 2-3 (a)) or by being encapsulated (Figure 2-3 (b)). A significant challenge of 3D printing the supporting structure is achieving a printing accuracy within the required tolerances [31]. This will not only depend on the precision of the 3D printing machine but also the machinability of the material and specifically the temperature variations the material will experience during printing. While in [31] a strategy was implemented to mitigate these effects, the air-gaps of 0.5 mm and 0.71 mm were still considered too small. Moreover, even with smaller achievable tolerances, part interference may occur as the structure will deflect due to the magneto-mechanical forces exerted on it. Therefore, a 3D printed Carbon Fibre Reinforced Polymer (CFRP) reinforced nylon may be used instead, to increase the stiffness of the structure [34], [35]. It is apparent that as the deflection depends heavily on the individual characteristics of each CMG, a comprehensive structural analysis is required to ensure excessive deflections are avoided, even with a stiffer structure, as shown in [34], [35].

Another similar configuration is a bar-supported modulator (Figure 2-4) [34], [35], [68], [69]. In this case, the supporting structure is formed by a number of separate bars, fixed at both ends, that mechanically interlock with the pole pieces. Apart from 3D printing [34], [35]), other

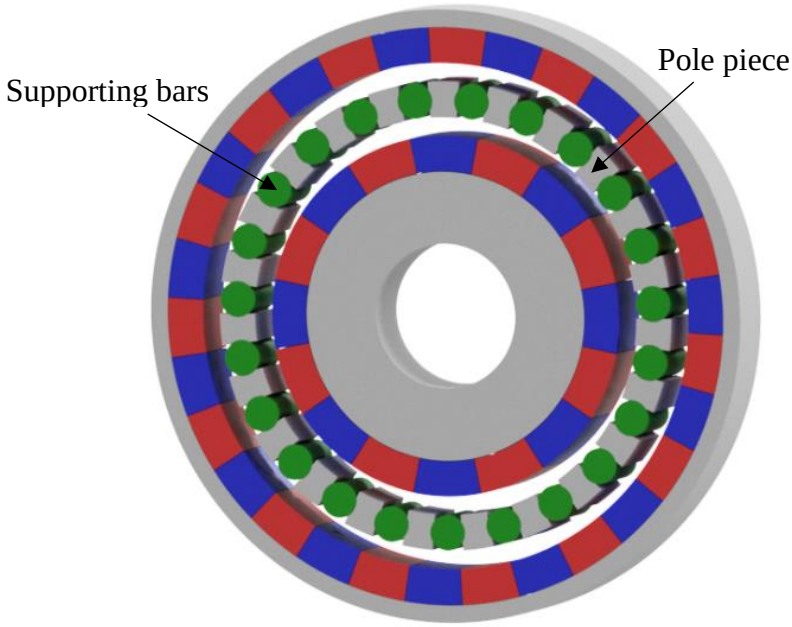

Figure 2-4 Bar-supported modulation ring

manufacturing processes for this design include machining operations (turning) of a magnetically inert steel, an engineering plastic such as PEEK or pultrusions of CFRP [68], [69]. The same manufacturing processes can be used for a modulation ring with inset supports (Figure 2-5), where the supporting bars are placed through the pole pieces [70]. While the design supports in this have

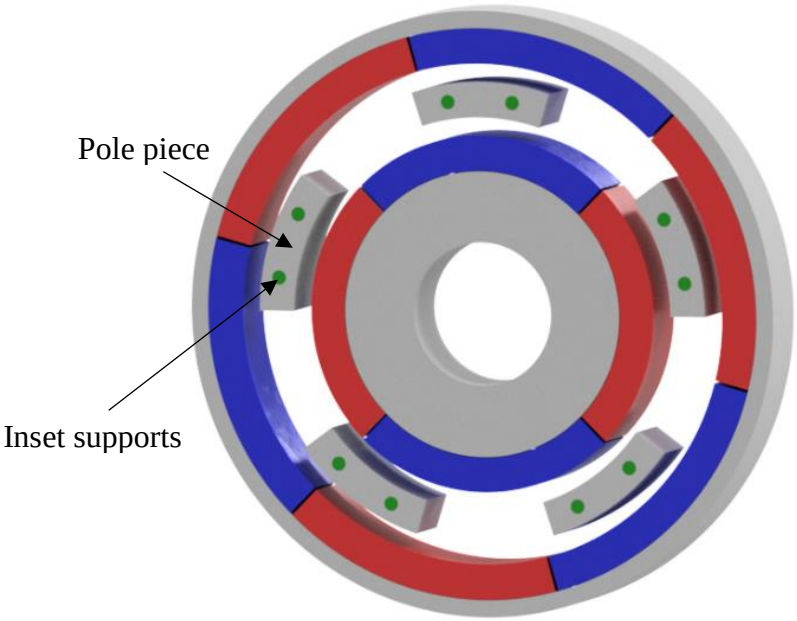

Figure 2-5 Modulation ring with inset supports

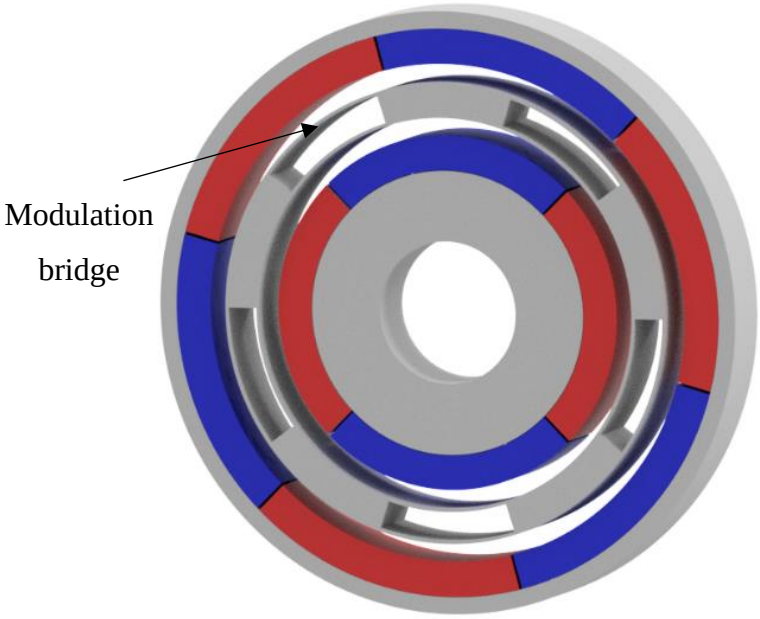

Figure 2-6 Bridged modulator

a minor effect on the magnetic circuit of the CMG, it could offer a robust and structurally secure support system.

Another interesting configuration is presented in Figure 2-6, in the form of a bridged modulator. In such a design, the modulation ring is a ferromagnetic annulus, with circumferentially equidistant slots [56], [71], [72]. These slots act as the high reluctance areas of the modulation ring, however the bridges between the pole pieces alter the reluctance paths and may adversely affect the performance of the gear. This configuration is particularly interesting as it has the potential to be self-supporting, while having laminated poles. To further enhance the structure, additional features may be added. Rods could be used similar to inset supports and connected to the end caps, as demonstrated in [71]. Alternatively, the slots could be filled with magnetically inert materials to increase the radial and axial stiffness.

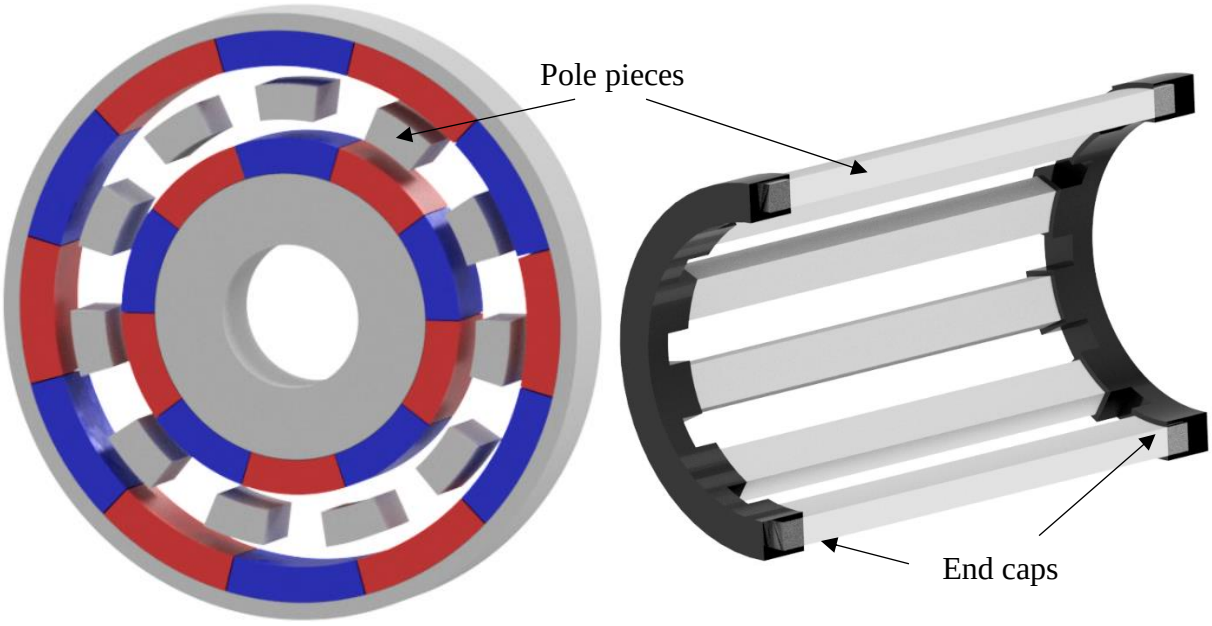

Figure 2-7 Caged modulation ring – (a) Section view of gear assembly, (b) Axial section of pole assembly illustrating ends caps connecting self-supporting pole pieces

A notable exception to the previous configurations is the caged modulator (Figure 2-7). This, mechanically simpler and self-supporting design does not accommodate the use of laminations as the pole pieces are solid ferromagnetic bars, whose ends are supported by ends caps outside the active envelope of the gear [73], [74]. Such designs can be useful in a research context, however their applicability in industrial applications will be limited due to their high susceptibility to eddy current generation, and consequently higher losses. An analytical overview on the expected manufacturing processes and tolerances for each configuration is presented in Table 4.

Table 4 Modulation Ring Sources of Error and Expected Tolerances

CMG Type	**Manufacturing Process – Pole pieces**		**Tolerance – Pole Pieces** [64]–[66]	**Manufacturing Process – Sup. Structure**	**Tolerance – Sup. Structure** [64]–[66]	**Reported Deviation**	**Rating**
NASA PT-1 [31]						< 0.71mm (assembly)	13.7 kW
NASA PT-2 (rebuild) [34]	Laminated pole pieces			3D Printing	± 0.1–0.5 mm	N/A	13.7 kW
NASA PT-4 [35]		Stamping	± 0.02–0.06 mm			< 0.5 mm (deflection)	16.1 kW
		Wire-EDM	± 0.01–0.125 mm				
Bridged Modulator [71]		LBM	± 0.015–0.125 mm	N/A	N/A	N/A	N/A
Bar Supported Modulator [68], [69]				Turning Pultrusion	± 0.08 – 0.06 mm ± 0.2 – 1 mm	0.5 mm (max)	3.9 MW
Inset support [70]				3D Printing Turning Pultrusion	± 0.1 – 0.5 mm ± 0.08 – 0.06 mm ± 0.2 – 1 mm	N/A	N/A
Caged Modulator [73], [74]		Milling Turning	± 0.02 – 0.06 mm ± 0.08 – 0.06 mm	N/A	N/A	0.018 – 0.36 mm (deflection)	90 W

2.2.3 Summary of 2.2

The previous two sections (2.2.1, 2.2.2) describe the potential manufacturing processes and the expected achievable tolerances in both the PM rotors and the modulation ring. Comparing the PM rotors and the modulation ring, it is evident that there is less variability in the design of surface mounted PM rotors. Furthermore, due to their technological maturity, PM rotor construction is better optimised than it is for the CMG modulation ring. It has, however, been noted that the manufacture of PM material, and the resultant variability in magnetic properties, is a significant source of error. Notwithstanding this point, this thesis will focus on the modulation ring for the following reasons:

1. Errors in PM properties cannot be influenced by the designer other than through material selection.
2. Errors in the modulation ring are a function of design choice.
3. Analytical techniques to define an arbitrary magnetisation (within an ideal geometry) are already available.

2.3 Literature Review

In common with other complex products, the compound effect of the various sources of error in a magnetic gear is most meaningfully assessed using statistical methods. Therefore, it is necessary to have computationally efficient modelling techniques to allow such statistical studies to be conducted. Analytical descriptions of the magnetic flux distributions or the structural deflections offer the potential to be used as the primary modelling methods. Sections 2.3.1 and 2.3.2 present a literature review on the magnetostatic and mechanical analytical modelling in a broad context regarding CMGs.

2.3.1 Magnetostatic Analytical Models

In [75] the authors presented a new analytical approach for the analysis of CMGs. This approach followed equivalent analyses used in the modelling of slotted electrical machines [76]–[81] and is based on solutions of the magnetic scalar potential. The gear is split into concentric regions and solutions of either the Laplace or the Poisson equation are obtained, depending on the material properties of each region. These are then solved for an appropriate range of magnetic harmonics. The results showed very good correlation with linear FEA, while some deviation was observed compared to non-linear FEA. This was expected as the analytical model assumes infinite permeability of the ferromagnetic regions. However, the computational efficiency of the analytical model was apparent as the FEA required 11 times the computational time of the analytical model, with the pre-processing time (e.g. mesh generation) not considered for the FEA approach. Lubin et al [82] proposed a similar analytical model using the magnetic vector potential. The results again showed excellent correlation to FEA, under the same infinite permeability assumption. The model was reported to be highly efficient over FEA, however its time saving was not quantified. In [83] the authors followed the same approach as in [82], however through algebraic manipulations they achieved a reduction in the size of the matrix of equations to be solved, therefore providing a further decrease in computational cost, without a loss in accuracy.

The computational time of an analytical model depends on the number of harmonics considered and this was investigated in [84]. The proposed harmonic selection methods were shown to considerably reduce the computational time at the expense of a small degree in accuracy. Depending on which harmonic selection method was employed, the error in calculated torque ranged from <1% to <5%, compared to the same analytical model considering a much wider range of harmonics.

Further considerations include the modelling of finite permeability. In [84] the analytical model was extended to consider finite permeability in the rotor yokes while retaining the infinite permeability assumption for the pole pieces. In addition, models have also been developed considering different magnetisation patterns and flux concentrating rotors, but are, in principle, very similar to the models described in this section [85]–[88].

Notwithstanding their computational advantages, the models highlighted above have certain limitations in common. In the first instance, there is an inherent inability to model intricate geometries, similar to the shape of the pole piece in [32] (Figure 2-3). In addition, it is very challenging to consider the non-linear permeability of the ferromagnetic pole regions and therefore take into account the saturation effect. Another common feature is that all these models are radially symmetric and cannot thus consider and assess the geometrical asymmetries that will either be introduced in the manufacture or during the operation of a CMG.

The equivalent research problem has been previously identified in PM machines, with a few authors developing analytical models capable of considering asymmetries [67], [89]–[91]. In [67] particular attention is given to the asymmetries caused by the manufacturing processes and the importance of the respective tolerances. The developed analytical model considered slot opening variations along with radial and tangential asymmetries of the rotors. It is apparent that the complexity of the model increases with increasing number of asymmetries considered and this is a possible reason why radial asymmetries in the stator slots were not considered. Another model considering similar imperfections was developed in [92]. Here, it was confirmed that the effect of these geometric deviations needs to be assessed statistically, and the low computational complexity of their analytical model allowed the authors to perform a simple Monte-Carlo analysis with 10,000 samples.

2.3.2 Mechanical Models

The overview of the mechanical structures and their potential manufacturing processes in Section 2.2, provides an insight on the likely geometric deviations that will be caused by errors during manufacturing. However, it is both evident and also widely reported that the magnetic and mechanical forces exerted on the modulation ring will cause a degree of deformation in the structure [34], [35], [69], [73], [93]. Therefore, the position of pole pieces will not be in the nominal orientation, considered in the design stage, as in [21].

Modelling the structural behaviour of the designs shown in Section 2.2.2 is very challenging, particularly for designs with laminated pole pieces. In those cases, multiple factors need to be taken into account for a comprehensive analysis. These range from the adhesion properties between individual lamina and the directional stiffness of the lamination stack, to the adhesion/interlocking mechanical properties between the pole pieces and the supporting structures. It is apparent, that even with FEA where geometric subtleties can be feasibly modelled, their quantification and incorporation is a significant challenge. Therefore, the models that have been presented in the literature feature a very large set of assumptions.

Furthermore, the quantification of the deflections is not a single calculation but rather an iterative process. As the structure deflects, and the relative position of the pole pieces changes, the forces exerted on them will also be different. Therefore, these new forces will cause different deflections and this process will continue until the structure has converged to its ‘true’ deflected shape. An iterative magnetomechanical model was developed in [73], using a 3D magnetomechanical FEA. This model considered the simple CMG structure of a caged modulation ring, however the deflections were studied in detail, with the load applied non-uniformly to the pole pieces. The iterative analysis allowed high accuracy to be achieved in the calculation of the

deflections compared to experimental results. However, the complexity and significant computational cost of a 3D multiphysics FE tool, makes such a method impractical for use in statistical studies.

In [69], [93] a multibody model is created for the bar-supported modulation ring. The support bars are assumed equivalent to fixed-end beams, while negligible stiffness is assumed for the pole pieces. This assumption stems from the likely higher stiffness of the supporting bars compared to the laminated pole pieces, however it does not accurately model the case where the pole pieces are circumferentially compressed. Notably, tangential deflections larger than the span angle of the pole pieces are reported, which would only happen if a complete failure of the pole piece assembly occurs. This multibody model showed that large deflections may occur (up to 0.5 mm), while offering a significant computational advantage over the combination of 2D magnetics and a 3D mechanical FEA. However, its accuracy compared to FEA is not shown. Furthermore, for a robust comparison to be made, the complete set of assumptions in the FE model would be needed and this was not provided. Another, more simplified model, was considered in [35], using the Euler-Bernoulli beam theory. The electromagnetic forces exerted on the pole pieces were calculated and then assumed as a distributed load on the support posts. They in turn, were modelled as fixed-end beams with trapezoidal cross section. This allowed the stress on the supporting structure to be determined. However, the support posts are analysed considering only the forces from the adjacent pole pieces. This means, the mechanical link between the pole pieces, and subsequent higher stiffness, provided by the ring was considered negligible, which is arguably overly conservative.

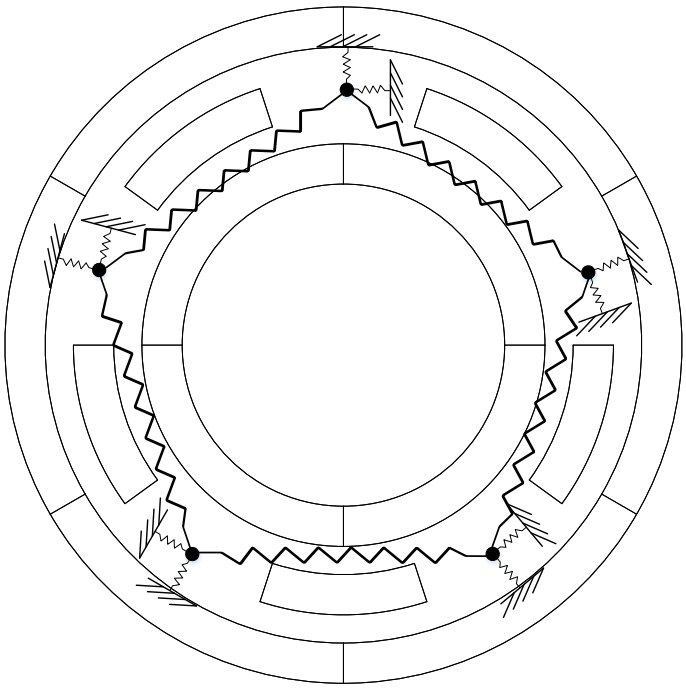

Figure 2-8 Spring system equivalent deflection model

An improved model based on the one reported in [35] could be developed by considering a system of linked springs as shown in Figure 2-8. Similar to [35] the support posts are considered as uniformly loaded fixed end beams, where the maximum deflection is at the midpoint of the beam and can be determined by (2.3.1), (2.3.2):

$$u(x) = \frac{q}{24EI}(x^4 - 2Lx^3 + L^2x^2) + \frac{q}{2\kappa GA}(Lx - x^2) \tag{2.3.1}$$

$$u_{max} = \frac{qL^4}{384EI} - \frac{qL^2}{4\kappa GA} \tag{2.3.2}$$

where L is the beam's length, A is the cross-sectional area, κ is the Timoshenko shear coefficient, q is the distributed load and E and G are the elastic and shear moduli, respectively.

The linearity of equation (2.3.2) leads to the development of the equivalent system, shown in Figure 2-8, which consists of a point mass and two springs. The elongation in each spring represents the deflection in each Degree of Freedom (DoF). Therefore, using the principle of

superposition, the resultant deflected position of the point mass, and hence the maximum deflection of the fixed-end support post can be determined.

As already outlined, due to the complexity of the problem, further assumptions are required to enable the use of such analytical structural models. In this case, the following assumptions have been adopted:

1. The Timoshenko beam theory is applied.
2. The laminated pole pieces are assumed incompressible but the torsional and bending stiffness of the laminations is considered negligible.
3. At the interface between the pole pieces and the supporting posts a rigid attachment is considered.
4. Both radial and tangential forces of each pole piece are split equally between the two supporting bars and act as Uniformly Distributed Loads (UDLs).

Expanding on assumption (1), the Timoshenko beam theory considers the deformations due to both bending and shearing and a special case of which is the classical (Euler-Bernoulli) beam theory, where the shear effects are negligible. Similar to [84] laminated pole pieces will have a negligible stiffness compared to their supporting structure, as outlined in assumption (2). However, their existence cannot be disregarded as they do form deflection limits between the supporting posts. More specifically, the minimum tangential distance between consecutive support posts cannot be less than the span angle of the pole pieces, as otherwise this would result in failure in the laminations. Consequently, the pole pieces are considered incompressible. Furthermore, an assumption is required to simplify the transmission of the forces from the pole pieces to the supporting posts. The main difficulty to consider is the adhesion properties at the interface between them, where usually adhesives and mechanical interlocking features would be present. The

complexity in considering those factors leads to the conservative assumptions that there is a rigid attachment at the interface, with the forces split equally between the supporting posts, as summarised in assumptions (3) and (4). This model can then be solved by determining the global stiffness matrix and calculating the individual deflections, and can have good correlation with FEA, if the FEA incorporates the same large set of assumptions.

This literature review shows that efficient analytical structural models can be developed. However, it is necessary to significantly simplify the problem through a large set of assumptions. Compared to the equivalent magnetic models, these simplified mechanical models are expected to have a lower correlation to a real case scenario. As such, at this stage their use in statistical studies assessing small geometric deviations would not yield meaningful results. This thesis will not directly calculate the deflections under load of each CMG. Instead, a framework is developed which can define distributions of static geometric deviations. Given these distributions, the effects on the performance of the CMG can be assessed.

2.4 Summary

This chapter presented an overview of the sources of error in a CMG and provided estimates on the expected variation for each one. It was identified that due to the standardised and well understood processes regarding the PM and rotor manufacture, there is much less need and opportunity to mitigate their associated effects compared to those of the modulation ring. Therefore, the modulation ring will be the focus of the thesis. The assessment of stochastic geometric deviations requires computationally efficient and accurate models. Radially symmetric analytical subdomain models using solutions of either the magnetic scalar or vector potential have been published. However, even though they show significant potential in terms of their computational efficiency, their modelling definitions do not allow the considerations of geometric

asymmetries. Asymmetric analytical models exist for PM machines but to the authors knowledge, none have yet been developed for CMGs. Mechanical models have also been published that could theoretically achieve the necessary computational efficiency, however, in each the underlying problem is significantly simplified through a very large set of assumptions. This will considerably decrease the correlation of such models to a realistic case and are therefore not yet suitable for this statistical analysis.

CHAPTER 3
ASYMMETRIC ANALYTICAL MODEL OF A COAXIAL MAGNETIC GEAR

3.1 Introduction

Analytical techniques can be used to develop accurate and highly computationally efficient models, which lend themselves to statistical analyses. This chapter presents a novel asymmetric model for a CMG, capable of assessing both radial and tangential deviations of individual pole pieces. The proposed model is validated with FEA, and a thorough exploration of its limitations is also presented. All the analytical simulations in this and subsequent chapters have been built and performed in Matlab, and the work of this chapter was published in [94].

3.2 Fundamental Principles of Analytical Modelling

An ideal CMG consists of the two radially symmetric and concentric PM rotors and a central modulation ring of equispaced and identical ferromagnetic pole pieces. The magnetic air-gap region of the CMG is formed by the area surrounding the modulation pole pieces and is enclosed by the PM rotors. Unlike FEA, a limitation of analytical modelling is that it is challenging to consider the air-gap as one region due to its complex shape. Therefore, the principle of this model

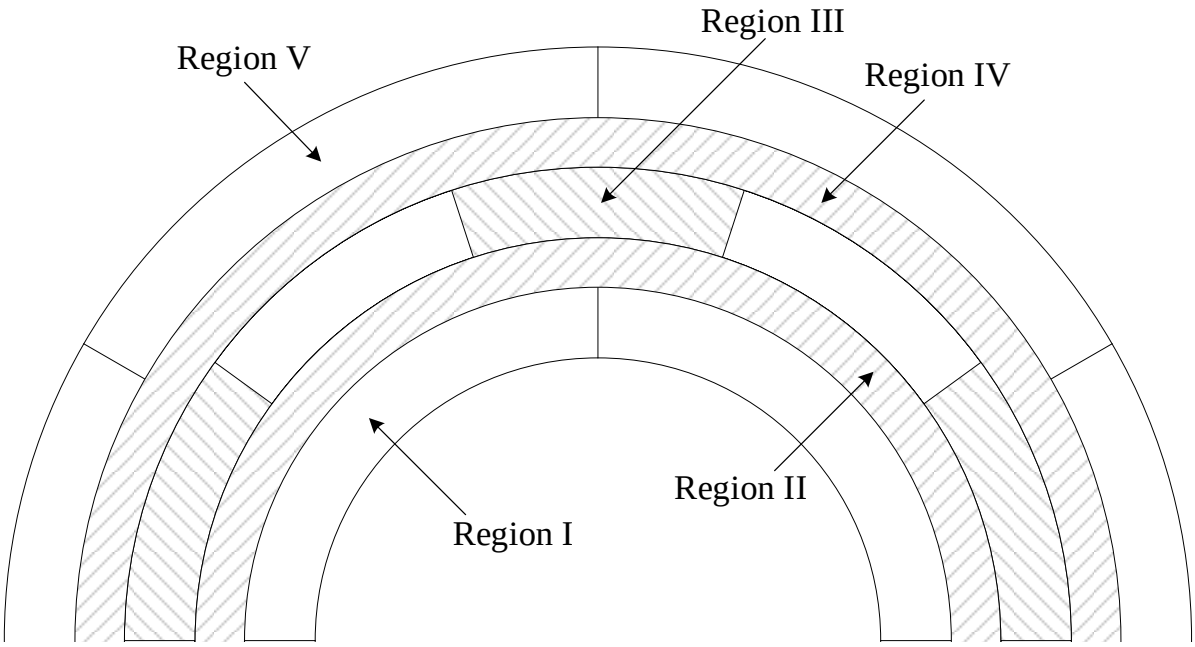

Figure 3-1 Region definition

is the separation of the CMG into individual, nominally concentric regions. Each of the rotors constitute a PM region (I, V) while the air-gap exists in three regions:

- Region II is the area between the modulation ring and the inner PM rotor.
- Region III is the air between the pole pieces.
- Region IV is the area between the modulation ring and the outer PM rotor.

The five regions are shown in Figure 3-1.

3.2.1 Modelling assumptions

In this model, the following assumptions, typical of analytical radial machine analyses are incorporated:

1. End effects are neglected.
2. In the PM regions, μ_r is equal to 1.
3. In the ferromagnetic regions, μ_r is equal to infinity.

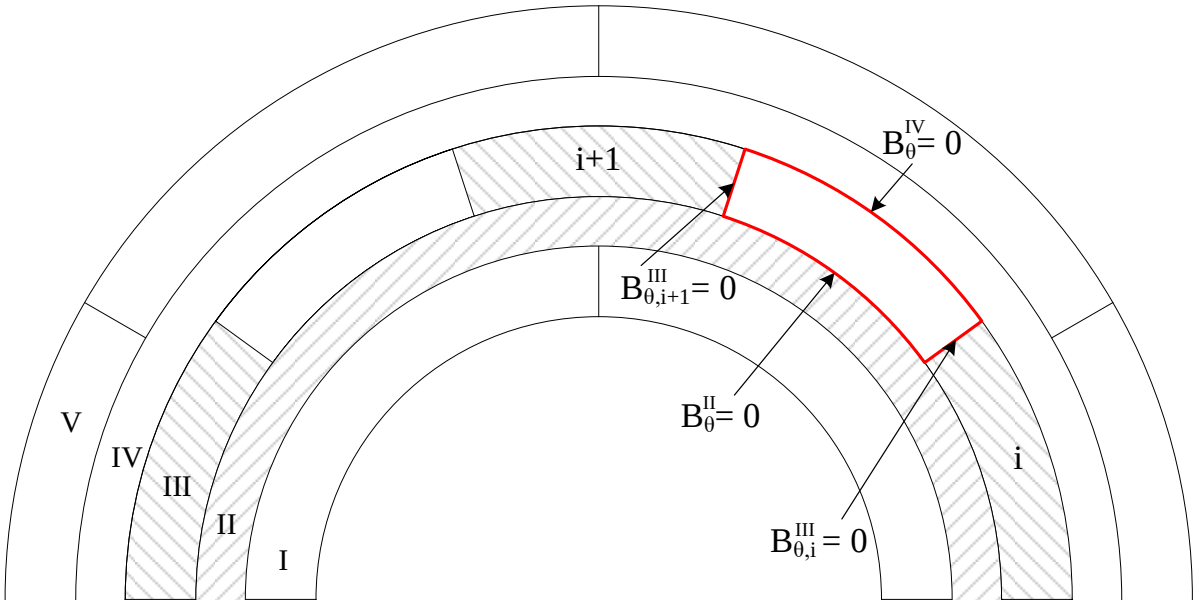

Figure 3-2 Pole piece emulation

A fundamental compromise with 2D radial flux analysis is that end-effects cannot be directly included in the model. However, in Chapter 1, literature was highlighted which provided an approach using aspect ratio to scale the 2D results to match the equivalent 3D. In addition, in 'long' machines the end effects are less dominant, and can therefore be assumed negligible. The recoil permeability (μ_r) of NdFeB PMs is very close to unity. It is therefore assumed equal to 1, due to the mathematical simplification it provides. Infinite permeability in the ferromagnetic regions is typically assumed in the analytical modelling of either CMGs or PM electric machines. In the CMG model, in addition to simplifying the mathematics, the effect of this assumption is that the magnetic vector potential in the ferromagnetic materials is not directly calculated. Instead, these materials are simulated using boundary conditions with the surrounding areas [82], [94]. For example, the pole piece highlighted in Figure 3-2 is emulated by considering the tangential component of the flux density to be zero (B_θ = 0) at the boundaries with the surrounding Region III slots and Region II and IV air-gaps. To facilitate this approximation, Region III is divided into

a number of subdomains, equal to that of pole pieces. Each subdomain therefore corresponds to an air-gap slot between consecutive pole pieces.

3.3 Asymmetric Analytical Model – Definition

In common with conventional analytical models, this asymmetric model is based on solutions of the magnetic vector potential ($\vec{A}$) in each region. Here a vector potential solution was adopted to follow the approach in [82], which focused on a radially symmetric model for a CMG. These solutions are developed using the definition of the magnetic vector potential (3.3.1) and Maxwell's Ampere law equation (3.3.2).

$$\vec{B} = \nabla \times \vec{A} \tag{3.3.1}$$

$$\nabla \times \vec{B} = \mu_0 \vec{J} + \mu_0 \varepsilon_0 \frac{\partial \vec{E}}{\partial t} \tag{3.3.2}$$

Considering equation (3.3.2), as a magnetostatic solution is required, the partial derivative of the electric flux density ($\vec{E}$) with respect to time disappears. Furthermore, as there is no applied current, the current density ($\vec{J}$) reduces to the curl of the magnetisation ($\vec{M}$) in the PM regions and zero elsewhere. Therefore, the equations (3.3.1) and (3.3.2) lead to (3.3.3) in the PM regions and (3.3.4) in all other regions. These take the form of the Poisson's (3.3.3) and Laplace's equations (3.3.4):

$$\nabla^2 \vec{A} = -\mu_0 \nabla \times \vec{M} \tag{3.3.3}$$

$$\nabla^2 \vec{A} = 0 \tag{3.3.4}$$

3.3.1 Region III – Modulation Ring Slots

The asymmetries considered in Region III are a combination of the dimensional and positional error of the pole pieces. Specifically, the geometric deviations considered are the length and span angle along with the radial and tangential position of each pole piece. The modelling of asymmetries in the modulation ring increases the complexity of the problem definition. As the magnetic vector potential is not directly calculated in the deviated materials, i.e., the pole pieces, their position will need to be emulated using the subdomains of Region III. However, any deviations will lead to an asymmetric air-gap slot, whose shape cannot be exactly replicated, as would be the case with the nominal, radially symmetric CMG. This additional challenge in the definition of Region III is not present when assessing PM rotor deviations, as the deviated component is directly defined as a modelling region.

Therefore, in this asymmetric analytical model three options are considered to define each Region III subdomain. The radial boundaries of each slot can be defined as follows:

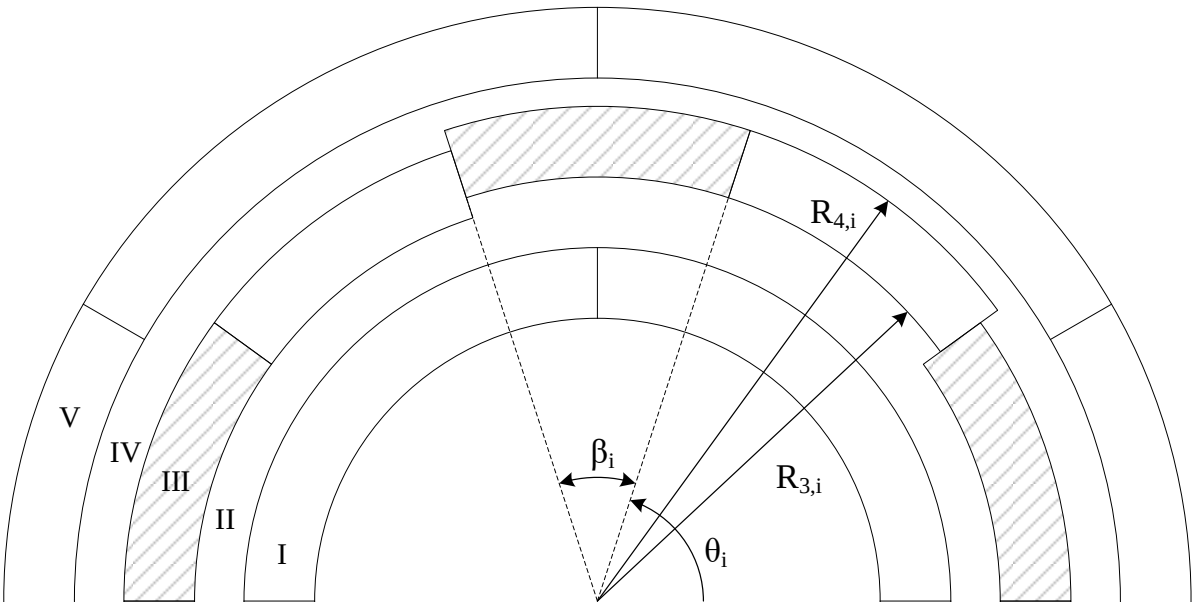

Figure 3-3 Definition of region III air-gap slot considering preceding pole piece

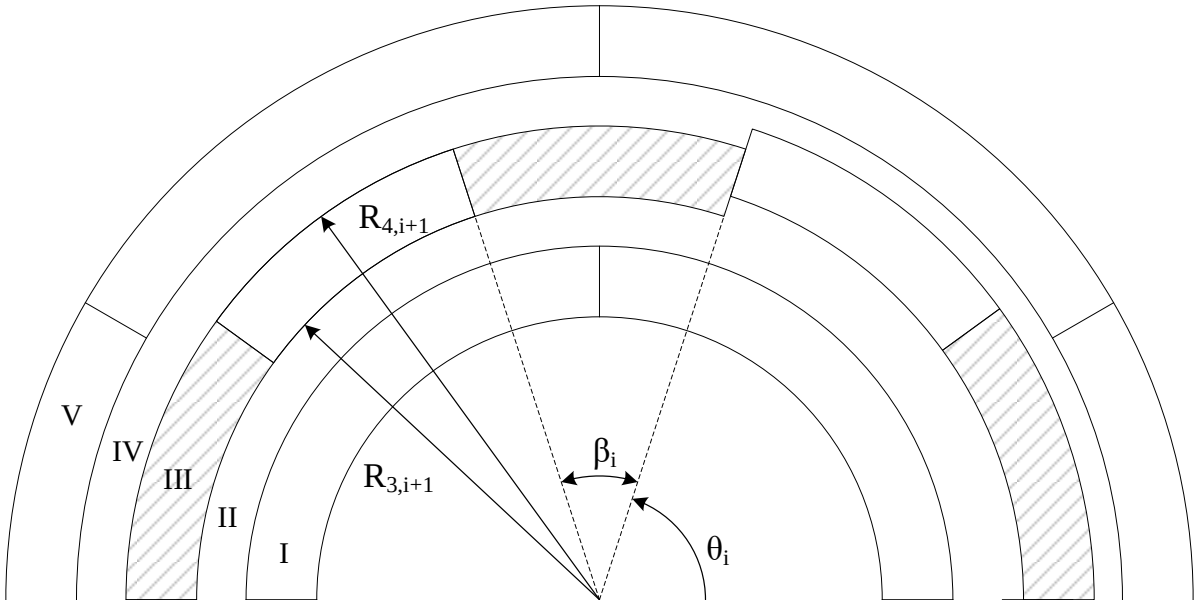

Figure 3-4 Definition of region III air-gap slot considering proceeding pole piece

1. Using the inner ($R_{3,\mathrm{i}}$) and outer ($R_{4,\mathrm{i}}$) radii of <u>preceding</u> (clockwise) pole piece (Figure 3-3).
2. Using the inner ($R_{3,\mathrm{i+1}}$) and outer ($R_{4,\mathrm{i+1}}$) radii of <u>proceeding</u> (anticlockwise) pole piece (Figure 3-4).
3. Using the <u>mean</u> inner $\left(R_{3,\mathrm{i}} + R_{3,\mathrm{i+1}}\right)/2$ and <u>mean</u> outer $\left(R_{4,\mathrm{i}} + R_{4,\mathrm{i+1}}\right)/2$ radii of the <u>preceding and proceeding</u> pole pieces (Figure 3-5).

The slot opening angle (β_i) and the initial angle of the subdomain with respect to a datum (θ_i) are defined as shown in the figures (Figure 3-3 – Figure 3-5). In this chapter the subdomains are defined with respect to the preceding pole piece (Figure 3-3) [94]. The differentiating factors between each definition are expanded further in Chapter 4. The general solution of $\vec{A}$ in each subdomain can now be derived from (3.3.4). The following notation in (3.3.5), (3.3.6) has been adopted for simplification:

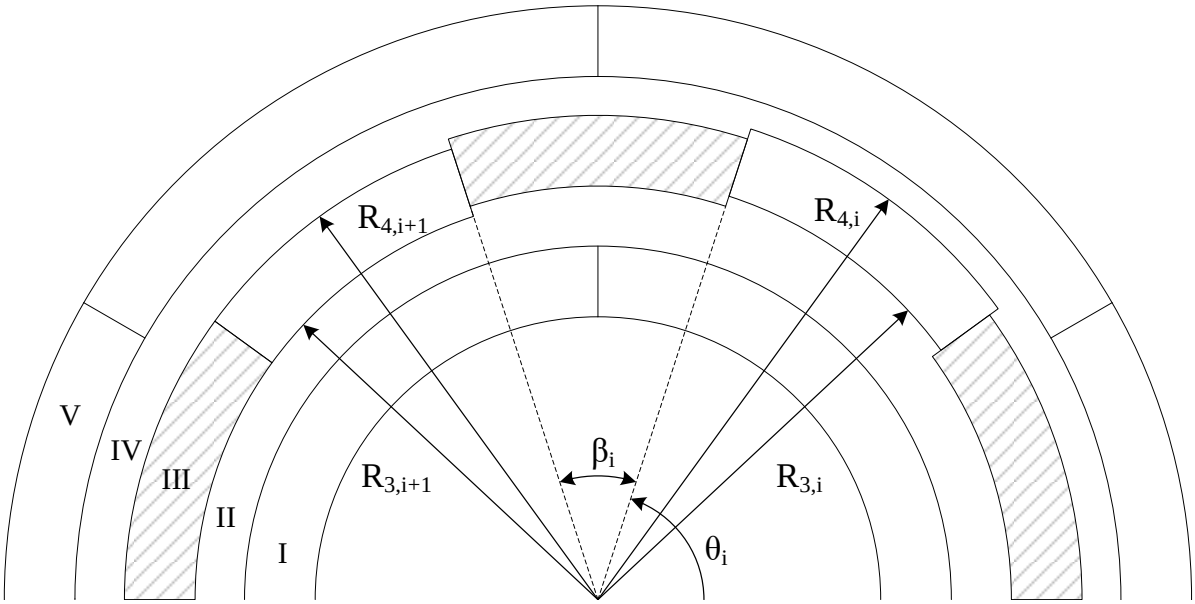

Figure 3-5 Definition of region III air-gap slot considering average radii

$$U_z(a,b) = \left(\frac{a}{b}\right)^z + \left(\frac{b}{a}\right)^z \tag{3.3.5}$$

$$X_z(a,b) = \left(\frac{a}{b}\right)^z - \left(\frac{b}{a}\right)^z \tag{3.3.6}$$

Using the separation of variables method, the general solution of the i[th] subdomain can be described by Fourier series and is provided in (3.3.7).

$$\begin{aligned} A_i^{(III)}(r,\theta) \; &= C_{III,i} + D_{III,i}\ln(r) \\ &+ \sum_{m=1}^{M}\left(E_{III,i,m}\frac{X_{f_{m,i}}(r,R_{4,s})}{X_{f_{m,i}}(R_{3,s},R_{4,s})} - F_{III,i,m}\frac{X_{f_{m,i}}(r,R_{3,s})}{X_{f_{m,i}}(R_{3,s},R_{4,s})}\right) \\ &\cdot\cos\left(f_{m,i}(\theta-\theta_i)\right) \end{aligned} \tag{3.3.7}$$

with

$$f_{m,i} = \frac{m\pi}{\beta_i} \tag{3.3.8}$$

$$s = i \tag{3.3.9}$$

where $C_{III,i}$, $D_{III,i}$, $E_{III,i,m}$ and $F_{III,i,m}$ are the Fourier coefficients and M denotes largest harmonic order considered.

3.3.2 Regions II, IV – Inner, Outer Airgaps

The geometric deviations considered in the modulation ring will also affect the definitions of the inner and outer air-gap regions, which are now asymmetric, similar to the Region III. To account for this asymmetry, Region II and IV variants are created, which are defined in the [0 – 2π] angular domain and are equal in number to the Region III subdomains [94]. This approach is similar to the one followed in [67], which modelled asymmetries in PM machine slots.

Each variant is associated with a Region III subdomain, which defines one of its radial boundaries. For example, the ith Region II variant is associated with the ith Region III subdomain. Therefore, its outer radial boundary will be $R_{3,s}$, with the inner boundary defined from Region I, i.e., R_2. The asymmetric solution of the magnetic field in the physical air-gap can then be synthesised by using the appropriate variant for the angular region it occupies (Figure 3-6).

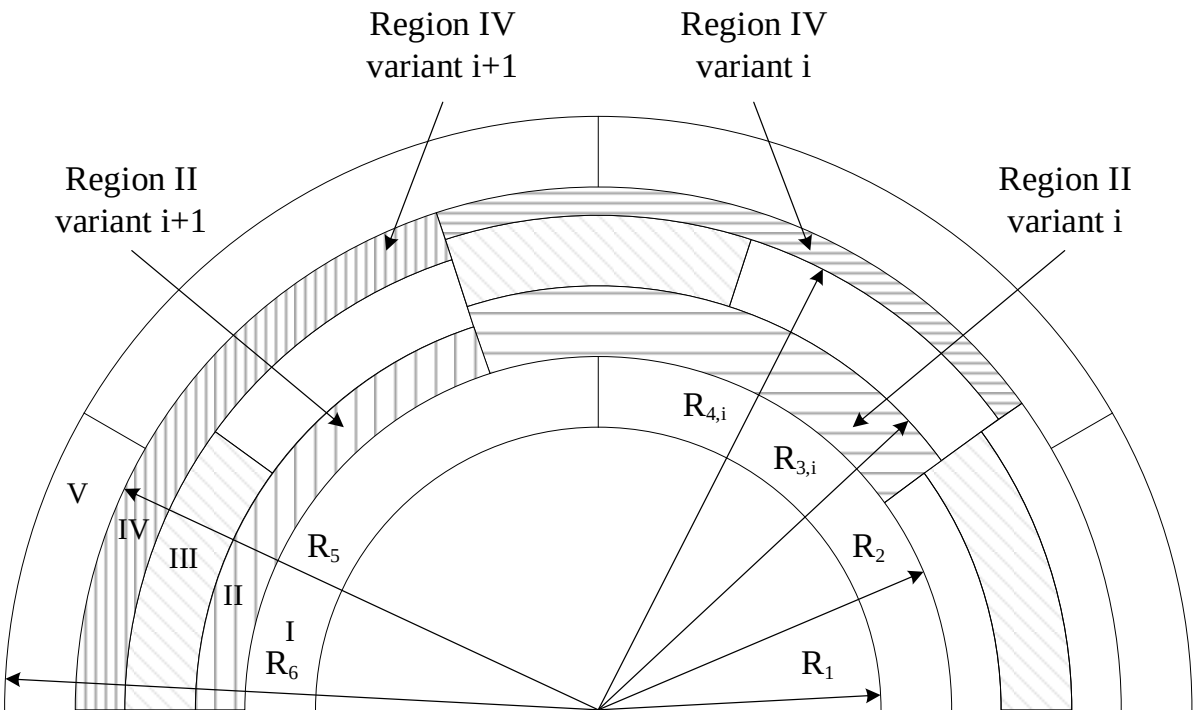

Figure 3-6 Region II / IV variant definitions considering the preceding definition

Similarly, each Region IV variant is associated with a Region III subdomain. In this case, the subdomain defines the inner radial boundary of the variant, e.g., $R_{4,s}$, with the outer boundary defined by Region V, i.e., R_5.

In common with section 3.3.1, using the separation of variables method and the Laplace equation (3.3.4), the general solution for each air-gap variant of Region II and IV can be derived. These solutions described by Fourier series are provided in (3.3.10), (3.3.11).

$$A_i^{(II)}(r,\theta) = \sum_{k=1}^{K}\left(C_{II,i}\frac{R_2}{k}\frac{U_k(r,R_{3,s})}{X_k(R_2,R_{3,s})} + D_{II,i}\frac{R_{3,s}}{k}\frac{U_k(r,R_2)}{X_k(R_{3,s},R_2)}\right)\cos(k\theta) + \sum_{k=1}^{K}\left(E_{II,i}\frac{R_2}{k}\frac{U_k(r,R_{3,s})}{X_k(R_2,R_{3,s})} + F_{II,i}\frac{R_{3,s}}{k}\frac{U_k(r,R_2)}{X_k(R_{3,s},R_2)}\right)\sin(k\theta) \tag{3.3.10}$$

$$A_i^{(IV)}(r,\theta) = \sum_{k=1}^{K}\left(C_{IV,i}\frac{R_{4,s}}{k}\frac{U_k(r,R_5)}{X_k(R_{4,s},R_5)} + D_{IV,i}\frac{R_5}{k}\frac{U_k(r,R_{4,s})}{X_k(R_5,R_{4,s})}\right)\cos(k\theta) + \sum_{k=1}^{K}\left(E_{IV,i}\frac{R_{4,s}}{k}\frac{U_k(r,R_5)}{X_k(R_{4,s},R_5)} + F_{IV,i}\frac{R_5}{k}\frac{U_k(r,R_{4,s})}{X_k(R_5,R_{4,s})}\right)\sin(k\theta) \tag{3.3.11}$$

where $C_{II/IV,i}$, $D_{II/IV,i}$, $E_{II/IV,i}$ and $F_{II/IV,i}$ are the Fourier coefficients and K denotes largest harmonic order considered.

3.3.3 Regions I, V – Inner, Outer PM Rotors

In this analysis, the inner and outer rotor PM regions are radially symmetric since geometric deviations of the rotors are assumed negligible and are thus not considered. N.B. – the inclusion of magnetisation errors can be modelled via the definition of the magnetisation function, building on the methods outlined in [67] and [95]. This model considers radial magnetisation of the PMs. Furthermore, infinite permeability is considered in the rotor yokes, leading to the following boundary conditions (3.3.12), (3.3.13):

$$B_\theta^{(I)}\Big|_{r=R_1} = 0 \tag{3.3.12}$$

$$B_\theta^{(V)}\Big|_{r=R_6} = 0 \tag{3.3.13}$$

Here, as the current density vector is non-zero due to the PM magnetisation, the general solutions are derived by solving the Poisson's equation (3.3.3) with the boundary conditions (3.3.12), (3.3.13), and are as follows:

$$A^{(I)}(r,\theta) = \sum_{k=1}^{K}\left(W_{1k}C_I + W_{2k}M_{rck}^{(I)}\right)\cos(k\theta) + \sum_{k=1}^{K}\left(W_{1k}E_I + W_{2k}M_{rsk}^{(I)}\right)\sin(k\theta) \tag{3.3.14}$$

$$A^{(V)}(r,\theta) = \sum_{k=1}^{K}\left(W_{3k}C_V + W_{4k}M_{rck}^{(V)}\right)\cos(k\theta) + \sum_{k=1}^{K}\left(W_{3k}E_V + W_{4k}M_{rsk}^{(V)}\right)\sin(k\theta) \tag{3.3.15}$$

where

$$W_{1k} = \frac{U_k(r,R_1)}{U_k(R_2,R_1)} \tag{3.3.16}$$

$$W_{2k} = \left[1+\frac{1}{k}\left(\frac{R_1}{r}\right)^{k+1}\right]\cdot r - \frac{U_k(r,R_1)}{U_k(R_2,R_1)}\left[1+\frac{1}{k}\left(\frac{R_1}{R_2}\right)^{k+1}\right]\cdot R_2 \tag{3.3.17}$$

$$W_{3k} = \frac{U_k(r,R_6)}{U_k(R_5,R_6)} \tag{3.3.18}$$

$$W_{4k} = \left[1+\frac{1}{k}\left(\frac{R_6}{r}\right)^{k+1}\right]\cdot r - \frac{U_k(r,R_6)}{U_k(R_5,R_6)}\left[1+\frac{1}{k}\left(\frac{R_6}{R_5}\right)^{k+1}\right]\cdot R_5 \tag{3.3.19}$$

and

$$M_{rck}^{(I,V)} = \frac{2PB_{rem}}{k\pi\mu_0} sin\left(\frac{k\pi\alpha_p}{P}\right)\cos(k\varphi_0) \tag{3.3.20}$$

$$M_{rsk}^{(I,V)} = \frac{2PB_{rem}}{k\pi\mu_0} sin\left(\frac{k\pi\alpha_p}{P}\right)\sin(k\varphi_0) \tag{3.3.21}$$

for k/P = 1, 3, 5, …

Each general solution is bounded by the inner (R_1, R_5) and outer (R_2, R_6) radii of each PM region. The parameter *k* denotes the order of harmonics in each region, with B_{rem} being the residual flux and *P*, μ_o, and α_p are the number of poles, the permeability of free space and the magnet arc to pole pitch ratio, respectively. The initial angular position of the rotor is defined by φ_o.

3.4 Asymmetric Analytical Model – Solution

The general solutions in (3.3.7), (3.3.10) – (3.3.15) can be solved as a system of equations by applying the necessary boundary conditions at the interfaces between regions. Considering the continuity of the radial component of the flux density and the tangential component of the field intensity, the following expressions can be defined at each interface.

3.4.1 Interface I – II

At the interface between the inner rotor (I) and the inner air-gap (II), the following boundary equations apply.

$$B_r^{(I)}\Big|_{r=R_2} = B_{r,i}^{(II)}\Big|_{r=R_2} \tag{3.4.1}$$

$$H_{\theta,i}^{(II)}\Big|_{r=R_2} = H_{\theta}^{(I)}\Big|_{r=R_2} \tag{3.4.2}$$

As each air-gap variant of Region II is defined in the whole annulus [0 – 2π], at this interface each variant exhibits the same continuity of H_θ and B_r with the PM region, as seen in (3.4.1), (3.4.2). Applying these boundary equations to (3.3.10) and (3.3.14) and using the respective Fourier series expansions the following equations are obtained.

$$C_I = \frac{1}{\pi}\int_0^{2\pi} B_{r,i}^{(II)}\Big|_{r=R_2} \cdot \cos(k\theta)\, d\theta \tag{3.4.3}$$

$$E_I = \frac{1}{\pi}\int_0^{2\pi} B_{r,i}^{(II)}\Big|_{r=R_2} \cdot \sin(k\theta)\, d\theta \tag{3.4.4}$$

$$C_{II,i,k} = \frac{1}{\pi}\int_0^{2\pi} H_\theta^{(I)}\Big|_{r=R_2} \cdot \cos(k\theta)\, d\theta \tag{3.4.5}$$

$$E_{II,i,k} = \frac{1}{\pi}\int_0^{2\pi} H_\theta^{(I)}\Big|_{r=R_2} \cdot \sin(k\theta)\, d\theta \tag{3.4.6}$$

Development of (3.4.3), (3.4.4) and (3.4.5), (3.4.6), results in equations (3.4.7) – (3.4.10), expressed in matrix form. The Fourier coefficients $\boldsymbol{C_I}, \boldsymbol{E_I}, \boldsymbol{C_{II}}, \boldsymbol{D_{II}}, \boldsymbol{E_{II}}$ and $\boldsymbol{F_{II}}$ are all column vector of length equal to $Q \cdot K$, where Q is the number of pole pieces and K the maximum number of harmonics of Region II. All constant terms are defined similarly and therefore the definition of only $\boldsymbol{G_1}$ is provided below. The same applies for the magnetisation column vectors that are defined as $\boldsymbol{M_{rck}^{(I)}}$ (3.4.17)**.**

$$\boldsymbol{I_{KQ}C_I + G_1C_{II} + G_2D_{II}} = 0 \tag{3.4.7}$$

$$\boldsymbol{I_{KQ}E_I + G_1E_{II} + G_2F_{II}} = 0 \tag{3.4.8}$$

$$\boldsymbol{G_3C_I + I_{KQ}C_{II}} = \boldsymbol{G_{13}} \cdot \boldsymbol{M_{rck}^{(I)}} \tag{3.4.9}$$

$$\boldsymbol{G_3E_I + I_{KQ}E_{II}} = \boldsymbol{G_{13}} \cdot \boldsymbol{M_{rsk}^{(I)}} \tag{3.4.10}$$

where

$$\boldsymbol{I_{KQ}} = \text{diag}(\boldsymbol{1}, \boldsymbol{1}, \dots, \boldsymbol{1})_{\boldsymbol{KQ}\times\boldsymbol{KQ}} \tag{3.4.11}$$

$$\boldsymbol{G_1} = \text{diag}(\boldsymbol{g_1(1)}, \boldsymbol{g_1(2)}, \dots, \boldsymbol{g_1(Q)})_{\boldsymbol{QK}\times\boldsymbol{QK}} \tag{3.4.12}$$

$$\boldsymbol{g_1(i)} = \boldsymbol{I_K} \cdot \left(-\frac{R_2}{k}\frac{U_k\left(R_2, R_{3,s}\right)}{X_k\left(R_2, R_{3,s}\right)}\right) \tag{3.4.13}$$

$$\boldsymbol{g_2(i)} = \boldsymbol{I_K} \cdot \left(-\frac{R_{3,s}}{k}\frac{2}{X_k\left(R_{3,s}, R_2\right)}\right) \tag{3.4.14}$$

$$\boldsymbol{g_3(i)} = \boldsymbol{I_K} \cdot \left(-\frac{k}{R_2}\frac{X_k(R_2, R_1)}{U_k(R_2, R_1)}\right) \tag{3.4.15}$$

$$\boldsymbol{g_{13}(i)} = \boldsymbol{I_K}\left(1 - \left(\frac{R_1}{R_2}\right)^{k+1} - \frac{k}{R_2}\frac{X_k(R_2, R_1)}{U_k(R_2, R_1)} \cdot \left(1 + \frac{1}{k}\left(\frac{R_1}{R_2}\right)^{k+1}\right)R_2\right) \tag{3.4.16}$$

$$\boldsymbol{M_{rck}^{(I)}} = \left[\boldsymbol{m_{rck}^{(I)}(1)}, \boldsymbol{m_{rck}^{(I)}(2)}, \dots, \boldsymbol{m_{rck}^{(I)}(Q)}\right]^{\boldsymbol{T}} \tag{3.4.17}$$

$$\boldsymbol{m_{rck}^{(I)}(i)} = \left[\boldsymbol{m_{rck}^{(I)}(1)}, \boldsymbol{m_{rck}^{(I)}(2)}, \dots, \boldsymbol{m_{rck}^{(I)}(K)}\right] \tag{3.4.18}$$

3.4.2 Interface II – III

Equations (3.3.7) and (3.3.10) can be developed further to obtain expressions for the interface between each inner air-gap variant of Region II and the modulation ring subdomains of Region III. The following boundary equations are be applied.

$$H_{\theta,i}^{(II)}\Big|_{r=R_{3,s}} = H_{\theta}^{(III)}\Big|_{r=R_{3,i=1}\rightarrow R_{3,i=Q}} \tag{3.4.19}$$

$$A_{i}^{(III)}\Big|_{r=R_{3,s}} = A_{i}^{(II)}\Big|_{r=R_{3,s}} \tag{3.4.20}$$

The geometric deviations create an asymmetric boundary between Regions II and III. However, mathematically, a continuity of H_θ and B_r must be defined at this interface. The boundary condition (3.4.19) maps the total field intensity of Region III $\left(H_{\theta}^{(III)}\right)$, at its asymmetric inner radial boundary $\left(R_{3,i=1} \rightarrow R_{3,i=Q}\right)$, to the field intensity of each Region II variant $\left(H_{\theta,i}^{(II)}\right)$, at its radially symmetric outer boundary $(R_{3,s})$. Furthermore, as at this interface there is no change of medium the continuity of the radial component of the flux density can be expressed as the continuity of the vector potential at the boundaries between each Region II variant and its associated Region III subdomain (3.4.20). Development of (3.3.7) and (3.3.10) along with these boundary conditions results in the following equations.

$$D_{II,i,k} = \frac{1}{\pi}\int_{0}^{2\pi} H_{\theta,i}^{(III)}\Big|_{r=R_{3,s}} \cdot \cos(k\theta)\, d\theta \tag{3.4.21}$$

$$F_{II,i,k} = \frac{1}{\pi}\int_{0}^{2\pi} H_{\theta,i}^{(III)}\Big|_{r=R_{3,s}} \cdot \sin(k\theta)\, d\theta \tag{3.4.22}$$

$$C_{III,i} + D_{III,i}\ln(R_{3,i}) = \frac{1}{\beta_i}\int_{\theta_i}^{\theta_i+\beta_i} A_i^{(II)}\Big|_{r=R_{3,s}} d\theta \tag{3.4.23}$$

$$E_{III,i} = \frac{2}{\beta_i}\int_{\theta_i}^{\theta_i+\beta_i} A_i^{(II)}\Big|_{r=R_{3,s}} \cdot \cos\big(f_{m,i}(\theta-\theta_i)\big)\, d\theta \tag{3.4.24}$$

Equations (3.4.21) – (3.4.24) can be expanded and expressed in matrix form (3.4.25) – (3.4.28). The Fourier coefficients $\boldsymbol{E_{III}}$ and $\boldsymbol{F_{III}}$ are column vectors of length $M \cdot Q$, with M representing the maximum number of harmonics in Region III. The coefficients $\boldsymbol{C_{III}}$ and $\boldsymbol{D_{III}}$ are column vectors of length equal to Q.

$$-\boldsymbol{I_{Ki\,R3}D_{II}} + \boldsymbol{\delta_i^T D_{III}} + \boldsymbol{\eta_i^T f_m G_4 E_{III}} - \boldsymbol{\eta_i^T f_m G_5 F_{III}} = 0 \tag{3.4.25}$$

$$-\boldsymbol{I_{Ki\,R3}F_{II}} + \boldsymbol{\sigma_i^T D_{III}} + \boldsymbol{\xi_i^T f_m G_4 E_{III}} - \boldsymbol{\xi_i^T f_m G_5 F_{III}} = 0 \tag{3.4.26}$$

$$\boldsymbol{\delta_{i,\pi} G_6 C_{II}} + \boldsymbol{\delta_{i,\pi} G_7 D_{II}} + \boldsymbol{\sigma_{i,\pi} G_6 E_{II}} + \boldsymbol{\sigma_{i,\pi} G_7 F_{II}} - \boldsymbol{I_Q C_{III}} - \boldsymbol{I_Q}\ln(R_{3,s})\,\boldsymbol{D_{III}} = 0 \tag{3.4.27}$$

$$\boldsymbol{\eta_{i,\pi} G_6 C_{II}} + \boldsymbol{\eta_{i,\pi} G_7 D_{II}} + \boldsymbol{\xi_{i,\pi} G_6 E_{II}} + \boldsymbol{\xi_{i,\pi} G_7 F_{II}} - \boldsymbol{I_{MQ} E_{III}} = 0 \tag{3.4.28}$$

where

$$\boldsymbol{I_{Ki\,R3}} = \mathrm{diag}(R_{3,1}, R_{3,2}, \dots, R_{3,Q})_{QK\times QK} \tag{3.4.29}$$

$$\delta(i,k) = \frac{1}{\pi}\int_{\theta_i}^{\theta_i+\beta_i} \cos(k\theta)\, d\theta \tag{3.4.30}$$

$$\boldsymbol{\delta_i} = \big(\delta(i,k), \delta(i,k), \dots, \delta(i,k)\big)_{Q\times QK} \tag{3.4.31}$$

$$\boldsymbol{\delta_{i,\pi}} = \mathrm{diag}\left(\frac{\pi}{\beta_i}\delta(1,k), \frac{\pi}{\beta_i}\delta(2,k) \dots, \frac{\pi}{\beta_i}\delta(Q,k)\right)_{Q\times QK} \tag{3.4.32}$$

$$\sigma(i,k) = \frac{1}{\pi}\int_{\theta_i}^{\theta_i+\beta_i} \sin(k\theta)\, d\theta \tag{3.4.33}$$

$$\eta(m,k,i) = \frac{1}{\pi}\int_{\theta_i}^{\theta_i+\beta_i} \cos(k\theta)\cdot\cos\big(f_{m,i}(\theta-\theta_i)\big)\, d\theta \tag{3.4.34}$$

$$\boldsymbol{\eta_i} = \begin{bmatrix} \eta(m,k,1) & \cdots & \eta(m,k,1) \\ \vdots & \ddots & \vdots \\ \eta(m,k,Q) & \cdots & \eta(m,k,Q) \end{bmatrix}_{QM\times QK} \tag{3.4.35}$$

$$\boldsymbol{\eta_{i,\pi}} = \mathrm{diag}\left(\frac{2\pi}{\beta_i}\boldsymbol{\eta}(m,k,1), \frac{2\pi}{\beta_i}\boldsymbol{\eta}(m,k,2), \dots, \frac{2\pi}{\beta_i}\boldsymbol{\eta}(m,k,Q)\right)_{QM\times QK} \tag{3.4.36}$$

$$\xi(m,k,i) = \frac{1}{\pi}\int_{\theta_i}^{\theta_i+\beta_i} \sin(k\theta)\cdot\cos\left(f_{m,i}(\theta-\theta_i)\right) d\theta \tag{3.4.37}$$

$$\boldsymbol{f_{m,i}} = f_{m,i}\cdot\boldsymbol{I_M} \tag{3.4.38}$$

$$\boldsymbol{f_m} = \mathrm{diag}\left(\boldsymbol{f_{m,i}}(1), \boldsymbol{f_{m,i}}(2), \dots, \boldsymbol{f_{m,i}}(Q)\right) \tag{3.4.39}$$

$$\boldsymbol{G_4} = \mathrm{diag}(\boldsymbol{g_4}(1), \boldsymbol{g_4}(2), \dots, \boldsymbol{g_4}(Q))_{QM\times QM} \tag{3.4.40}$$

$$\boldsymbol{g_4(i)} = \boldsymbol{I_M} \cdot \left(\frac{U_{f_{m,i}}\left(R_{3,s}, R_{4,s}\right)}{X_{f_{m,i}}\left(R_{3,s}, R_{4,s}\right)} \right) \tag{3.4.41}$$

$$\boldsymbol{g_5(i)} = \boldsymbol{I_M} \cdot \left(\frac{2}{X_{f_{m,i}}\left(R_{3,s}, R_{4,s}\right)} \right) \tag{3.4.42}$$

$$\boldsymbol{g_6(i)} = \boldsymbol{I_K} \cdot \left(\frac{R_2}{k} \frac{2}{X_k\left(R_2, R_{3,s}\right)} \right) \tag{3.4.43}$$

$$\boldsymbol{g_7(i)} = \boldsymbol{I_K} \cdot \left(\frac{R_{3,s}}{k} \frac{U_k\left(R_{3,s}, R_2\right)}{X_k\left(R_{3,s}, R_2\right)} \right) \tag{3.4.44}$$

3.4.3 Interface III – IV

Similar to section 3.4.2, the respective boundary conditions applied to the interface between the Region III slot and Region IV outer air-gap subdomains are as follows:

$$H_{\theta,i}^{(IV)}\Big|_{r=R_{4,s}} = H_{\theta}^{(III)}\Big|_{r=R_{4,i=1}\rightarrow R_{4,i=Q}} \tag{3.4.45}$$

$$A_i^{(III)}\Big|_{r=R_{4,s}} = A_i^{(IV)}\Big|_{r=R_{4,s}} \tag{3.4.46}$$

Here, the boundary condition (3.4.45) maps the total field intensity of Region III $\left(H_{\theta}^{(III)}\right)$, at its asymmetric outer radial boundary $\left(R_{4,i=1} \rightarrow R_{4,i=Q}\right)$, to the field intensity of each Region IV variant $\left(H_{\theta,i}^{(IV)}\right)$, at its radially symmetric outer boundary ($R_{4,s}$). In common with (3.4.20), boundary condition (3.4.46) defines the continuity of the magnetic vector potential at the radially symmetric boundary between each Region IV variant and its associated Region III subdomain.

The application of boundary equations (3.4.45), (3.4.46) to (3.3.10), (3.3.15) results in the following expressions:

$$C_{IV,i,k} = \frac{1}{\pi}\int_{0}^{2\pi} H_{\theta,i}^{(III)}\Big|_{r=R_{4,s}} \cdot \cos(k\theta)\, d\theta \tag{3.4.47}$$

$$E_{IV,i,k} = \frac{1}{\pi}\int_{0}^{2\pi} H_{\theta,i}^{(III)}\Big|_{r=R_{4,s}} \cdot \sin(k\theta)\, d\theta \tag{3.4.48}$$

$$C_{III,i} + D_{III,i}\ln\left(R_{4,s}\right) = \frac{1}{\beta_i}\int_{\theta_i}^{\theta_i+\beta_i} A_i^{(IV)}\Big|_{r=R_{4,s}} d\theta \tag{3.4.49}$$

$$F_{III,i} = \frac{2}{\beta_i}\int_{\theta_i}^{\theta_i+\beta_i} A_i^{(IV)}\Big|_{r=R_{4,s}} \cdot \cos(f_{m,i}(\theta-\theta_i))\, d\theta \tag{3.4.50}$$

Development of equations (3.4.47) – (3.4.50) , expressed in matrix form, leads to (3.4.51) – (3.4.54).

$$-\boldsymbol{I_{Ki\,R4}C_{IV}} + \boldsymbol{\delta_i^T D_{III}} + \boldsymbol{\eta_i^T f_m G_5 E_{III}} - \boldsymbol{\eta_i^T f_m G_4 F_{III}} = 0 \tag{3.4.51}$$

$$-\boldsymbol{I_{Ki\,R4}E_{IV}} + \boldsymbol{\sigma_i^T D_{III}} + \boldsymbol{\xi_i^T f_m G_5 E_{III}} - \boldsymbol{\xi_i^T f_m G_4 F_{III}} = 0 \tag{3.4.52}$$

$$\boldsymbol{\delta_{i,\pi} G_8 C_{IV}} + \boldsymbol{\delta_{i,\pi} G_9 D_{IV}} + \boldsymbol{\sigma_{i,\pi} G_8 E_{IV}} + \boldsymbol{\sigma_{i,\pi} G_9 F_{IV}} - \boldsymbol{I_Q C_{III}} - \boldsymbol{I_Q}\ln\left(R_{4,s}\right)\boldsymbol{D_{III}} = 0 \tag{3.4.53}$$

$$\boldsymbol{\eta_{i,\pi} G_8 C_{IV}} + \boldsymbol{\eta_{i,\pi} G_9 D_{IV}} + \boldsymbol{\xi_{i,\pi} G_8 E_{IV}} + \boldsymbol{\xi_{i,\pi} G_9 F_{IV}} - \boldsymbol{I_{MQ} F_{III}} = 0 \tag{3.4.54}$$

where

$$\boldsymbol{g_8(i) = I_K \cdot \left(\frac{R_{4,s}}{k} \frac{U_k\left(R_{4,s}, R_5\right)}{X_k\left(R_{4,s}, R_5\right)} \right)} \tag{3.4.55}$$

$$\boldsymbol{g_9(i) = I_K \cdot \left(\frac{R_5}{k} \frac{2}{X_k\left(R_5, R_{4,s}\right)} \right)} \tag{3.4.56}$$

3.4.4 Interface IV – V

The fourth interface, between the outer air-gap (IV) and outer rotor PM subdomains (V) can be expressed similar to section 3.4.1. Therefore, the respective boundary conditions are provided in (3.4.57), (3.4.58).

$$B_r^{(V)}\Big|_{r=R_5} = B_{r,i}^{(IV)}\Big|_{r=R_5} \tag{3.4.57}$$

$$H_{\theta,i}^{(IV)}\Big|_{r=R_5} = H_\theta^{(V)}\Big|_{r=R_5} \tag{3.4.58}$$

Algebraic manipulation of (3.3.15), (3.3.17) along with boundary conditions (3.4.57), (3.4.58) results in the following equations, expressed in matrix form.

$$\boldsymbol{I_{KQ} C_V + G_{10} C_{IV} + G_{11} D_{IV}} = 0 \tag{3.4.59}$$

$$\boldsymbol{I_{KQ} E_V + G_{10} E_{IV} + G_{11} F_{IV}} = 0 \tag{3.4.60}$$

$$\boldsymbol{G_{12} C_V + I_{KQ} D_{IV} = G_{14} \cdot M_{rck}^{(V)}} \tag{3.4.61}$$

$$\boldsymbol{G_{12} E_V + I_{KQ} F_{IV} = G_{14} \cdot M_{rsk}^{(V)}} \tag{3.4.62}$$

where

$$\boldsymbol{g_{10}(i)} = \boldsymbol{I_K} \cdot \left(-\frac{R_{4,i}}{k} \frac{2}{X_k\left(R_{4,s}, R_5\right)} \right) \tag{3.4.63}$$

$$\boldsymbol{g_{11}(i)} = \boldsymbol{I_K} \cdot \left(-\frac{R_5}{k} \frac{U_k\left(R_5, R_{4,s}\right)}{X_k\left(R_5, R_{4,s}\right)} \right) \tag{3.4.64}$$

$$\boldsymbol{g_{12}(i)} = \boldsymbol{I_K} \cdot \left(-\frac{k}{R_5} \frac{X_k(R_5, R_6)}{U_k(R_5, R_6)} \right) \tag{3.4.65}$$

$$\boldsymbol{g_{14}(i)} = \boldsymbol{I_K} \left(1 - \left(\frac{R_6}{R_5}\right)^{k+1} - \frac{k}{R_5} \frac{X_k(R_5, R_6)}{U_k(R_5, R_6)} \cdot \left(1 + \frac{1}{k} \left(\frac{R_6}{R_5}\right)^{k+1} \right) R_5 \right) \tag{3.4.66}$$

3.4.5 Overall Solution

The equations developed in this chapter form a system of linear equations that are solved simultaneously to calculate all the unknown Fourier coefficients. The flux density distributions in each Region II/IV variant can then be calculated using the following expressions:

$$\begin{aligned} B_{r,i}^{(II)}(r,\theta) = &\sum_{k=1}^{K} -\left(C_{II,i} \frac{R_2}{r} \frac{U_k\left(r, R_{3,s}\right)}{X_k\left(R_2, R_{3,s}\right)} + D_{II,i} \frac{R_{3,s}}{r} \frac{U_k(r, R_2)}{X_k\left(R_{3,s}, R_2\right)} \right) \sin(k\theta) \\ &+ \sum_{k=1}^{K} \left(E_{II,i} \frac{R_2}{r} \frac{U_k\left(r, R_{3,s}\right)}{X_k\left(R_2, R_{3,s}\right)} + F_{II,i} \frac{R_{3,s}}{r} \frac{U_k(r, R_2)}{X_k\left(R_{3,s}, R_2\right)} \right) \cos(k\theta) \end{aligned} \tag{3.4.67}$$

$$\begin{aligned} B_{\theta,i}^{(II)}(r,\theta) = &\sum_{k=1}^{K} -\left(C_{II,i} \frac{R_2}{r} \frac{X_k\left(r, R_{3,s}\right)}{X_k\left(R_2, R_{3,s}\right)} + D_{II,i} \frac{R_{3,s}}{r} \frac{X_k(r, R_2)}{X_k\left(R_{3,s}, R_2\right)} \right) \cos(k\theta) \\ &- \sum_{k=1}^{K} \left(E_{II,i} \frac{R_2}{r} \frac{X_k\left(r, R_{3,s}\right)}{X_k\left(R_2, R_{3,s}\right)} + F_{II,i} \frac{R_{3,s}}{r} \frac{X_k(r, R_2)}{X_k\left(R_{3,s}, R_2\right)} \right) \sin(k\theta) \end{aligned} \tag{3.4.68}$$

$$B_{r,i}^{(IV)}(r,\theta) = \sum_{k=1}^{K} -\left(C_{IV,i}\frac{R_{4,s}}{k}\frac{U_k(r,R_5)}{X_k(R_{4,s},R_5)} + D_{IV,i}\frac{R_5}{k}\frac{U_k(r,R_{4,s})}{X_k(R_5,R_{4,s})}\right)\sin(k\theta) + \sum_{k=1}^{K}\left(E_{IV,i}\frac{R_{4,s}}{r}\frac{U_k(r,R_5)}{X_k(R_{4,s},R_5)} + F_{IV,i}\frac{R_5}{r}\frac{U_k(r,R_{4,s})}{X_k(R_5,R_{4,s})}\right)\cos(k\theta) \tag{3.4.69}$$

$$B_{\theta,i}^{(IV)}(r,\theta) = \sum_{k=1}^{K} -\left(C_{IV,i}\frac{R_{4,s}}{r}\frac{X_k(r,R_5)}{X_k(R_{4,s},R_5)} + D_{IV,i}\frac{R_5}{r}\frac{X_k(r,R_{4,s})}{X_k(R_5,R_{4,s})}\right)\cos(k\theta) - \sum_{k=1}^{K}\left(E_{IV,i}\frac{R_{4,s}}{r}\frac{X_k(r,R_5)}{X_k(R_{4,s},R_5)} + F_{IV,i}\frac{R_5}{r}\frac{X_k(r,R_{4,s})}{X_k(R_5,R_{4,s})}\right)\sin(k\theta) \tag{3.4.70}$$

A key novelty of this analytical model lies in treatment of the asymmetric boundaries between Regions II-III and III-IV. It is reasonable to expect that the primary flux density discrepancy from each deviation will be spatially focused on the vicinity of the deviation. This effect is taken into account through the synthesis of the flux distribution using the equivalent air-gap variants. Considering Region II, the flux distribution in this physical air-gap is synthesised by concatenating the flux distributions of each variant for the angular domain they occupy, as explained in section 3.3.2 and Figure 3-6. However, each deviation will also have an effect on the whole field distribution. This is approximated through the selected boundary conditions at the interface between Regions II-III and III-IV, as shown in sections 3.4.2 and 3.4.3, respectively. Specifically, as the total, and thus same Region III field intensity is mapped to the radial boundaries of each Region II/IV variant, the effect of each deviation on the flux distribution is not only quantified in the vicinity of the deviation but also in the remaining space.

An alternative modelling approach would be to use the principle of superposition, as shown in [96] in the context of electric machines. With this method, the resultant air-gap flux distribution would again be synthesised but from a series of radially symmetric CMG instances. Each instance

would adopt the deviated radius of its respective pole piece. However, such an approach considers each deviation in isolation and therefore does not account for the effects on the complete flux distribution, rather just in the vicinity of the deviation. This will introduce an error, which will become more dominant when larger deviations are present. In addition, this approach would also increase the computational time from the introduction of additional Fourier coefficients. Specifically, as full CMG models are used, the number of unknown coefficients in Region III will be multiplied by the number CMG models used, i.e., the number of pole pieces.

3.4.6 Torque and Force Calculation

The torque exerted on each rotor is calculated using the Maxwell Stress Tensor (MST). The air-gap subdomain is integrated along a contour, placed in the middle of the narrowest air-gap section. Therefore, the torque is given by (3.4.71):

$$T = \frac{L \cdot R_{air-gap}^2}{\mu_0} \int_0^{2\pi} B_r^{(II/IV)}(R_{air-gap}, \theta) \cdot B_\theta^{(II/IV)}(R_{air-gap}, \theta) \cdot d\theta \tag{3.4.71}$$

Due to the synthesis of the resultant flux density distributions, the distribution of each variant needs to be evaluated prior to the evaluation of the integral. Therefore, for the HSR torque (Region II), algebraic manipulation of equation (3.4.71) leads to (3.4.72). A similar expression can be deduced for the LSR torque (Region IV):

$$T = \frac{L \cdot R_{air-gap}^2}{\mu_0} \left(\sum_{i=1}^{Q} \left(\sum_{k=1}^{2K} \sum_{l=1}^{k} O_{II,i,k} \cdot V_{II,i,j} - \sum_{k=1}^{K} \sum_{l=K+1}^{2K-k+1} O_{II,i,k} \cdot V_{II,i,l} \right) \right) \tag{3.4.72}$$

where

$$j = k - l + 1 \tag{3.4.73}$$

$$\begin{aligned} O_{II,i,k} = &-\left(C_{II,i,k}\frac{R_2}{r}\frac{U_k(r,R_{3,i})}{X_k(R_2,R_{3,i})} + D_{II,i,k}\frac{R_{3,i}}{r}\frac{U_k(r,R_2)}{X_k(R_{3,i},R_2)}\right)\cdot\int_{\theta_i}^{\theta_{i+1}}\sin(k\theta)\,d\theta \\ &+\left(E_{II,i,k}\frac{R_2}{r}\frac{U_k(r,R_{3,i})}{X_k(R_2,R_{3,i})} + F_{II,i,k}\frac{R_{3,i}}{r}\frac{U_k(r,R_2)}{X_k(R_{3,i},R_2)}\right)\cdot\int_{\theta_i}^{\theta_{i+1}}\cos(k\theta)\,d\theta \end{aligned} \tag{3.4.74}$$

$$\begin{aligned} V_{II,i,j} = &-\left(C_{II,i,j}\frac{R_2}{r}\frac{X_k(r,R_{3,i})}{X_k(R_2,R_{3,i})} + D_{II,i,j}\frac{R_{3,i}}{r}\frac{X_k(r,R_2)}{X_k(R_{3,i},R_2)}\right)\cdot\int_{\theta_i}^{\theta_{i+1}}\cos(j\theta)\,d\theta \\ &-\left(E_{II,i,j}\frac{R_2}{r}\frac{X_k(r,R_{3,i})}{X_k(R_2,R_{3,i})} + F_{II,i,j}\frac{R_{3,i}}{r}\frac{X_k(r,R_2)}{X_k(R_{3,i},R_2)}\right)\cdot\int_{\theta_i}^{\theta_{i+1}}\sin(j\theta)\,d\theta \end{aligned} \tag{3.4.75}$$

Similarly, the magnetostatic force exerted on each pole piece can be calculated by integrating the MST along a contour, enclosing the respective pole piece. Therefore, the radial and tangential forces are given by (3.4.76), (3.4.77).

$$F_r = \frac{L}{\mu_0}\int_S \frac{B_r^2 - B_\theta^2}{2}ds \tag{3.4.76}$$

$$F_\theta = \frac{L}{\mu_0}\int_S B_r B_\theta ds \tag{3.4.77}$$

Table 5 CMG Parameters for Model Validation

Variables	CMG 1	CMG 2
Number of pole pieces	5	7
Inner rotor poles	4	6
Outer rotor poles	6	8
Inner rotor OD (mm)	100 mm	100 mm
Outer rotor OD (mm)	148 mm	148 mm
PM length (mm)	10 mm	10 mm
Pole pieces length (mm)	10 mm	10 mm
Air-gap length (mm)	2 mm	0.5 mm
Axial length (mm)	100 mm	100 mm

3.5 Asymmetric Analytical Model – Validation

The analytical model is validated by comparing a solution of two sample deviated CMGs to their 2D FEA equivalent of the same geometry. For the purpose of this validation, a degree of error has been arbitrarily introduced to the two dimensions and radial and tangential position of each pole piece. The parameters of the CMGs along with the respective geometric errors are provided in Table 5 and Table 6.

For both air-gap Regions (II and IV) along with the modulation ring subdomains (III), the first 200 harmonics are considered. The analytical model field solution is calculated at the middle of the narrowest inner air-gap section, i.e., between Region I and the most inward deviated pole piece, and is compared to the respective FEA results in Figure 3-7 and Figure 3-8. The resultant flux plots show the very good correlation between the analytical model and FEA, under the same assumption of infinite permeability in the ferromagnetic regions. It must be noted that in the case of CMG 2 (Figure 3-8), because of the much smaller air-gap, the infinite permeability assumption results in some unrealistic flux density values near 3 T.

Table 6 Parameter Error for Model Validation

Variable	Pole Piece Error						
CMG 1							
	No. 1	***No. 2***	***No. 3***	***No. 4***	***No. 5***		
Length (mm)	0.018	-0.014	0.001	-0.020	-0.019		
Span angle (deg)	0.019	-0.018	0.001	0.009	0.018		
Radial position (mm)	-0.001	0.204	-0.103	0.050	-0.030		
Angular position (deg)	0.206	0.011	-0.199	-0.099	-0.142		
CMG 2							
	No. 1	***No. 2***	***No. 3***	***No. 4***	***No. 5***	***No. 6***	***No. 7***
Length (mm)	0.009	0.005	0.060	0.012	-0.002	0.011	0.008
Span angle (deg)	-0.038	-0.007	-0.023	-0.012	-0.024	0.012	0.012
Radial position (mm)	0.122	-0.087	0.185	-0.004	0.099	-0.081	0.069
Angular position (deg)	0.058	0.023	0.202	-0.014	0.095	0.109	-0.020

The fundamental advantage of this model over its FE equivalent is the computational efficiency. The computational efficiency of this approach is directly linked to the number of harmonics used. The consideration of higher-order harmonics can increase the accuracy of the model, however this comes at the expense of computational time. The relationship between the number of harmonics and the accuracy and speed of the model is shown in Figure 3-9. Here, a common number of harmonics has been considered for all regions. It is observed that the analytical torque results for CMG 1 and CMG 2 converge to the FEA after the first 70 and 100 harmonics, respectively. The computational time for this harmonic set is 1.7 s for CMG 1 and 6.5 s for CMG 2, using a computer of the following specifications (Intel(R) Core(TM) i7-6700 CPU @ 3.40GHz, 16 GB RAM). For comparison, the FEA required 2:05 minutes, thus representing a very significant decrease in computational efficiency. High finite element mesh density is necessary in order to minimise the error induced by the change in the mesh form. Specifically, in such asymmetric

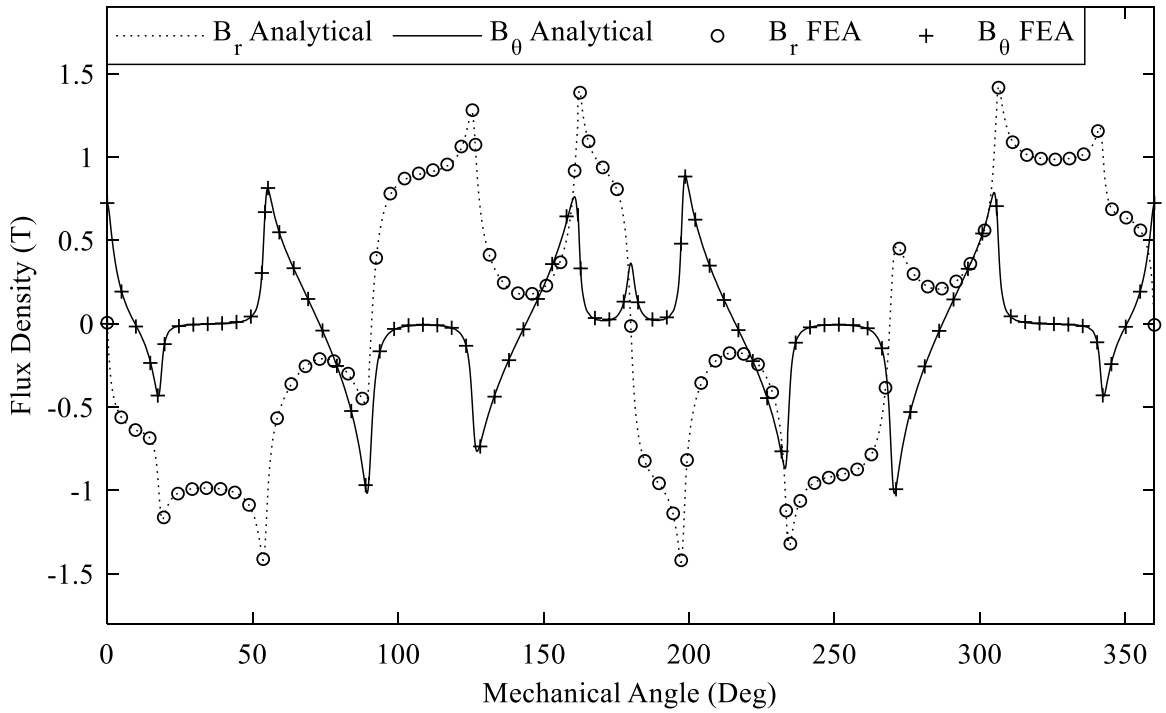

Figure 3-7 Analytical vs linear FEA flux density comparison – CMG 1

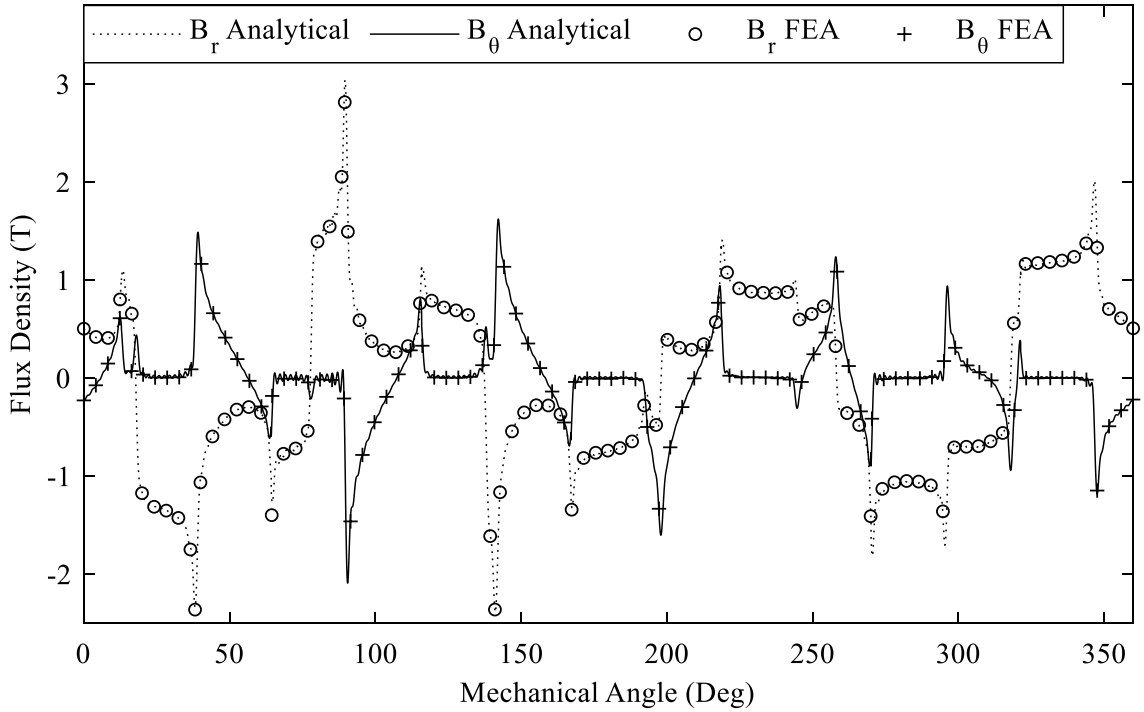

Figure 3-8 Analytical vs linear FEA flux density comparison – CMG 2

models the mesh form will be different to the nominal even with the same mesh parameters, as they are practically a new geometry. This change in the mesh form alone induces a small error in the output variable and if this error is of the same order of magnitude as the error of the asymmetry, the results will be inconclusive. It must be noted that the FEA is not optimised for speed, however, considering the difference in computational times even an optimised FE model would still be significantly slower than the equivalent analytical solution.

Finally, due to the separation of the model in its regions, different order of harmonics can be used for each one and therefore the computational efficiency can be increased further depending on the required task. For example, if the accuracy in the torque calculation is more important than in the forces exerted on the pole pieces, then a lower order of harmonics for Region III can be selected, while retaining the desired accuracy and increasing the computational speed.

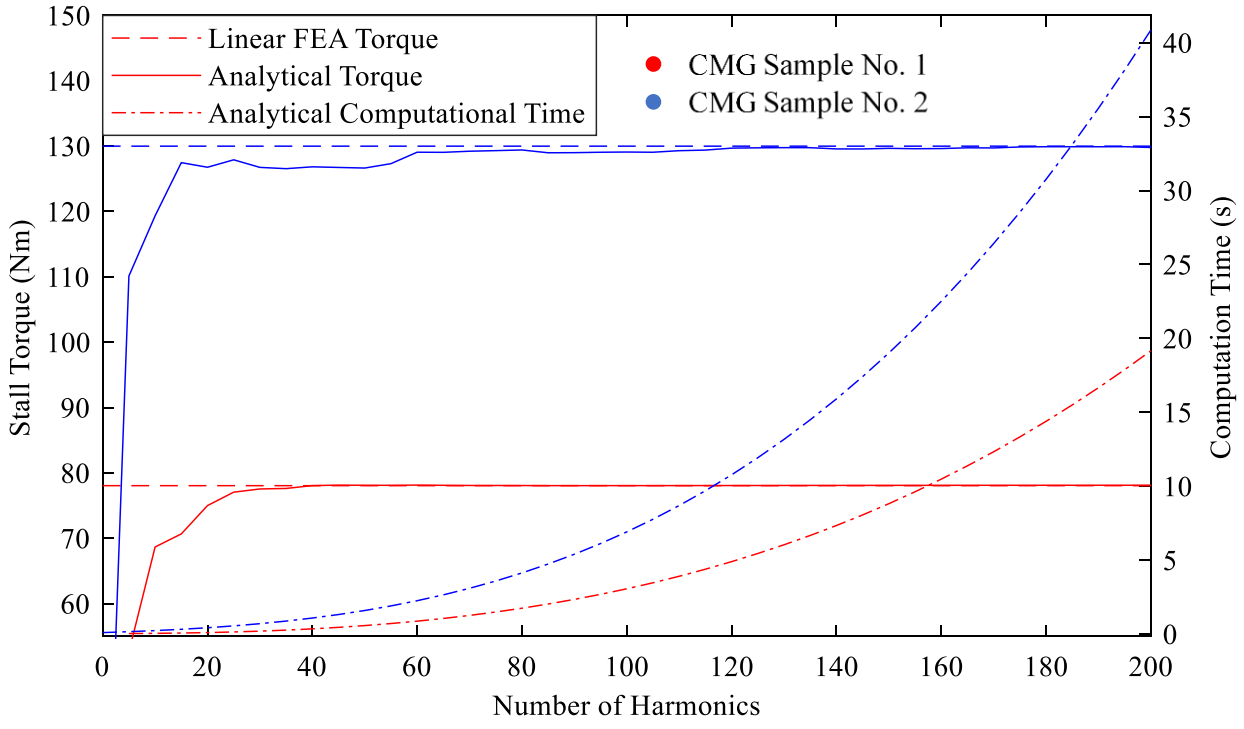

Figure 3-9 Model Harmonics vs accuracy and speed for sample CMG

3.6 Asymmetric Analytical Model – Limitations

3.6.1 Limitations due to assumption of infinite permeability in the pole pieces

One limitation of the analytical model stems from the assumption of infinite permeability in the pole pieces. The saturation in the gear has a deteriorating effect on the analytical model's accuracy. This is evident from the difference in absolute torque between the analytical model, and FEA, considering non-linear permeability. In particular, considering the deviated sample of CMG 1, the difference in terms of absolute torque is 11%. In Chapter 4, it is shown that in Monte-Carlo simulations, normalisation of the results with respect to the nominal torque allows the analytical model to yield accurate statistical results. Notwithstanding this, the fact that the analytical model cannot synthesise saturation in the poles, must be appreciated when generally considering its usage.

3.6.2 Limitations due to modelling definition

Similar to the infinite permeability assumption, all the assumptions considered, along with the subsequent limitations, restrict the use and accuracy of an analytical model. As explained in sections 3.2, 3.3, geometric deviations will create an asymmetry in the air-gap slot between consecutive pole pieces. This is much harder to model than the nominal case. Therefore, it is approximated by defining the Region III subdomains as detailed in 3.3.1 and Figure 3-3 – Figure 3-5. In the author's view, this is the root of the main limitation of this analytical model.

Figure 3-10 presents the simple deviated case where the only deviation is the radial deviation of just one pole piece. Therefore, according to the Region III air-gap slot definitions of section 3.3.1 and for the $s = i$ case, the "i^{th}" subdomain will be defined radially by the boundaries of the deviated pole piece. A fundamental assumption in this definition is that the tangential component

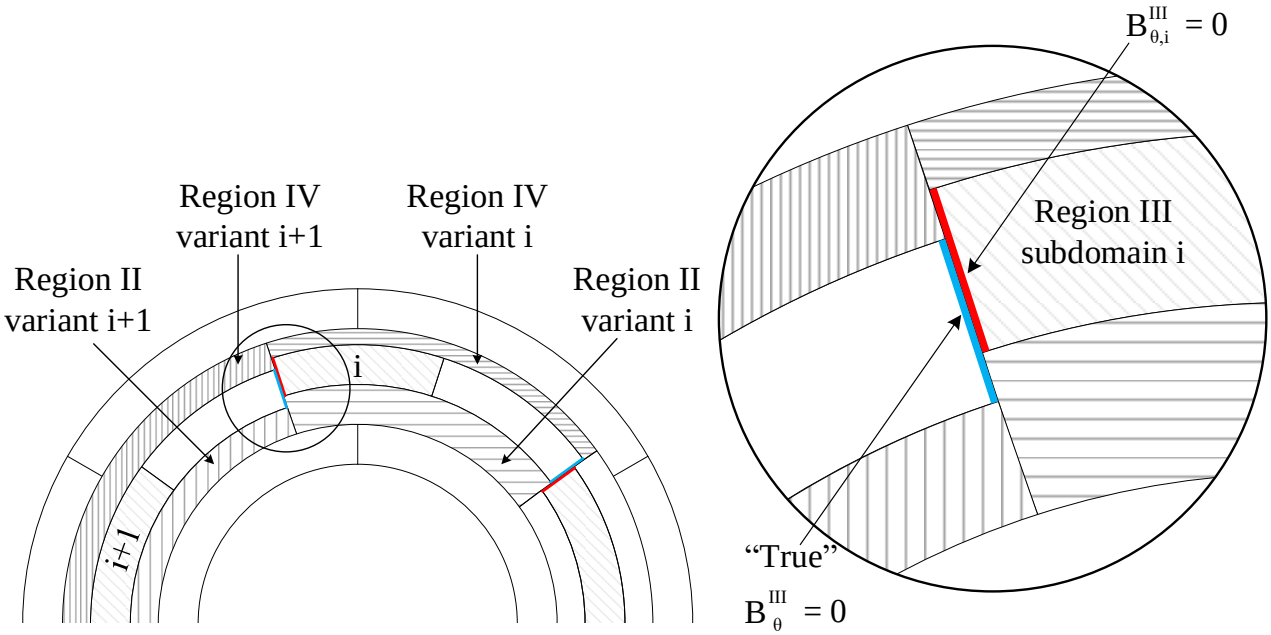

Figure 3-10 Discontinuities in a simple deviated case

of the field density, B_θ, is equal to 0 at the tangential boundaries of each subdomain. As observed in the inset of Figure 3-10, a discontinuity is created at the interface between the i^{th} Region III subdomain and the following pole piece. Specifically, at the interface shown the i^{th} subdomain assumes zero B_θ between ($R_{3,i}$, $R_{4,i}$), while the same assumption for the following (i^{th}+1) subdomain extends from ($R_{3,i+1}$, $R_{4,i+1}$). Similarly, if the definition of the proceeding or average radii is selected, an equivalent discontinuity will be created.

As shown in the analytical model validation section 3.5, in cases with small geometric deviations, the effect of the mentioned discontinuity is very small. However, in a study where large variations in the theoretical position of individual pole pieces are considered, the effects of this discontinuity may be more evident.

Another practical limitation of this model can arise from the number of pole pieces. In an FE model, assuming the mesh element size and active area remain the same, the mesh density, and therefore the required computational time is constant and independent of the individual CMG

parameters. Conversely, with the proposed analytical model, an increase in the number of pole pieces means that additional subdomains are created. This results in an increase in the number of unknowns that are to be calculated. While such a computational time increase may be negligible in most cases, this will depend on the particular study the model is being used in. In cases where this becomes significant, methods to increase the computational efficiency may be employed, such as harmonic selection or further algebraic manipulation to decrease the size with this model definition [83].

An additional limitation of the presented model stems from the 2D approximation. As discussed in Chapter 1 and section 3.2.1, end effects are an important consideration in CMG analysis, with their structure being inherently prone to leakage and fringing. While longer gears and a compensation, through the knowledge of the aspect ratio, would minimise the discrepancies between 2D and 3D analyses, further work is required to comprehensively determine the correlation between those two methods, in the context of geometric deviations.

3.7 Summary

In this chapter a novel, asymmetric analytical model for CMGs was proposed and its advantages and limitations were reported. The presented model was shown to be capable of considering geometric deviations in the pole dimensions as well as in radial and tangential position. Furthermore, it was shown that mapping of H_θ from the asymmetric boundaries of Region III to the radially symmetric boundaries of Region II/IV variants, can effectively consider the gear-level effect of each deviation. Two deviated CMGs of different nominal parameters were used to prove the accuracy of the model. It was shown that excellent correlation was achieved with linear FEA, under the same assumption of an infinite permeability in the ferromagnetic regions. In addition to

the high level of accuracy, this flexible method offered a significant increase in computational efficiency, being more than an order of magnitude faster compared to the FEA.

CHAPTER 4
STATISTICAL METHODOLOGY AND HYBRID STOCHASTIC MODEL

4.1 Introduction

The asymmetric model described in Chapter 3 demonstrates the significant advantages of analytical modelling over FEA, mainly in terms of computational efficiency. However, similar to any other analysis method, the assumptions and simplifications made in the model's formulations do result in some limitations.

This chapter presents a methodology, which uses the analytical model to conduct statistical studies. In doing so, key limitations of the analytical model of Chapter 3 are addressed and approaches to compensate for their effect on the statistical results are developed.

4.2 Statistical Methodology

The analytical model developed in Chapter 3 provides an efficient tool to assess the effect of geometric deviations. In a mass production environment, defining the acceptable range of product performance is as important as calculating ideal performance. Manufacturing tolerances can be specified to achieve an economically acceptable probability of a specific product falling into this range. The stochastic nature of manufacturing error means assessment of its effect requires the use

of statistical methods. In general, the range of outputs of such statistical studies can be described through a Probability Density Function (PDF) of the desired performance variable. However, in many real-world cases, the PDF form is unknown and therefore PDF estimators can be used in conjunction with a number of samples to construct the PDF.

In this thesis, the effect of geometric deviation of the pole pieces of a CMG is discerned through a Monte-Carlo analysis. A number of deviated samples is analysed, each employing a different set of parameters. The parameters considered are the radial and angular position along with the length and span angle of each pole piece. For each simulation sample, the value of each parameter is obtained through random sampling of their respective distribution. The results from the total number of samples can then be used to construct the PDFs and draw conclusions.

4.2.1 Probability Density Function Estimation

A PDF can be estimated using parametric or nonparametric methods. Nonparametric methods are well suited to cases where there is insufficient information regarding the profile of the PDF, whereas parametric estimators initially assume an underlying PDF form [97]. A very common estimator is a histogram, however the accuracy of the results is highly dependent on the selection, volume and placement of the bins, which require careful consideration. Another alternative that has been used in Monte-Carlo analyses is the functional expansion technique, which has its own drawbacks [97], [98]. The estimator used in this study is the Kernel Density Estimator (KDE), which is a nonparametric method approximating the true PDF at discrete points rather than volumetrically. The KDE formula is defined in (4.2.1) and the properties of the kernel function are provided in (4.2.2) [97].

$$\hat{f}_h(x) = \frac{1}{Nh}\sum_{i=1}^{N} k\left(\frac{x - x_i}{h}\right) \tag{4.2.1}$$

$$\int_{-\infty}^{\infty} k(u)du = 1, \quad \int_{-\infty}^{\infty} uk(u)du = 0, \quad \int_{-\infty}^{\infty} u^2 k(u)du = k_2 \neq 0 \tag{4.2.2}$$

where $x_1, \ldots, x_N$ are the samples of the unknown distribution, h is the bandwidth and k is the user-defined kernel function.

The bandwidth has a significant effect on the results of the KDE. In the literature, an optimal bandwidth has been reported which minimises the Mean Integrated Square Error (MISE) [97]. This bandwidth is calculated using (4.2.3).

$$h = \left(\frac{4}{3N}\right)^{\frac{1}{5}} \sigma \tag{4.2.3}$$

where σ is an initial estimate of the standard deviation of $\hat{f}_h(x)$ and is calculated as in [99]. The Epanechnikov kernel [100], which is also known to minimise the MISE according to the properties in (4.2.2), has also been used throughout this study.

4.2.2 Number of Samples

Along with the PDF estimator, the other important factor of a Monte-Carlo analysis is the number of samples. The larger the number of samples, the better the correlation will be between the simulated and true PDFs. However, this comes at a cost of increasing computational time. Therefore, it is critical to use the least samples possible to ensure computational efficiency and accuracy are balanced.

Equation (4.2.4) is provided in [101] as a mean of calculating the required, and hence minimum, number of samples when investigating the probability of an event.

$$N = \frac{p'(1-p')}{E^2} z^2_{(1+\gamma)/2} \tag{4.2.4}$$

where *p'* is an estimate of the probability, *E* is the allowable error in the estimation of *p'*, γ represents the confidence interval and $z_{(1+\gamma)/2}$ is the 100((1+ γ)/2) percent point of a standard normal distribution [101].

It is apparent that there is no 'singular' minimum number of samples, as it depends on the predefined parameters (*p', z*) and allowable error *E*. Furthermore, since the required number of samples by equation (4.2.4) is an estimation, its use does not guarantee an optimised study in terms of computational efficiency. The computational efficiency can be increased further by actively re-calculating the required number of samples during the analysis. A complex system with several stochastic inputs will have an output PDF with an initially unknown form and parameters. Therefore, the re-calculation of the required samples is a key operation for equation (4.2.4) to be effective, and is performed as follows:

1. For the first iteration of (4.2.4) the most conservative estimate of the probability will be used, equal to 0.5. This will initially result in an overestimation on the required number of samples. Considering this overestimation, the analysis through the analytical model can be initiated.
2. After a number of samples, the PDF can be re-estimated using the method in 4.2.1, resulting in a better estimation of *p'*.
3. A more accurate calculation of the minimum number of samples can then be performed.

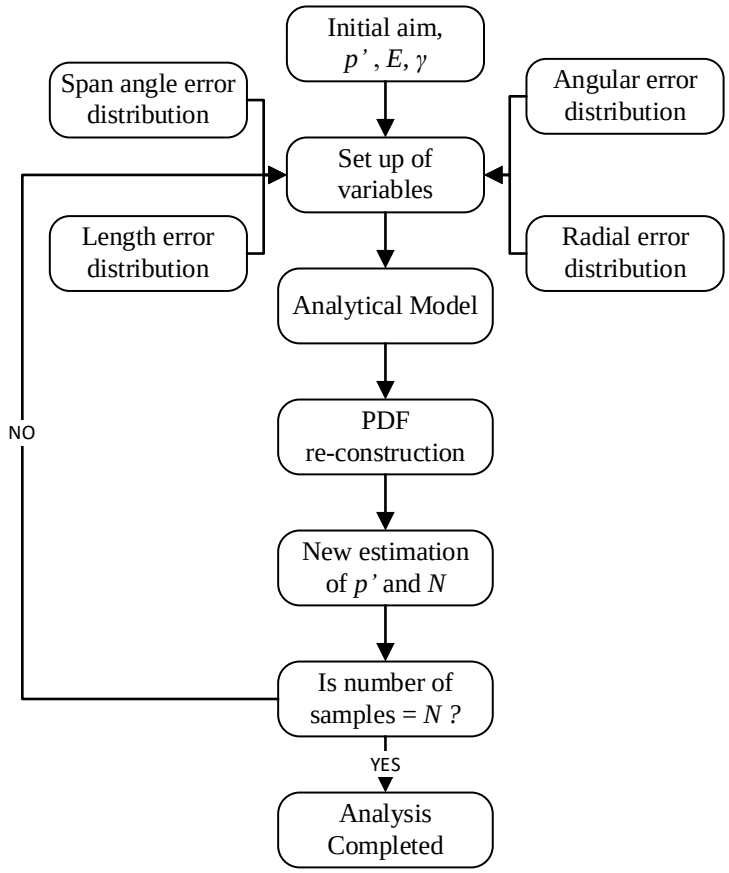

Figure 4-1 Process diagram of the Monte-Carlo analysis

The process diagram of this methodology is shown in Figure 4-1. Initially, the aim is set and the statistical parameters *p', E* and *γ* are selected. The first conservative estimation *p'* of 0.5 is set and the value of each variable is obtained from their respective distributions. The analytical part of the model then generates and analyses samples. Following each assessed sample, the torque is calculated and normalised with respect to the nominal value of a non-deviated CMG. Using the KDE the PDF is re-constructed and a better estimate of *p'* is obtained. The required number of samples is then updated automatically according to (4.2.4) and, when reached, the simulation is completed.

4.3 Review of Analytical Model Limitations in the context of Statistical Analyses

In Chapter 3, a thorough review of the limitations of the asymmetric analytical model was provided. It was identified that the infinite permeability assumption in the pole pieces results in a large discrepancy in absolute stall torque, with respect to FEA. In addition, it was mentioned that the boundary discontinuities, created by the modelling definitions of the Region II/IV variants and the Region III subdomains, could have a significant effect in studies where larger variations in the position of individual pole pieces are considered.

These limitations can be mitigated to an extent in two ways:

1. Defining the Region III subdomains using the average radii of the neighbouring pole pieces, as outlined in Chapter 3, section 3.3.1.
2. Normalising and calibrating the stall torque values with respect to the nominal for both FEA and analytical.

To demonstrate this, a simple Monte-Carlo simulation is performed using CMG 1, as outlined in Table 5 of Chapter 3. The individual geometric deviations of each pole piece are sampled from the distributions of the error sources. Each error source is defined by a tolerance, equal to the three-sigma value of the assumed distribution. The details of these errors are provided in Table 7.

Table 7 Parameters for the assessment of limitations

Parameters	Tolerance Value (3σ)	Distribution
Length (mm)	0.05	Normal
Span angle (deg)	0.05	Normal
Radial position (mm)	0.4	Normal
Angular position (deg)	0.4	Normal

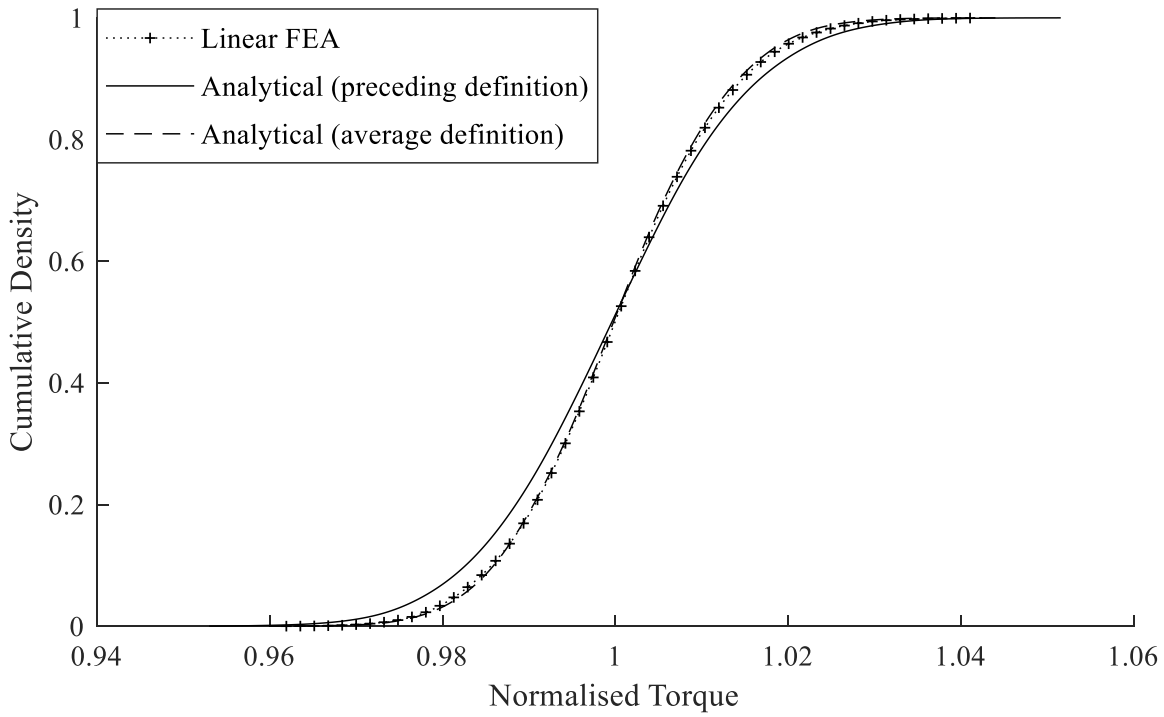

Figure 4-2 CDF comparing normalised linear FEA with the analytical model, considering both the preceding and average definitions of the Region III subdomains

4.3.1 Effect of improved definition of Region III subdomains

Figure 4-2 compares the resultant analytical Cumulative Distribution Function (CDF) plots (preceding and average definitions of Region III subdomains) to the equivalent linear FEA. Here, as samples with larger deviations are inevitably present, the effect of the discontinuities is more evident. However, Figure 4-2 shows that the discrepancy between the CDFs of the analytical model and linear FEA can be minimised by using the average definition of the Region III subdomains, rather than the preceding (or proceeding) definition. By considering the mean radii between consecutive pole pieces, the discontinuities between them and the enclosed subdomain are reduced, and therefore more accurate statistical results are obtained.

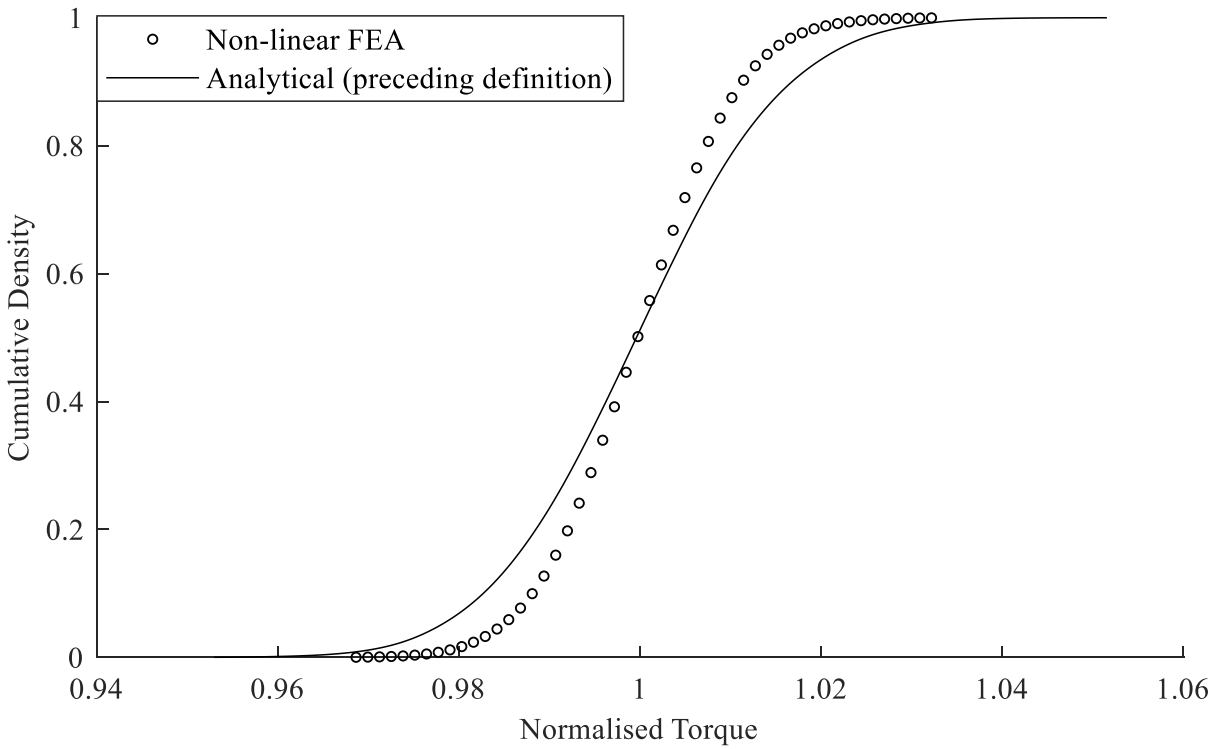

Figure 4-3 CDF comparing normalised non-linear FEA with the analytical model, considering the preceding definition of the Region III subdomains

4.3.2 CDF calibration

The saturation effects are apparent when comparing the absolute value of the stall torque from the analytical model to non-linear FEA. In this study, the stall torque discrepancy for the nominal case was around 11%. For small error distributions, normalisation of stall torque (w.r.t. nominal case) can significantly improve the correlation between the analytical and non-linear FEA CDFs. However, as is evident from Figure 4-3, studies with larger deviations still have a non-negligible discrepancy between analytical and non-linear FEA CDFs. This correlation will naturally worsen with increasing errors. To account for this error, further calibration is required.

A calibration factor (between the analytical and non-linear FEA CDFs) can be determined by comparing a number of deviated samples, analysed using both methods. The selection of those CMG samples is critical for the accuracy of the calibration. Assuming the input errors are normally

distributed the stall torques of the majority of the samples will be clustered near the nominal one (Figure 4-4). The lack of spread from this clustered sample distribution hinders the determination of a valid calibration factor for the discrepancy. To avoid this, the samples should be uniformly distributed along the torque spectrum. As a perfectly uniform distribution cannot be achieved, the closer to the ideal case they are, the better the calibration will be. Such a sample distribution can be achieved by uniformly sampling the torque spectrum and then identify the corresponding deviated CMGs that achieve these torque values (Figure 4-5). In order to reduce the required number of samples, the torque spectrum can be divided into equal sections with the same random sampling applied in each one, therefore facilitating the generation of evenly distributed samples. This approach effectively forces the sample selection to include a greater spread of results, and thus increase the accuracy of the calibration.

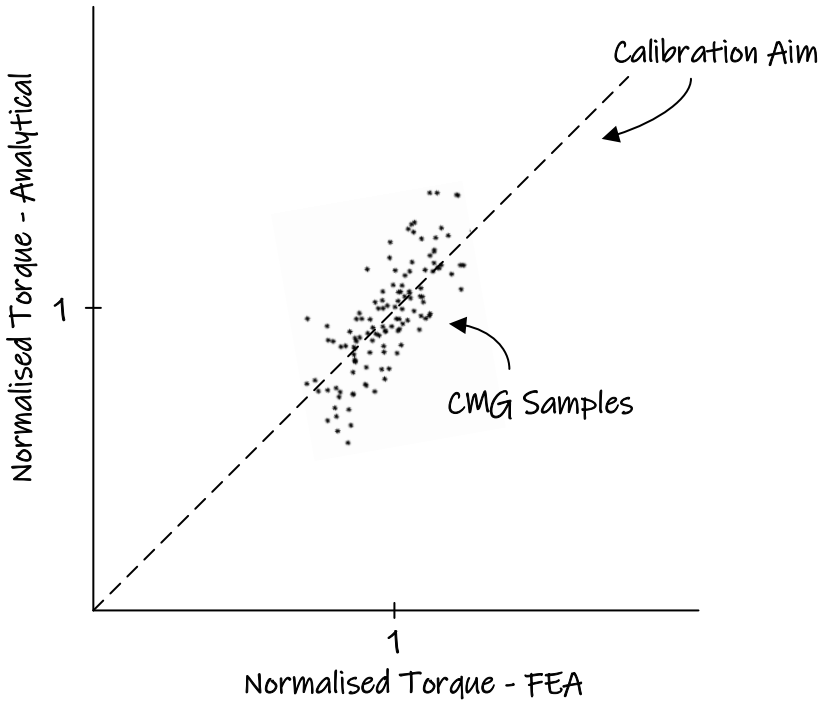

Figure 4-4 Conceptual illustration of the calibration method with sampling of the normally distributed samples

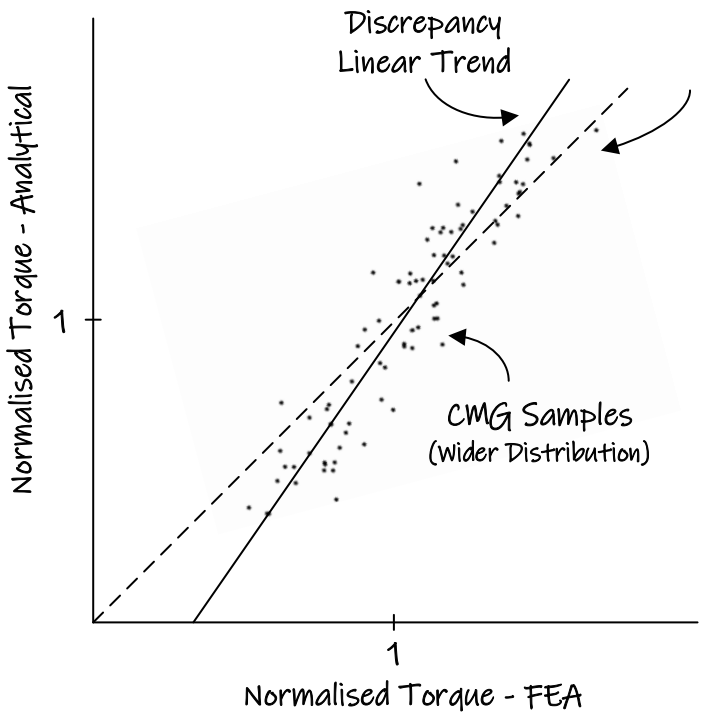

Figure 4-5 Conceptual illustration of the calibration method with uniform sampling of the torque spectrum

4.4 Hybrid Stochastic Model

For the purpose of studying CMGs, analytical magnetostatic modelling and FEA have opposing advantages and disadvantages. The analytical model presents a significant increase in computational efficiency over FEA, but its accuracy is limited in conditions outlined in 4.3. By contrast, and notwithstanding the loss in accuracy due to 2D rather than 3D modelling, high fidelity non-linear FEA can be assumed to be accurate in most conditions. Therefore, in this study the FEA serves as the benchmark. However, the high computational cost of FEA makes it impractical for use in statistical studies. CMGs with low saturation levels could be assessed accurately using the analytical model. However, in cases, the infinite permeability assumption results in larger inaccuracies. In this section, an extension to the analytical model is presented, where the analytical

statistical results are calibrated according to a limited number of non-linear FEA instances, effectively creating a hybrid stochastic model.

With the hybrid stochastic model, samples are selected during a Monte-Carlo simulation and are then assessed with non-linear FEA. As explained in 4.3.2, the torque spectrum of the generated samples is divided into 5 equal sections, which are then sampled. The number of samples is crucial in order to ensure computational efficiency is achieved. This can simply be minimised by checking their convergence. Therefore, identifying the number of samples at which this convergence is achieved, ensures an accurate and computationally efficient calibration.

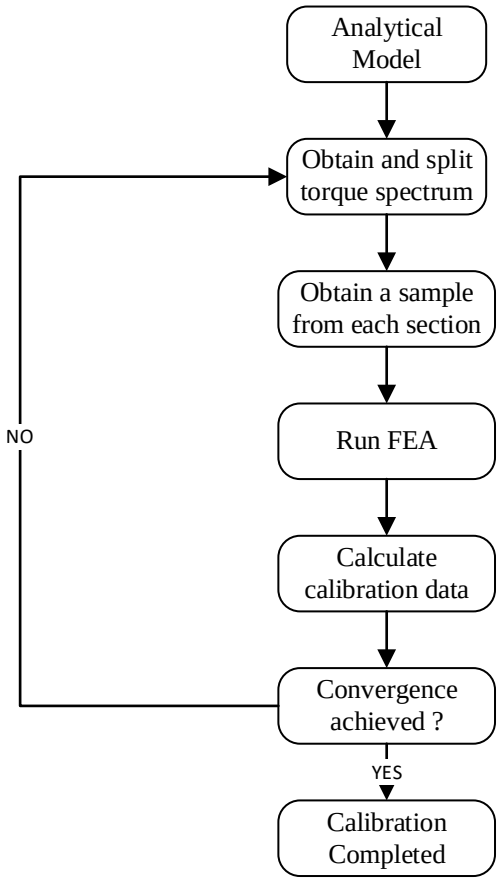

Figure 4-6 Hybrid stochastic model process diagram

The hybrid stochastic model is better explained by Figure 4-6. The analytical model during a statistical study is used to continuously generate and analyse samples. The calibration process is initiated by post-processing those samples and obtaining their range of the results. This range is then split into sections and one sample is randomly selected from each one. These selected samples are then analysed using non-linear FE and their calibration data is calculated. This process is automatically repeated until convergence has been achieved.

4.4.1 Hybrid Stochastic Model Validation

In order to validate and demonstrate the capabilities of this hybrid stochastic model, two case studies are assessed. The nominal CMG used in this section is the same as in 4.3. Each case study consists of a set of 7000 deviated CMGs that have been generated according to previously defined error distributions. The differentiating factor between these case studies is the width of the distribution. In the first case the specified tolerance corresponds to the three-sigma value (Table 8) while in the second, which represents a relatively worse manufactured case, to two-sigma (Table 10). The calibrated results are validated by comparing them to non-linear FE data from an equal number of similarly generated CMG samples. Linear FEA results are also presented for comparison purposes.

Table 8 Parameters for model calibration – Standard Case

Parameters	Tolerance Value (3σ)	Distribution
Length (mm)	0.05	Normal
Span angle (deg)	0.05	Normal
Radial position (mm)	0.4	Normal
Angular position (deg)	0.4	Normal

4.4.1.1 Hybrid Stochastic Model Validation – Standard Case

Table 8 presents the error parameters with which the CMG samples have been generated. These samples have been analysed and calibrated according to the process diagram of Figure 4-6, leading to the following conclusions.

Figure 4-7 maps out 150 data points, which correspond to the non-linear FE and analytical results of 150 identical samples. As expected, the appropriate selection of (relatively) evenly distributed samples leads to an obvious linear trend between the two methods. This trend is also illustrated by applying a best fit line among the scattered data points, which can be used to calibrate the analytical results and therefore accommodate for the discrepancy between the two methods.

The accuracy of the calibration can be demonstrated by analysing a similar number of samples, generated according to Table 8, using non-linear FEA. Due to the very significant computational time required, the FEA study was completed by operating 16 computers (Intel(R) Core(TM) i7-

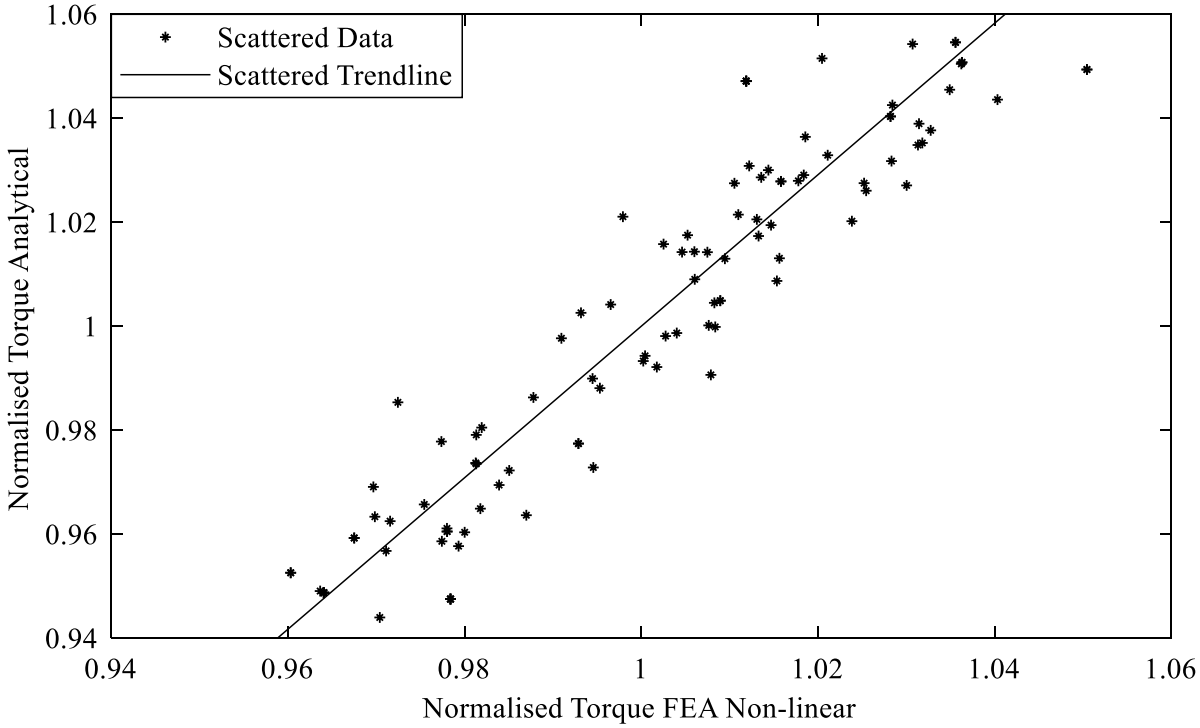

Figure 4-7 Analytical vs Non-linear FEA – Standard Case

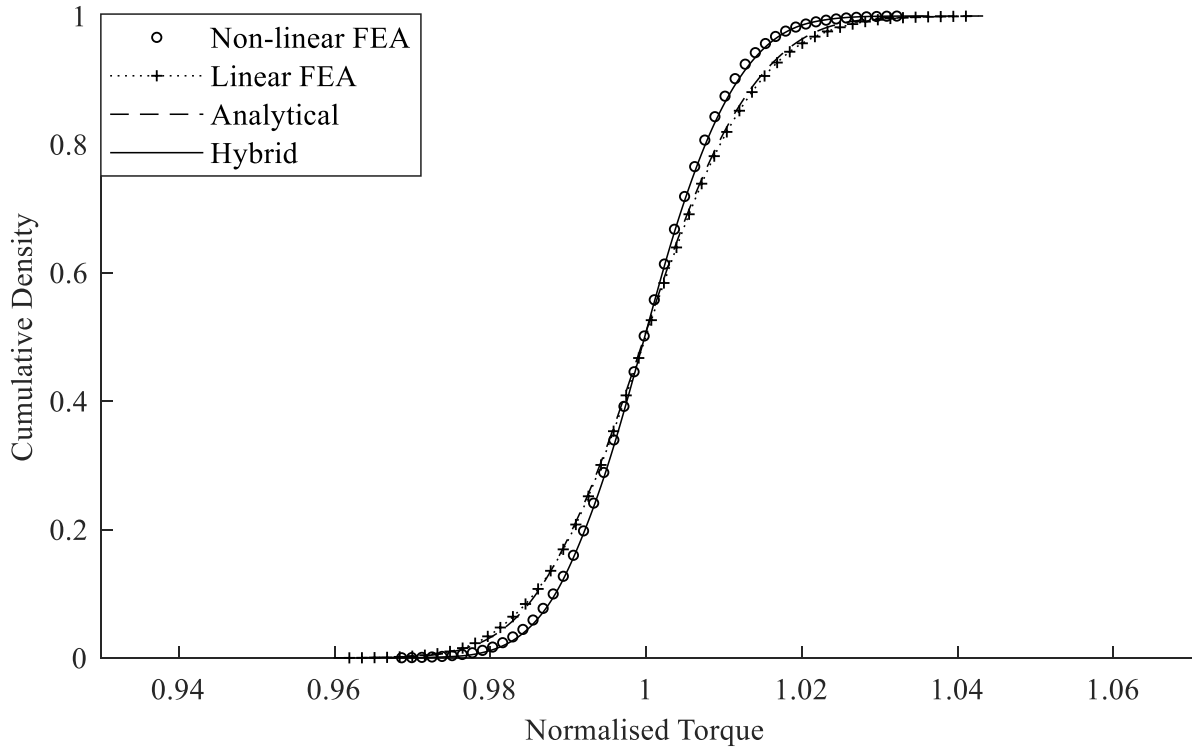

Figure 4-8 Comparison of CDFs – Standard Case

6700 CPU @ 3.40GHz, 16 GB RAM) concurrently for around 16 hours. The resultant CDF plot, along with the linear FE, are presented in Figure 4-8.

Figure 4-8 clearly shows how this calibration can be used to increase the correlation between the analytical and non-linear FE results. In the first instance, there is a notable difference between the raw analytical data and the calibrated ones. A similar discrepancy can be observed between the linear and non-linear FEA results, thus quantifying the effects of saturation and finite permeability. Furthermore, a small difference between the linear FE and raw analytical data can be identified,

Table 9 Probabilities – Standard Case

Linear FEA	Non-linear FEA	Analytical Model	Hybrid Model
0.61	0.73	0.61	0.73

Table 10 Parameters for model calibration – Poorly manufactured case

Parameters	Tolerance Value (2σ)	Distribution
Length (mm)	0.05	Normal
Span angle (deg)	0.05	Normal
Radial position (mm)	0.4	Normal
Angular position (deg)	0.4	Normal

which quantifies the limitations of the model definitions, as discussed in section 3.6.2. The accuracy of the calibration is illustrated through the correlation of CDFs. It can also be examined further by evaluating the probability of an event. In this case the considered event is the probability of a sample achieving a stall torque within ± 1% of the nominal. The accuracy improvement is presented in Table 9, where the calibrated analytical and non-linear FE methods output the same probability. The probabilities calculated using the remaining methods are also presented as a reference.

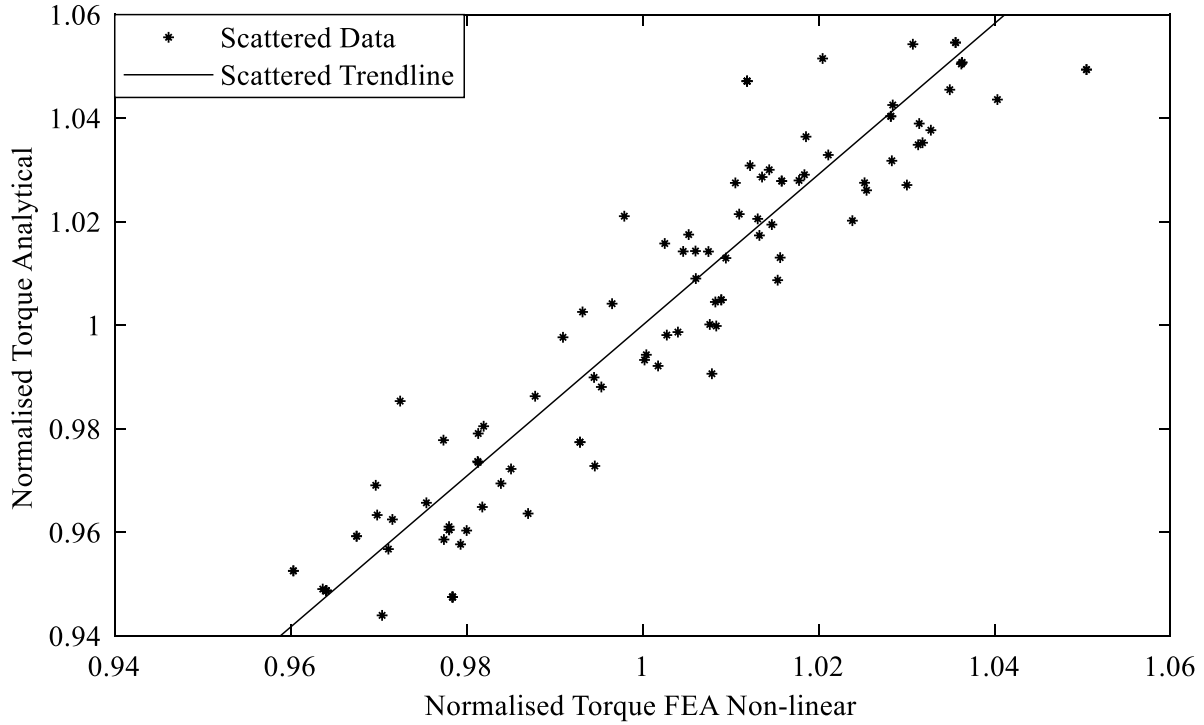

Figure 4-9 Analytical vs Non-linear FEA – Poorly Manufactured Case

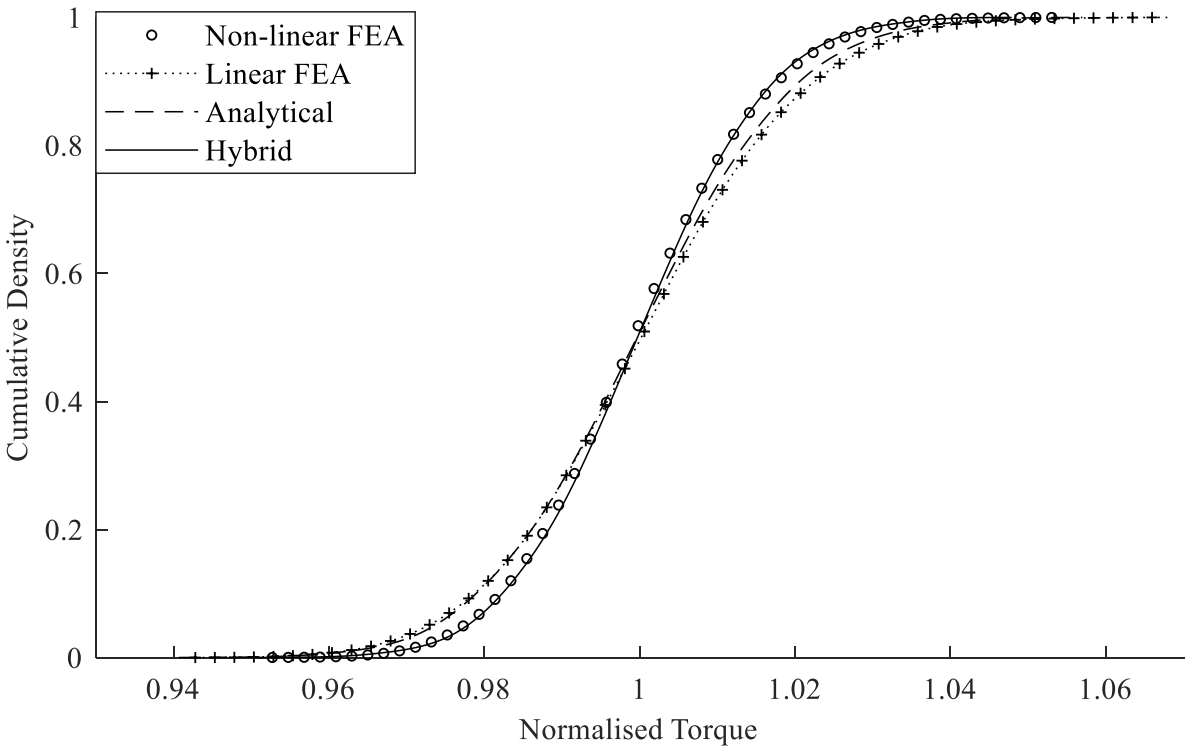

Figure 4-10 Comparison of CDFs – Poorly Manufactured Case

4.4.1.2 Hybrid Stochastic Model Validation – Poorly Manufactured Case

This second case study represents a scenario where larger deviations are more frequent in the generated samples, as the tolerances correspond to the two-sigma values of the respective error distributions (Table 10). Therefore, further aspects of the hybrid stochastic model are assessed and validated, through Figure 4-9, Figure 4-10 and Table 11. These samples have been analysed using the analytical model, non-linear FEA and as well as through the hybrid model. The resultant CDFs are presented in Figure 4-10. Similar to the comparison in section 4.4.1.1, the accuracy is quantified in terms of the probability of a sample achieving a torque within ± 1% of the nominal and is presented in Table 11, along with the total computational time.

Figure 4-10 shows that, as expected, the hybrid stochastic model achieves excellent correlation with the non-linear FEA, while a discrepancy is observed compared to the raw data, due to the

Table 11 Comparison metrics - Poorly manufactured case

	Non-linear FEA	**Analytical Model**	**Hybrid Model**
Probability	0.53	0.40	0.53
Computational time (hr)	480	7.3	8.75
Efficiency increase	N/A	98.5%	98.2%

effects of saturation. Furthermore, as the tolerance is specified for the two-sigma value, a wider error distribution has been considered. Therefore, as expected, there is a more significant difference between the raw analytical and linear FEA results, compared to the case presented in Figure 4-8. Similar to 4.4.1.1, the accuracy of the hybrid model is quantified and verified in Table 11. It is apparent that both the analytical and the hybrid models are significantly more efficient, providing a decrease in computational time by 98.5% and 98.2% compared to FEA, respectively. Although the hybrid model achieves a longer computational time than the analytical (≈ 16%), the significant increase in accuracy combined with the minimal difference in terms of efficiency decrease w.r.t. FEA, demonstrates the superiority of the model. Finally, the computational advantages of the hybrid model become more prominent with the increasing total number of samples calculated. This would occur in cases where the torque ripple is also assessed. Specifically, each sample will require additional calculations in different rotor positions, therefore increasing by a significant factor the total number of solutions for the analytical model.

4.5 Summary

This chapter presented the complete methodology for a statistical assessment of the effects of geometric deviations on the stall torque of CMGs. In the first instance, the statistical methodology of this thesis was presented. KDEs were employed to reconstruct the PDFs (and hence CDFs) through a non-parametric method, as there is initially insufficient information regarding the

underlying profile of the distribution plots. In addition, a technique was discussed with which the number of Monte-Carlo samples could be reduced and hence minimise the computational time of the study. Furthermore, a hybrid stochastic model was presented, which could be used to take into consideration the saturation effects. It was shown that a small number of non-linear FEA instances could calibrate the analytical results and achieve high accuracy even compared to non-linear FEA. This effectively formed a hybrid version of the model from Chapter 3, capable of overcoming some of the mentioned limitations.

CHAPTER 5
EFFECT OF MODULATION RING DESIGN PARAMETERS ON SENSITIVITY TO ERROR

5.1 Introduction

In the preceding chapters, an analytical tool and an associated statistical methodology were presented, which enable the effect of geometric imperfections on the performance of CMGs to be assessed. The purpose of this chapter is twofold:

1. To assess the influence of two design variables, air-gap length and pole piece number, on the effects of geometric deviations on the stall torque.
2. To assess the effects of geometric deviations on torque ripple and to thereby investigate the use of the analytical solution in this context.

5.2 Motivation

A given CMG design will be developed and optimised with respect to its target application. Such studies may focus on particular performance metrics, such as the specific torque. While increasing the specific torque of a CMG is very desirable in mass-critical applications, another key requirement is the accurate determination of the stall torque. This is particularly critical in certain applications, such as in the wind and marine energy generation sector. In those environments, stall

toque can be used for fault mitigation, where in extreme conditions with high loads, the CMG will slip, preventing damage from occurring. Apart from stall torque, the torque ripple is also frequently of interest. Geometric deviations in the pole pieces may create peaks in the gear's torque profile, effectively increasing the slipping torque and the torque ripple.

The air-gap length is a key design parameter of a CMG. Smaller air-gaps are typically desirable as they reduce the reluctance paths and can consequently significantly increase the specific torque. However, larger air-gaps can, in cases, be necessary to accommodate the mechanical structure, particularly when the modulation ring is used to transmit torque. The number of pole pieces is another important parameter. It has been shown that for a fixed cogging torque factor, higher torque ripple is observed in CMGs with lower number of pole pieces [102]. However, increasing the part count in this way may be undesirable from a manufacturing perspective [50]. The cogging torque factor is given by:

$$c_f = \frac{2pQ}{LCM} \tag{5.2.1}$$

where c_f is the cogging torque factor, p is the number of pole pairs of the respective rotor and LCM is the lowest common multiple between p and Q.

It is evident that these parameters will be varied depending on the requirements of the particular application. Therefore, knowledge of their influence on the effects of geometric deviations could provide very useful inputs for the design of the gear, especially with regards to an accurate determination of the stall torque.

Table 12 Baseline CMG Parameters

Variables	CMG 1
Number of pole pieces	5
Inner rotor poles	4
Outer rotor poles	6
Inner rotor OD (mm)	100 mm
Outer rotor OD (mm)	148 mm
PM length (mm)	10 mm
Pole pieces length (mm)	10 mm
Air-gap length (mm)	1 mm
Axial length (mm)	100 mm

5.3 Case Studies

In this section the influence of the nominal air-gap length and the pole piece number on the susceptibility of gear performance to the effects of geometric deviations is discerned. The results are presented through CDF plots. In addition, to retain consistency with the preceding chapters, CDFs are also assessed to determine the probability of a sample gear achieving a stall torque within ± 1% of the nominal.

The base CMG used in this study will be similar to the one used throughout the thesis and with parameters outlined in Table 12. Each parameter is assessed in isolation, with the remaining parameters retaining their nominal specifications. A range is specified in which the specific design parameter is incrementally varied and thus the effect of the geometric deviations on the torque

Table 13 Design parameter variation range

Parameters	Range	Increments
Airgap length (mm)	0.5 – 2	4
P_{HSR}/P_{LSR}	2/3, 3/4, 4/5, 5/6	4

Table 14 Error distributions for the assessment of design parameters

Parameters	Tolerance Value (3σ)	Distribution
Length (mm)	0.05	Normal
Span angle (deg)	0.05	Normal
Radial position (mm)	0.4	Normal
Angular position (deg)	0.4	Normal

performance is assessed. The investigated design parameters along with their variation range are outlined in Table 13. The pole piece error distributions are provided in Table 14.

5.4 Results

5.4.1 Airgap length

Smaller airgaps are normally desirable as they decrease the reluctance in the magnetic circuit and will therefore increase the torque capability of the gear. The torque performance is studied considering a varying airgap as specified in Table 13. The results of this assessment are provided

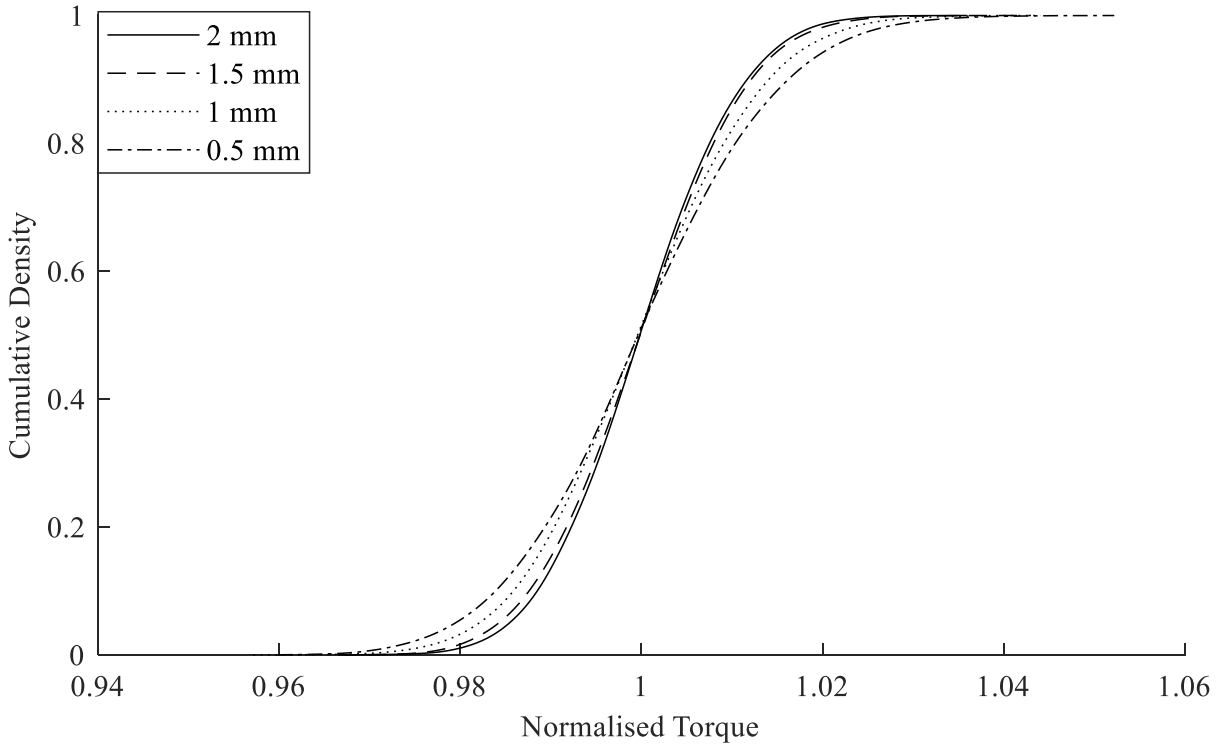

Figure 5-1 Normalised hybrid stall torque CDF with varying airgap length

Table 15 Probabilities for varying airgap length

0.5 mm	1 mm	1.5 mm	2 mm
0.58	0.63	0.70	0.73

in the CDF plots of Figure 5-1 and the probabilities outlined in Table 15 . In order to retain a degree of consistency with the base CMG, the outer rotor is modified to contain the same PM volume.

Figure 5-1 clearly shows the higher effect of geometric deviations when the airgap is decreased. This decrease is quantified in Table 15, through the probability of a gear achieving a stall torque within ±1% of the nominal. In this study, it is 15% more probable to achieve this performance requirement for the CMG with largest air-gap (2 mm) compared to the gear with the smallest air-gap (0.5 mm). Therefore, a decreasing air-gap length, increases the susceptibility of the a gear's stall torque to the effects of geometric deviations. This is an expected observation as by increasing the reluctance of the magnetic circuit, any effects for positional or dimensional deviations of the pole pieces should be of smaller magnitude.

5.4.2 Pole pairs ratio

The pole pairs ratio is another important design characteristic of the modulation ring as it effectively defines the number of the pole pieces. As discussed in the introduction section of this chapter, depending on the particular application, both higher and lower number of pole pieces may be desirable. In this section four CMGs, with the same cogging torque factor equal to 1, are analysed with their specifications outlined in Table 12 and Table 13. The resultant CDF plots are provided in Figure 5-2 and the respective probabilities in Table 16.

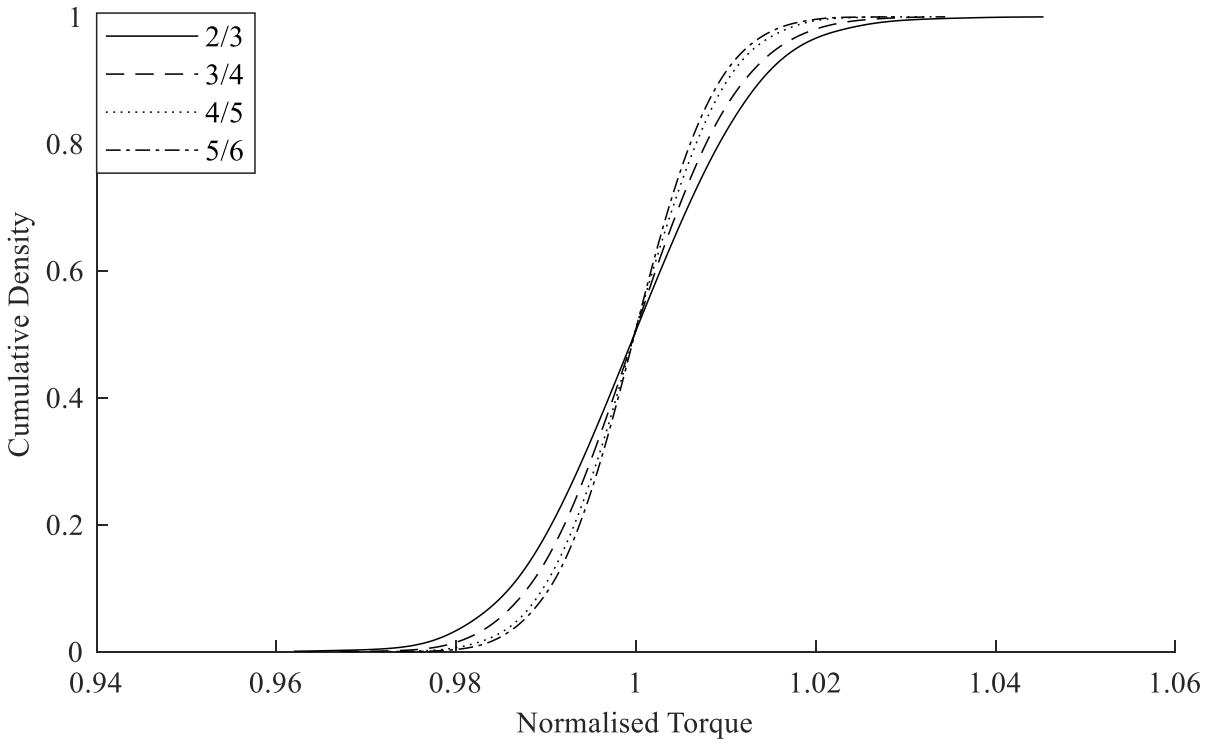

Figure 5-2 Normalised hybrid stall torque CDF with varying pole pairs ratio

A clear trend is identified in Figure 5-2, where the geometric deviations of similar magnitude have less dominant effects with an increasing number of pole pieces. This observation is quantified in Table 16, where the CMG with the highest number of pole pieces is 19% more likely to meet the defined performance requirements compared to the one with the lowest. A higher number of pole pieces in a defined space will consequently decrease the contribution of each one in the total magnetic field modulation. A similar consequence could be expected for the effects of individual geometric deviations, which leads to the observed trend. Here, the effects from geometric deviations become less dominant, even with an increase in specific torque. Specifically, a

Table 16 Probabilities for varying pole pairs ratio

2/3	**3/4**	**4/5**	**5/6**
0.63	0.71	0.79	0.82

minimum of 30% and maximum of 60% increase in specific torque is achieved by increasing the number of pole pieces, with a reduction however, on the effect of deviations.

This particular analysis also emphasises the practical limits of the analytical model. As explained in Chapter 3, due to the approach taken, an increasing number of pole pieces will linearly increase the number of unknowns. Specifically, the 40% increase between the 2/3 and 3/4 cases results in an equivalent increase in the average time for a single solution, which from 3.5s increases to 5.5s. However, even though the number of unknowns increases linearly with Q, the model becomes solver-limited as the computational time increases at an even greater rate. For the remaining cases the average computational time increased to around 11s and 18s, respectively. It must be noted that the software implementation of the presented model is not fully optimised for speed and the author expects that with an alternative platform, substantial improvements can be achieved. This is expanded further in Chapter 6.

5.4.3 Effect of Saturation

The studies of 5.4.1 and 5.4.2 do not include high levels of saturation in the gears. Therefore, the assumption of linearity in the analytical model holds. As a result, similar CDFs would be produced with either the raw analytical data or the hybrid model. The small differences between the two approaches are quantified in Table 17, where the analytical probabilities of both case studies are compared to the hybrid results.

Table 17 Analytical and hybrid probabilities for both case studies

	0.5 mm	**1 mm**	**1.5 mm**	**2 mm**
Hybrid	0.58	0.63	0.70	0.73
Analytical	0.47	0.51	0.58	0.63
	2/3	**3/4**	**4/5**	**5/6**
Hybrid	0.63	0.71	0.79	0.82
Analytical	0.51	0.65	0.72	0.76

However, when a gear design has pole pieces which are highly saturated, the effect of calibration is more pronounced. Such a case has been purposely constructed, by performing a Monte-Carlo simulation with the nominal CMG, employing 4 mm thick pole pieces. While this is arguably an unrealistic gear, it significantly increases the saturation level in the pole pieces, and

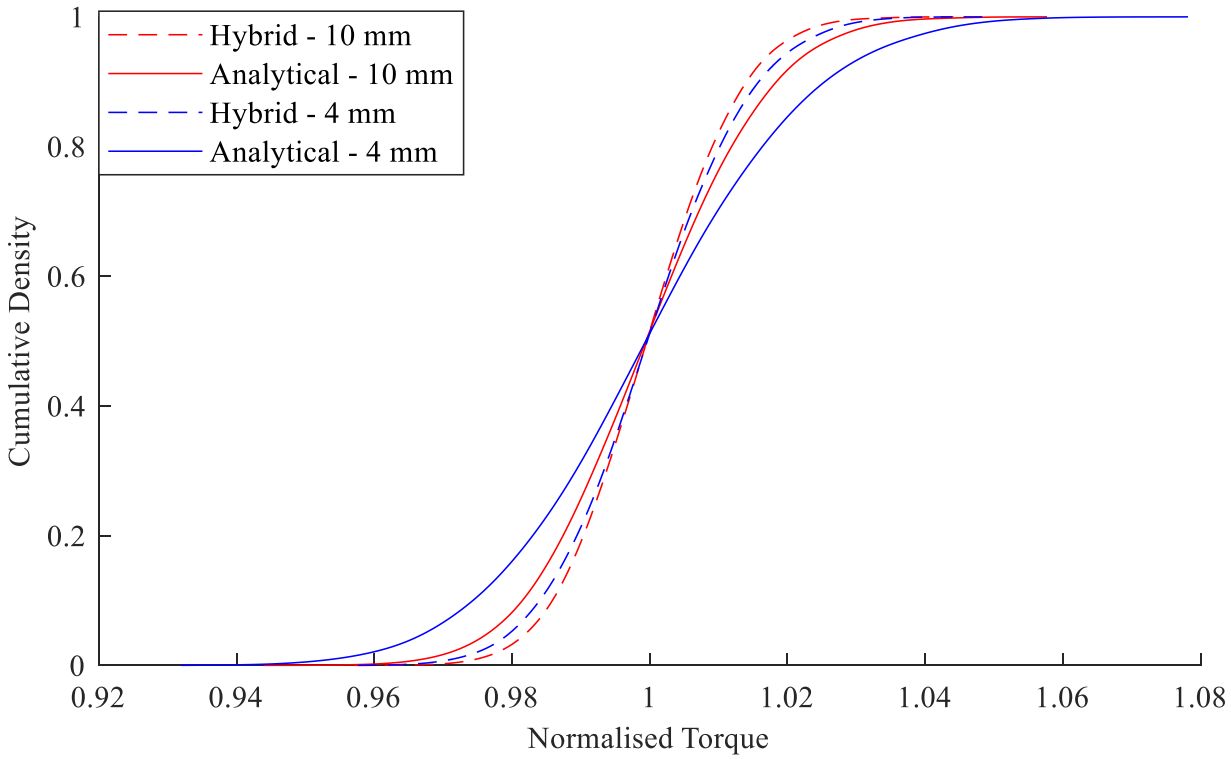

Figure 5-3 Hybrid vs Analytical results for nominal (10 mm pole piece thickness) and highly saturated gear (4 mm pole piece thickness)

therefore highlights this effect. In terms of absolute stall torque, the nominal, 4 mm pole thickness CMG has a 44% difference between analytical and non-linear FEA, as would be expected given the high levels of saturation. This is better observed in Figure 5-3. Here, the difference between hybrid and analytical CDFs is much more distinct in the highly saturated case (4 mm thickness) compared to the results considering the nominal gear. It is the author's view that when highly saturated gear designs are being analysed, some caution must be applied when using the hybrid approach. In such circumstances further FEA studies may be needed to develop confidence in the calibration process. It is important to note that the calibration (and the subsequent hybrid stochastic model) serves to calibrate the CDFs rather than an individual gear's stall torque.

5.4.4 Torque Ripple

Up to this point, the effects of the geometric deviations are always expressed with regards to the stall torque of each CMG. It is expected that torque ripple will also be susceptible to geometric error. However, unlike the assessment of stall torque, one magnetic cycle must be studied incrementally for each gear. This proportionately increases the already considerable number of required samples. As such, even with the high computational efficiency of the model presented in this thesis, full statistical assessment of the effect of geometric error on torque ripple is impractical.

Nonetheless, efficient tools to develop single-geometry solutions for torque ripple would be valuable. In addition, few deviated cases, while not giving a full statistical picture, may provide a useful insight into the possible effects of geometric deviations on torque ripple. As such, two deviated samples of the gear studied in this chapter are selected and analysed over one HSR pole pair pitch. Since the two rotors are rotating at different speeds, a HSR pole pair may not correspond to a magnetic cycle. However, it represents an angular domain in which the torque ripple can be

assessed. The results are compared to the nominal gear, as well as results from linear and non-linear FEA. The exact errors of those samples are outlined in Table 19 at the end of this section.

Figure 5-4 and Figure 5-5 present the torque ripple profiles over one HSR pole pair pitch for both samples. The presented torque ripple plots are developed by subtracting the mean torque from the raw profile, before normalising the ripple with respect to the peak of the nominal gear. These are compared to the profile of the nominal (Figure 5-4) and the equivalent linear FEA ones (Figure 5-5). In Figure 5-4, it is evident that for similar deviations, there are larger effects in the magnitude of the pulsating torque, compared to those of the stall torque from the previous sections. For both samples, torque pulsations can exceed the nominal by around 20%. This can have a significant effect on the performance of the gear, particularly if a fault mitigation perspective exists, as in such a case this 20% increase represents the effective slipping torque at that instant. Figure 5-5, shows that good correlation is also achieved with respect to linear FEA. The discontinuities created by

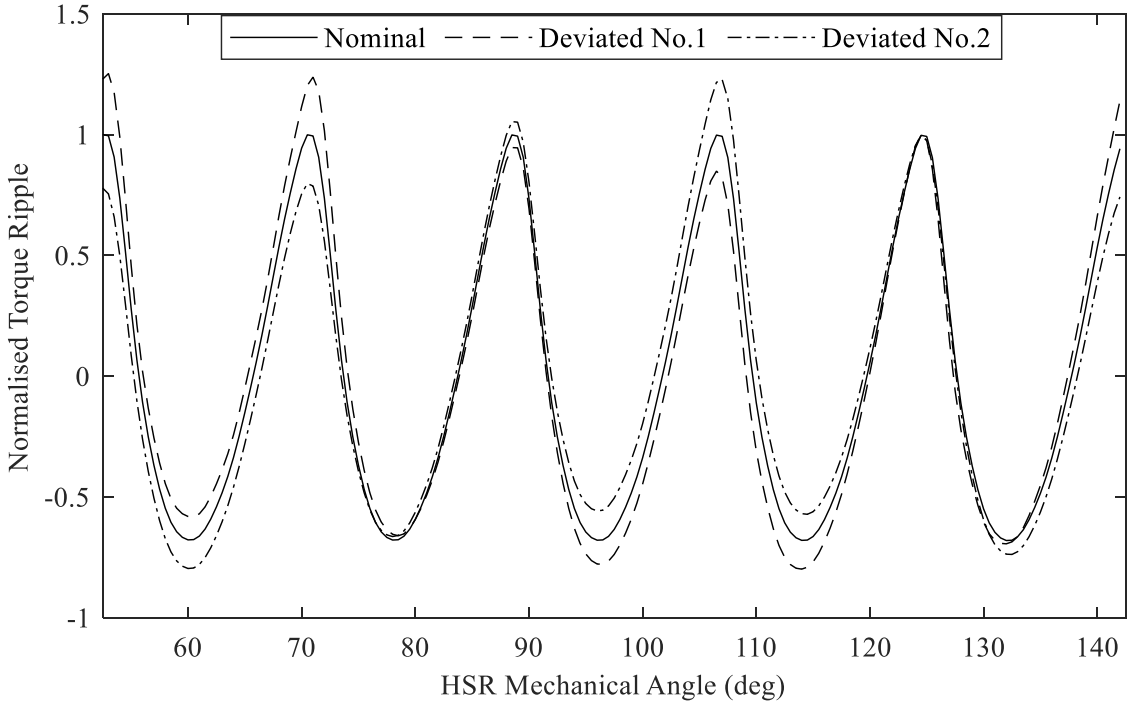

Figure 5-4 Normalised torque ripple over 1 HSR pole pair pitch–Analytical Model

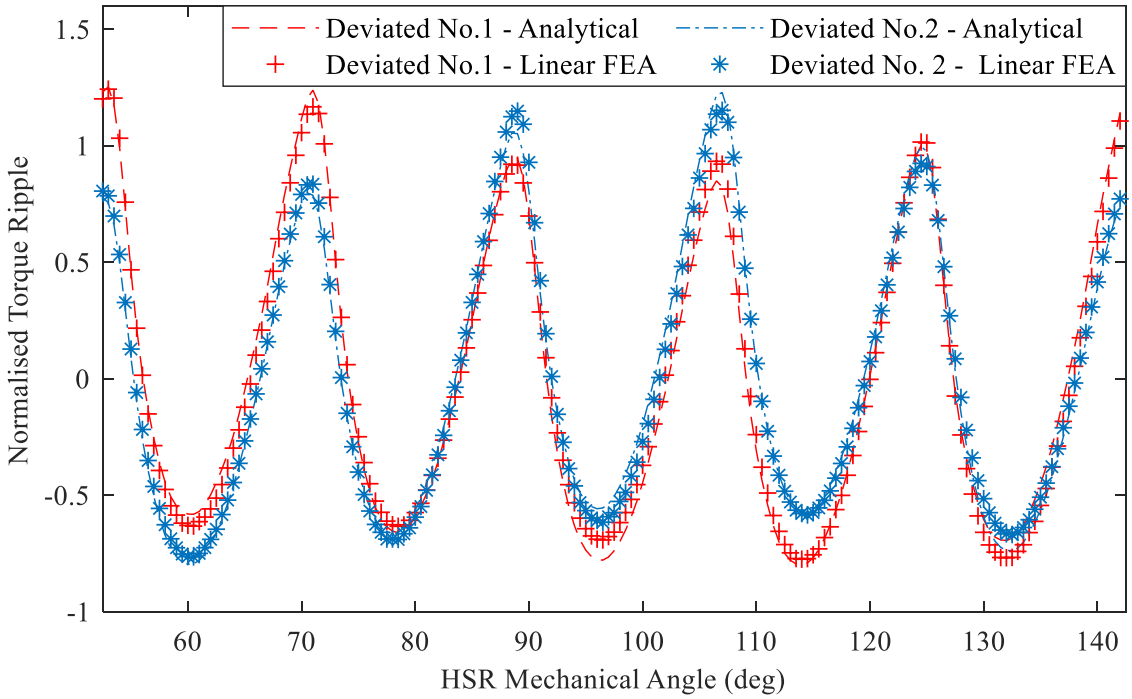

Figure 5-5 Normalised torque ripple over 1 HSR pole pair pitch–linear FEA comparison

the modelling definitions, along with the synthesis of the air-gap flux densities, result in some discrepancies over a HSR pole pair pitch. However, even considering these discrepancies, the analytical model is sufficiently accurate to provide a useful estimate on the effects of manufacturing errors on torque ripple.

These effects can also be expressed through the torque ripple coefficient (T_{ripple}) of the gears, as defined in [103] and (5.4.1), along with the total harmonic distortion (THD) are calculated and presented in Table 18.

$$T_{ripple} = \frac{T_{max} - T_{min}}{T_{mean}} \tag{5.4.1}$$

where $T_{max}, T_{min}, T_{mean}$ are the maximum, minimum and average torque over one HSR pole pair pitch respectively.

Table 18 Torque ripple coefficient and total harmonic distortion comparison

Analytical			
	Nominal	***Sample 1***	***Sample 2***
$\boldsymbol{T_{ripple}}$ **(%)**	29.5	36 (+22% w.r.t Nom)	35.7 (+ 17% w.r.t Nom)
THD **(%)**	7.13	7.55 (+5.9% w.r.t Nom)	7.14 (+0.1% w.r.t Nom)
Linear FEA			
	Nominal	***Sample 1***	***Sample 2***
$\boldsymbol{T_{ripple}}$ **(%)**	29.1	34.9 (+20% w.r.t Nom)	33.5 (+15% w.r.t Nom)
THD **(%)**	7.05	7.41 (+5.1% w.r.t Nom)	7.00 (-0.7% w.r.t Nom)
Non-linear FEA			
	Nominal	***Sample 1***	***Sample 2***
$\boldsymbol{T_{ripple}}$ **(%)**	24.0	27.9 (+16% w.r.t Nom)	27.4(+14% w.r.t Nom)
THD **(%)**	5.85	6.06 (+3.6% w.r.t Nom)	5.82(-0.5% w.r.t Nom)

The data of Table 18 confirm that, for the samples analysed, more significant effects are expected in the torque ripple rather than in the stall torque. The correlation of the analytical results with respect to both linear and non-linear FEA is also verified. For sample No. 1, there are only a 1.1 and 0.36 percentage points difference compared to linear FEA, for T_{ripple} and THD, respectively. The percentage differences with respect to their nominal values are also presented, where, regarding T_{ripple}, there are increases of 22% and 20% (with respect to the nominal) for the analytical and linear FEA, respectively. This is also a good comparison metric for the non-linear FEA. Here, for sample No.2, the analytical percentage increase of T_{ripple}, is closely aligned even to non-linear FEA, where a 17% increase is observed compared to 14%. This is an important observation as, apart from normalising w.r.t nominal, there is no other scaling or calibration applied to the analytical results. The correlation to non-linear FEA is also presented in Figure 5-6 and Figure 5-7.

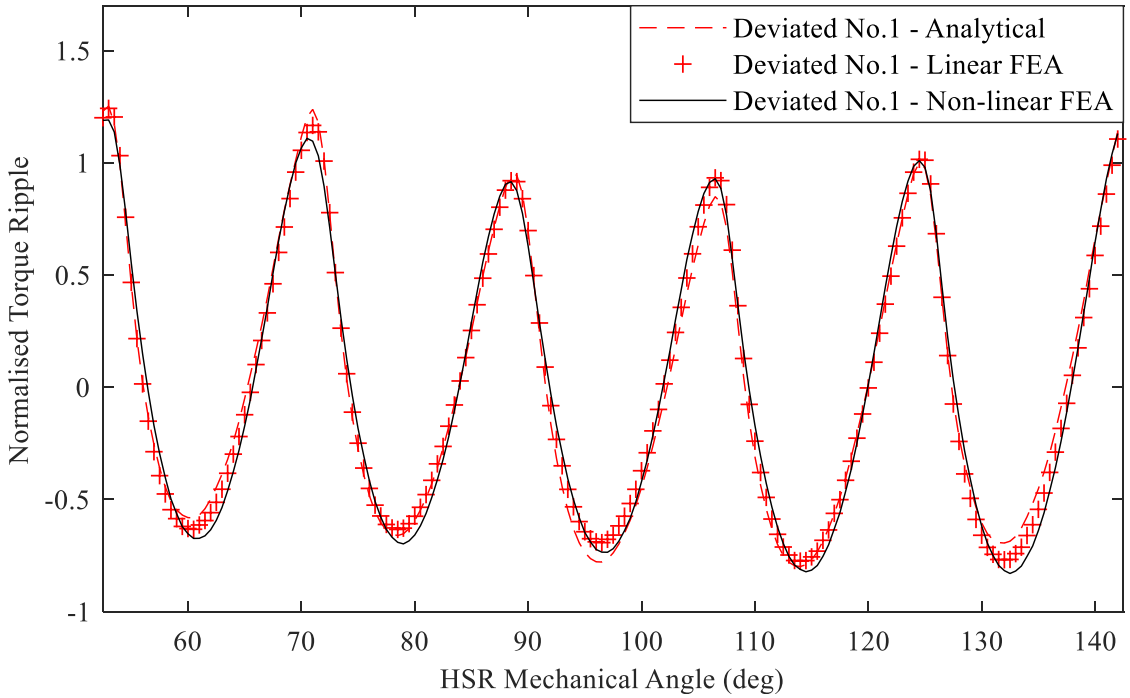

Figure 5-6 Normalised torque ripple comparison between analytical, linear and non-linear FEA – Deviated Sample No. 1

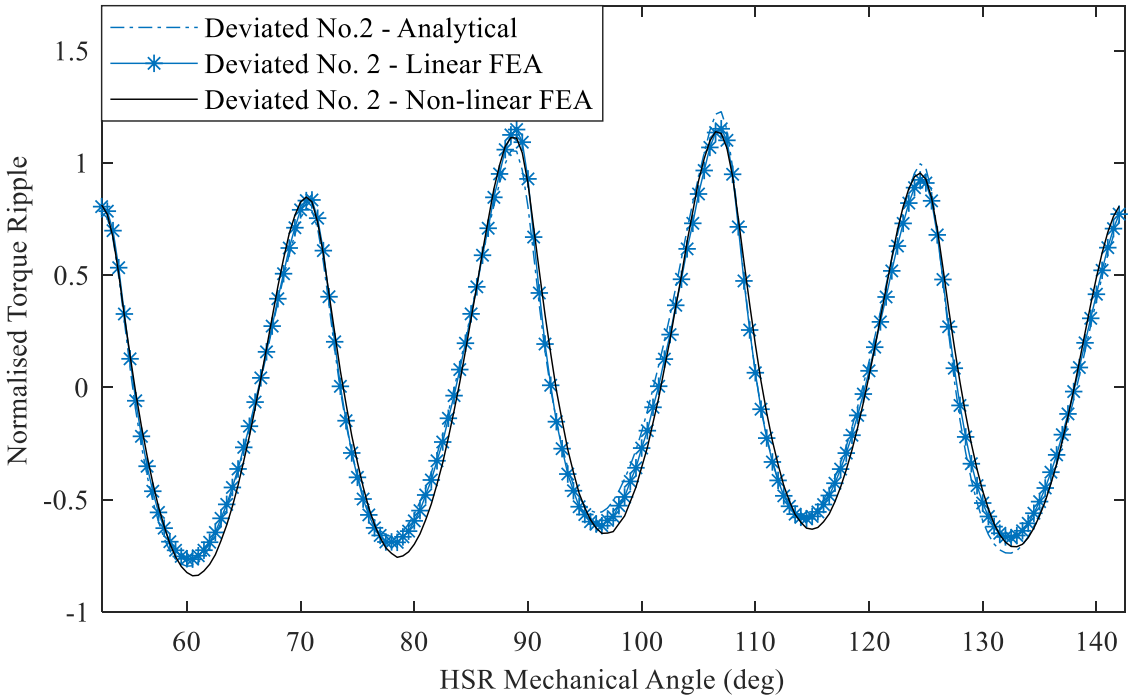

Figure 5-7 Normalised torque ripple comparison between analytical, linear and non-linear FEA – Deviated Sample No. 2

Figure 5-6 and Figure 5-7, along with Table 18, validate the accuracy of the analytical method in assessing the torque ripple of a specified CMG. In addition, the analytical model also offers a significant computational advantage, with the analytical study being ~7 and ~26 times faster the linear and non-linear FEA studies, respectively. However, they also highlight some of the limitations. In the first instance, as discussed in 3.6.2 and observed in Figure 5-5, the air-gap flux synthesis combined with pole radii discontinuities in the analytical model, result in some discrepancies compared to FEA. These are not precisely calculated with the analytical model and therefore reduce its accuracy in terms of reproducing the form of the torque pulsations. However, the significant computational efficiency increase over FEA, along with the good correlation to linear and non-linear FEA, demonstrate the strong potential of this model for the assessment of the effects of geometric deviations on the torque ripple of a CMG.

Table 19 Error for Torque Ripple Samples

Variable	**Pole Piece Error**				
Deviated Sample No. 1					
	No. 1	***No. 2***	***No. 3***	***No. 4***	***No. 5***
Length (mm)	0.000	0.037	0.014	0.011	-0.021
Span angle (deg)	-0.015	0.016	0.014	-0.026	0.014
Radial position (mm)	-0.284	-0.122	0.005	0.086	-0.196
Angular position (deg)	0.009	-0.236	-0.108	0.167	0.185
Deviated Sample No. 2					
	No. 1	***No. 2***	***No. 3***	***No. 4***	***No. 5***
Length (mm)	0.022	-0.028	-0.023	-0.012	-0.006
Span angle (deg)	-0.003	-0.029	-0.009	-0.014	0.015
Radial position (mm)	0.256	0.200	-0.099	-0.178	0.153
Angular position (deg)	-0.108	-0.074	0.014	-0.018	0.027

5.5 Summary

This chapter demonstrated how the proposed methodology can be used to assess the geometric deviations in CMGs. The influence of two key design parameters, the air-gap length and the number of pole pieces, on the effect of geometric deviations was discussed. Regarding the air-gap length, it was shown that a smaller air-gap will increase the effect of the deviations, which is an important but also expected observation. The number of pole pieces were shown to decrease the effects of the geometric deviations, while providing a higher specific torque. The effects on the torque ripple were also discussed. The computational time of the analytical model is not low enough to practically perform a complete statistical study. Therefore, two sample deviated gears were selected for the nominal CMG of this chapter and assessed over one HSR pole pair pitch. An important observation was that, for the same deviations, a much higher effect is expected in the torque ripple profiles, compared to stall torque. The torque pulsations of the deviated gear over a HSR pole pair pitch could be around 20% higher compared to the nominal. Such discrepancies would become even more important when a fault mitigation perspective is considered. In addition, good correlation was shown even to non-linear FEA results. The analytical model can provide a very useful insight on the effects of geometric deviations on the torque ripple of a CMG. However, for their statistical assessment, further computational efficiency improvements are required.

CHAPTER 6
SUMMARY OF THESIS

6.1 Thesis Overview

Coaxial magnetic gears are a highly promising technology, offering contactless transmission and defined torque characteristics for specialist applications. The design of the modulation ring and subsequent route to manufacture is not yet a mature technology and it has been shown that gear performance is sensitive to its geometric accuracy.

Chapter 1 introduced magnetic gearing technology. A brief history on MGs was provided, from their inception over a century ago, to the modern topologies, such as the CMG. CMGs, due to their inherent advantages over their mechanical counterparts, have been considered as promising alternatives in applications ranging from aerospace to the energy generation sector. Discrepancies between modelled and experimentally realised performance have often been reported, a degree of which has been attributed to ‘manufacturing error’. Furthermore, calculated performance in research studies has typically assumed exact geometry. Therefore, the effects of geometric imperfections have rarely been considered. It was also discussed that knowledge of those effects would be even more important when viewed from an application perspective, especially when mass production is considered. In such a case, the use of statistical tools would be necessary

accurately predict the range in expected performance. As FEA, due to the computational requirements, would be impractical for such studies, this is an area analytical modelling could offer significant advantages.

Chapter 2 presented an overview of the sources of error in a CMG and provided estimates on the expected variation for each one. It was identified that, due in part to their use on PM machines, there is much less variability in the processes regarding the rotors, compared to those of the modulation ring. Consequently, in the absence of standardised processes, fewer options and strategies exist, which could be employed to mitigate the associated errors. It was therefore stated that the effect from geometric deviations in the modulation ring, if identified and understood, could be significantly reduced. Furthermore, a literature review was provided on the magnetic and mechanical models available. The potential of analytical modelling has been explored through radially symmetric models, however accurate consideration of asymmetries, within a computationally efficient model, would be necessary for the assessment of the effects from geometric deviations.

Chapter 3 proposed a novel, asymmetric analytical model for CMGs, capable of considering individual dimensional and positional asymmetries of each pole piece. Furthermore, it was shown that mapping of H_θ from the asymmetric boundaries of Region III to the radially symmetric boundaries of Region II/IV variants, could effectively consider the gear-level effect of each deviation. The model was validated with the use of linear FEA, which also highlighted the significant increase in computational efficiency. In addition, the limitations of this model were thoroughly explored and discussed.

Chapter 4 presented the complete methodology for a statistical assessment of the effects of geometric deviations on the stall torque of CMGs. In the first instance, the statistical methodology

of this thesis was presented, using KDEs to non-parametrically reconstruct the, initially unknown, PDFs (and hence CDFs). Furthermore, a hybrid stochastic model was presented, which could be used to account for the saturation effects. It was shown that few non-linear FEA instances could calibrate the analytical CDFs and achieve high correlation even compared to non-linear FEA. This effectively formed a hybrid version of the model from Chapter 3, capable of overcoming some of the mentioned limitations.

Chapter 5 demonstrated how the proposed methodology could be used to assess the geometric deviations in CMGs. The influence of two key design parameters, the air-gap length and the number of pole pieces, on the effect of geometric deviations was discussed. Increasing air-gap length, along with increasing number of pole pieces, were found to decrease the susceptibility of the gear to the effects from geometric deviations. In addition, it was shown that for the same geometric deviations, a more significant effect was observed in the torque ripple. A complete statistical assessment of the torque ripple could not be performed, as a substantially larger number of samples would be required, and even the high computational efficiency of the analytical model would not be high enough to feasibly conduct this analysis. However, an analysis was performed for two deviated CMGs, and the results were compared to both linear and non-linear FEA, with which good correlation was achieved. This highlighted the significant potential of the analytical model for further analysis with regards to torque ripple.

6.2 Conclusions

Statistical analysis of the effect of manufacturing errors in complex products requires fast and accurate models. This thesis has developed and verified a novel stochastic model to assess the effects of geometric deviations in the modulation ring of a CMG. It has been proved that the asymmetric boundaries, created by those deviations, can be approximated by careful consideration

of the modelling regions. Specifically, radially symmetric variants of the air-gap regions (II, IV) are created, each employing the deviations of a pole piece. Furthermore, the mapping of the field intensity on the asymmetric boundary of Region III to the radially symmetric boundaries of Region II/ IV air-gap variants has been validated. This permitted the global capture of the spatial effects from each deviation, which would not have been the case with the superposition method. In addition, the proposed model provided a significant computational increase over the superposition method, by decreasing the number of unknowns in Region III by a factor, equal to the number of pole pieces (Q).

Excellent correlation of this approach has been shown compared to 2D linear FEA, considering the same infinite permeability assumption. However, two key limitations exist: the discontinuities in the emulation of the pole pieces, and the inability to account for saturation effects. It has been shown that the first limitation can be mitigated through the definition of the radial Region III subdomain boundaries, by considering the average radii of the neighbouring pole pieces. The second limitation is addressed in Chapter 4, where a hybrid modelling technique has been presented, that can calibrate the analytical results using a few instances of non-linear FEA. This significantly improves the CDF correlation to that developed using non-linear FEA, while still retaining a substantial computational efficiency advantage over finite elements methods.

Finally, it has been identified that torque ripple is more susceptible to the effects from geometric deviations compared to the gear's initial stall torque. While the analytical model is a powerful tool, further improvements in its computational efficiency are required to utilise it to its full potential.

6.3 Recommendations for Further Research

6.3.1 Further Design Metrics - Torque Ripple & Magnetostatic Forces

In this thesis, the proposed models can effectively discern the effects of modulation ring geometric deviations in a CMG, primarily with respect to the gear's stall torque. However, other performance metrics can be equally important, such as the torque ripple. To accurately assess the torque ripple effects, ideally one magnetic cycle must be studied for each CMG statistical sample. Considering that one magnetic cycle can be significantly longer than a rotor's pole pair pitch, the already high total number of samples are substantially increased. It has been shown that smaller angular domains, such as an HSR pole pair pitch, can used to discern the effects on the torque ripple, however the number of samples is still too high to prevent a complete statistical assessment to be conducted. To enable such an assessment within a statistical analysis, a further increase of computational efficiency is required. Possible routes to achieve this include further improvements to the mathematical modelling and solving. Specifically, the matrix size of unknowns that is solved can be reduced by employing harmonic selection methods or different modelling definitions. However, their accuracy would have to be validated. Furthermore, significant improvements in efficiency could be achieved with a better solving approach. As the computational time is almost entirely dominated by the solution of a single matrix of unknowns, any improvements in that aspect could substantially decrease the required time for a solution.

Apart from the calculation of torque, the proposed model has the capacity to determine the cyclic radial and tangential magnetostatic forces exerted on the pole pieces, as shown in Chapter 3. These forces are a primary source for vibrations in the gear and are also important for the definition of the structural requirements of the modulation ring. Similar to the stall torque and torque ripple, geometric deviations will also have an effect on the magnitude of these forces and

the subsequent vibrations. Therefore, this thesis provides the modelling tools and the methodology for such a statistical assessment to be conducted.

6.3.2 Further Deviations – 3D Effects

In this thesis, the presented analytical model is capable of assessing radial and tangential deviations in both the dimensions and the positions of each of the pole pieces. Further geometric deviations can also exist, whose effects could be of interest. Notable errors in concentricity could arise during the assembly of the modulation ring and a methodology capable of assessing their effect would be valuable. However, it is a considerable challenge to model such errors within a highly computationally efficient framework. Furthermore, some deviations, as the ones considered in this thesis, could be assessed through 2D modelling. However, many geometric deviations are inherently three dimensional, and cannot be approximated in two dimensions. Errors in coaxiality or large structural deflection within the modulation ring, would vary along the length of the CMG. As efficient modelling techniques would still be necessary, a potential approach could be the axial discretisation of the gear into 2D models.

Another area of further work, that has been frequently highlighted in this thesis, is the correlation between 2D and 3D results. Specifically, CMGs are known to have more dominant end effects, compared to PM machines, and further research is required to discern how the 2D effects from geometric deviations would translate in a 3D scenario.

Finally, in Chapter 2 it was identified that one of the biggest deviations in a gear is in the magnetic properties of the PMs. Particularly, increasing temperature causes a notable reduction in the value of B_{rem} of approximately 0.12% per ^{o}C. Considering the relatively large typical operating temperature range, significant effects on the performance of the gear could be expected. However,

the techniques and models developed and validated in this thesis provide a comprehensive framework for these effects to be incorporated in the analysis of coaxial magnetic gears.

References

[1] C. C. Chan and Y. S. Wong, “Electric vehicles charge forward,” *IEEE Power and Energy Magazine*. 2004, doi: 10.1109/MPAE.2004.1359010.

[2] S. Brown, D. Pyke, and P. Steenhof, “Electric vehicles: The role and importance of standards in an emerging market,” *Energy Policy*, 2010, doi: 10.1016/j.enpol.2010.02.059.

[3] A. Ajanovic, “The future of electric vehicles: Prospects and impediments,” *Wiley Interdisciplinary Reviews: Energy and Environment*. 2015, doi: 10.1002/wene.160.

[4] M. A. Hannan, F. A. Azidin, and A. Mohamed, “Hybrid electric vehicles and their challenges: A review,” *Renewable and Sustainable Energy Reviews*. 2014, doi: 10.1016/j.rser.2013.08.097.

[5] K. Atallah, J. Rens, S. Mezani, and D. Howe, “A novel ‘pseudo’ direct-drive brushless permanent magnet machine,” *IEEE Trans. Magn.*, vol. 44, no. 11 PART 2, pp. 4349–4352, 2008, doi: 10.1109/TMAG.2008.2001509.

[6] P. O. Rasmussen, H. H. Mortensen, T. N. Matzen, T. M. Jahns, and H. A. Toliyat, “Motor integrated permanent magnet gear with a wide torque-speed range,” *2009 IEEE Energy Convers. Congr. Expo. ECCE 2009*, pp. 1510–1518, 2009, doi: 10.1109/ECCE.2009.5316280.

[7] L. Jian, K. T. Chau, and J. Z. Jiang, “A magnetic-geared outer-rotor permanent-magnet brushless machine for wind power generation,” *IEEE Trans. Ind. Appl.*, vol. 45, no. 3, pp. 954–962, 2009, doi: 10.1109/TIA.2009.2018974.

[8] C. G. Armstrong, “Power transmitting device,” *Pat. US687292*, no. 687, 1901.

[9] H. T. Faus, “Magnet gearing,” *Pat. US2243555 A*, 1941.

[10] E. P. Furlani, “A two-dimensional analysis for the coupling of magnetic gears,” *IEEE Trans. Magn.*, vol. 33, no. 3, pp. 2317–2321, 1997, doi: 10.1109/20.573848.

[11] R. M. Hornreich and S. Shtrikman, “Optimal design of synchronous torque couplers,” *IEEE Trans. Magn.*, vol. 14, no. 5, pp. 800–802, 1978, doi: 10.1109/TMAG.1978.1060016.

[12] J. P. Yonnet, “A new type of permanent magnet coupling,” *IEEE Trans. Magn.*, vol. 17, no. 6, pp. 2991–2993, 1981, doi: 10.1109/TMAG.1981.1061486.

[13] Y. D. Yao, D. R. Huang, C. C. Hsieh, D. Y. Chiang, and S. J. Wang, “Simulation study of the magnetic coupling between radial magnetic gears,” *IEEE Trans. Magn.*, 1997, doi: 10.1109/20.582770.

[14] M. A. Rahman and G. R. Slemon, “Promising applications of neodymium boron iron magnets in electrical machines (invited),” *IEEE Trans. Magn.*, 1985, doi: 10.1109/TMAG.1985.1064113.

[15] K. Tsurumoto and S. Kikuchi, “A new magnetic gear using permanent magnet,” *IEEE Trans. Magn.*, vol. 23, no. 5, pp. 3622–3624, 1987, doi: 10.1109/TMAG.1987.1065208.

[16] S. Kikuchi and K. Tsurumoto, “Design and Characteristics of a New Magnetic Worm Gear Using Permanent Magnet,” *IEEE Trans. Magn.*, vol. 29, no. 6, pp. 2923–2925, 1993, doi: 10.1109/20.280916.

[17] A. H. Neuland, “Apparatus for transmitting power,” *Pat. US1171351*, 1916.

[18] T. B. Martin, “Magnetic transmission,” *Pat. US3378710*, 1968, doi:

10.1074/JBC.274.42.30033.(51).

[19] B. Ackermann and L. Honds, “Magnetic drive arrangement comprising a plurality of magnetically cooperating parts which are movable relative to one another,” *Pat. US5633555A*, 1997.

[20] P. M. Tlali, R. J. Wang, and S. Gerber, “Magnetic gear technologies: A review,” 2014, doi: 10.1109/ICELMACH.2014.6960233.

[21] K. Atallah and D. Howe, “A novel high-performance magnetic gear,” in *IEEE Transactions on Magnetics*, 2001, vol. 37, no. 4 I, pp. 2844–2846, doi: 10.1109/20.951324.

[22] G. Schüssler and J. Lindner, “Eccentric drive having magnetic torque transmission,” DE Pat 19.944, 1995.

[23] F. T. Jørgensen, T. O. Andersen, and P. O. Rasmussen, “The cycloid permanent magnetic gear,” *IEEE Trans. Ind. Appl.*, vol. 44, no. 6, pp. 1659–1665, 2008, doi: 10.1109/TIA.2008.2006295.

[24] J. Rens, K. Atallah, S. D. Calverley, and D. Howe, “A novel magnetic harmonic gear,” *IEEE Trans. Ind. Appl.*, vol. 46, no. 1, pp. 206–212, 2010, doi: 10.1109/TIA.2009.2036507.

[25] J. Rens, R. Clark, S. Calverley, K. Atallah, and D. Howe, “Design, analysis and realization of a novel magnetic harmonic gear,” *Proc. 2008 Int. Conf. Electr. Mach. ICEM’08*, pp. 1–4, 2008, doi: 10.1109/ICELMACH.2008.4800163.

[26] Cheng-Chi Huang, Mi-Ching Tsai, D. G. Dorrell, and Bor-Jeng Lin, “Development of a Magnetic Planetary Gearbox,” *IEEE Trans. Magn.*, vol. 44, no. 3, pp. 403–412, 2008, doi: 10.1109/TMAG.2007.914665.

[27] M. C. Tsai and C. C. Huang, “Development of a variable-inertia device with a magnetic planetary gearbox,” *IEEE/ASME Trans. Mechatronics*, vol. 16, no. 6, pp. 1120–1128, 2011, doi: 10.1109/TMECH.2010.2077679.

[28] F. Kong, Y. Ge, X. Zhu, L. Qiao, and L. Quan, “Optimizing design of magnetic planetary gearbox for reduction of cogging torque,” *2013 9th IEEE Veh. Power Propuls. Conf. IEEE VPPC 2013*, pp. 239–243, 2013, doi: 10.1109/VPPC.2013.6671697.

[29] Magnomatics, “Energy Efficient Motors and Generators.” https://www.magnomatics.com/ (accessed Apr. 02, 2021).

[30] NASA, “Vertical Lift.” https://www.nasa.gov/ames/aeronautics/vertical-lift (accessed Apr. 02, 2021).

[31] V. Asnani, J. Scheidler, and T. Tallerico, “Magnetic gearing research at NASA,” *Annu. Forum Proc. - AHS Int.*, vol. 2018-May, 2018.

[32] J. J. Scheidler, V. M. Asnani, and T. F. Tallerico, “NASA’s Magnetic Gearing Research for Electrified Aircraft Propulsion,” *2018 AIAA/IEEE Electr. Aircr. Technol. Symp. EATS 2018*, pp. 1–12, 2018, doi: 10.2514/6.2018-4988.

[33] J. J. Scheidler, Z. A. Cameron, and T. F. Tallerico, “Dynamic Testing of a High-Specific-Torque Concentric Magnetic Gear,” *Vert. Flight Soc. 75th Annu. Forum Technol. Disp.*, 2019.

[34] Z. A. Cameron, T. T. Tallerico, and J. J. Scheidler, “Lessons Learned in Fabrication of a High-Specific-Torque Concentric Magnetic Gear,” *Vert. Flight Soc. 75th Annu. Forum Technol. Disp.*, 2019.

[35] T. Tallerico, Z. A. Cameron, and J. J. Scheidler, “Design of a Magnetic Gear for NASA’s Vertical Lift Quadrotor Concept Vehicle,” *AIAA Propuls. Energy 2019 Forum*, pp. 1–21, 2019, doi: 10.2514/6.2019-4477.

[36] E. K. Hussain, K. Atallah, M. Odavic, R. S. Dragan, and R. E. Clark, “Pseudo direct drive electrical machines for flight control surface actuation,” *IET Conf. Publ.*, vol. 2016, no. CP684, pp. 1–6, 2016, doi: 10.1049/cp.2016.0237.

[37] R. S. Dragan, R. E. Clark, E. K. Hussain, K. Atallah, and M. Odavic, “Magnetically geared pseudo direct drive for safety critical applications,” *IEEE Trans. Ind. Appl.*, vol. 55, no. 2, pp. 1239–1249, 2019, doi: 10.1109/TIA.2018.2873511.

[38] Ricardo, “Breakthrough in Ricardo Kinergy ‘second generation’ high-speed flywheel technology.” https://ricardo.com/news-and-media/news-and-press/breakthrough-in-ricardo-kinergy-‘second-generation (accessed Apr. 02, 2021).

[39] A. Atkins and P. Feulner, “The Ricardo mechanical hybrid drive,” in *11th Stuttgart International Symposium: Automotive and engine technology*, 2011, pp. 28–33, doi: 10.1007/s38313-011-1036-7.

[40] “Ricardo to showcase ‘TorqStor’ high efficiency flywheel energy storage at CONEXPO.” https://ricardo.com/news-and-media/news-and-press/ricardo-to-showcase-‘torqstor’-high-efficiency-fly.

[41] L. Jian and K. T. Chau, “Design and Analysis of an Integrated Halbach-magnetic-geared Permanent-magnet Motor for Electric Vehicles,” *J. Asian Electr. Veh.*, vol. 7, no. 1, pp. 1213–1219, 2009, doi: 10.4130/jaev.7.1213.

[42] K. T. Chau, D. Zhang, J. Z. Jiang, C. Liu, and Y. Zhang, “Design of a magnetic-geared outer-rotor permanent-magnet brushless motor for electric vehicles,” in *IEEE Transactions on Magnetics*, 2007, vol. 43, no. 6, pp. 2504–2506, doi: 10.1109/TMAG.2007.893714.

[43] Magnomatics, “Wind Energy.” https://www.magnomatics.com/renewable-wind-energy (accessed Apr. 02, 2021).

[44] Seaplace, “Tidal energy devices.” https://www.seaplace.es/ship-design/tidal-energy-devices/ (accessed Apr. 02, 2021).

[45] N. W. Frank and H. A. Toliyat, “Gearing ratios of a magnetic gear for wind turbines,” *2009 IEEE Int. Electr. Mach. Drives Conf. IEMDC ’09*, pp. 1224–1230, 2009, doi: 10.1109/IEMDC.2009.5075359.

[46] B. McGilton, R. Crozier, A. McDonald, and M. Mueller, “Review of magnetic gear technologies and their applications in marine energy,” *IET Renew. Power Gener.*, vol. 12, no. 2, pp. 174–181, 2018, doi: 10.1049/iet-rpg.2017.0210.

[47] K. Atallah, S. D. Calverley, and D. Howe, “Design, analysis and realisation of a high-performance magnetic gear,” *IEE Proceedings-Electric Power Appl.*, vol. 151, no. 2, pp. 135–143, 2004.

[48] J. X. Shen, H. Y. Li, H. Hao, and M. J. Jin, “A Coaxial Magnetic Gear With Consequent-Pole Rotors,” *IEEE Trans. Energy Convers.*, vol. 32, no. 1, pp. 267–275, 2017, doi: 10.1109/TEC.2016.2609338.

[49] L. Jian, S. Member, K. T. Chau, and S. Member, “A Coaxial Magnetic Gear With Halbach Permanent-Magnet Arrays,” *IEEE Trans. Energy Convers.*, vol. 25, no. 2, pp. 319–328,

2010.

[50] M. Filippini and P. Alotto, “Coaxial magnetic gears design and optimization,” *IEEE Trans. Ind. Electron.*, vol. 64, no. 12, pp. 1–1, 2017, doi: 10.1109/TIE.2017.2721918.

[51] P. O. Rasmussen, T. O. Andersen, F. T. Jørgensen, and O. Nielsen, “Development of a high-performance magnetic gear,” *IEEE Trans. Ind. Appl.*, vol. 41, no. 3, pp. 764–770, 2005, doi: 10.1109/TIA.2005.847319.

[52] S. Gerber and R. J. Wang, “Analysis of the end-effects in magnetic gears and magnetically geared machines,” *Proc. - 2014 Int. Conf. Electr. Mach. ICEM 2014*, pp. 396–402, 2014, doi: 10.1109/ICELMACH.2014.6960211.

[53] A. Matthee, S. Gerber, and R. Wang, “A high performance concentric magnetic gear,” *Proc. - South. African Univ. Power Eng. Conf. 2015*, pp. 203–207, 2015, doi: 10.13140/RG.2.1.1493.6167.

[54] A. Matthee, R.-J. Wang, C. J. Agenbach, D. N. J. Els, and M. J. Kamper, “Evaluation of a magnetic gear for air-cooled condenser applications,” *IET Electr. Power Appl.*, vol. 12, no. 5, pp. 677–683, 2018, doi: 10.1049/iet-epa.2017.0714.

[55] X. Liu, K. T. Chau, J. Z. Jiang, and C. Yu, “Design and analysis of interior-magnet outer-rotor concentric magnetic gears,” *J. Appl. Phys.*, vol. 105, no. 7, pp. 103–106, 2009, doi: 10.1063/1.3058619.

[56] S. Gerber and R. J. Wang, “Evaluation of a prototype magnetic gear,” *Proc. IEEE Int. Conf. Ind. Technol.*, pp. 319–324, 2013, doi: 10.1109/ICIT.2013.6505692.

[57] A. Leontaritis, A. Nassehi, and J. M. Yon, “Causes and effects of Geometric Deviation in

Magnetic Gears," in *Proc. IEEE Workshop on Electrical Machines Design Control and Diagnosis (WEMDCD 2019)*, 2019, pp. 34–39.

[58] Arnold Magnetic Technologies, "Magnet Manufacturing Process." https://www.arnoldmagnetics.com/resources/magnet-manufacturing-process/ (accessed Nov. 09, 2020).

[59] G. Bramerdorfer, "A General Investigation of the Sensitiveness of Brushless," vol. 56, no. 1, 2020.

[60] I. Coenen, M. Van Der Giet, and K. Hameyer, "Manufacturing tolerances: Estimation and prediction of cogging torque influenced by magnetization faults," *IEEE Trans. Magn.*, vol. 48, no. 5 PART 2, pp. 1932–1936, 2012, doi: 10.1109/TMAG.2011.2178252.

[61] H. Qian, H. Guo, Z. Wu, and X. Ding, "Analytical solution for cogging torque in surface-mounted permanent-magnet motors with magnet imperfections and rotor eccentricity," *IEEE Trans. Magn.*, 2014, doi: 10.1109/TMAG.2014.2312179.

[62] Arnold Magnetic Technologies, "Arnold Magnetic Catalog," 2017. https://www.arnoldmagnetics.com/wp-content/uploads/2017/10/Catalog-151021.pdf (accessed Dec. 02, 2020).

[63] W. Tong, *Mechanical design of electric motors*. 2014.

[64] K. G. Swift and J. D. Booker, *Manufacturing Process Selection Handbook*. 2013.

[65] E. Oberg, F. D. Jones, H. L. Horton, and H. H. Ryffel, *Machinery's Handbook*. Industrial Press Inc., 2016.

[66] J. Bralla, "Design for Manufacturability Handbook," *McGraw-Hill Psrofesional*, 1998, doi:

10.1007/978-1-4614-1761-3.

[67] A. J. Piña, “Modeling and Analysis of Asymmetries in Permanent Magnet Synchronous Machines,” *PhD Thesis*, p. 211, 2016, [Online]. Available: https://etd.ohiolink.edu/!etd.send_file?accession=osu1469034099&disposition=inline.

[68] S. D. Calverley and D. J. Powell, “Magnetic Pole-Piece Support,” US Patent Number 9,425,655 B2, 2016.

[69] M. Desvaux, B. Multon, H. Ben Ahmed, and S. Sire, “Supporting the laminated ferromagnetic pole pieces in a magnetic gear: A structure behaviour analysis from a multibody model,” *Mech. Mach. Sci.*, vol. 54, pp. 85–94, 2018, doi: 10.1007/978-3-319-67567-1_8.

[70] K. Atallah, R. E. Clark, and J. J. Rens, “Magnetic Pole-Piece Structure,” US 9,099,895 B2, 2015.

[71] A. Hawksworth, “Pole-Piece Structure for a Magnetic Gear,” US Patent Number 2017/0005559 A1, 2017.

[72] D. Z. Abdelhamid and A. M. Knight, “The Effect of Modulating Ring Design on Magnetic Gear Torque,” vol. 53, no. 11, pp. 2–5, 2017.

[73] K. K. Uppalapati and J. Z. Bird, “An Iterative Magnetomechanical Deflection Model for a Magnetic Gear,” *IEEE Trans. Magn.*, vol. 50, no. 2, pp. 4–7, 2014.

[74] C. U. Ubadigha, M. C. Tsai, and M. F. Hsieh, “Modulating Ring Structural Configuration Influence on the Dual Air-Gap Magnetic Gear Electric Machine,” *IEEE Trans. Magn.*, vol. 53, no. 11, 2017, doi: 10.1109/TMAG.2017.2718111.

[75] L. Jian and K.-T. Chau, “Analytical Calculation of Magnetic Field Distribution in Coaxial Magnetic Gears,” *Prog. Electromagn. Res.*, vol. 92, pp. 1–16, 2009, doi: 10.2528/PIER09032301.

[76] B. Ackermann and R. Sottek, “Analytical modeling of the cogging torque in permanent magnet motors,” *Electr. Eng.*, 1995, doi: 10.1007/BF01245643.

[77] Z. Q. Zhu and D. Howe, “Instantaneous magnetic field distribution in brushless permanent magnet dc motors, Part III: Effect of stator slotting,” *IEEE Trans. Magn.*, 1993, doi: 10.1109/20.195559.

[78] D. Žarko, D. Ban, and T. A. Lipo, “Analytical calculation of magnetic field distribution in the slotted air gap of a surface permanent-magnet motor using complex relative air-gap permeance,” *IEEE Trans. Magn.*, 2006, doi: 10.1109/TMAG.2006.874594.

[79] Z. J. Liu and J. T. Li, “Analytical solution of air-gap field in permanent-magnet motors taking into account the effect of pole transition over slots,” *IEEE Trans. Magn.*, 2007, doi: 10.1109/TMAG.2007.903417.

[80] Z. J. Liu and J. T. Li, “Accurate prediction of magnetic field and magnetic forces in permanent magnet motors using an analytical solution,” *IEEE Trans. Energy Convers.*, 2008, doi: 10.1109/TEC.2008.926034.

[81] T. Lubin *et al.*, “Exact Analytical Method for Magnetic Field Computation in the Air Gap of Cylindrical Electrical Machines Considering Slotting Effects To cite this version :,” *Magn. IEEE Trans.*, vol. 46, no. 4, pp. 1092–1099, 2011.

[82] T. Lubin, S. Mezani, and A. Rezzoug, “Analytical computation of the magnetic field

distribution in a magnetic gear," *IEEE Trans. Magn.*, vol. 46, no. 7, pp. 2611–2621, 2010, doi: 10.1109/TMAG.2010.2044187.

[83] X. Zhang, X. Liu, Z. Song, and Z. Chen, "Fast calculation of magnetic field distribution in magnetic gear for high torque application," *2016 XXII International Conference on Electrical Machines (ICEM)*. pp. 1742–1748, 2016, doi: 10.1109/ICELMACH.2016.7732759.

[84] M. Desvaux, B. Traullé, R. Le Goff Latimier, S. Sire, B. Multon, and H. Ben Ahmed, "Computation Time Analysis of the Magnetic Gear Analytical Model," *IEEE Trans. Magn.*, vol. 53, no. 5, 2017, doi: 10.1109/TMAG.2017.2671787.

[85] A. Penzkofer and K. Atallah, "Magnetic gears for high torque applications," *IEEE Trans. Magn.*, vol. 50, no. 11, 2014, doi: 10.1109/TMAG.2014.2328093.

[86] A. Penzkofer and K. Atallah, "Scaling of Pseudo Direct Drives for Wind Turbine Application," *IEEE Trans. Magn.*, vol. 52, no. 7, pp. 1–5, 2016, doi: 10.1109/TMAG.2016.2524205.

[87] H. M. Shin and J. H. Chang, "Analytical Magnetic Field Calculation of Coaxial Magnetic Gear with Flux Concentrating Rotor," *IEEE Trans. Magn.*, vol. 52, no. 7, 2016, doi: 10.1109/TMAG.2015.2512587.

[88] A. Rahideh, A. A. Vahaj, M. Mardaneh, and T. Lubin, "Two-dimensional analytical investigation of the parameters and the effects of magnetisation patterns on the performance of coaxial magnetic gears," *IET Electr. Syst. Transp.*, vol. 7, no. 3, pp. 230–245, 2017, doi: 10.1049/iet-est.2016.0070.

[89] J. Fu and C. Zhu, “Subdomain model for predicting magnetic field in slotted surface mounted permanent-magnet machines with rotor eccentricity,” *IEEE Trans. Magn.*, vol. 48, no. 5 PART 2, pp. 1906–1917, 2012, doi: 10.1109/TMAG.2011.2178250.

[90] U. Kim and D. K. Lieu, “Magnetic field calculation in permanent magnet motors with rotor eccentricity: Without slotting effect,” *IEEE Trans. Magn.*, vol. 34, no. 4 PART 2, pp. 2243–2252, 1998, doi: 10.1109/20.703862.

[91] H. Qian, H. Guo, Z. Wu, and X. Ding, “Analytical solution for cogging torque in surface-mounted permanent-magnet motors with magnet imperfections and rotor eccentricity,” *IEEE Trans. Magn.*, vol. 50, no. 8, 2014, doi: 10.1109/TMAG.2014.2312179.

[92] S. Gerber and R. J. Wang, “Statistical analysis of cogging torque considering various manufacturing imperfections,” *Proc. - 2016 22nd Int. Conf. Electr. Mach. ICEM 2016*, pp. 2066–2072, 2016, doi: 10.1109/ICELMACH.2016.7732807.

[93] M. Desvaux, B. Multon, H. Ben Ahmed, and S. Sire, “Magneto-mechanical analysis of magnetic gear pole pieces ring from analytical models for wind turbine applications,” *Wind Eng.*, vol. 42, no. 4, pp. 276–285, 2018, doi: 10.1177/0309524X18777314.

[94] A. Leontaritis, A. Nassehi, and J. M. Yon, “A Monte Carlo Analysis of the Effects of Geometric Deviations on the Performance of Magnetic Gears,” *IEEE Trans. Ind. Appl.*, 2020, doi: 10.1109/TIA.2020.3008115.

[95] P. H. Mellor and R. Wrobel, “Optimization of a multipolar permanent-magnet rotor comprising two arc segments per pole,” *IEEE Trans. Ind. Appl.*, 2007, doi: 10.1109/TIA.2007.900479.

[96] Y. Li, Q. Lu, Z. Q. Zhu, L. J. Wu, G. J. Li, and D. Wu, “Analytical Synthesis of Air-Gap Field Distribution in Permanent Magnet Machines with Rotor Eccentricity by Superposition Method,” *IEEE Trans. Magn.*, vol. 51, no. 11, pp. 2–5, 2015, doi: 10.1109/TMAG.2015.2442297.

[97] T. P. Burke, “Kernel Density Estimation Techniques for Monte Carlo Reactor Analysis,” 2016.

[98] D. P. Griesheimer, “Functional expansion tallies for Monte Carlo simulations,” 2005.

[99] A. W. Bowman and A. Azzalini, *Applied Smoothing Techniques for Data Analysis*. New York: Oxford University Press Inc., 1997.

[100] V. Epanechnikov, “Nonparametric estimation of a multidimensional probability density,” *Theory Probab. Its Appl.*, 1969.

[101] G. J. Hahn, “Sample Sizes for Monte Carlo Simulation.,” *IEEE Trans. Syst. Man Cybern.*, vol. SMC-2, no. 5, pp. 678–680, 1972, doi: 10.1109/TSMC.1972.4309200.

[102] A. Ometto, A. Rotondale, N. Rotondale, and G. Gentile, “Analysis and optimization of coaxial magnetic gears,” *2016 Int. Symp. Power Electron. Electr. Drives, Autom. Motion, SPEEDAM 2016*, pp. 843–848, 2016, doi: 10.1109/SPEEDAM.2016.7525832.

[103] L. Kalaivani, P. Subburaj, and M. Willjuice Iruthayarajan, “Speed control of switched reluctance motor with torque ripple reduction using non-dominated sorting genetic algorithm (NSGA-II),” *Int. J. Electr. Power Energy Syst.*, 2013, doi: 10.1016/j.ijepes.2013.04.005.

[104] P. H. Mellor, S. G. Burrow, T. Sawata, and M. Holme, “A wide-speed-range hybrid

variable-reluctance/permanent-magnet generator for future embedded aircraft generation systems," *IEEE Trans. Ind. Appl.*, vol. 41, no. 2, pp. 551–556, 2005, doi: 10.1109/TIA.2005.844381.

[105] T. Lubin, S. Mezani, and A. Rezzoug, "Exact analytical method for magnetic field computation in the air gap of cylindrical electrical machines considering slotting effects," *IEEE Trans. Magn.*, 2010, doi: 10.1109/TMAG.2009.2036257.

Appendix A – Supplementary Chapter

FURTHER MODEL APPLICATIONS – VRM

A.1. Introduction

This thesis has demonstrated the capabilities and effectiveness of the proposed asymmetric analytical model in the context of CMGs. However, the modelling framework is very flexible as it considers only two categories of regions. As explained in Chapter 3, the main differentiation between those categories is the magnetisation, which, if present, leads to the solution of Poisson's equation and otherwise to the Laplace's equation. Regions, variants and subdomains of each category can then be employed to analyse the system under consideration. Therefore, it is apparent that a very similar model to the one used for CMGs could be used to analyse similar problems, such as some topologies of Variable Reluctance Machines (VRM), similar to the one developed in [104]. To aid the reader, and minimise the need for cross-references to Chapter 3, the mathematical approach to this model development is presented in full in this chapter. In addition, all input parameters and subsequent results are used purely for correlation and validation purposes, and therefore the results do not correspond to realistic performance.

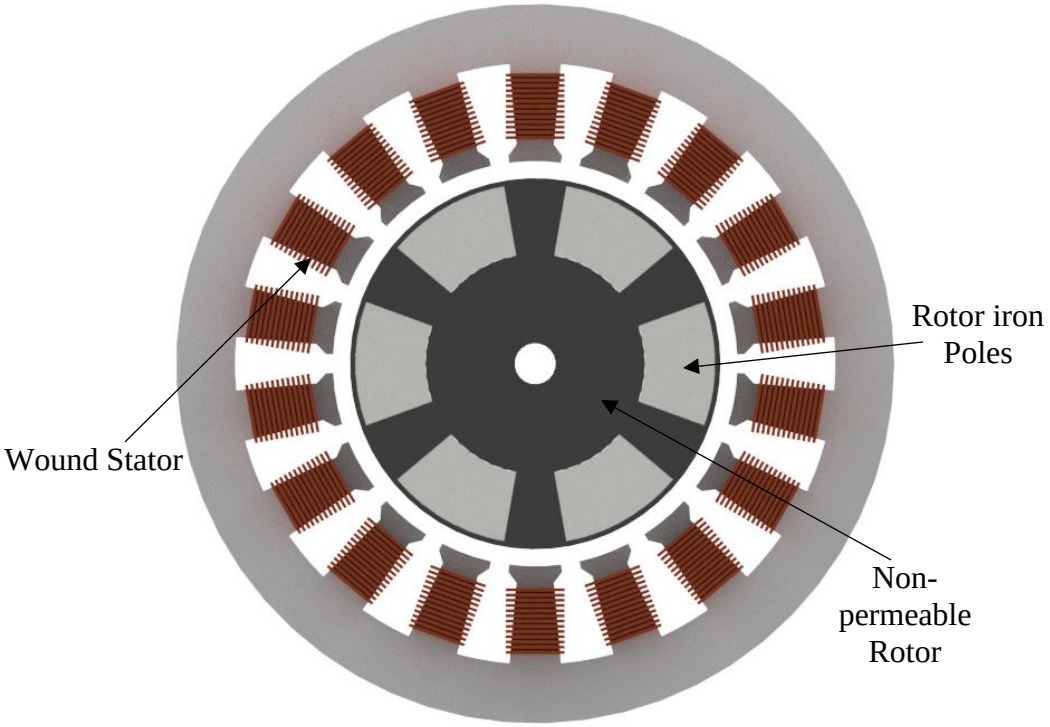

Figure A-1 A simplified VRM

A.2. Variable Reluctance Machine Analytical Model – Definition

Considering modelling regions, a VRM of the type shown in Figure A-1 is very similar to a CMG. Specifically, the subdomain definition of the VRM's rotor is equivalent to the modulation ring (Region III) and the air-gap adjacent to the LSR (Region IV) of a CMG. The main differences relate to the CMG's PM rotors, where the LSR is replaced by a stator and the HSR is not existent. Assuming the magnetic field from the stator can be expressed mathematically by defining H at the stator inner radius boundary, the problem definition can be presented as shown in Figure A-2 [105].

Similar to the proposed model of Chapter 3, the asymmetric analytical model for a VRM is also based on solutions of the $\vec{A}$ in each region. These solutions are again developed using the definition of $\vec{A}$ (A.2.1) and Maxwell's Ampere law equation (A.2.2).

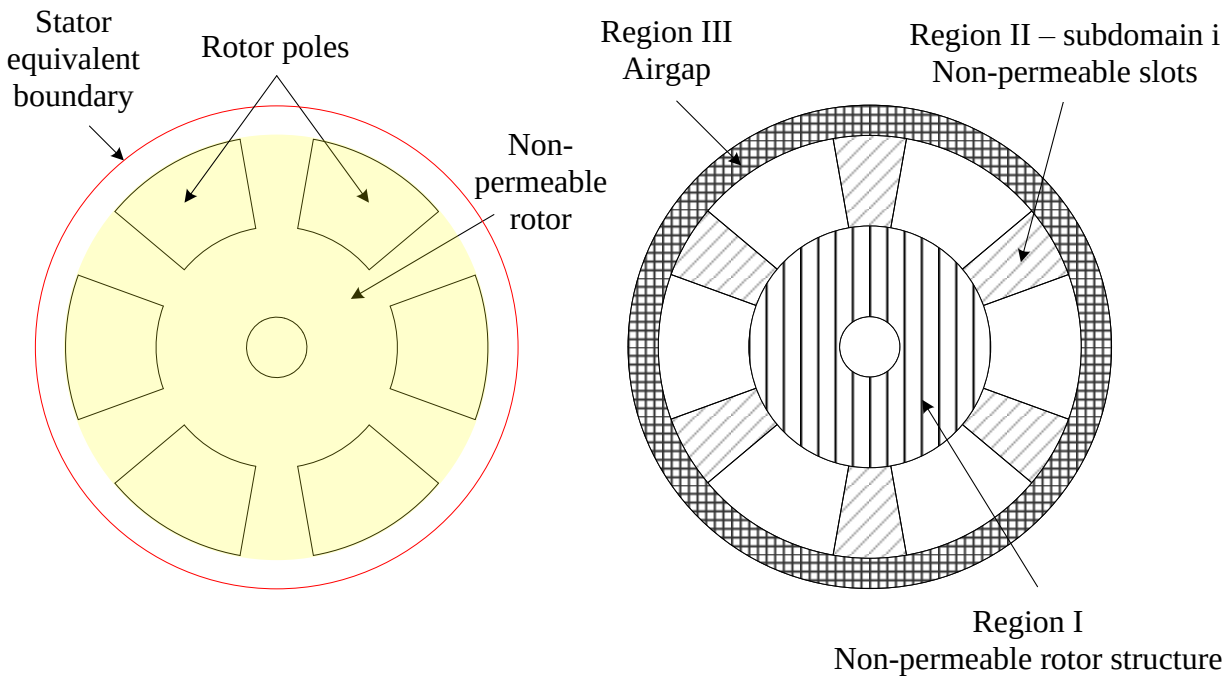

Figure A-2 VRM region definitions

$$\vec{B} = \nabla \times \vec{A} \tag{A.2.1}$$

$$\nabla \times \vec{B} = \mu_0 \vec{J} + \mu_0 \varepsilon_0 \frac{\partial \vec{E}}{\partial t} \tag{A.2.2}$$

Assuming magnetostatic conditions, the partial derivative of $\vec{E}$ with respect to time disappears. Furthermore, there is no applied current in any of the defined regions since the stator is not modelled as a region and its magnetic field distribution (H) is just considered at its boundary. In addition, the absence of a magnetisation vector (no PM material) reduces $\vec{J}$ to zero in all defined regions. Therefore, the equations (A.2.1) and (A.2.2) combined take the form of the Laplace equation (A.2.3) in all regions:

$$\nabla^2 \vec{A} = 0 \tag{A.2.3}$$

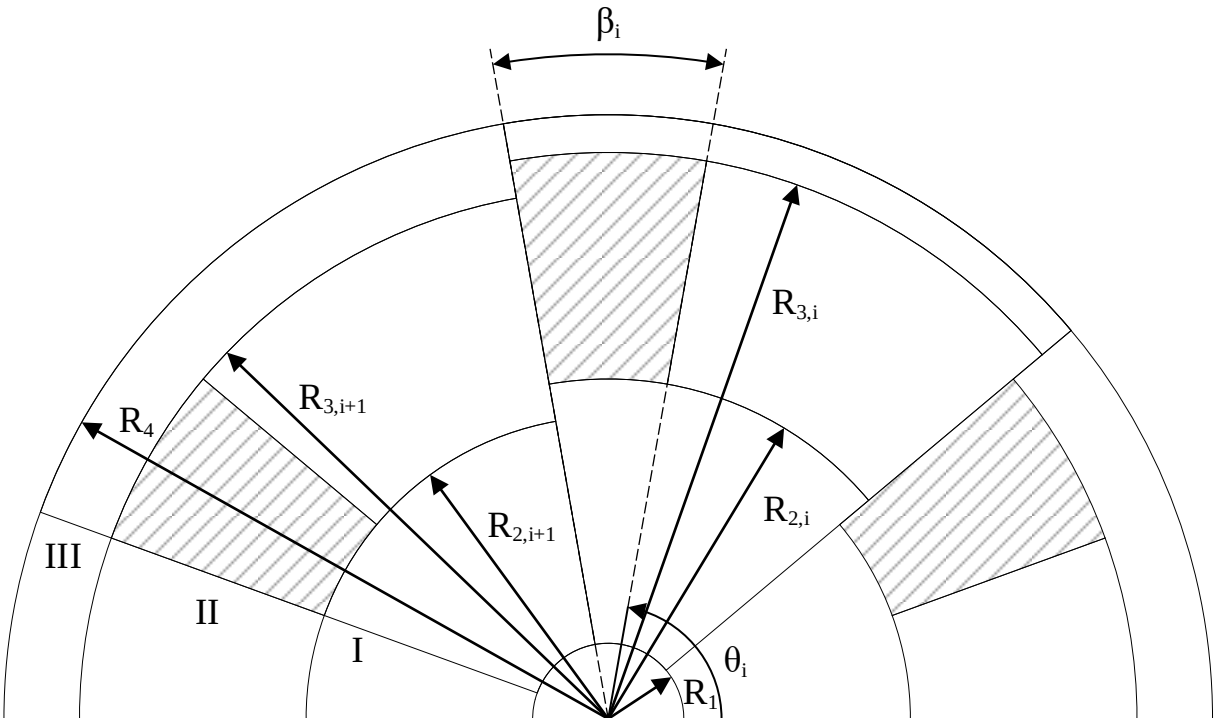

Figure A-3 Geometry of VRM Region II subdomains

A.2.1. Region II – Non-permeable Rotor Slots

In common with the CMG equivalent, any radial deviations of the rotor poles will create an asymmetric air-gap. Furthermore, as infinite permeability in the ferromagnetic regions is assumed, the additional challenge of assessing those deviations is still present, since the deviated poles are not directly defined as a modelling subdomain. Therefore, they are again emulated by applying a boundary condition of $B_\theta = 0$ along the pole edge.

In this asymmetric model, Region II is divided into a number of air-gap subdomains, each corresponding to an air-gap slot between consecutive poles. For the development of the model, the three options to define those subdomains are used, as also outlined in 3.3.1:

1. Using the inner ($R_{2,\mathrm{i}}$) and outer ($R_{3,\mathrm{i}}$) radii of preceding (clockwise) pole (Figure A-3).
2. Using the inner ($R_{2,\mathrm{i+1}}$) and outer ($R_{3,\mathrm{i+1}}$) radii of proceeding (anticlockwise) pole.

3. Using the mean inner $\left(R_{2,\mathrm{i}} + R_{2,\mathrm{i+1}}\right)/2$ and mean outer $\left(R_{3,\mathrm{i}} + R_{3,\mathrm{i+1}}\right)/2$ radii of the preceding and proceeding poles.

The opening angle (β_i) and the initial angle of the subdomain with respect to a datum (θ_i) are defined in Figure A-3. The general solution of $\vec{A}$ in each subdomain can now be derived from (A.2.3). The following notation in (A.2.4), (A.2.5) has been adopted for simplification:

$$U_z(a,b) = \left(\frac{a}{b}\right)^z + \left(\frac{b}{a}\right)^z \tag{A.2.4}$$

$$X_z(a,b) = \left(\frac{a}{b}\right)^z - \left(\frac{b}{a}\right)^z \tag{A.2.5}$$

Using the separation of variables method, the general solution of the i[th] subdomain can be described by Fourier series and is provided in (A.2.6).

$$\begin{aligned} A_i^{(II)}(r,\theta) \; &= C_{II,i} + D_{II,i}\ln(r) \\ &+ \sum_{m=1}^{M}\left(E_{II,i,m}\frac{X_{f_{m,i}}(r,R_{3,s})}{X_{f_{m,i}}(R_{2,s},R_{3,s})} - F_{II,i,m}\frac{X_{f_{m,i}}(r,R_{2,s})}{X_{f_{m,i}}(R_{2,s},R_{3,s})}\right) \\ &\cdot\cos\left(f_{m,i}(\theta-\theta_i)\right) \end{aligned} \tag{A.2.6}$$

with

$$f_{m,i} = \frac{m\pi}{\beta_i} \tag{A.2.7}$$

$$s = i \tag{A.2.8}$$

where $C_{II,i}$, $D_{II,i}$, $E_{II,i,m}$ and $F_{II,i,m}$ are the Fourier coefficients, with M being the largest harmonic under consideration.

A.2.2. Region I/III – Non-permeable Rotor / Airgap

The asymmetries of the iron poles result in asymmetric boundaries between Region II and Regions I, III, i.e., the non-permeable section of the rotor and the airgap, respectively. Similar to Chapter 3, a series of variants of each region are defined, equal in number to the ferromagnetic poles. Each variant is again associated with a Region II subdomain, which defines its radial boundaries (Figure A-4).

In common with A.2.1, using the separation of variables method and the Laplace equation (A.2.3), the resultant general solutions for each variant can be derived. These are described by Fourier series and are provided in (A.2.9), (A.2.10). Similar to the model of Chapter 3, the resultant flux distribution for the air-gap is synthesised by using the appropriate Region III variant for the angular region it occupies (Figure A-4).

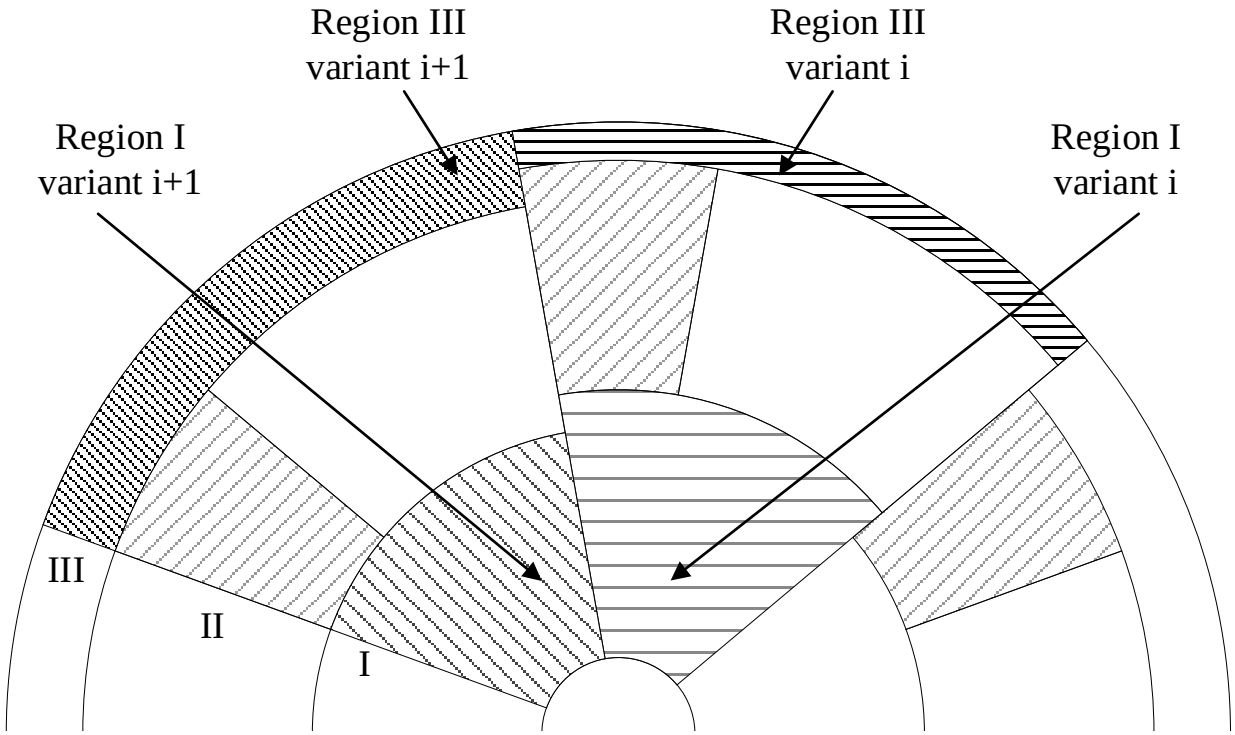

Figure A-4 Asymmetric VRM Region I/III variant definitions

$$A_i^{(I)}(r,\theta) = \sum_{k=1}^{K}\left(D_{I,i}\frac{R_{2,s}}{k}\frac{U_k(r,R_1)}{X_k(R_{2,s},R_1)}\right)\cos(k\theta) + \sum_{k=1}^{K}\left(F_{I,i}\frac{R_{2,s}}{k}\frac{U_k(r,R_1)}{X_k(R_{2,s},R_1)}\right)\sin(k\theta) \tag{A.2.9}$$

$$A_i^{(III)}(r,\theta) = \sum_{k=1}^{K}\left(C_{III,i}\frac{R_{3,s}}{k}\frac{U_k(r,R_4)}{X_k(R_{3,s},R_4)} + D_{III,i}\frac{R_4}{k}\frac{U_k(r,R_{3,s})}{X_k(R_4,R_{3,s})}\right)\cos(k\theta) + \sum_{k=1}^{K}\left(E_{III,i}\frac{R_{3,s}}{k}\frac{U_k(r,R_4)}{X_k(R_{3,s},R_4)} + F_{III,i}\frac{R_4}{k}\frac{U_k(r,R_{3,s})}{X_k(R_4,R_{3,s})}\right)\sin(k\theta) \tag{A.2.10}$$

where $C_{I/III,i}$, $D_{I/III,i}$, $E_{I/III,i}$ and $F_{I/III,i}$ are the Fourier coefficients and *K* denotes highest order of harmonics considered.

A.3. Variable Reluctance Machine Analytical Model – Solution

The general solutions of (A.2.6), (A.2.9), (A.2.10) can be solved as a system of equations by applying the necessary boundary conditions at the interfaces between regions. The resultant expressions are presented in the following subsections.

A.3.1. Interface I – II

The geometric asymmetries of the iron poles result in an asymmetric interface between the non-permeable section of the rotor (I) and the non-permeable slots between the poles (II). A solution is derived by considering the following boundary conditions.

$$H_{\theta,i}^{(I)}\Big|_{r=R_{2,s}} = H_{\theta}^{(II)}\Big|_{r=R_{2,i=1}\to R_{2,i=Q}} \tag{A.3.1}$$

$$A_{i}^{(II)}\Big|_{r=R_{2,s}} = A_{i}^{(I)}\Big|_{r=R_{2,s}} \tag{A.3.2}$$

In common with Chapter 3, while the effect of each deviation on the flux distribution is spatially focused in its vicinity, there is still an effect on the remaining space. This effect is captured by (A.3.1), which maps the total field intensity of Region II $\left(H_{\theta}^{(II)}\right)$, at its asymmetric inner radial boundary $\left(R_{2,i=1} \to R_{2,i=Q}\right)$, to the field intensity of each Region I variant $\left(H_{\theta,i}^{(I)}\right)$, at its radially symmetric outer boundary ($R_{2,s}$). Furthermore, as it this interface there is no change of medium the continuity of the radial component of the flux density can be expressed as the continuity of the vector potential (A.3.2). Development of (A.2.6) and (A.2.9) along with these boundary conditions results in the following equations.

$$D_{I,i,k} = \frac{1}{\pi}\int_{0}^{2\pi} H_{\theta,i}^{(II)}\Big|_{r=R_{2,s}} \cdot \cos(k\theta)\, d\theta \tag{A.3.3}$$

$$F_{I,i,k} = \frac{1}{\pi}\int_{0}^{2\pi} H_{\theta,i}^{(II)}\Big|_{r=R_{2,s}} \cdot \sin(k\theta)\, d\theta \tag{A.3.4}$$

$$C_{II,i} + D_{II,i}\ln\left(R_{2,i}\right) = \frac{1}{\beta_i}\int_{\theta_i}^{\theta_i+\beta_i} A_{i}^{(I)}\Big|_{r=R_{2,s}} d\theta \tag{A.3.5}$$

$$E_{II,i} = \frac{2}{\beta_i} \int_{\theta_i}^{\theta_i+\beta_i} A_i^{(I)}\Big|_{r=R_{2,s}} \cdot \cos\left(f_{m,i}(\theta - \theta_i)\right) d\theta \tag{A.3.6}$$

Equations (A.3.3) – (A.3.6) can be expanded and expressed in matrix form (A.3.7) – (A.3.10). The Fourier coefficients of Region I, $\boldsymbol{D_I}, \boldsymbol{F_I}$ are column vectors of length $K \cdot Q$, with K and Q denoting the maximum number of harmonics in the region and the number of iron poles, respectively. The Fourier coefficients of Region II, $\boldsymbol{E_{II}}, \boldsymbol{F_{II}}$ are column vectors of length $M \cdot Q$ and $\boldsymbol{C_{II}}, \boldsymbol{D_{II}}$ of length equal to Q, with M being the maximum harmonic order considered in Region II.

$$-\boldsymbol{I_{Ki\,R2}}\boldsymbol{D_I} + \boldsymbol{\delta_i^T}\boldsymbol{D_{II}} + \boldsymbol{\eta_i^T}\boldsymbol{f_m}\boldsymbol{G_4}\boldsymbol{E_{II}} - \boldsymbol{\eta_i^T}\boldsymbol{f_m}\boldsymbol{G_5}\boldsymbol{F_{II}} = 0 \tag{A.3.7}$$

$$-\boldsymbol{I_{Ki\,R2}}\boldsymbol{F_I} + \boldsymbol{\sigma_i^T}\boldsymbol{D_{II}} + \boldsymbol{\xi_i^T}\boldsymbol{f_m}\boldsymbol{G_4}\boldsymbol{E_{II}} - \boldsymbol{\xi_i^T}\boldsymbol{f_m}\boldsymbol{G_5}\boldsymbol{F_{II}} = 0 \tag{A.3.8}$$

$$\boldsymbol{\delta_{i,\pi}}\boldsymbol{G_7}\boldsymbol{D_I} + \boldsymbol{\sigma_{i,\pi}}\boldsymbol{G_7}\boldsymbol{F_I} - \boldsymbol{I_Q}\boldsymbol{C_{II}} - \boldsymbol{I_Q}\ln\left(R_{2,s}\right)\boldsymbol{D_{II}} = 0 \tag{A.3.9}$$

$$\boldsymbol{\eta_{i,\pi}}\boldsymbol{G_7}\boldsymbol{D_I} + \boldsymbol{\xi_{i,\pi}}\boldsymbol{G_7}\boldsymbol{F_I} - \boldsymbol{I_{MQ}}\boldsymbol{E_{II}} = 0 \tag{A.3.10}$$

where

$$\boldsymbol{I_{Ki\,R2}} = \mathrm{diag}(R_{2,1}, R_{2,2}, \dots, R_{2,Q})_{QK\times QK} \tag{A.3.11}$$

$$\delta(i,k) = \frac{1}{\pi} \int_{\theta_i}^{\theta_i+\beta_i} \cos(k\theta) d\theta \tag{A.3.12}$$

$$\boldsymbol{\delta_i} = \left(\delta(i,k), \delta(i,k), \dots, \delta(i,k)\right)_{Q\times QK} \tag{A.3.13}$$

$$\boldsymbol{\delta_{i,\pi}} = \mathrm{diag}\left(\frac{\pi}{\beta_i}\delta(1,k), \frac{\pi}{\beta_i}\delta(2,k)\ldots, \frac{\pi}{\beta_i}\delta(Q,k)\right)_{Q\times QK} \tag{A.3.14}$$

$$\sigma(i,k) = \frac{1}{\pi}\int_{\theta_i}^{\theta_i+\beta_i} \sin(k\theta)d\theta \tag{A.3.15}$$

$$\eta(m,k,i) = \frac{1}{\pi}\int_{\theta_i}^{\theta_i+\beta_i} \cos(k\theta)\cdot\cos\left(f_{m,i}(\theta-\theta_i)\right)d\theta \tag{A.3.16}$$

$$\boldsymbol{\eta_i} = \begin{bmatrix} \eta(m,k,1) & \cdots & \eta(m,k,1) \\ \vdots & \ddots & \vdots \\ \eta(m,k,Q) & \cdots & \eta(m,k,Q) \end{bmatrix}_{QM\times QK} \tag{A.3.17}$$

$$\boldsymbol{\eta_{i,\pi}} = \cos\left(\frac{2\pi}{\beta_i}\boldsymbol{\eta}(m,k,1), \frac{2\pi}{\beta_i}\boldsymbol{\eta}(m,k,2), \ldots, \frac{2\pi}{\beta_i}\boldsymbol{\eta}(m,k,Q)\right)_{QM\times QK} \tag{A.3.18}$$

$$\xi(m,k,i) = \frac{1}{\pi}\int_{\theta_i}^{\theta_i+\beta_i} \sin(k\theta)\cdot\cos\left(f_{m,i}(\theta-\theta_i)\right)d\theta \tag{A.3.19}$$

$$\boldsymbol{f_{m,i}} = f_{m,i}\cdot\boldsymbol{I_M} \tag{A.3.20}$$

$$\boldsymbol{f_m} = \mathrm{diag}\left(\boldsymbol{f_{m,i}}(1), \boldsymbol{f_{m,i}}(2), \ldots, \boldsymbol{f_{m,i}}(Q)\right) \tag{A.3.21}$$

$$\boldsymbol{G_4} = \mathrm{diag}(\boldsymbol{g_4}(1), \boldsymbol{g_4}(2), \ldots, \boldsymbol{g_4}(Q))_{QM\times QM} \tag{A.3.22}$$

$$\boldsymbol{g_4}(\boldsymbol{i}) = \boldsymbol{I_M}\cdot\left(\frac{U_{f_{m,i}}(R_{2,s}, R_{3,s})}{X_{f_{m,i}}(R_{2,s}, R_{3,s})}\right) \tag{A.3.23}$$

$$\boldsymbol{g_5(i)} = \boldsymbol{I_M} \cdot \left(\frac{2}{X_{f_{m,i}}\left(R_{2,s}, R_{3,s}\right)} \right) \tag{A.3.24}$$

$$\boldsymbol{g_7(i)} = \boldsymbol{I_K} \cdot \left(\frac{R_{2,s}}{k} \frac{U_k\left(R_{2,s}, R_1\right)}{X_k\left(R_{2,s}, R_1\right)} \right) \tag{A.3.25}$$

A.3.2. Interface II – III

Similar to section A.3.1, the respective boundary conditions applied to the interface between the Region II subdomains and Region III air-gap variants are as follows:

$$H_{\theta,i}^{(III)}\Big|_{r=R_{3,s}} = H_{\theta}^{(II)}\Big|_{r=R_{3,i=1} \to R_{3,i=Q}} \tag{A.3.26}$$

$$A_i^{(II)}\Big|_{r=R_{3,s}} = A_i^{(III)}\Big|_{r=R_{3,s}} \tag{A.3.27}$$

The application of boundary equations (A.3.26), (A.3.27) to (A.2.9), (A.2.10) results in the following expressions:

$$C_{III,i,k} = \frac{1}{\pi} \int_0^{2\pi} H_{\theta,i}^{(II)}\Big|_{r=R_{3,s}} \cdot \cos(k\theta)\, d\theta \tag{A.3.28}$$

$$E_{III,i,k} = \frac{1}{\pi} \int_0^{2\pi} H_{\theta,i}^{(II)}\Big|_{r=R_{3,s}} \cdot \sin(k\theta)\, d\theta \tag{A.3.29}$$

$$C_{II,i} + D_{II,i} \ln\left(R_{3,s}\right) = \frac{1}{\beta_i} \int_{\theta_i}^{\theta_i+\beta_i} A_i^{(III)}\Big|_{r=R_{3,s}} d\theta \tag{A.3.30}$$

$$F_{II,i} = \frac{2}{\beta_i} \int_{\theta_i}^{\theta_i+\beta_i} A_i^{(III)}\Big|_{r=R_{3,s}} \cdot \cos\left(f_{m,i}(\theta - \theta_i)\right) d\theta \tag{A.3.31}$$

Development of equations (A.3.28) – (A.3.31), expressed in matrix form, leads to (A.3.32) – (A.3.35).

$$-\boldsymbol{I_{Ki\,R3}C_{III}} + \boldsymbol{\delta_i^T D_{II}} + \boldsymbol{\eta_i^T f_m G_5 E_{II}} - \boldsymbol{\eta_i^T f_m G_4 F_{II}} = 0 \tag{A.3.32}$$

$$-\boldsymbol{I_{Ki\,R3}E_{III}} + \boldsymbol{\sigma_i^T D_{II}} + \boldsymbol{\xi_i^T f_m G_5 E_{II}} - \boldsymbol{\xi_i^T f_m G_4 F_{II}} = 0 \tag{A.3.33}$$

$$\boldsymbol{\delta_{i,\pi} G_8 C_{III}} + \boldsymbol{\delta_{i,\pi} G_9 D_{III}} + \boldsymbol{\sigma_{i,\pi} G_8 E_{III}} + \boldsymbol{\sigma_{i,\pi} G_9 F_{III}} - \boldsymbol{I_Q C_{II}} - \boldsymbol{I_Q} \ln\left(R_{3,s}\right) \boldsymbol{D_{II}} = 0 \tag{A.3.34}$$

$$\boldsymbol{\eta_{i,\pi} G_8 C_{III}} + \boldsymbol{\eta_{i,\pi} G_9 D_{III}} + \boldsymbol{\xi_{i,\pi} G_8 E_{III}} + \boldsymbol{\xi_{i,\pi} G_9 F_{III}} - \boldsymbol{I_{MQ} F_{II}} = 0 \tag{A.3.35}$$

where

$$\boldsymbol{g_8(i)} = \boldsymbol{I_K} \cdot \left(\frac{R_{3,s}}{k} \frac{U_k\left(R_{3,s}, R_4\right)}{X_k\left(R_{3,s}, R_4\right)}\right) \tag{A.3.36}$$

$$\boldsymbol{g_9(i)} = \boldsymbol{I_K} \cdot \left(\frac{R_4}{k} \frac{2}{X_k\left(R_4, R_{3,s}\right)}\right) \tag{A.3.37}$$

A.3.3. Interface III – Stator

The stator is not directly considered as a region. It is approximated by defining its field intensity at the Region III outer boundary (R_5), as shown in [105] (A.3.39). Therefore, at that radius the following boundary condition applies.

$$H_{\theta,i}^{(III)}\Big|_{r=R_5} = H_{\theta}^{(Stator)}\Big|_{r=R_5} \tag{A.3.38}$$

$$H_{\theta}^{(Stator)}\Big|_{r=R_5} = \sum_{k=1}^{K} H_k \cdot cos\big(kp(\theta - \varphi_0)\big) \tag{A.3.39}$$

where H_k is the peak value of the kth harmonic, p the number of stator pole pairs and φ_0 the angular position. In this analysis, a sinusoidal stator field distribution is assumed, i.e., $K = 1$.

Algebraic manipulation of (A.2.10) along with boundary conditions (A.3.38) results in the following equations, expressed in matrix form.

$$\boldsymbol{I_{KQ}D_{IV}} = \boldsymbol{H_{\theta ck}^{(Stator)}} \tag{A.3.40}$$

$$\boldsymbol{I_{KQ}F_{IV}} = \boldsymbol{H_{\theta sk}^{(Stator)}} \tag{A.3.41}$$

where

$$\boldsymbol{H_{\theta ck}^{(Stator)}} = \left[h_{\theta ck}^{(Stator)}, h_{\theta ck}^{(Stator)}, \dots, h_{\theta ck}^{(Stator)}\right]_{QK\times 1} \tag{A.3.42}$$

$$\boldsymbol{H_{\theta sk}^{(Stator)}} = \left[h_{\theta sk}^{(Stator)}, h_{\theta sk}^{(Stator)}, \dots, h_{\theta sk}^{(Stator)}\right]_{QK\times 1} \tag{A.3.43}$$

$$h_{\theta ck}^{(Stator)}(k,1) = \frac{\mu_0}{\pi}\int_0^{2\pi} H_k \cdot \cos(k\theta)\cos\big(kp(\theta-\varphi_0)\big)\,d\theta \tag{A.3.44}$$

$$h_{\theta sk}^{(Stator)}(k,1) = \frac{\mu_0}{\pi}\int_0^{2\pi} H_k \cdot \sin(k\theta)\cos\big(kp(\theta-\varphi_0)\big)\,d\theta \tag{A.3.45}$$

A.3.4. Overall Solution

The equations developed in this chapter can be solved as a system of linear equations, to deduce all the unknown Fourier coefficients. These can then be used to calculate the flux distributions of each Region III variant, as follows:

$$\begin{aligned} B_{r,i}^{(III)}(r,\theta) = &\sum_{k=1}^{K} -\left(C_{III,i}\frac{R_{3,s}}{k}\frac{U_k(r,R_4)}{X_k(R_{3,s},R_4)} + D_{III,i}\frac{R_4}{k}\frac{U_k(r,R_{3,s})}{X_k(R_4,R_{3,s})}\right)\sin(k\theta) \\ &+ \sum_{k=1}^{K}\left(E_{III,i}\frac{R_{3,s}}{r}\frac{U_k(r,R_4)}{X_k(R_{3,s},R_4)} + F_{III,i}\frac{R_4}{r}\frac{U_k(r,R_{3,s})}{X_k(R_4,R_{3,s})}\right)\cos(k\theta) \end{aligned} \tag{A.3.46}$$

$$\begin{aligned} B_{\theta,i}^{(III)}(r,\theta) = &\sum_{k=1}^{K} -\left(C_{III,i}\frac{R_{3,s}}{r}\frac{X_k(r,R_4)}{X_k(R_{3,s},R_4)} + D_{III,i}\frac{R_4}{r}\frac{X_k(r,R_{3,s})}{X_k(R_4,R_{3,s})}\right)\cos(k\theta) \\ &- \sum_{k=1}^{K}\left(E_{III,i}\frac{R_{3,s}}{r}\frac{X_k(r,R_4)}{X_k(R_{3,s},R_4)} + F_{III,i}\frac{R_4}{r}\frac{X_k(r,R_{3,s})}{X_k(R_4,R_{3,s})}\right)\sin(k\theta) \end{aligned} \tag{A.3.47}$$

The resultant and total Region III air-gap flux distribution is then synthesised by concatenating the flux distributions of each variant for the angular domain they occupy, similar to Chapter 3.

A.4. Variable Reluctance Machine Analytical Model – Validation

The accuracy of this analytical model is validated by comparing a solution of two deviated VRMs to their 2D linear FEA equivalent, considering infinite permeability in ferromagnetic

Table 20 VRM Parameters for Model Validation

Variables	VRM 1	VRM 2
Number of rotor poles	6	8
Stator pole pairs	3	4
Rotor OD (mm)	140	100
Rotor poles length (mm)	30	20
Rotor poles span angle (deg)	40	28.5
Air-gap length (mm)	0.5	0.5
Axial length (mm)	100	100
Peak stator field intensity (A/m)	$7.5 \cdot 10^4$	$1 \cdot 10^5$

regions. The specifications of the sample VRMs, along with their respective errors are outlined in Table 20 and Table 21.

In all regions the first 200 harmonics are considered. The torque is calculated at the middle of the smallest airgap section (i.e., at a radius between the stator and the most outwardly deviated pole) for both the analytical model and the FEA. The resultant flux distribution plots of both methods are provided in Figure A-5 and Figure A-6. The accuracy of the model, depending on the number of harmonics considered, is shown in Figure A-7.

In both validation cases an excellent correlation between the analytical model and FEA can be observed. This proves that the effect of such asymmetric deviations on the flux distribution in a VRM can be accurately tracked through the presented analytical model.

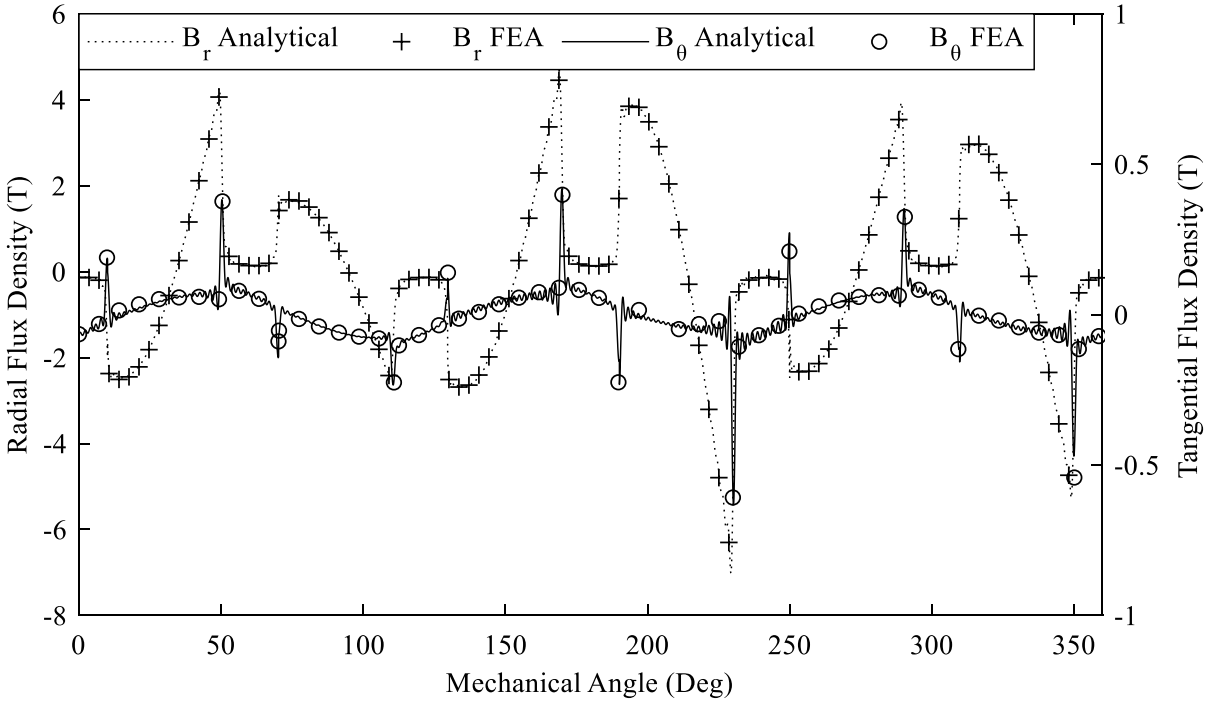

Figure A-5 Analytical vs linear FEA flux density – VRM No. 1

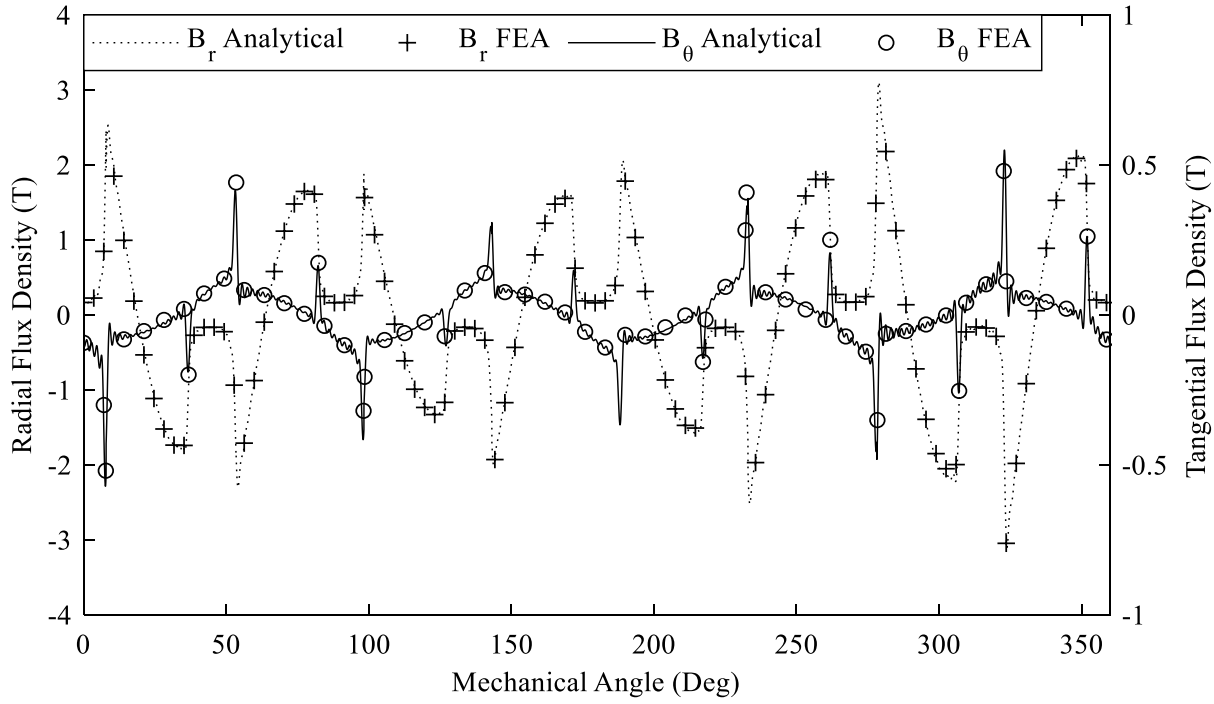

Figure A-6 Analytical vs linear FEA flux density – VRM No. 2

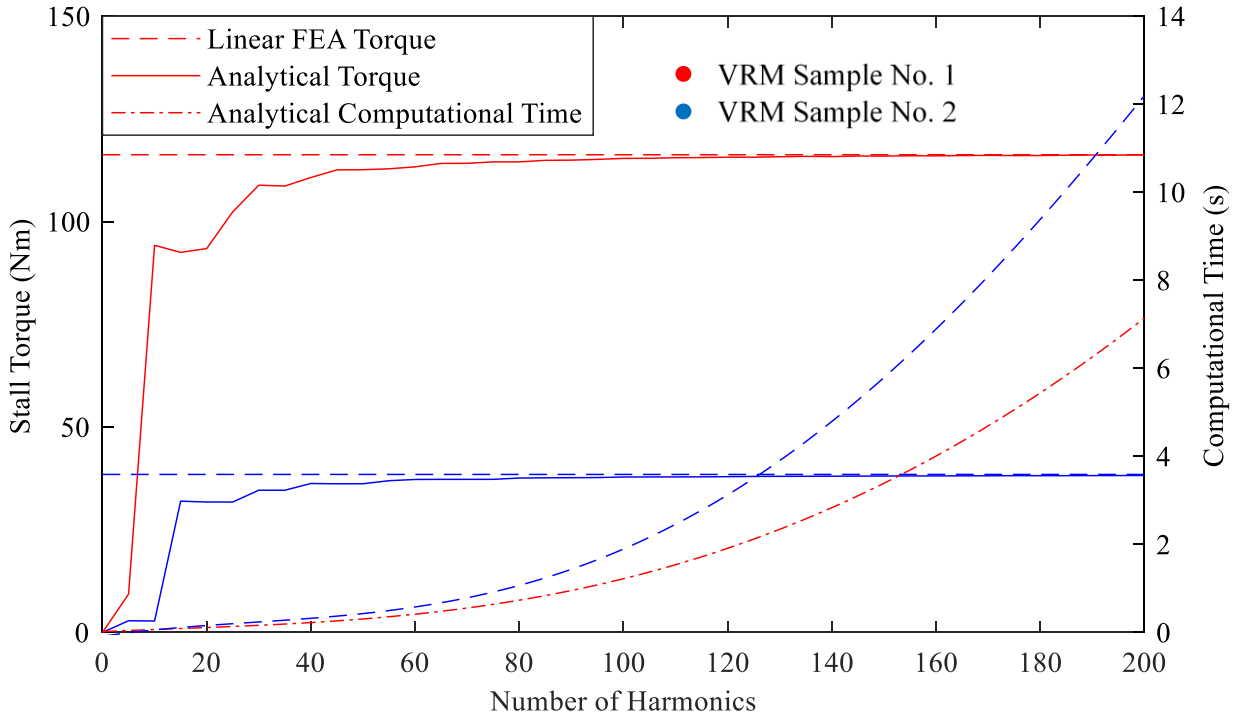

Figure A-7 Model computational speed and accuracy

The dominant feature of this method, which is its high computational efficiency, is illustrated further in Figure A-7. This figure shows the accuracy in the stall torque calculation along with the computational time for an increasing number of harmonics considered. The plot indicates that around 100-120 harmonics are required to achieve converged stall torque results, with the respective computational time being less than 2 s for both VRMs. On the contrary, the equivalent FEA was completed in 2:10 minutes.

A.5. Summary

In this chapter the asymmetric CMG analytical model of Chapter 3 has been adapted to a VRM application. It has been noted that, similar to the model of Chapter 3, the assumptions adopted introduce some limitations. These include the inability to take into account the saturation effects, due to the infinite permeability assumption, and the creation of discontinuous boundaries between regions. The effects of these discontinuities are typically very small, however in studies

Table 21 Parameter Error for VRM Model Validation

Variable	Rotor Pole Error							
VRM 1								
	No. 1	***No. 2***	***No. 3***	***No. 4***	***No. 5***	***No. 6***		
Length (mm)	-0.007	0.006	0.060	0.046	-0.023	0.051		
Span angle (deg)	0.012	-0.001	0.012	-0.003	-0.002	0.025		
Radial position (mm)	0.090	-0.161	0.096	0.2174	0.065	0.138		
Angular position (deg)	-0.072	0.245	-0.301	0.115	0.043	-0.174		
VRM 2								
	No. 1	***No. 2***	***No. 3***	***No. 4***	***No. 5***	***No. 6***	***No. 7***	***No. 8***
Length (mm)	0.012	-0.005	0.005	-0.013	0.015	-0.019	-0.018	-0.014
Span angle (deg)	0.024	0.024	0.011	-0.020	0.012	0.027	0.008	0.017
Radial position (mm)	0.043	0.042	-0.115	-0.004	-0.022	0.084	0.146	0.148
Angular position (deg)	-0.392	0.192	0.043	-0.101	0.187	-0.228	-0.014	-0.032

investigating larger positional deviations of the iron poles, their effect may be more prominent. However, it has been shown that the model definitions of Chapter 3, together with the selected boundary conditions along with their treatment (e.g., mapping of the asymmetric Region II field intensity to the radially symmetric boundaries of each Region III variant) are still valid. Two deviated VRMs of different nominal parameters have been used to prove the accuracy of the model. It was shown that excellent correlation is achieved with linear FEA, under the same assumption of an infinite permeability in the ferromagnetic regions. In addition to the high level of accuracy, this flexible method offers a significant increase in computational efficiency, being more than an order of magnitude faster compared to linear FEA.

Appendix B – Publication 1

Causes and effects of Geometric Deviation in Magnetic Gears

A. Leontaritis, A. Nassehi, J. Yon
Electrical Energy Management Group
University of Bristol, UK

***Abstract* -- This paper presents a study of geometric deviations in a Coaxial Magnetic Gear. Large discrepancies between Finite Element Analysis and experimental performance are often reported. These are, in some part, often attributed to manufacturing error. Manufacturing error causes the physical geometry of a gear to differ from its modelled design which will clearly affect its performance. However, geometric deviations can also be caused by defection of the gears structure under the large cyclic electromagnetic loads exerted on the active components. A comprehensive overview of the causes of geometric deviation in the PM rotors and the modulation ring is provided, along with their potential manufacturing processes and expected tolerances. The effect of these deviations is assessed and the importance of proper treatment of such geometric subtleties is outlined.**

***Index Terms*— magnetic gears, tolerances, manufacturing error**

I. Introduction

MANY engineering applications require a multiplication of either angular speed or torque, and there is a wide range of transmission systems which can be used for this purpose. Mechanical gears are a highly developed technology that has traditionally dominated the transmission sector of many engineering applications, however they do have some fundamental drawbacks. The basis of the problem is the mechanical contact between the gears which leads to undesirable effects such as thermal losses through friction and wear of the components. Such effects contribute to decreased efficiency and increased maintenance costs. Magnetic gears (MG) are devices that rely on the magnetic interaction between their components to allow the transmission of power. The contactless nature of MGs leads to low maintenance requirements and the magnetic coupling gives a benign slipping behaviour in the event of overload.

A variety of MG topologies have been investigated throughout the last century. A common topology seen in the literature is the Coaxial Magnetic Gear (CMG) [1]–[10]. A CMG (Fig. 1) consists of two coaxial Permanent Magnet (PM) rotors with a ring of ferromagnetic pole pieces placed between them. This ring modulates and therefore allows coupling of the magnetic fields of the two rotors. The modulation ring should be strong enough to withstand the forces exerted on the pole pieces. These forces vary depending on the design of the CMG and the application.

Research of CMGs has shown achievable torque densities exceeding 100 kNm/m^3, which is comparable to that of two- and three-stage helical gearboxes [1]. Therefore, MGs can theoretically replace their mechanical counterparts in certain applications varying from tidal turbines to small scale robotics [2], [3]. High specific output designs have been prototyped, however experimentally realised performance is often significantly lower than predicted by the analysis. Multiple examples in the literature have reported discrepancies of around 30% between two-dimensional (2D) Finite Element Analysis (FEA) and experimental data [4], [5]. This is attributed to a combination of end effects and to manufacturing error, however the balance of these contributors is seldom assessed. The authors in [6] performed an extensive three-dimensional (3D) FEA study, including almost all supporting components, and a discrepancy of 9% was reported. This was solely attributed to "manufacturing error", however this error was not quantified in geometric terms. Understanding the processes and mechanisms that lead to geometric error in a CMG is clearly important when attempting to understand or improve the correlation between analyses and prototype performance.

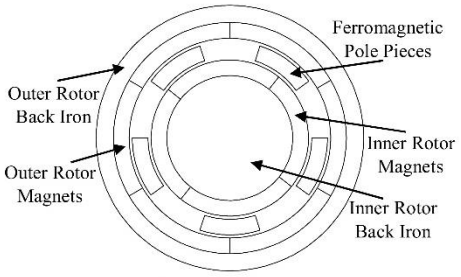

Fig. 1 Component identification in a CMG

This paper presents a comprehensive overview of the various causes of geometric deviation in an MG along with an assessment of their potential effects on performance. The term "manufacturing error" mentioned in the literature is one source of geometric deviations, however they can also be caused by deflection of components under load. This paper outlines the potential manufacturing processes used in the production of a CMG and discusses the manufacturing accuracy of these processes. The loads which affect the pole pieces of the central modulating ring are also assessed and the impact of geometric deviations is quantified.

II. Geometric Deviations Due To Manufacturing Error

Several geometric deviations are caused by errors in the

This research has been funded by the Engineering and Physical Sciences Research Council (EPSRC)

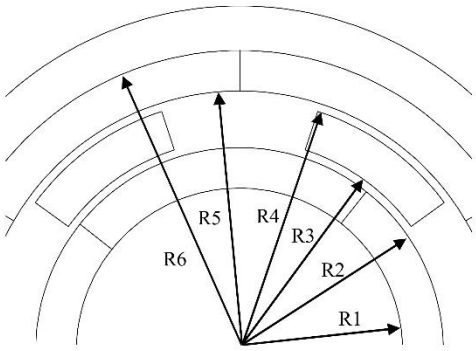

Fig. 2 Definition of radii in a CMG

manufacturing of MG components. This section presents the expected manufacturing processes and discusses the achievable tolerances in the PM rotors and the modulation ring.

A. *Manufacturing Error in the Permanent Magnet Rotors*

Each rotor consists of a back iron to which magnetised arcs of rare earth metal are attached (Fig. 1). Therefore, geometric deviations in the rotors are either due to manufacturing error in the construction of the back iron or errors in the manufacture and assembly of the PMs. PM rotors used in MGs are a well-known and mature technology as similar assemblies are widely used in surface mounted PM electrical machines. Their manufacturing methods are therefore well understood and largely consistent across the sector [11]. Table I presents the possible manufacturing processes for each part of a PM rotor along with expected tolerances [12]–[14].

Depending on the magnetic field distribution, different constructions may be used. A high flux distribution in the back iron will increase eddy current losses, and a laminated back iron will therefore be preferable. In this case the laminations can either be manufactured by stamping, Laser Beam Machining (LBM) or wire Electrical Discharge Machining (EDM) and welded or bonded using adhesives to form a stack [11]. In the case where a laminated rotor stack is not required, a turning process can be employed. For the two back irons in a CMG, the parameters where manufacturing error is of interest are the outer radius (R1) of the inner back iron; the inner radius (R6) of the outer back iron; and the concentricity, coaxiality and cylindricity of both rotors with respect to a common datum (Fig. 2). The manufacturing and assembly methods mentioned above have been widely used in electrical machines and tight tolerances on the key radii can be achieved [11]–[14]. The concentricity and coaxiality of the rotors will also depend on the manufacturing error of the supporting structure. This will typically consist of assemblies with bearings and conventional Geometric Dimensioning and Tolerances (GD&T) standards can be used to obtain a tight stack-up tolerance.

The manufacturing of the PMs and their attachment to the rotor back iron is another potential source of error. PMs can be formed into their final shape through grinding or by EDM for low volume manufacturing, with both options offering very high precision [18]. Neodymium Iron Boron (NdFeB) magnets are brittle and prone to corrosion. The edges are therefore usually rounded off, typically with 0.13 - 0.38 mm radii. An epoxy coating may also be applied to protect against corrosion [18]. While the accuracy of these processes is well defined, these geometric subtleties are not always considered in analyses. Furthermore, surface-mounted PMs are typically bonded to the rotor back iron using adhesives which create a glue-gap between the back iron and the PMs. Tooling serves to minimise the asymmetry of the glue-gap but some effect on the radial (R1, R6) and tangential positioning of the PMs is inevitable.

B. *Manufacturing Error in the Modulation Ring*

The ferromagnetic pole pieces, which modulate the magnetic field, are constrained in space by a supporting structure. A non-magnetic material or high circumferential reluctance structure is required in order not to interfere with the field distribution. In addition, a non-conductive material or laminated assembly is also desirable to minimise eddy current losses.

TABLE I
ROTOR SOURCES OF DEVIATION AND EXPECTED TOLERANCES

Deviation Description	Cause of Deviation	Expected Manufacturing Processes [11]	Expected Tolerance
Radius of inner/outer rotor back iron (R1, R6)	Manufacturing error	Machining – Turning	± 0.008 - 0.06 mm [12]–[14]
		Stamping	± 0.02 - 0.06 mm [12]–[14]
		Wire EDM	± 0.003 - 0.05 mm [13], [14]
		LBM	± 0.015 - 0.125 mm [12]
Total Runout (⌰) Concentricity of inner/outer rotor; Coaxiality of inner/outer rotor; Cylindricity of inner/outer rotor	Error in supporting structures/ Manufacturing error	N/A	0.01 – 0.03 mm [11]
Magnet Pitch Angle	Manufacturing error	Grinding	± 0.0125 mm [12], [14]
		Wire EDM	± 0.003 - 0.05 mm [13], [14]
Magnet Thickness	Manufacturing error	Grinding	± 0.0125 mm [12], [14]
		Wire EDM	± 0.003 - 0.05 mm [13], [14]
Magnet Length	Manufacturing error	Grinding	± 0.0125 mm [12], [14]
		Wire EDM	± 0.003 - 0.05 mm [13], [14]
Magnetisation Fault	Error in magnetisation	External Magnetic Field	± 5 - 10% [15], [16]
Asymmetry in glue gap length	N/A	N/A	± 0.02 - 0.08 mm [17]

a) Single part laminated modulation ring b) Laminated pole pieces supported through bars c) Support structure with laminated pole pieces using additive manufacturing

Fig. 3 Possible support structure designs

Manufacturing error in the modulation ring is relevant to gear performance if it affects the dimensions, location and orientation of each pole piece. In contrast to PM rotors, the manufacturing methods for modulation rings in CMGs are less developed and not 'standardised'.

Various concepts have been developed for the supporting structure. One modulation ring design, patented by Hawksworth [7], is illustrated in Fig. 3a. This patent details a laminated supporting structure of annular plates with circumferentially equidistant hollow (and thus high reluctance) sections. In this case the pole pieces are the solid sections of the annular plate, which are linked together by the bridges around the hollow openings (Fig. 3a). In [9] another design is presented where a set of circular non-magnetic steel bars, coated with an electrical insulator, act as a supporting structure. These bars are placed between pole pieces (Fig. 3b). A similar design has been patented by Calverley in [8]. This modulation ring has the supporting bars manufactured from either a composite structure (i.e. carbon fibre or glass fibre pultrusions) or a machined engineering plastic, such as PEEK. A supporting structure similar to Fig. 3c, could be manufactured from an engineering plastic using additive manufacturing. For a small aspect ratio CMG, such a structure could also be machined in a milling operation, however the manufacturing error along the length would worsen with increasing aspect ratio. The edges of the slots, and therefore the pole pieces, will also have to be rounded due to the radius of the cutter. Other options could include casting. The dimensions of the laminated pole pieces, which will either be stamped or manufactured using EDM and joined in a similar way to the rotor back iron laminations, will also have a manufacturing error. The expected tolerances of each process are listed in Table II [12]–[14].

It should be noted that while Fig. 1 presented the simplistic, classical shape of the pole pieces, the more realistic designs outlined above and illustrated in Fig. 3, lead to a different pole piece shape. Therefore, understanding the specific design of the modulation ring is critical in obtaining good correlation between modelling and prototypes. It should also be noted that all these designs require further supporting components located outside of the 'active envelope'. As well as affecting geometric error in the assembly, these components may create further eddy current losses if they are made out of a conducting material and exposed to a changing magnetic field via end effects.

III. Geometric Deviations from Deflections due to Magnetic and Mechanical Forces

Another important source of geometric deviation is the deflection of components due to the exerted magnetic and mechanical forces – this is rarely quantified in the literature. Magnetic and mechanical loads are exerted on both the inner and outer PM rotors. However, the same applies for the rotors of PM machines and, if their manufacturing and assembly standards are followed, minimal deflections will be expected. In this paper, the modulation ring is assumed stationary and

TABLE II
Modulation Ring Sources of Deviation and Expected Tolerances

Deviation Description	Cause of Deviation	Expected Manufacturing Processes	Expected Tolerance
Inner/outer radii of pole pieces (R3, R4)	Manufacturing error	Type 1 – Stamping	± 0.02 - 0.06 mm [12]–[14]
		Type 2 – Pultrusion	± 0.2 - 1 mm [12], [14]
		Type 3 - Additive Manufacturing / Milling	± 0.1 - 0.25 mm / ± 0.01 - 0.06 mm [12]–[14]
Pole Piece Pitch Angle	Manufacturing error	Stamping	± 0.02 - 0.06 mm [12]–[14]
		Wire EDM	± 0.003 - 0.05 mm [13], [14]
Pole Piece Thickness	Manufacturing error	Stamping	± 0.02 - 0.06 mm [12]–[14]
		Wire EDM	± 0.003 - 0.05 mm [13], [14]
Pole Piece Length	Manufacturing error	Stamping	± 0.02 - 0.06 mm [12]–[14]
		Wire EDM	± 0.003 - 0.05 mm [13], [14]

therefore only magnetic forces are exerted on the pole pieces. If the modulation ring could rotate, inertial forces will also be applied.

As mentioned in Section II various modulation ring designs can be employed. Each design will have different mechanical properties depending on the topology and the materials used. Therefore, general estimates of pole piece deflection cannot be provided. However, during the design phase of a CMG, this deflection must be considered, as it can have a significant effect on performance. The magnetic forces exerted on the pole pieces will lead to some deflection in the modulation ring. This deflection will be determined by the mechanical properties of the supporting material. The new position of the pole pieces will modify the loads exerted on the modulation ring which could lead to further deflections. In addition, the geometric deviations due to manufacturing error, described in Section II, will also affect the magnitude of the exerted forces.

A magnetostatic FEA study was performed using the CMG, outlined in Table III and illustrated in Fig. 4. The software used was FEMM [19]. A magnetic remanence of 1.23 T was used for the PM material. The inner rotor stall torque of this CMG is 68 Nm. The radial and tangential forces on each pole piece were determined resulting in magnitudes of up to 1200 N. In an ideal CMG, without any geometric deviations, all pole pieces will, at some point, experience the same forces. In Fig. 5, the variation of the radial force for one magnetic period is presented. Each coloured plot represents a pole piece. A similar profile is followed for the tangential force. It is obvious that the magnitude of these loads cannot be considered negligible. As would be expected, Fig. 5 also shows that large cyclic loads will be exerted on the pole pieces. The deflection of the modulation ring under those loads will depend on various factors.

The authors of [9] found that the location of the pole pieces in their design varied by -0.4 to 0.2 mm in the radial direction and up to 0.45 mm circumferentially. These are highly significant compared to the deviations due to manufacturing error from Table I and II.

IV. Effects of Geometric Deviations

Geometric deviations, either due to error in the manufacturing process or deflections under load will certainly have an effect on the performance of the CMG. These should be considered in the analysis to ensure that a gear meets its performance requirements. Knowing the effect of geometric deviations can also facilitate the definition of permissible tolerances for critical components in order to satisfy the design specifications.

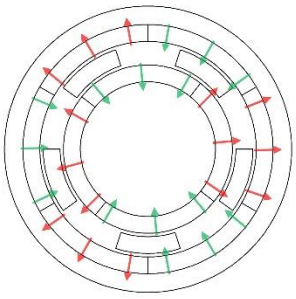

Fig. 4 Direction of magnetisation

TABLE III
CMG Specifications

Quantity	Value
Number of pole pieces	5
Inner rotor pole pairs	2
Outer rotor pole pairs	3
R1	40 mm
R2	50 mm
R3	52 mm
R4	62 mm
R5	64 mm
R6	74 mm
Axial length	100 mm
PM remanence	1.23
PM relative permeability	1

A general assessment of geometric deviations can be performed by conducting a statistical study. This involves several analyses of an MG design where key dimensions are perturbed based on the expected probability distributions of the relevant manufacturing errors. This can be done using an FEA model. However, if using FEA, a very high mesh density is a prerequisite to produce accurate results. Therefore, the computational cost is very high. In [20] the effect of manufacturing error on the cogging torque of a PM machine is investigated statistically. Monte Carlo simulations of 10,000 samples were performed, and the Probability Density Function (PDF) of the cogging torque was derived. This analysis was performed using an analytical solution due to the computational time required for FEA. In a CMG, due to the presence of two rotors and the stationary modulation ring, simplifications such as periodicity can rarely be applied. Therefore, FEA on a CMG would be even more computationally intense.

To gauge the impact of geometric deviations within the limits specified in Tables I and II, a short magnetostatic study was performed where a set of 40 samples of the same CMG assessed in Section III were analysed with random geometric deviations applied. The study used a very high mesh density

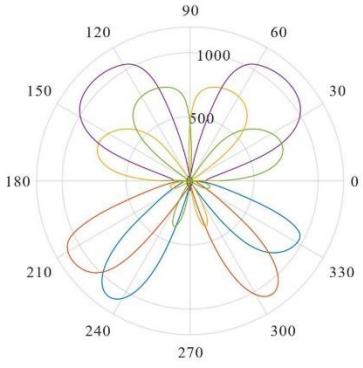

Fig. 5 Radial force variation over one magnetic period – Each colour represents a pole piece with the force (N) given in the radial contours

in the air-gap. Random deviations have been applied to the radii of both rotors; the concentricity of the inner rotor; and the angular and radial position of each pole piece. These are outlined in Table IV. An additional mechanical model would also be required to assess deviations due to load. This aspect is therefore not included in this analysis.

The number of samples is not sufficient to derive a PDF for the stall torque. However, with certain adjustments, this study can provide an indication on the degree of spread in the gear's performance. Each of the errors in the manufacturing processes will tend to have a normal or skewed distribution, similar to [17]. The maximum degree of spread will be determined by the extreme cases, close to the limits of the PDF. However, with a normal or skewed distribution many samples would be required to ensure that such cases are considered, due to their very low probabilities. Therefore, in this short study, square distributions have been applied to give a quick indication on the degree of spread rather than calculating a representative PDF. As mentioned in Section III, all pole pieces will experience the same cyclic loads (Fig. 5). However, any geometric deviations which lead to asymmetries will mean that each pole piece has a unique force profile. The effects on the magnitude of the radial and tangential forces are presented in Fig. 6 which shows the most severely affected pole piece. It can be observed that these are affected by up to 4% and 1%, respectively, assuming the deviations of Table IV.

The stall torque will also be affected by geometric deviations. In Fig. 7, this effect is presented by normalising the stall torque values of each deviated model with respect to the nominal geometry. Maximum discrepancies in the region of 3% and 2% can be detected, for the inner and outer rotor respectively.

V. Conclusions

This paper has outlined the different causes of geometric deviation in a CMG. The term "manufacturing error" mentioned in the literature has been extended to the more general "geometric deviations", of which manufacturing error is one category, and the other is the deflection of components under load. The causes of manufacturing error in the PM rotors and the modulation ring are identified and their origins, along with expected manufacturing processes and thus achievable tolerances, are discussed.

PM rotors are also used in electrical machines and their manufacturing processes are therefore well defined. This together with the relatively simple mechanical construction of these parts means tight tolerances can be achieved, and the manufacturing error of the subassembly can be estimated. In the modulation ring, neither its design or its manufacturing processes are standard. The manufacturing error will therefore depend on the selected manufacturing approach for an individual gear design.

TABLE IV
Deviations Limits of Samples

Feature	Tolerance Limit
Inner rotor PMs – R2	± 0.05 mm
Inner rotor eccentricity	± 0.1 mm
Outer rotor PMs – R5	± 0.05 mm
Radial position of pole pieces	± 0.1 mm
Angular position of pole pieces	± 0.1 °

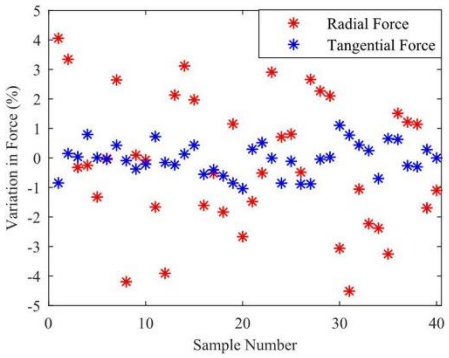

Fig. 6 Variation of forces on the pole pieces due to deviations

While deviations due to manufacturing error will clearly lead to discrepancies in performance between model and prototype, deflections under load could have an even more dramatic effect if the mechanical design does not minimise compliance in the support structure. The cyclic loading which the pole pieces experience adds further complexity when considering the long-term performance of a CMG. The need to account for these loads will constrain the range of options available to the CMG electromagnetic designer, and the process of developing a concept design is therefore an inherently multifaceted exercise.

Whether geometric deviations are caused by manufacturing error or deflections under load, the absence of computationally efficient methods capable of assessing small geometric deviations in a CMG significantly increases the difficulty in conducting a statistical study to determine the likely effect on performance. Even so, this study has shown that the range of possible outcomes in terms of gear performance is high. The combined effects of manufacturing error and deflections under load can only make it more important that these geometric subtleties are properly assessed. Such analysis would be

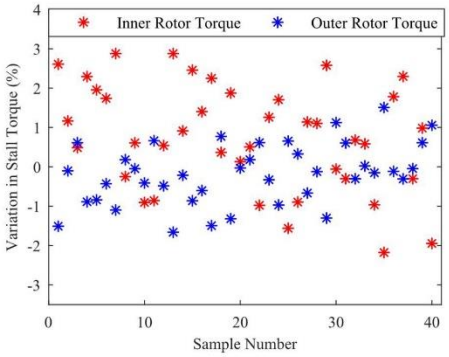

Fig. 7 Variations of stall torque due to deviations

particularly important if an MG was to be employed in an application where there was a need to slip at a precise torque value. More conventional applications would require the possible variation in performance to be accounted for by some factor of safety. This will lead to a more conservative and therefore less competitive design.

If better correlation between models and prototypes can be achieved, and if the range of manufacturing processes associated with the central modulating ring can be better defined and understood, the uptake of CMGs in applications currently dominated by mechanical gears may increase.

VI. Bibliography

[1] K. Atallah and D. Howe, "A novel high-performance magnetic gear," in *IEEE Transactions on Magnetics*, 2001, vol. 37, no. 4 I, pp. 2844–2846.

[2] L. Shah, A. Cruden, and B. W. Williams, "A magnetic gear box for application with a contra-rotating tidal turbine," *Proc. Int. Conf. Power Electron. Drive Syst.*, pp. 989–993, 2007.

[3] R. Z. A. Borisavljevic, J. W. Jansen, and E. A. Lomonova, "Modeling , Design and Experimental Validation of a Small-Sized Magnetic Gear," no. 2, pp. 560–565, 2013.

[4] K. Atallah, S. D. Calverley, and D. Howe, "Design, analysis and realisation of a high-performance magnetic gear," *IEE Proceedings-Electric Power Appl.*, vol. 151, no. 2, pp. 135–143, 2004.

[5] P. O. Rasmussen, T. O. Andersen, F. T. Jørgensen, and O. Nielsen, "Development of a high-performance magnetic gear," *IEEE Trans. Ind. Appl.*, vol. 41, no. 3, pp. 764–770, 2005.

[6] S. Gerber and R. J. Wang, "Evaluation of a prototype magnetic gear," *Proc. IEEE Int. Conf. Ind. Technol.*, pp. 319–324, 2013.

[7] A. Hawksworth, "Pole-Piece Structure for a Magnetic Gear," US Patent Number 2017/0005559 A1, 2017.

[8] S. D. Calverley and D. J. Powell, "Magnetic Pole-Piece Support," US Patent Number 9,425,655 B2, 2016.

[9] M. Desvaux, B. Multon, H. Ben Ahmed, and S. Sire, "Supporting the laminated ferromagnetic pole pieces in a magnetic gear: A structure behaviour analysis from a multibody model," *Mech. Mach. Sci.*, vol. 54, pp. 85–94, 2018.

[10] D. Z. Abdelhamid and A. M. Knight, "The Effect of Modulating Ring Design on Magnetic Gear Torque," vol. 53, no. 11, pp. 2–5, 2017.

[11] W. Tong, *Mechanical design of electric motors*. 2014.

[12] K. G. Swift and J. D. Booker, *Manufacturing Process Selection Handbook*. 2013.

[13] E. Oberg, F. D. Jones, H. L. Horton, and H. H. Ryffel, *Machinery's Handbook*. Industrial Press Inc., 2016.

[14] J. Bralla, "Design for Manufacturability Handbook," *McGraw-Hill Psrofesional*, 1998.

[15] I. Coenen, M. Van Der Giet, and K. Hameyer, "Manufacturing tolerances: Estimation and prediction of cogging torque influenced by magnetization faults," *IEEE Trans. Magn.*, vol. 48, no. 5 PART 2, pp. 1932–1936, 2012.

[16] H. Qian, H. Guo, Z. Wu, and X. Ding, "Analytical solution for cogging torque in surface-mounted permanent-magnet motors with magnet imperfections and rotor eccentricity," *IEEE Trans. Magn.*, vol. 50, no. 8, 2014.

[17] A. J. Piña, "Modeling and Analysis of Asymmetries in Permanent Magnet Synchronous Machines," PhD Thesis, 2016.

[18] Arnold Magnetic Technologies, "Magnet Manufacturing Process." [Online]. Available: https://www.arnoldmagnetics.com/resources/magnet-manufacturing-process/. [Accessed: 09-Nov-2018].

[19] D. Meeker, "FEMM." 2012.

[20] S. Gerber and R. J. Wang, "Statistical analysis of cogging torque considering various manufacturing imperfections," *Proc. - 2016 22nd Int. Conf. Electr. Mach. ICEM 2016*, pp. 2066–2072, 2016.

VII. Biographies

Alexandros Leontaritis received the M.Eng. degree in Mechanical Engineering from the Department of Mechanical Engineering, University of Bristol, Bristol, U.K., in 2017. He is currently working toward the PhD degree with the Electrical Energy Management Group, Faculty of Engineering, University of Bristol.

Aydin Nassehi is a Reader in Manufacturing Systems and Head of the Department of Mechanical Engineering, University of Bristol. He received his PhD in Innovative Manufacturing Technology from the University of Bath, Bath, U.K. in 2007. His research interests are in informatics and artificial intelligence in manufacturing.

Jason M. Yon received the MEng degree in Avionic Systems Engineering in 2007 and a PhD in Aerospace Electrical Systems in 2012, both from the University of Bristol. He is now a Lecturer in Electromechanical Systems at the University of Bristol. His research covers a broad range of topics related to electric machines, design and manufacture and the development of novel characterisation techniques for electromechanical systems.

Appendix C – Publication 2

Assessing the Effect of Geometric Error on the Performance of Magnetic Gears

Alexandros Leontaritis, Aydin Nassehi, Jason Yon
Electrical Energy Management Group
University of Bristol
Bristol, United Kingdom
a.leontaritis@bristol.ac.uk

***Abstract*—This paper presents and compares different methods for assessing the effect of planar geometric errors on the performance of magnetic gears using both Finite Element Analysis (FEA) and analytical techniques. In FEA, small geometrical deviations lead to the generation of different forms of the mesh, even when mesh size and type are constant. However, to accurately assess the effect of small deviations on performance, the influence of the specific mesh form must be negligible. Different torque calculation methods, along with different mesh parameters, have been used to obtain specific mesh form independence and hence accuracy in results. It is observed that both Maxwell's stress tensor and virtual work methods are computationally inefficient and, if many studies are to be conducted, FEA becomes impractical. Analytical solutions of magnetic potential offer a computationally efficient and accurate alternative for assessing magnetic gears under certain assumptions. This could allow the sensitivity of a magnetic gear's performance to be assessed with respect to manufacturing error, enabling the designer to appropriately specify tolerances and manufacturing processes.**

Keywords— Magnetic gears, geometric error, 2D FEA, magnetic vector potential, analytical solutions

I. INTRODUCTION

Since the beginning of the 21st century, magnetic gears (MGs) have received increased attention due to their low maintenance requirements and inherent overload protection. Researchers have also shown that torque densities exceeding 100 kNm/m^3 can be achieved; comparable to two and three stage helical gearboxes [1]. They are therefore being considered as promising alternatives in applications ranging from tidal turbines to small scale robotics [2], [3].

In radial flux Permanent Magnet (PM) machines, two-dimensional (2D) Finite Element Analysis (FEA) has become the dominant study method. In most machines, end effects can either be considered negligible or accounted for in subsequent analysis. Accurate results can therefore be achieved by investigating a planar geometry. Further simplification, and hence computational efficiency, can be gained by exploiting rotational symmetry, with only a section of the model being investigated using periodic boundary conditions. Similarly, most analyses of MGs are also conducted using FEA.

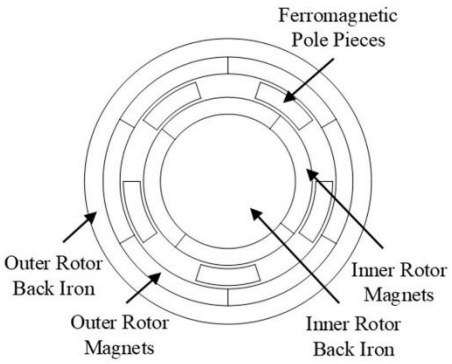

Fig. 1. CMG component identification

However, while 2D solutions do offer accessibility and give a reasonable indication of performance, there are limitations to the use of 2D FEA in the analysis of MGs. Coaxial magnetic gears (CMG) (Fig. 1) have two concentric rotors and a salient central ring, each with a different number of magnetic poles. As such, when analysing CMGs, periodic simplifications can rarely be used. In addition, in common with radial flux machines, three-dimensional (3D) effects cannot be assessed using a planar analysis. However, in MGs these are often significant; especially in designs with a small aspect ratio. This can lead to difficulties in the experimental validation of new gear designs.

There are a number of examples in the literature where large discrepancies in stall torque between 2D FEA and prototypes are reported, ranging from 20% to 40% [4],[5],[6]. These discrepancies are attributed to some combination of end effects and manufacturing error, however little work has been published quantifying the contribution of each.

TABLE I. CMG PARAMETERS

Quantity	Value
Number of pole pieces (Q)	5
Inner rotor poles (P_{in})	4
Outer rotor poles (P_{out})	6
Inner rotor OD	100 mm
Outer rotor OD	148 mm
Axial Length	100 mm

In [7] a 3D FEA model of a CMG is presented with almost all the supporting structures included in the analysis. In this study a 9% discrepancy is reported. The authors attribute this to "manufacturing error" however, the degree of the error in geometric terms is not quantified. In [8] the effects of manufacturing imperfections on cogging torque in a PM machine are investigated with a Monte-Carlo analysis of 10,000 samples. Similar studies for CMGs would clearly be valuable, however accurate and computationally efficient analysis techniques would be essential.

This paper presents an evaluation of both FEA and analytical solutions for assessing small geometrical deviations due to manufacturing error in a CMG (illustrated in Fig. 1 and outlined in Table I). For the FEA techniques, the effect of the mesh size and specific mesh form on the stall torque are both analysed, and two different torque calculating methods are used. Analytical techniques, using solutions of the magnetic potential, are an alternative analysis option for MGs and electric machines. In [9] such an analytical model has been developed for a CMG, exploiting rotational symmetry of the components. The analytical solution presented in this paper, has been developed to account for rotational asymmetries due to geometric error. A framework for the robust use of 2D FEA has been defined and the capabilities of analytical techniques when assessing small geometrical deviations has been explored.

II. FEA Methods of Calculating Torque and Effects of the Mesh Form

In FEA, two common methods can be used to calculate torque, one is field-based and the other energy-based. The dominant field-based method of calculating torque in rotary machines integrates the Maxwell stress tensor along a surface. The surface must be placed in free space and enclose the part on which torque is being applied. In a CMG, a contour is created in each air-gap. The FEA software used, FEMM [10], integrates the Maxwell stress tensor along this contour and calculates the torque on each rotor. This method is best applied in cases where a fine mesh density is used with the air-gap mesh being well defined [11]. A common energy-based approach is the virtual work method. Torque is equal to the rate of change of co-energy with respect to angular displacement. The main disadvantage of this method is that it requires the calculation of the co-energy between at least two positions and therefore requires more calculations than the Maxwell stress tensor method. However, with this approach a coarser mesh can be used while the movement increment between the positions must be fine [11]. Similar to the previous method, FEMM's postprocessor can calculate the value of co-energy for each simulation instance.

This research has been funded by the Engineering and Physical Sciences Research Council (EPSRC)

III. Assessment of FEA

Appropriate mesh discretisation is critical for any FEA model as its quality will determine the accuracy of the results. In FEA packages similar to FEMM, the mesh form is defined by the position of arbitrarily defined nodes according to the block area and mesh element size. Therefore, a minor change in the geometrical design of the model will lead to a different specific mesh form, even if the specified mesh element size remains unchanged. The effects of small geometrical deviations due to manufacturing error can only be assessed accurately if the method used for calculating torque is independent of the specific mesh form for a given error.

Various sources of manufacturing error exist in a CMG, which can only be assessed accurately if the analysis method has a required resolution. This resolution will depend on the effect the error has on a CMG's performance. To gauge the influence of such an error, a small number of cases have been analysed with a very high mesh density FEA model. An example case has been used with deviations, less than or equal to ± 0.1 mm applied only to the x and y axis position of each pole piece. A triangular mesh type was adopted using the FEMM's default mesh generator, Triangle [12]. This analysis resulted in a 1% variation in the value of stall torque, thus confirming the need to assess manufacturing error at this level of resolution.

In order to create a case with different specific mesh forms, two rings each consisting of 720 equidistant nodes were placed circumferentially in each airgap, bounding each Maxwell stress tensor contour. One node set can be rotated incrementally creating a slightly different mesh in each iteration while using the same mesh element size and component geometry. The angular spacing of 0.5° was selected because, at this value, the percentage change in total number of elements between iterations was similar to the difference in element count between the normal and geometrically deviated cases discussed above. Four instances were calculated for each mesh size, with one of the nodes sets rotated incrementally between 0° and 0.375° for each instance. It can reasonably be assumed that a solution independent of the specific mesh form in the case with the equidistant nodes, will also be independent of the specific mesh form in the analysis of geometric imperfections of similar magnitude.

From the definition of the Maxwell stress tensor method, the accuracy is expected to improve with a finer mesh in the airgaps. Global mesh element size is held fixed while the air gap mesh element size is decreased incrementally between 0.8 to 0.06 mm. The specific mesh form independence of the virtual work method was investigated through decreasing

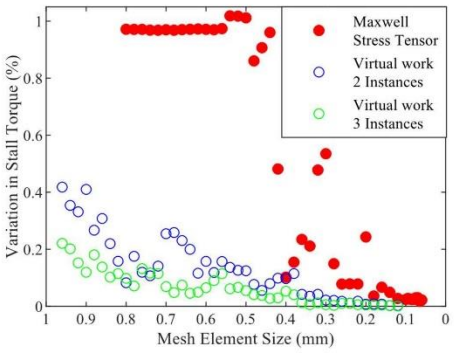

Fig. 2. Variation of stall torque for FEA methods studied

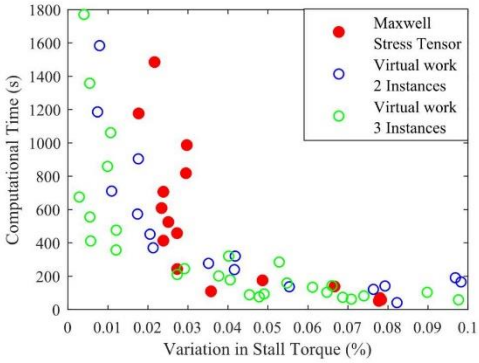

Fig. 3. Computational time of the FEA methods studied

the global mesh size between 1 mm and 0.1 mm and increasing the number of instances used to calculate the output torque, from two to three. The specific mesh form independence is assessed from the variation between each set of four rotated study instances. A direct comparison between the two methods can be performed considering the computational time required. The inner rotor torque results using the Maxwell stress tensor and virtual work methods are presented in Fig. 2 and Fig. 3. The computer used in the analysis was of the following specifications: Intel(R) Core(TM) i7-6700 CPU @ 3.40GHz, 16 GB RAM.

It is observed that both methods initially exhibit a significant variation, which can be reduced to less than 0.02%. For a variation less than 0.1% both methods have converged torque values and therefore the mesh independence is more important. In the first instance it be observed that for the same mesh, the virtual work method with three calculated instances produces a smaller torque variation than the one with two instances (Fig. 2). To achieve small torque variations, less than 0.03%, the required time for the Maxwell stress tensor method is similar to the virtual work method, with the latter capable of calculating even smaller variations more efficiently. However, in this region the minimum computational time for either method is around 250 s for a set of four iterations. Therefore, if a statistical analysis must be performed in order to assess the effect of geometrical deviations on the performance of a CMG, similar to the one in [8], FEA analysis becomes impractical, even if further time optimisation is performed.

IV. Analytical Solution

In the literature CMG analytical models have been developed using solutions of the magnetic vector potential (A) however, these assume radial symmetry for each of the three main components, i.e. the two PM rotors and the modulation ring of ferromagnetic pole pieces [9], [13]. The manufacturing error will inherently induce asymmetries in the design, which cannot be considered with the models mentioned above. To account for the effect of this class of deviation, a similar analytical solution to [9] has been adapted following the approach taken in [14], which assessed asymmetric deviations in PM machines using analytical methods. The current formulation of the analytical solution permits radial deviation to the inner and outer radii of each PM ($R_{1,j}$, $R_{2,j}$, $R_{5,w}$, $R_{6,w}$) and deviation to the circumferential position and width of each pole piece.

The CMG is separated in nominally concentric regions, which are bounded according to two boundary conditions: 1) the continuity of the radial component of the flux density (B_r) and 2) the tangential component of the field intensity (H_θ). To account for potential asymmetries, each PM and air-gap region is divided further into a number of subdomains equal to the number of poles (P_{in}, P_{out}) of each PM rotor. It is assumed that A is a function of r and θ and only has a vector component in the z-direction. Infinite permeability in the ferromagnetic

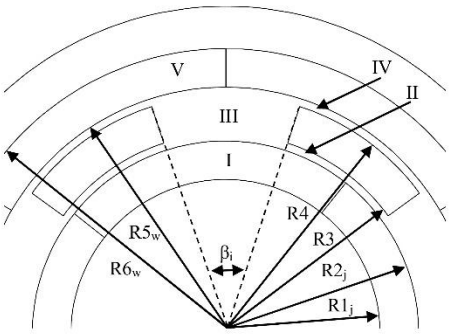

Fig. 4. Definition of regions, radii and slot angle

regions and linear behaviour of the PMs are assumed with the end effects being neglected.

The magnetic vector potential in each region can be calculated by solving Poisson's equation and Laplace's equation in the PM and non-magnetised regions, respectively. The general solutions have been simplified by adopting the following notations:

$$U_z(a,b) = \left(\frac{a}{b}\right)^z + \left(\frac{b}{a}\right)^z \tag{1}$$

$$Q_z(a,b) = \left(\frac{a}{b}\right)^z - \left(\frac{b}{a}\right)^z \tag{2}$$

Using the separation of variables method, the general solution for each region can be derived. The solutions, described by Fourier series, are provided in (3), (4), (10) – (12). In the rotor PM regions (I, V) the general solutions are the following:

$$\begin{aligned} A_j^{(I)}(r,\theta) = &\sum_{k=1}^{K} \left(C_{1kj} A_{I,j} \right. \\ &\left. + C_{2k}\, M_{rck}^{(I)}\right)\cos(k\theta) \\ &+ \sum_{k=1}^{K} \left(C_{1kj} C_{I,j} \right. \\ &\left. + C_{2kj} M_{rsk}^{(I)}\right)\sin(k\theta) \end{aligned} \tag{3}$$

$$\begin{aligned} A_w^{(V)}(r,\theta) = &\sum_{k=1}^{K} \left(C_{5kw} A_{V,w} \right. \\ &\left. + C_{6kw} M_{rck}^{(V)}\right)\cos(k\theta) \\ &+ \sum_{k=1}^{K} \left(C_{5kw} C_{V,w} \right. \\ &\left. + C_{6kw} M_{rsk}^{(V)}\right)\sin(k\theta) \end{aligned} \tag{4}$$

where

$$C_{1kj} = \frac{U_k\left(r, R_{1,j}\right)}{U_k\left(R_{2,j}, R_{1,j}\right)} \tag{5}$$

$$\begin{aligned} C_{2kj} = &\left[1 + \frac{1}{k}\left(\frac{R_{1,j}}{r}\right)^{k+1}\right]\cdot r \\ &- \frac{U_k\left(r, R_{1,j}\right)}{U_k\left(R_{2,j}, R_{1,j}\right)}\left[1 + \frac{1}{k}\left(\frac{R_{1,j}}{R_{2,j}}\right)^{k+1}\right]\cdot R_{2,j} \end{aligned} \tag{6}$$

$$C_{5kw} = \frac{U_k\left(r, R_{6,w}\right)}{U_k\left(R_{5,w}, R_{6,w}\right)} \tag{7}$$

$$\begin{aligned} C_{6kw} = &\left[1 + \frac{1}{k}\left(\frac{R_{6,w}}{r}\right)^{k+1}\right]\cdot r \\ &- \frac{U_k\left(r, R_{6,w}\right)}{U_k\left(R_{5,w}, R_{6,w}\right)}\left[1 + \frac{1}{k}\left(\frac{R_{6,w}}{R_{5,w}}\right)^{k+1}\right]\cdot R_{5,w} \end{aligned} \tag{8}$$

and [15]

$$\begin{aligned} M_{rck}^{(I,V)} &= \frac{2PB_{rm}}{k\pi\mu_0} sin\left(\frac{k\pi\alpha_p}{P}\right) cos(k\varphi_0) \\ M_{rsk}^{(I,V)} &= \frac{2PB_{rm}}{k\pi\mu_0} sin\left(\frac{k\pi\alpha_p}{P}\right) sin(k\varphi_0) \\ &for\ {}^{k}/_{P} = 1, 3, 5, \dots \end{aligned} \tag{9}$$

The subscripts j, w represent the j^{th} and w^{th} PM of the inner and outer rotor, respectively, and every subdomain is defined by the inner $(R_{1,j}, R_{5,w})$ and outer $(R_{2,j}, R_{6,w})$ radii of each PM. The parameter k denotes the order of harmonics in each region, with B_{rm} being the residual flux and P, μ_0, α_p are the number of poles, relative permeability of air and magnet arc to pole pitch ratio, respectively. The initial angular position of the rotor is defined by φ_0.

Similarly, the general solution for each air-gap subdomain (II, IV) and the pole-pieces region (III) can be described as:

$$\begin{aligned} &A_j^{(II)}(r,\theta) \\ &= \sum_{k=1}^{K}\left(A_{II,j}\frac{R_{2,j}}{k}\frac{U_k(r,R_3)}{Q_k\left(R_{2,j},R_3\right)}\right. \\ &\left. + B_{II,j}\frac{R_3}{k}\frac{U_k\left(r,R_{2,j}\right)}{Q_k\left(R_3,R_{2,j}\right)}\right)\cos(k\theta) \\ &+ \sum_{k=1}^{K}\left(C_{II,j}\frac{R_{2,j}}{k}\frac{U_k(r,R_3)}{Q_k\left(R_{2,j},R_3\right)}\right. \\ &\left. + D_{II,j}\frac{R_3}{k}\frac{U_k\left(r,R_{2,j}\right)}{Q_k\left(R_3,R_{2,j}\right)}\right)\sin(k\theta) \end{aligned} \tag{10}$$

$$\begin{aligned} &A_w^{(IV)}(r,\theta) \\ &= \sum_{k=1}^{K}\left(A_{IV,w}\frac{R_4}{k}\frac{U_k\left(r,R_{5,w}\right)}{Q_k\left(R_4,R_{5,w}\right)}\right. \\ &\left. + B_{II,w}\frac{R_{5,w}}{k}\frac{U_k(r,R_4)}{Q_k\left(R_{5,w},R_4\right)}\right)\cos(k\theta) \\ &+ \sum_{k=1}^{K}\left(C_{IV,w}\frac{R_4}{k}\frac{U_k\left(r,R_{5,w}\right)}{Q_k\left(R_4,R_{5,w}\right)}\right. \\ &\left. + D_{II,w}\frac{R_{5,w}}{k}\frac{U_k(r,R_4)}{Q_k\left(R_{5,w},R_4\right)}\right)\sin(k\theta) \end{aligned} \tag{11}$$

$$A_i^{(III)}(r,\theta) = A_{III,i} + B_{III,i}\ln(r) + \sum_{m=1}^{M}\left(C_{III,i,m}\frac{Q_{f_{m,i}}(r,R_4)}{Q_{f_{m,i}}(R_3,R_4)} - D_{III,i,m}\frac{Q_{f_{m,i}}(r,R_3)}{Q_{f_{m,i}}(R_3,R_4)}\right)\cdot\cos\left(f_{m,i}(\theta-\theta_i)\right) \quad (12)$$

with

$$f_{m,i} = \frac{m\pi}{\beta_i} \quad (13)$$

where m defines the order of harmonics and β_i, θ_i are the opening angle and angular position of the i^{th} slot between consecutive pole pieces.

The continuity of the radial component of the flux density and the tangential component of the field intensity leads to the following boundary equations:

$$H_{\theta,j}^{(I)}\big|_{r=R_{2,j}} = H_{\theta,j}^{(II)}\big|_{r=R_{2,j}} \quad (14)$$

$$B_{r,j}^{(I)}\big|_{r=R_{2,j}} = B_{r,j}^{(II)}\big|_{r=R_{2,j}} \quad (15)$$

$$H_{\theta,j}^{(II)}\big|_{r=R_3} = H_{\theta}^{(III)}\big|_{r=R_3} \quad (16)$$

$$A_j^{(II)}\big|_{r=R_3} = A^{(III)}\big|_{r=R_3} \quad (17)$$

$$H_{\theta}^{(III)}\big|_{r=R_4} = H_{\theta,j}^{(IV)}\big|_{r=R_4} \quad (18)$$

$$A^{(III)}\big|_{r=R_4} = A_j^{(IV)}\big|_{r=R_4} \quad (19)$$

$$H_{\theta,w}^{(IV)}\big|_{r=R_{5,w}} = H_{\theta,w}^{(V)}\big|_{r=R_{5,w}} \quad (20)$$

$$B_{r,w}^{(IV)}\big|_{r=R_{5,w}} = B_{r,w}^{(V)}\big|_{r=R_{5,w}} \quad (21)$$

The complete solution can be determined by applying the boundary conditions (14) – (21) to the general solutions (3), (4), (10) – (12). The subsequent equations can be expressed in matrix form and solved as a system of linear equations.

A. Interface I-II

At the interface between the inner rotor PM subdomains and the inner air-gap subdomains the following expressions can be derived (22) – (25). The Fourier coefficients $\boldsymbol{A_I}, \boldsymbol{C_I}, \boldsymbol{A_{II}}, \boldsymbol{B_{II}}, \boldsymbol{C_{II}}$ and $\boldsymbol{D_{II}}$ are all column vector of length equal to $P_{in} \cdot K$. All constant terms are defined similarly and therefore the definition of only $\boldsymbol{G_1}$ is provided below. Same applies for the magnetisation column vectors that are defined as $\boldsymbol{M_{rck}^{(I)}}$ (32).

$$\boldsymbol{I_K A_I} + \boldsymbol{G_1 A_{II}} + \boldsymbol{G_2 B_{II}} = 0 \quad (22)$$

$$\boldsymbol{I_K C_I} + \boldsymbol{G_1 C_{II}} + \boldsymbol{G_2 D_{II}} = 0 \quad (23)$$

$$\boldsymbol{G_3 A_I} + \boldsymbol{I_K A_{II}} = \boldsymbol{G_{13}} \cdot \boldsymbol{M_{rck}^{(I)}} \quad (24)$$

$$\boldsymbol{G_3 C_I} + \boldsymbol{I_K C_{II}} = \boldsymbol{G_{13}} \cdot \boldsymbol{M_{rsk}^{(I)}} \quad (25)$$

where

$$\boldsymbol{I_K} = diag(1,1,\dots,1)_{K\times K} \quad (26)$$

$$\boldsymbol{G_1} = diag(\boldsymbol{g_1}(1),\boldsymbol{g_1}(2),\dots,\boldsymbol{g_1}(P_{in}))_{P_{in}K\times P_{in}K} \quad (27)$$

$$\boldsymbol{g_1(j)} = \boldsymbol{I_K}\cdot\left(-\frac{R_{2,j}}{k}\frac{U_k(R_{2,j},R_3)}{Q_k(R_{2,j},R_3)}\right) \quad (28)$$

$$\boldsymbol{g_2(j)} = \boldsymbol{I_K}\cdot\left(-\frac{R_3}{k}\frac{2}{Q_k(R_3,R_{2,j})}\right) \quad (29)$$

$$\boldsymbol{g_3(j)} = \boldsymbol{I_K}\cdot\left(-\frac{k}{R_{2,j}}\frac{Q_k(R_{2,j},R_{1,j})}{U_k(R_{2,j},R_{1,j})}\right) \quad (30)$$

$$\boldsymbol{g_{13}(j)} = \boldsymbol{I_K}\left(1-\left(\frac{R_{1,j}}{R_{2,j}}\right)^{k+1} - \frac{k}{R_{2,j}}\frac{Q_k(R_{2,j},R_{1,j})}{U_k(R_{2,j},R_{1,j})}\left(1+\frac{1}{k}\left(\frac{R_{1,j}}{R_{2,j}}\right)^{k+1}\right)R_{2,j}\right) \quad (31)$$

$$\boldsymbol{M_{rck}^{(I)}} = \left[\boldsymbol{m_{rck}^{(I)}}(1),\boldsymbol{m_{rck}^{(I)}}(2),\dots,\boldsymbol{m_{rck}^{(I)}}(P_{in})\right]^{\boldsymbol{T}} \quad (32)$$

$$\boldsymbol{m_{rck}^{(I)}}(\mathrm{j}) = \left[m_{rck}^{(I)}(1), m_{rck}^{(I)}(2), \dots, m_{rck}^{(I)}(K)\right] \quad (33)$$

B. Interface II-III

Algebraic manipulation of (10), (12) and boundary conditions (16), (17) lead to the following relationships at the inner airgap and slot subdomains interface. The Fourier coefficients $\boldsymbol{C_{III}}, \boldsymbol{D_{III}}$ are column vectors of length $M \cdot Q$ and $\boldsymbol{A_{III}}, \boldsymbol{B_{III}}$ of length equal to Q.

$$-\boldsymbol{I_{Kj\,R3}}\boldsymbol{B_{II}} + \boldsymbol{\delta_j^T}\boldsymbol{B_{III}} + \boldsymbol{\eta_j^T}\boldsymbol{f_m}\boldsymbol{G_4}\boldsymbol{C_{III}} - \boldsymbol{\eta_j^T}\boldsymbol{f_m}\boldsymbol{G_5}\boldsymbol{D_{III}} = 0 \quad (34)$$

$$-\boldsymbol{I_{Kj\,R3}}\boldsymbol{D_{II}} + \boldsymbol{\sigma_j^T}\boldsymbol{B_{III}} + \boldsymbol{\xi_j^T}\boldsymbol{f_m}\boldsymbol{G_4}\boldsymbol{C_{III}} - \boldsymbol{\xi_j^T}\boldsymbol{f_m}\boldsymbol{G_5}\boldsymbol{D_{III}} = 0 \quad (35)$$

$$\boldsymbol{\delta_{j,\pi}}\boldsymbol{G_6}\boldsymbol{A_{II}} + \boldsymbol{\delta_{j,\pi}}\boldsymbol{G_7}\boldsymbol{B_{II}} + \boldsymbol{\sigma_{j,\pi}}\boldsymbol{G_6}\boldsymbol{C_{II}} + \boldsymbol{\sigma_{j,\pi}}\boldsymbol{G_7}\boldsymbol{D_{II}} - \boldsymbol{I_Q}\boldsymbol{A_{III}} - \boldsymbol{I_Q}\ln(R_3)\,\boldsymbol{B_{III}} = 0 \quad (36)$$

$$\boldsymbol{\eta_{j,\pi}}\boldsymbol{G_6}\boldsymbol{A_{II}} + \boldsymbol{\eta_{j,\pi}}\boldsymbol{G_7}\boldsymbol{B_{II}} + \boldsymbol{\xi_{j,\pi}}\boldsymbol{G_6}\boldsymbol{C_{II}} + \boldsymbol{\xi_{j,\pi}}\boldsymbol{G_7}\boldsymbol{D_{II}} - \boldsymbol{I_{MQ}}\boldsymbol{C_{III}} = 0 \quad (37)$$

where

$$\boldsymbol{I_{Kj\,R3}} = R_3 \cdot diag(1, 1, \dots, 1)_{P_{in}K \times P_{in}K} \quad (38)$$

$$\delta(i,k) = \frac{1}{\pi}\int_{\theta_i}^{\theta_i+\beta} \cos(k\theta)d\theta \quad (39)$$

$$\boldsymbol{\delta_j} = diag\big(\delta(i,k)\big)_{QK \times QK} \quad (40)$$

$$\boldsymbol{\delta_{j,\pi}} = \frac{\pi}{\beta_i}\boldsymbol{\delta_j} \quad (41)$$

$$\sigma(i,k) = \frac{1}{\pi}\int_{\theta_i}^{\theta_i+\beta} \sin(k\theta)d\theta \quad (42)$$

$$\eta(m,k,i) = \frac{1}{\pi}\int_{\theta_i}^{\theta_i+\beta} \cos(k\theta)\cos\left(f_{m,i}(\theta-\theta_i)\right)d\theta \quad (43)$$

$$\boldsymbol{\eta_j} = \begin{bmatrix} \eta(m,k,1) & \cdots & \eta(m,k,1) \\ \vdots & \ddots & \vdots \\ \eta(m,k,Q) & \cdots & \eta(m,k,Q) \end{bmatrix}_{QM \times P_{in}K} \quad (44)$$

$$\boldsymbol{\eta_{j,\pi}} = \frac{\pi}{\beta_i \cdot P_{in}}\boldsymbol{\eta_j} \quad (45)$$

$$\xi(m,k,i) = \frac{1}{\pi}\int_{\theta_i}^{\theta_i+\beta} \sin(k\theta)\cos\left(f_{m,i}(\theta-\theta_i)\right)d\theta \quad (46)$$

$$\boldsymbol{f_{m,i}} = f_{m,i} \cdot \boldsymbol{I_M} \quad (47)$$

$$\boldsymbol{f_m} = diag\left(\boldsymbol{f_{m,i}}(1), \boldsymbol{f_{m,i}}(2), \dots, \boldsymbol{f_{m,i}}(Q)\right) \quad (48)$$

$$\boldsymbol{G_4} = diag(\boldsymbol{g_4}(1), \boldsymbol{g_4}(2), \dots, \boldsymbol{g_4}(Q))_{QM \times QM} \quad (49)$$

$$\boldsymbol{g_4(i)} = \boldsymbol{I_M} \cdot \left(\frac{U_{f_{m,i}}(R_3, R_4)}{Q_{f_{m,i}}(R_3, R_4)}\right) \quad (50)$$

$$\boldsymbol{g_5(i)} = \boldsymbol{I_M} \cdot \left(\frac{2}{Q_{f_{m,i}}(R_3, R_4)}\right) \quad (51)$$

$$\boldsymbol{g_6(j)} = \boldsymbol{I_K} \cdot \left(\frac{R_{2,j}}{k}\frac{2}{Q_k\left(R_{2,j}, R_3\right)}\right) \quad (52)$$

$$\boldsymbol{g_7(j)} = \boldsymbol{I_K} \cdot \left(\frac{R_3}{k}\frac{U_k\left(R_3, R_{2,j}\right)}{Q_k\left(R_3, R_{2,j}\right)}\right) \quad (53)$$

C. Interface III-IV

Similar to the interface with the inner air-gap, the interface between the outer air-gap and the slot subdomains is described as:

$$-\boldsymbol{I_{Kw\,R4}}\boldsymbol{A_{IV}} + \boldsymbol{\delta_w^T}\boldsymbol{B_{III}} + \boldsymbol{\eta_w^T}\boldsymbol{f_m}\boldsymbol{G_5}\boldsymbol{C_{III}} - \boldsymbol{\eta_w^T}\boldsymbol{f_m}\boldsymbol{G_4}\boldsymbol{D_{III}} = 0 \quad (54)$$

$$-\boldsymbol{I_{Kw\,R4}}\boldsymbol{C_{IV}} + \boldsymbol{\sigma_w^T}\boldsymbol{B_{III}} + \boldsymbol{\xi_w^T}\boldsymbol{f_m}\boldsymbol{G_5}\boldsymbol{C_{III}} - \boldsymbol{\xi_w^T}\boldsymbol{f_m}\boldsymbol{G_4}\boldsymbol{D_{III}} = 0 \quad (55)$$

$$\boldsymbol{\delta_{w,\pi} G_8 A_{IV} + \delta_{w,\pi} G_9 B_{IV} + \sigma_{w,\pi} G_8 C_{IV} + \sigma_{w,\pi} G_9 D_{IV} - I_Q A_{III} - I_Q \ln(R_3)\, B_{III} = 0} \quad (56)$$

$$\boldsymbol{\eta_{w,\pi} G_8 A_{IV} + \eta_{w,\pi} G_9 B_{IV} + \xi_{w,\pi} G_8 C_{IV} + \xi_{w,\pi} G_9 D_{II} - I_{MQ} C_{III} = 0} \quad (57)$$

where

$$\boldsymbol{g_8(w) = I_K \cdot \left(\frac{R_4}{k} \frac{U_k(R_4, R_{5,w})}{Q_k(R_4, R_{5,w})} \right)} \quad (58)$$

$$\boldsymbol{g_9(w) = I_K \cdot \left(\frac{R_{5,w}}{k} \frac{2}{Q_k(R_{5,w}, R_4)} \right)} \quad (59)$$

D. Interface IV-V

The equations at the interface between the outer air-gap and outer rotor PM subdomains can be derived adopting the same approach as for the inner rotor. The Fourier coefficients $\boldsymbol{A_{IV}, B_{IV}, C_{IV}, D_{IV}, A_V}$ and $\boldsymbol{C_V}$ are column vectors of length $P_{out} \cdot K$ and they are described as:

$$\boldsymbol{G_{10} A_{IV} + G_{11} B_{IV} + I_K A_V = 0} \quad (60)$$

$$\boldsymbol{G_{10} C_{IV} + G_{11} D_{IV} + I_K C_V = 0} \quad (61)$$

$$\boldsymbol{I_K B_{IV} + G_{12} A_V = G_{14} \cdot M_{rck}^{(V)}} \quad (62)$$

$$\boldsymbol{I_K D_{IV} + G_{12} C_V = G_{13} \cdot M_{rsk}^{(V)}} \quad (63)$$

where

$$\boldsymbol{g_{10}(w) = I_K \cdot \left(-\frac{R_4}{k} \frac{2}{Q_k(R_4, R_{5,w})} \right)} \quad (64)$$

$$\boldsymbol{g_{11}(w) = I_K \cdot \left(-\frac{R_{5,w}}{k} \frac{U_k(R_{5,w}, R_4)}{Q_k(R_{5,w}, R_4)} \right)} \quad (65)$$

$$\boldsymbol{g_{12}(w) = I_K \cdot \left(-\frac{k}{R_{5,w}} \frac{Q_k(R_{5.w}, R_{6,w})}{U_k(R_{5,w}, R_{6,w})} \right)} \quad (66)$$

$$\boldsymbol{g_{14}(w) = I_K \left(1 - \left(\frac{R_{6,w}}{R_{5,w}} \right)^{k+1} - \frac{k}{R_{5,w}} \frac{Q_k(R_{5,w}, R_{6,w})}{U_k(R_{5,w}, R_{6,w})} \left(1 + \frac{1}{k} \left(\frac{R_{6,w}}{R_{5,w}} \right)^{k+1} \right) R_{5,w} \right)} \quad (67)$$

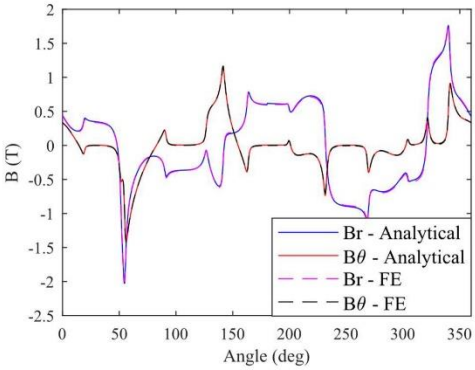

Fig. 5. Analytical vs FEA flux density comparison

V. Assessment of Analytical Solution

The capabilities of the analytical model, provided in Section IV, have been investigated by assessing a deviated sample model of the CMG shown in Fig.1. For the purpose of this study, a degree of error has been arbitrarily introduced to the outer radii (R2) of each inner rotor PM and the angular position of each pole piece, which in the analytical model is translated into the error of the slot opening angle β_i. This error is quantified in Table II. A unit arc to pole pitch ratio has also been selected. The field solution shows excellent correlation with FEA results (Fig. 5), under the same infinite permeability assumption. The main advantage of the analytical technique is its computational efficiency, with the model solved in 3.1 s, which is significantly faster than FEA.

Since the infinite permeability assumption is not true in a real case scenario, a discrepancy with FEA results considering non-linear permeability is expected. In particular, for the case analysed above this discrepancy translates into about 11% for the value of the inner rotor stall torque. An additional study was performed, assessing the two deviated parameters individually. The inner rotor PM radii and the slot angle were assessed incrementally between [–0.3, 0.3] mm and [–1.5, 1.5] degrees, respectively. The normalised results (Fig. 6), with respect to a non-deviated CMG, show that the analytical and the FE method considering non-linear permeability follow very similar trendlines. Therefore, for minor geometric deviations, the

TABLE II. Geometric Error of Each Component

Error	Component				
	Permanent Magnet				
	No. 1	No. 2	No. 3	No. 4	
Radial (mm)	0.1	–0.05	0.2	–0.1	
	Pole Piece				
	No. 1	No. 2	No. 3	No. 4	No. 5
Angular (°)	1	0.75	1.25	–1	–1.5

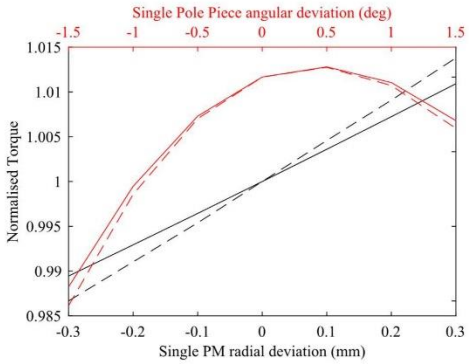

Fig. 6. Effects of single parameter variation
Continuous line: Analytical Solution , Dashed line: FEA

percent change in stall torque, which is the quantity describing the effect of the deviations, can be assessed with an accuracy of around 0.1% compared to FEA.

VI. Conclusions

This paper presents three methods for assessing the effect of small geometrical deviations due to geometric error in a CMG. For both 2D FEA techniques, the analysis has highlighted the fact that accurate results require specific mesh form independence. Both FEA methods can be modified to output accurate results, at a cost of computational power or time. Therefore, if a large number of studies must be undertaken, FEA becomes impractical. Analytical techniques are much more computationally efficient being more than an order of magnitude faster than FEA. The proposed analytical model can produce results with excellent correlation to FEA, assuming infinite permeability in the ferromagnetic regions. However, as the effects follow a very similar trend to FEA considering non-linear permeability, the difference in stall torque due to the minor geometric deviations can be assessed with very good accuracy. The significantly lower computational time in addition to the accuracy show great potential of such an analytical method. In particular, the proposed model can be developed further to account for additional types of asymmetrical deviations along with the consideration of finite permeabilities, which will further reduce the error to a complete FEA solution.

References

[1] K. Atallah and D. Howe, "A novel high-performance magnetic gear," in *IEEE Transactions on Magnetics*, 2001, vol. 37, no. 4 I, pp. 2844–2846.

[2] L. Shah, A. Cruden, and B. W. Williams, "A magnetic gear box for application with a contra-rotating tidal turbine," *Proc. Int. Conf. Power Electron. Drive Syst.*, pp. 989–993, 2007.

[3] R. Z. A. Borisavljevic, J. W. Jansen, and E. A. Lomonova, "Modeling , Design and Experimental Validation of a Small-Sized Magnetic Gear," no. 2, pp. 560–565, 2013.

[4] K. Atallah, S. D. Calverley, and D. Howe, "Design, analysis and realisation of a high-performance magnetic gear," *IEE Proceedings-Electric Power Appl.*, vol. 151, no. 2, pp. 135–143, 2004.

[5] P. O. Rasmussen, T. O. Andersen, F. T. Jørgensen, and O. Nielsen, "Development of a high-performance magnetic gear," *IEEE Trans. Ind. Appl.*, vol. 41, no. 3, pp. 764–770, 2005.

[6] S. Gerber and R. J. Wang, "Analysis of the end-effects in magnetic gears and magnetically geared machines," *Proc. - 2014 Int. Conf. Electr. Mach. ICEM 2014*, pp. 396–402, 2014.

[7] S. Gerber and R. J. Wang, "Evaluation of a prototype magnetic gear," *Proc. IEEE Int. Conf. Ind. Technol.*, pp. 319–324, 2013.

[8] S. Gerber and R. J. Wang, "Statistical analysis of cogging torque considering various manufacturing imperfections," *Proc. - 2016 22nd Int. Conf. Electr. Mach. ICEM 2016*, pp. 2066–2072, 2016.

[9] T. Lubin, S. Mezani, and A. Rezzoug, "Analytical computation of the magnetic field distribution in a magnetic gear," *IEEE Trans. Magn.*, vol. 46, no. 7, pp. 2611–2621, 2010.

[10] D. Meeker, "FEMM." 2012.

[11] J. Mizia, A. R. Eastham, G. E. Dawson, and K. Adamiak, "Finite element force calculation: Comparison of methods for electric machines," *IEEE Trans. Magn.*, vol. 24, no. 1, pp. 447–450, 1988.

[12] J. R. Shewchuk, "Delaunay refinement algorithms for triangular mesh generation.pdf," *Comput. Geom.*, vol. 22, pp. 21–74, 2002.

[13] X. Zhang, X. Liu, Z. Song, and Z. Chen, "Fast calculation of magnetic field distribution in magnetic gear for high torque application," *2016 XXII International Conference on Electrical Machines (ICEM)*. pp. 1742–1748, 2016.

[14] A. J. Piña, "Modeling and Analysis of Asymmetries in Permanent Magnet Synchronous Machines," PhD Thesis, 2016.

[15] Z. Q. Zhu, L. J. Wu, Z. P. Xia, and S. P. Machines, "An Accurate Subdomain Model for Magnetic Field Computation in Slotted," *IEEE Trans. Magn.*, vol. 46, no. 4, pp. 1100–1115, 2010.

Appendix D – Publication 3

A Monte-Carlo Analysis of the Effects of Geometric Deviations on the Performance of Magnetic Gears

Alexandros Leontaritis
Electrical Energy Management Group
Faculty of Engineering
University of Bristol
United Kingdom
a.leontaritis@bristol.ac.uk

Aydin Nassehi
Engineering Systems and Design Group
Faculty of Engineering
University of Bristol
United Kingdom
aydin.nassehi@bristol.ac.uk

Jason Yon
Electrical Energy Management Group
Faculty of Engineering
University of Bristol
United Kingdom
jason.yon.02@bristol.ac.uk

***Abstract*— Magnetic gears offer several advantages over mechanical transmissions. However, across a broad range of research studies, their practical performance has not matched design predictions. Even with extensive 3D Finite Element Analysis (FEA), large discrepancies of 4% to 10% can exist – usually attributed to manufacturing error. Research studies typically assume ideal realization of the prototype geometry while employing basic, poorly characterized manufacturing processes in the hardware development. Geometric deviations due to manufacturing error are difficult to predict and inherently random. Therefore, their effect needs to be assessed through a statistical approach, which requires a rapid but accurate model of the gear. This paper assesses the effect of geometric error on the performance of a magnetic gear using a new computationally efficient asymmetric analytical model to conduct a Monte-Carlo simulation. The analytical technique is validated by comparing the results with a finite element solution and very close agreement is observed. By repeatedly analyzing the gear, with the position and size of each pole piece independently varied each time, a resultant distribution of performance can be derived. It is also shown that, for this case study, the distribution derived using the analytical model can be scaled to match the equivalent, but much more computationally onerous, FEA based solution. A predicted statistical distribution of a gear's performance, based on a set of manufacturing tolerances, would provide designers with a more realistic estimate of a gear's capability than an idealized analysis. This will be increasingly important as magnetic gears become more widely adopted.**

Keywords—Magnetic gears, asymmetric analytical method, geometric deviation, manufacturing error, Monte-Carlo

I. INTRODUCTION

Many engineering applications require a multiplication of either angular speed or torque, and there is a wide range of transmission systems which can be used for this purpose. Mechanical gears are a highly developed technology which dominates the transmission sector of many engineering applications. However, the mechanical contact between the gears creates some fundamental drawbacks, including friction-induced wear and vibrations, increased maintenance requirements and reduced reliability. Since the beginning of the 21st century, Magnetic Gears (MGs) have received increased attention due to their contactless nature, low maintenance requirements and inherent overload protection. Researchers have also shown torque densities exceeding 100 kNm/m^3 can be achieved; comparable to two and three stage helical gearboxes [1]. They are therefore considered as promising alternatives in applications ranging from electrified vertical takeoff vehicles to tidal turbines and small-scale robotics [2]–[4].

There is a substantial body of work in the literature investigating a number of different topologies, including coaxial, harmonic and planetary MGs [5]–[13]. Such research projects typically concentrate on the optimization of the gear for a particular performance metric, with much of the literature focusing on torque density. The most common analysis method for MGs is Finite Element Analysis (FEA). However, there are numerous examples in the literature where a discrepancy is observed between FEA and experimental outcomes. Two-dimensional (2D) FEA is frequently used as it offers accessibility and gives a reasonable indication of performance. In studies using 2D FEA, large discrepancies can be observed ranging from 20% to 40% [10], [14], [15]. These are attributed to some combination of end-effects and manufacturing error. Three-dimensional (3D) FEA is significantly more computationally intensive but, can be employed to overcome the inherent limitations of 2D planar models. This can include the modelling of end effects and allow the influence of supporting structures to be assessed. However, as shown in [15], for the analysis of Coaxial Magnetic Gears (CMGs) (Fig. 1), knowledge of the aspect ratio allows compensation to be applied to 2D results with very good correlation to those obtained using 3D FEA. Even so, 3D FEA can still give a discrepancy of 4% to 10% [16]–[19]. In particular, in [19], 3D FEA is used and the end-effects due to almost all the supporting structures are considered, in addition to those of the active components. In this study a discrepancy of 9% is reported, which is attributed to "manufacturing error".

Despite extensive research studies, very few MGs can be found in the transmission industry. The reasons for this are unclear but, accurate techniques for predicting real-world performance will be essential for widespread adoption. MGs implemented in real-world applications would require a more wholistic design approach having to consider a wide range of characteristics including electromagnetic performance, thermal management, structural requirements and cost. The design philosophy must also be suited to scalable production processes. In particular, large scale production is only viable if the range in expected performance of the product can be predicted and deemed acceptable.

Calculated performance in research studies typically assumes exact geometry. Therefore, the effects of geometric imperfections are rarely considered. These imperfections are effectively a combination of geometric deviations due to manufacturing error and deflection of components under

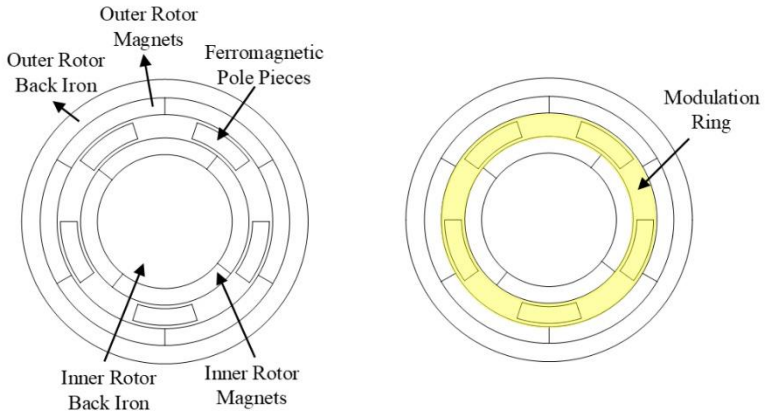

Fig. 1. CMG component identification

load [20]. This may be confounded by the fact that practical development of research machines is typically undertaken in a prototyping environment where manufacturing and assembly controls are basic. Consideration of the effect of geometric deviations can lead to better estimation of the expected performance and, in cases where deflections can be calculated, better correlation between modelling and prototypes.

This paper presents an analysis of the effects of geometric deviations on the performance of a CMG (illustrated in Fig. 1 with parameters outlined in Table I). This study focuses on geometric deviations in the modulation ring which are expected to be most significant [20]. The effects are assessed through a Monte-Carlo analysis for which an efficient and accurate analysis method is required. FEA, due to its high dependency on the mesh form, requires very high mesh density and, as a result, becomes computationally expensive and impractical for such a study [21]. Therefore, an asymmetric analytical subdomain model has been developed considering individual radial and tangential deviations of each ferromagnetic pole piece.

II. Asymmetric Analytical Model

In the literature, analytical models for CMGs have been developed using solutions of the magnetic vector potential (A) [22]–[27]. However, these assume radial symmetry for each of the three main components (the two PM rotors and the modulation ring) and are therefore only able to model simple bulk geometric errors, such as incorrect radii. More realistic geometric deviations are inherently asymmetric and cannot be considered with the models mentioned above.

In [28], Pina et. Al presented an asymmetric analytical model of a permanent magnet machine, which allowed efficient analysis of rotor and stator asymmetries. With this they were able to study the effect of manufacturing error on cogging torque. Following their approach, in [21] Leontaritis et. Al presented an initial asymmetric model of a CMG, however this model considered only tangential deviation of each pole piece and radial deviation of each PM. In [20] it was concluded that realistic deviation of the modulation ring pole pieces in r and θ is likely to be a more significant source of error than incorrect rotor geometry. This stems from the fact that PM rotors are now a relatively mature technology and their manufacturing processes are likely to be relatively well controlled – even in research prototypes.

Here an analytical model is presented that allows the size and position of each pole piece to be deviated, emulating realistic manufacturing error in the modulation ring. In common with [21], the CMG is separated into concentric regions (Fig. 2) and the modulation ring is divided further into angular subdomains equal to the number of pole pieces (Q). However, to account for the asymmetries in the radial and tangential position of each pole piece, careful treatment of the boundary conditions is required. Here the air-gaps are also divided into angular subdomains to match the modulation ring. Each region II subdomain is now bounded to its equivalent subdomain of region III. The full set of boundary conditions is given in (15) – (22). The following assumptions are also applied:

- A is a function of r and θ and only has a vector component in the z-direction;
- Infinite permeability is applied to the ferromagnetic regions;
- The PMs are assumed to be linear and have unity relative permeability;
- End effects are neglected.

TABLE I. CMG Parameters

Quantity	Value
Number of pole pieces (Q)	5
Inner rotor poles (P_{in})	4
Outer rotor poles (P_{out})	6
Inner rotor OD	100 mm
Outer rotor OD	148 mm
Axial Length	100 mm

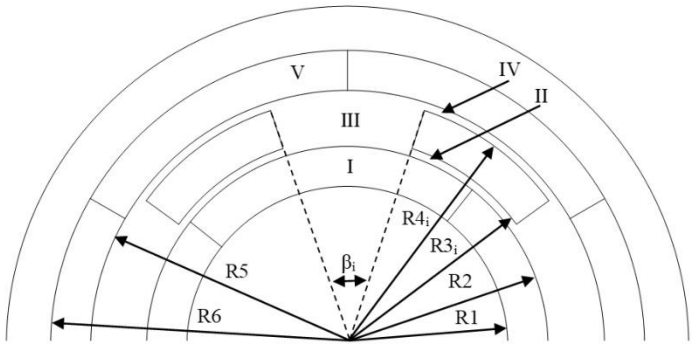

Fig. 2. Definition of regions, radii and slot angle

The magnetic vector potential in each region can be calculated by solving Poisson's equation and Laplace's equation in the PM and non-magnetized regions, respectively. The general solutions have been simplified by adopting the following notations:

$$U_z(a,b) = \left(\frac{a}{b}\right)^z + \left(\frac{b}{a}\right)^z \tag{1}$$

$$Q_z(a,b) = \left(\frac{a}{b}\right)^z - \left(\frac{b}{a}\right)^z \tag{2}$$

Using the separation of variables method, the general solution for each region can be derived. The solutions, described by Fourier series, are provided in (3), (4), (11) – (13). In the rotor PM regions (I, V) the general solutions are as follows:

$$A^{(I)}(r,\theta) = \sum_{k=1}^{K}\left(W_{1k}C_I + W_{2k}M_{rck}^{(I)}\right)\cos(k\theta) + \sum_{k=1}^{K}\left(W_{1k}E_I + W_{2k}M_{rsk}^{(I)}\right)\sin(k\theta) \tag{3}$$

$$A^{(V)}(r,\theta) = \sum_{k=1}^{K}\left(W_{3k}C_V + W_{4k}M_{rck}^{(V)}\right)\cos(k\theta) + \sum_{k=1}^{K}\left(W_{3k}E_V + W_{4k}M_{rsk}^{(V)}\right)\sin(k\theta) \tag{4}$$

where

$$W_{1k} = \frac{U_k(r,R_1)}{U_k(R_2,R_1)} \tag{5}$$

$$w_{2k} = \left[1+\frac{1}{k}\left(\frac{R_1}{r}\right)^{k+1}\right]\cdot r - \frac{U_k(r,R_1)}{U_k(R_2,R_1)}\left[1+\frac{1}{k}\left(\frac{R_1}{R_2}\right)^{k+1}\right]\cdot R_2 \tag{6}$$

$$W_{3k} = \frac{U_k(r,R_6)}{U_k(R_5,R_6)} \tag{7}$$

$$W_{4k} = \left[1+\frac{1}{k}\left(\frac{R_6}{r}\right)^{k+1}\right]\cdot r - \frac{U_k(r,R_6)}{U_k(R_5,R_6)}\left[1+\frac{1}{k}\left(\frac{R_6}{R_5}\right)^{k+1}\right]\cdot R_5 \tag{8}$$

and

$$M_{rck}^{(I,V)} = \frac{2PB_{rm}}{k\pi\mu_0} sin\left(\frac{k\pi\alpha_p}{P}\right) cos(k\varphi_0) \tag{9}$$

$$M_{rsk}^{(I,V)} = \frac{2PB_{rm}}{k\pi\mu_0} sin\left(\frac{k\pi\alpha_p}{P}\right) sin(k\varphi_0) \tag{10}$$

for $k/P = 1, 3, 5, \ldots$

Each general solution is bounded by the inner (R_1, R_5) and outer (R_2, R_6) radii of each PM region. The parameter k denotes the order of harmonics in each region, with B_{rm} being the residual flux and P, μ_o, α_p are the number of poles, the permeability of free space and the magnet arc to pole pitch ratio, respectively. The terms C_I and E_I are Fourier coefficients. The initial angular position of the rotor is defined by φ_o.

Similarly, the general solution for each air-gap subdomain (II, IV) and the pole-pieces region (III) can be described as:

This research has been funded by the Engineering and Physical Sciences Research Council (EPSRC).

$$A_i^{(II)}(r,\theta) = \sum_{k=1}^{K}\left(C_{II,\mathrm{i}}\frac{R_2}{k}\frac{U_k(r,R_{3,\mathrm{i}})}{Q_k(R_2,R_{3,\mathrm{i}})} + D_{II,\mathrm{i}}\frac{R_{3,\mathrm{i}}}{k}\frac{U_k(r,R_2)}{Q_k(R_{3,\mathrm{i}},R_2)}\right)\cos(k\theta) + \sum_{k=1}^{K}\left(E_{II,\mathrm{i}}\frac{R_2}{k}\frac{U_k(r,R_{3,\mathrm{i}})}{Q_k(R_2,R_{3,\mathrm{i}})} + F_{II,\mathrm{i}}\frac{R_{3,\mathrm{i}}}{k}\frac{U_k(r,R_2)}{Q_k(R_{3,\mathrm{i}},R_2)}\right)\sin(k\theta) \quad (11)$$

$$A_i^{(IV)}(r,\theta) = \sum_{k=1}^{K}\left(C_{IV,\mathrm{i}}\frac{R_{4,\mathrm{i}}}{k}\frac{U_k(r,R_5)}{Q_k(R_{4,\mathrm{i}},R_5)} + D_{IV,i}\frac{R_5}{k}\frac{U_k(r,R_{4,\mathrm{i}})}{Q_k(R_5,R_{4,\mathrm{i}})}\right)\cos(k\theta) + \sum_{k=1}^{K}\left(E_{IV,\mathrm{i}}\frac{R_{4,\mathrm{i}}}{k}\frac{U_k(r,R_5)}{Q_k(R_{4,\mathrm{i}},R_5)} + F_{IV,i}\frac{R_5}{k}\frac{U_k(r,R_{4,\mathrm{i}})}{Q_k(R_5,R_{4,\mathrm{i}})}\right)\sin(k\theta) \quad (12)$$

$$A_i^{(III)}(r,\theta) = C_{III,i} + D_{III,i}\ln(r) + \sum_{m=1}^{M}\left(E_{III,i,m}\frac{Q_{f_{m,i}}(r,R_{4,s})}{Q_{f_{m,i}}(R_{3,s},R_{4,s})} - F_{III,i,m}\frac{Q_{f_{m,i}}(r,R_{3,s})}{Q_{f_{m,i}}(R_{3,s},R_{4,s})}\right)\cdot\cos\left(f_{m,i}(\theta-\theta_i)\right) \quad (13)$$

with

$$f_{m,i} = \frac{m\pi}{\beta_i} \quad (14)$$

where m defines the order of harmonics and β_i, θ_i are the opening angle and angular position of the ith slot between consecutive pole pieces and s is equal to i or i-1 depending on the matching of pole pieces and slots in the clockwise or anticlockwise directions. The terms $C_{II,\mathrm{i}}$, $D_{II,\mathrm{i}}$, $E_{II,\mathrm{i}}$ and $F_{II,\mathrm{i}}$ are Fourier coefficients.

Each air-gap subdomain solution is calculated for the $[0, 2\pi]$ angular domain. The complete solution in the air-gap can then be constructed by using the appropriate subdomain for the angular region it occupies (Fig. 3). This fact, in addition to the continuity of the radial component of the flux density and the tangential component of the field intensity leads to the following boundary equations that are used to define the expressions at each interface:

$$H_\theta^{(I)}\big|_{r=R_2} = H_{\theta,\mathrm{i}}^{(II)}\big|_{r=R_2} \quad (15)$$

$$B_r^{(I)}\big|_{r=R_2} = B_{r,\mathrm{i}}^{(II)}\big|_{r=R_2} \quad (16)$$

$$H_{\theta,i}^{(II)}\big|_{r=R_{3,\mathrm{i}}} = H_\theta^{(III)}\big|_{r=R_{3,\mathrm{i}}} \quad (17)$$

$$A_i^{(II)}\big|_{r=R_{3,\mathrm{i}}} = A_i^{(III)}\big|_{r=R_{3,\mathrm{i}}} \quad (18)$$

$$H_\theta^{(III)}\big|_{r=R_{4,\mathrm{i}}} = H_{\theta,i}^{(IV)}\big|_{r=R_{4,\mathrm{i}}} \quad (19)$$

$$A_i^{(III)}\big|_{r=R_{4,\mathrm{i}}} = A_i^{(IV)}\big|_{r=R_{4,\mathrm{i}}} \quad (20)$$

$$H_{\theta,\mathrm{i}}^{(IV)}\big|_{r=R_5} = H_\theta^{(V)}\big|_{r=R_5} \quad (21)$$

$$B_{r,\mathrm{i}}^{(IV)}\big|_{r=R_5} = B_r^{(V)}\big|_{r=R_5} \quad (22)$$

Applying the boundary equations (15) – (22) to the general solutions in each subdomain (3), (4), (11) – (13) the complete solution can be derived and expressed in matrix form as in (23).

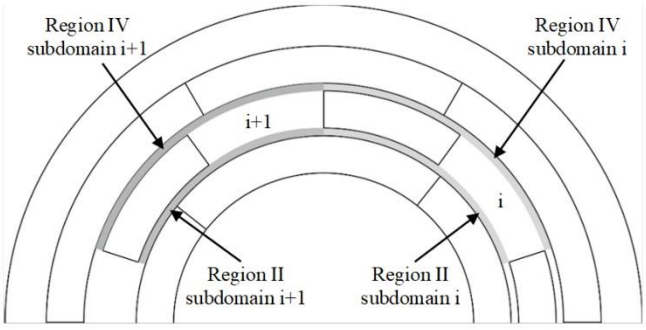

Fig. 3. Angular regions occupied by the air-gap subdomain

TABLE II. PARAMETER ERROR FOR MODEL VALIDATION

Variable	Pole Piece Error				
	No. 1	*No. 2*	*No. 3*	*No. 4*	*No. 5*
Length (mm)	0.018	-0.014	0.001	-0.020	-0.019
Angular arc (deg)	0.019	-0.018	0.001	0.009	0.018
Radial position (mm)	-0.001	0.204	-0.103	0.050	-0.030
Angular position (deg)	0.206	0.011	-0.199	-0.099	-0.142

$$\boldsymbol{X} \cdot \boldsymbol{K} = \boldsymbol{Y} \tag{23}$$

where $\boldsymbol{K}$ is a column matrix containing all the unknown Fourier coefficients of each general solution. The supplementary matrices $\boldsymbol{X}, \boldsymbol{Y}$ are defined through algebraic manipulation. This analytical solution is presented in more detail in Appendix A.

A. Analytical Model Validation

The accuracy of the analytical model is assessed by comparing a solution of a sample deviated gear to a 2D finite element analysis of the same geometry. For the purpose of this study, a degree of error has been arbitrarily introduced to the two dimensions and radial and tangential position of each pole piece. This error is recorded in Table II. For each region the first 200 harmonics were considered. The field solution shows excellent correlation with FEA results (Fig. 4), under the same infinite permeability assumption. The FEA software used in this analysis is FEMM [29]. The mesh density in the FE model was set using the approach outlined in [21].

The computational efficiency of this approach depends on the number of harmonics used. The consideration of higher-order harmonics can increase the accuracy of the model; however, this comes at the expense of computational time. The relationship between the number of harmonics and the accuracy and speed of the model is shown in Fig. 5. It is observed that the analytical torque results converge to the FEA after the first 50 harmonics. For the purpose of the Monte-Carlo analysis, the first 100 harmonics are considered, as the simulation samples will differ slightly to the sample model of Fig. 4. The computational time of the model with the selected harmonics is 2.9 s, more than an order of magnitude faster than the equivalent FEA. It must be noted the relationship between speed and number of harmonics is unique for each CMG. CMGs with higher number of poles, and hence higher number of pole pieces, will increase the computational time. Therefore, harmonic selection methods

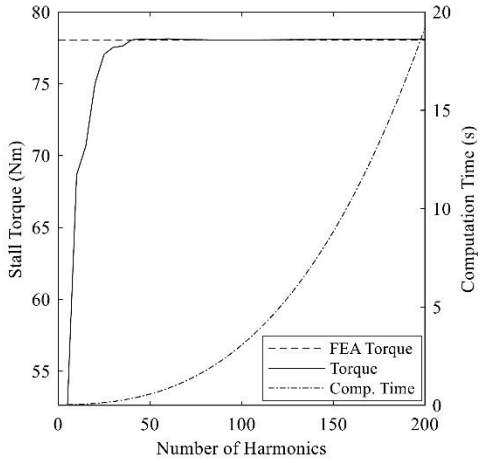

Fig. 5. Model harmonics vs accuracy and speed for sample CMG

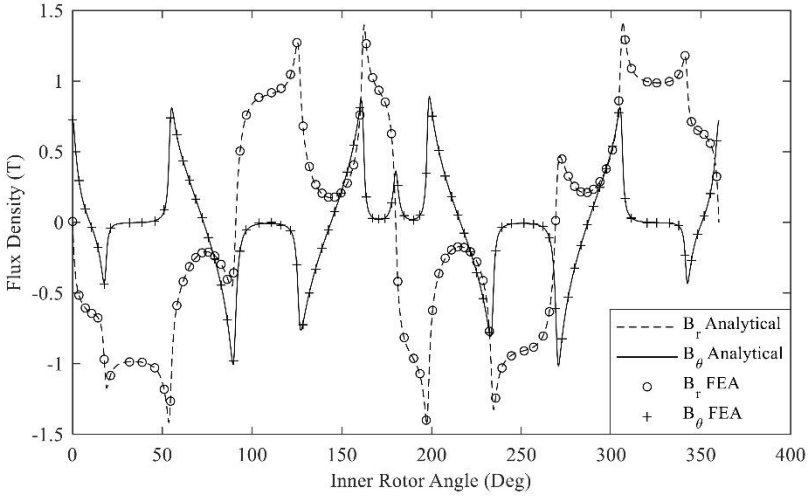

Fig. 4. Analytical vs FEA flux density comparison, assuming infinite permeability

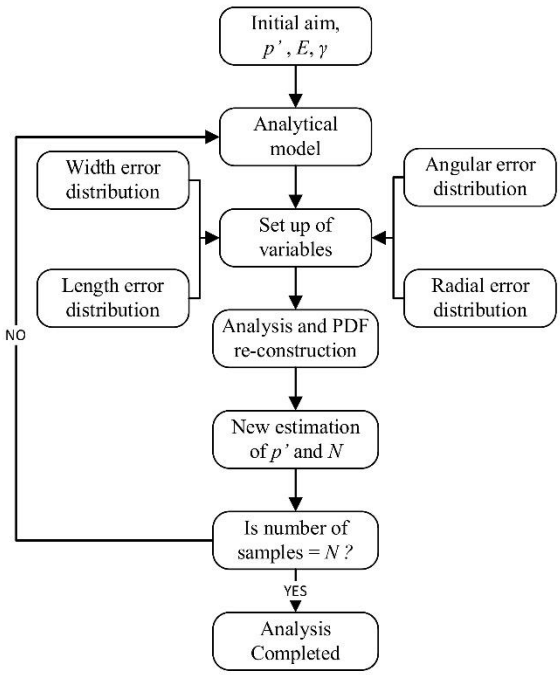

Fig. 6. Process diagram of the Monte-Carlo analysis

such as the ones presented in [27], [30] may be required to speed up the model.

III. Monte-Carlo Analysis

In a mass production environment, defining the acceptable range of product performance is as important as calculating ideal performance. Manufacturing tolerances are then specified to achieve an economically acceptable probability of a specific product falling into this range. The stochastic nature of manufacturing error means assessment of its effect requires the use of statistical methods. The range of outputs from a manufacturing process can be described through a Probability Density Function (PDF) of the desired performance variable. In cases where the PDF is unknown, PDF estimators can be used in conjunction with a number of samples to construct the PDF.

In this study the effect of geometric deviation of the pole pieces of a CMG is discerned through a Monte-Carlo analysis. A group of deviated samples is analyzed, each employing a different set of parameters. The parameters considered are the radial and angular position along with the length and angular arc of each pole piece. For each simulation the value of each parameter is obtained through random sampling of their respective distribution. It is assumed that the manufacturing error in the dimensions of the pole pieces is normally distributed [28]. In [20] the expected tolerances with respect to a selected manufacturing process are provided. A tolerance of 0.05 mm has been selected as the three-sigma value for the respective distribution, which corresponds to stamping and Electric Discharge Machining (EDM). The position of the pole pieces is affected by errors in manufacture and assembly but also by deflection due to magnetic forces within the gear. Assessing the distribution of pole piece position is therefore much more complicated than pole piece dimensions. This deflection due to magnetic forces is highly dependent on the mechanical properties of the pole pieces themselves and their supporting structure. Furthermore, as the pole pieces deflect, they will experience new magnetic loads which lead to further deflections [20], [31]. Proper assessment of this is likely to require an iterative solution such as [31] and can only be meaningfully undertaken with a full mechanical design. Therefore, for the purpose of this study, the position distributions have also been assumed to be normally distributed with a three-sigma value of 0.4 mm for the radial error and 0.4 deg for the tangential error. These values are similar to the positional error reported in [31], [32].

A PDF can be estimated using parametric or nonparametric methods. Nonparametric methods are well suited to cases where there is insufficient information regarding the profile of the PDF, whereas parametric estimators initially assume an underlying PDF form [33]. The estimator used in this study is the Kernel Density Estimator (KDE) which is a nonparametric method approximating the true PDF at discrete points rather than volumetrically. The KDE formula is defined in (24):

$$\hat{f}_h(x) = \frac{1}{Nh}\sum_{i=1}^{N} k\left(\frac{x - x_i}{h}\right) \tag{24}$$

TABLE III. PARAMETERES FOR MONTE-CARLO ANALYSIS

Parameter	Value	Distribution
Tolerance		
Length (mm)	0.05	Normal
Angular arc (deg)	0.05	Normal
Radial position (mm)	0.4	Normal
Angular position (deg)	0.4	Normal
Statistical Parameters		
E	0.01	N/A
z	1.96	N/A
Initial p'	0.5	N/A

where $x_1, \ldots, x_N$ are the samples of the unknown distribution, h is the bandwidth and k is the user-defined kernel function. The properties of k are provided in (25) [33]

$$\int k(u)du = 1, \quad \int uk(u)\,du = 0, \quad \int u^2k(u)du = k_2 \neq 0 \tag{25}$$

The bandwidth has a significant effect on the results of the KDE. In the literature, an optimal bandwidth has been reported which minimizes the Mean Integrated Square Error (MISE) [34]. The KDE is obtained through the KDE function in Matlab [35], which uses (24) with the optimal bandwidth calculated from (26) [36].

$$h = \left(\frac{4}{3N}\right)^{\frac{1}{5}}\sigma \tag{26}$$

where σ is an initial estimate of the standard deviation of $\hat{f}_h(x)$ and is calculated as in [36]. The Epanechnikov kernel [37], which is also known to minimize the MISE according to the properties in (25) [33], has also been used throughout this study.

The last important factor of the Monte-Carlo analysis is the number of samples. The larger the number of samples, the better the correlation will be between the simulated and true PDFs. However, this comes at a cost of increasing computational time. Equation (27) is provided in [38] as a mean of calculating the required number of samples when investigating the probability of an "event". Therefore, computational efficiency is maximized.

$$N = \frac{p'(1-p')}{E^2}z^2_{(1+\gamma)/2} \tag{27}$$

where p' is an estimate of the probability, E is the allowable error in the estimation of p', γ represents the confidence interval and z_a is the 100(α) percent point of a standard normal distribution [38].

The process diagram of the Monte-Carlo analysis is shown in Fig. 6. Initially, the aim is set and the statistical parameters p', E and γ are selected. An initially conservative p' of 0.5 is set and the value of each variable is obtained from their respective distributions. A solution is then calculated from the analytical model in Section II and a value of the stall torque is obtained. This is normalized with respect to the nominal torque of a non-deviated CMG. Using the KDE the PDF is re-constructed and a better estimate of p' is obtained. The required number of samples is then updated automatically according to (27) and, when reached, the simulation is completed. For validation and comparison purposes the same Monte-Carlo analysis is performed in FEMM and the two results are discussed in Section IV.

IV. RESULTS

For the purpose of this study, an initial aim was set to determine the probability of a sample achieving an inner rotor stall torque within ± 1% of the nominal. The acceptable error E was set to 0.01 and the 95% confidence interval was selected, leading to a z value of 1.96. The complete set of parameters of the analysis is provided in Table III. Two scenarios were considered; a standard and a "poorly manufactured" case, where the stated tolerance corresponds to the three-sigma and two-sigma values, respectively. For each case, a Monte-Carlo simulation was performed using three modelling techniques: non-linear FEA; linear FEA assuming infinite permeability in the iron regions and the analytical model.

The Monte-Carlo simulation for the standard case was completed according to Fig. 6 and 7545 samples were required. The total computational time using the analytical solution was approximately 7.3 hours using a computer with the following specifications: Intel(R) Core(TM) i7-6700 CPU @ 3.40GHz, 16 GB RAM. In comparison, the linear FEA took approximately 150 hours, with the more computationally heavy non-linear FEA requiring around 480 hours to complete. Consequently, the latter was completed by operating 30 computers of the same specification concurrently for approximately 16 hours.

The results of each of the three analysis methods are shown in their re-constructed Cumulative Distribution Function (CDF) plots of Fig. 7 and Fig. 8. Considering the standard case (Fig. 7), the CDF shows good correlation between the analytical solution and the linear FEA. However, both linear analyses give a more conservative distribution (i.e.

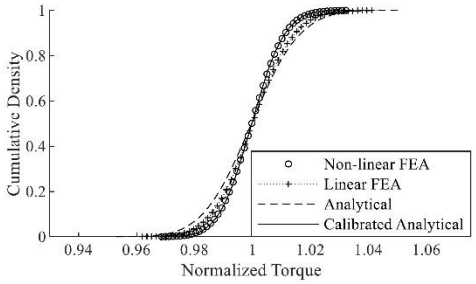

Fig. 7. Analytical vs FEA comparison CDF – Standard case

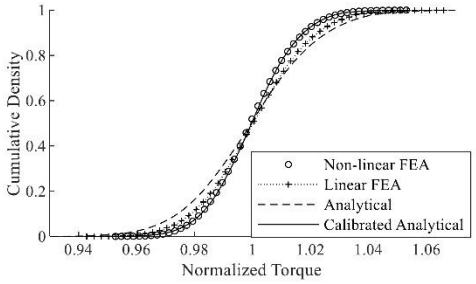

Fig. 8. Analytical vs FEA comparison CDF – Poorly manufactured case

it predicts a higher probability of poor performance) than the non-linear FEA. This is even more pronounced for the poorly manufactured case.

However, when comparing stall torque results for a specific gear instance (i.e. a defined set of geometric deviations) calculated using the analytical model and non-linear FEA, a linear trend can be observed. This indicates that a scaling factor could be applied to calibrate the analytical results. Fig. 9 shows the normalised stall torque results for 115 gear instances using both types of analysis. A line of fit can be applied through the central point (1,1) and the gradient of this line can then be used to scale results of the analytical model as a function of the stall torque.

From Fig. 7 and Fig. 8 it is evident that excellent correlation is achieved between the calibrated analytical and the non-linear FEA with only a small number of FEA solutions required for the calibration. This translates into very similar results in the calculation of the probability *p'* (Table IV), the initial aim of this section.

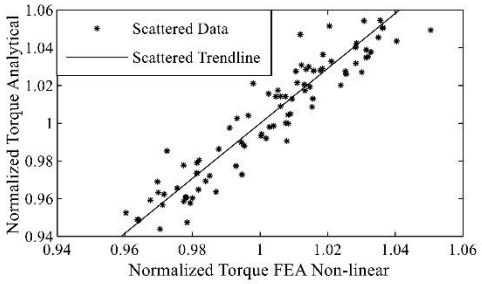

Fig. 9. Analytical calibration – Poorly manufactured case

TABLE IV. RESULTS OF MONTE-CARLO ANALYSIS

Standard Case				
	Analytical	***Linear FEA***	***FEA***	***Calibrated Analytical***
p'	0.58	0.61	0.73	0.73
Poorly manufactured Case				
	Analytical	***Linear FEA***	***FEA***	***Calibrated Analytical***
p'	0.40	0.45	0.53	0.53

V. DISCUSSION

The nature of stochastic manufacturing variations in a complex system makes experimental validation of probable performance impractical. However, fast and accurate models allow a large number of products, each with unique manufacturing errors, to be simulated so that a distribution of product performance can be predicted.

The analytical model has been shown to be very computationally efficient but conservative in overestimating the probability of poor performance when compared to FEA. On the other hand, while non-linear FEA is in practice too slow to complete Monte-Carlo studies of this nature, it does precisely model subtleties of geometry and material non-linearity. A hybrid approach is clearly the ideal solution combining the accuracy of FEA and computational efficiency of the analytical model. This way, even if the raw data from the analytical model overestimates the effect of manufacturing error (compared with the FEA), the results can be easily calibrated using a small number of FEA solutions. Thus, accuracy and computational efficiency are both maximized.

Considering the results of the study, the extent to which geometric deviations can affect the stall torque of the CMG is related to how well the manufacturing processes are controlled. From Fig. 7 and Fig. 8 it is clear that poorly controlled manufacturing processes substantially widen the cumulative density function. For the well-manufactured case, approximately 1.5% of the gear instances have a stall torque more than 2% lower than the nominal. For this design with these manufacturing tolerances, a relatively modest safety factor could ensure that virtually all gears meet the required performance. However, if manufacturing processes are not well controlled, the situation worsens. This can be seen in Fig. 8 with 7.5% of gear instances having a stall torque more than 2% lower than the nominal.

It is likely that the methods outlined in this study could be equally applied to similar gear designs. However, the number of FEA studies required to ensure an accurate calibration needs to be considered. This could relate to both the underlying manufacturing distributions and the specific gear parameters. In addition, further work would be required to apply an asymmetric model of this type to other gear topologies - for example those where a permeable mechanical bridge exists between adjacent pole pieces [39]. A general conclusion on the applicability of this method would probably require a large sample of CMGs of different types to be analyzed.

To relate this work to discrepancies in gear performance reported in the literature, specific knowledge of the manufacturing processes for each case would be required, along with enough evidence to predict the relevant underlying distributions. As outlined earlier, practical development of research machines is typically undertaken in a prototyping

environment with limited controls on manufacturing and assembly error. These underlying distributions could therefore be much worse that those considered in this study.

In addition to manufacturing error, geometric deviations caused by deflections of the structure under its own magnetic loads will also have an effect. These deflections are a more complex consideration than manufacturing error as it would be difficult to accurately approximate this effect by assuming an underlying distribution. As stated in Section III and in [31], calculating deflections is likely to require an iterative process linking a mechanical model with an electromagnetic simulation. If these calculations could be performed with comparable efficiency to the model presented in this paper, the compounding effects of manufacturing error and deflection of the structure could be assessed in similar statistical studies.

In terms of performance of the analytical model itself, it can be observed that the correlation with both linear and non-linear FEA deteriorates for gear instances with large geometric deviations. While this can be calibrated as demonstrated here for a statistical analysis, this observation may suggest that there are limits to the approximation of an asymmetric problem using Fourier Series. Further research to quantify this limitation is certainly warranted.

VI. Conclusions

Statistical analysis of the effect of manufacturing errors in complex products requires fast and accurate models. This study has developed and verified a statistical method using a novel asymmetric analytical model to calculate the effects of geometric deviations on the performance of CMGs. A complete methodology has been demonstrated and several conclusions and indications for further study have been drawn from the results.

The new analytical model can simulate realistic asymmetric variations in the modulation ring; previously found to be the most susceptible region for geometric error. It is flexible and computationally efficient and can therefore be used as part of a Monte-Carlo analysis. A balanced approach has been demonstrated using the analytical model to develop the output distribution profile and a small number of FEA solutions to calibrate the results. This maximizes both accuracy and computational efficiency. The set of statistical techniques employed is as important as the system model. In a study such as, this the resultant PDF is always an unknown. The Kernel Density Estimator, which does not assume a parametric distribution, has been shown to be well-suited to this task.

Close correlation has been achieved between the CDFs developed using the calibrated analytical model and non-linear FEA – with calibration in this case being achieved with only 115 data pairs. The methods presented in this paper provide a practicable means to assess the effect of manufacturing processes, and their errors, on CMG performance.

Authors

Alexandros Leontaritis received the M.Eng. degree in Mechanical Engineering from the Department of Mechanical Engineering, University of Bristol, Bristol, U.K., in 2017. He is currently working toward the PhD degree with the Electrical Energy Management Group, Faculty of Engineering, University of Bristol.

Aydin Nassehi is a Reader in Manufacturing Systems and Head of the Department of Mechanical Engineering, University of Bristol. He received his PhD in Innovative Manufacturing Technology from the University of Bath, Bath, U.K. in 2007. His research interests are in modelling and analysis at manufacturing systems and informatics and artificial intelligence in manufacturing.

Jason M. Yon received the MEng degree in Avionic Systems Engineering in 2007 and a PhD in Aerospace Electrical Systems in 2012, both from the University of Bristol. He is now a Lecturer in Electromechanical Systems at the University of Bristol. His research covers a broad range of topics related to electric machines, design and manufacture and the development of novel characterization techniques for electromechanical systems.

APPENDIX

A. Asymmetric Analytical Model

The analytical method is based on solutions of the magnetic vector potential (A). These solutions reduce to the Laplace's and Poisson's equations using magnetic flux density (B), which is the curl of A (A-1), and Maxwell's Ampere law equation (A-2).

$$\vec{B} = \nabla \times \vec{A} \tag{A-1}$$

$$\nabla \times \vec{B} = \mu_0 \vec{J} + \mu_0 \varepsilon_0 \frac{\partial \vec{E}}{\partial t} \tag{A-2}$$

Since a magnetostatic solution is required, the partial derivative of the electric flux density (E) disappears. Furthermore, as there is no applied current, the current density (J) is given by the curl of the magnetization vector (M) in the PM regions and is zero elsewhere. Therefore, equations (A-1) and (A-2) lead to (A-3) in the PM regions and (A-4) in all other regions:

$$\nabla^2 \vec{A} = -\mu_0 \nabla \times \vec{M} \tag{A-3}$$

$$\nabla^2 \vec{A} = 0 \tag{A-4}$$

The general solutions of equations (A-3), (A-4), described by Fourier series, are provided in (A-7), (A-8), (A-15) – (A-17). These solutions have been simplified by adopting the notation in (A-5), (A-6).

$$U_z(a,b) = \left(\frac{a}{b}\right)^z + \left(\frac{b}{a}\right)^z \tag{A-5}$$

$$Q_z(a,b) = \left(\frac{a}{b}\right)^z - \left(\frac{b}{a}\right)^z \tag{A-6}$$

In the rotor PM regions (I, V) the general solutions are as follows:

$$\begin{aligned} A^{(I)}(r,\theta) = &\sum_{k=1}^{K} \left(W_{1k} C_I + W_{2k} M_{rck}^{(I)}\right) \cos(k\theta) \\ &+ \sum_{k=1}^{K} \left(W_{1k} E_I + W_{2k} M_{rsk}^{(I)}\right) \sin(k\theta) \end{aligned} \tag{A-7}$$

$$\begin{aligned} A^{(V)}(r,\theta) = &\sum_{k=1}^{K} \left(W_{3k} C_V + W_{4k} M_{rck}^{(V)}\right) \cos(k\theta) \\ &+ \sum_{k=1}^{K} \left(W_{3k} E_V + W_{4k} M_{rsk}^{(V)}\right) \sin(k\theta) \end{aligned} \tag{A-8}$$

where

$$W_{1k} = \frac{U_k(r,R_1)}{U_k(R_2,R_1)} \tag{A-9}$$

$$\begin{aligned} W_{2k} = &\left[1 + \frac{1}{k}\left(\frac{R_1}{r}\right)^{k+1}\right] \cdot r \\ &- \frac{U_k(r,R_1)}{U_k(R_2,R_1)}\left[1 + \frac{1}{k}\left(\frac{R_1}{R_2}\right)^{k+1}\right] \cdot R_2 \end{aligned} \tag{A-10}$$

$$W_{3k} = \frac{U_k(r,R_6)}{U_k(R_5,R_6)} \tag{A-11}$$

$$\begin{aligned} W_{4k} = &\left[1 + \frac{1}{k}\left(\frac{R_6}{r}\right)^{k+1}\right] \cdot r \\ &- \frac{U_k(r,R_6)}{U_k(R_5,R_6)}\left[1 + \frac{1}{k}\left(\frac{R_6}{R_5}\right)^{k+1}\right] \cdot R_5 \end{aligned} \tag{A-12}$$

and

$$M_{rck}^{(I,V)} = \frac{2PB_{rm}}{k\pi\mu_0} sin\left(\frac{k\pi\alpha_p}{P}\right) cos(k\varphi_0) \tag{A-13}$$

$$M_{rsk}^{(I,V)} = \frac{2PB_{rm}}{k\pi\mu_0} sin\left(\frac{k\pi\alpha_p}{P}\right) sin(k\varphi_0) \tag{A-14}$$

for $k/P = 1, 3, 5, \ldots$

Each general solution is bounded by the inner (R_1, R_5) and outer (R_2, R_6) radii of each PM region. The parameter k denotes the order of harmonics in each region, with B_{rm} being the residual flux and P, μ_o, α_p are the number of poles, the permeability of free space and the magnet arc to pole pitch ratio, respectively. The terms C_I and E_I are Fourier coefficients. The initial angular position of the rotor is defined by φ_o.

Similarly, the general solution for each air-gap subdomain (II, IV) and the pole-pieces region (III) can be described as:

$$\begin{aligned} A_i^{(II)}(r,\theta) = &\sum_{k=1}^{K} \left(C_{II,\mathrm{i}} \frac{R_2}{k} \frac{U_k(r,R_{3,\mathrm{i}})}{Q_k(R_2,R_{3,\mathrm{i}})} \right. \\ &\left. + D_{II,\mathrm{i}} \frac{R_{3,\mathrm{i}}}{k} \frac{U_k(r,R_2)}{Q_k(R_{3,\mathrm{i}},R_2)}\right) \cos(k\theta) \\ &+ \sum_{k=1}^{K} \left(E_{II,\mathrm{i}} \frac{R_2}{k} \frac{U_k(r,R_{3,\mathrm{i}})}{Q_k(R_2,R_{3,\mathrm{i}})} \right. \\ &\left. + F_{II,\mathrm{i}} \frac{R_{3,\mathrm{i}}}{k} \frac{U_k(r,R_2)}{Q_k(R_{3,\mathrm{i}},R_2)}\right) \sin(k\theta) \end{aligned} \tag{A-15}$$

$$A_i^{(IV)}(r,\theta)=\sum_{k=1}^{K}\left(C_{IV,\mathrm{i}}\frac{R_{4,\mathrm{i}}}{k}\frac{U_k(r,R_5)}{Q_k(R_{4,\mathrm{i}},R_5)}+D_{IV,i}\frac{R_5}{k}\frac{U_k(r,R_{4,\mathrm{i}})}{Q_k(R_5,R_{4,\mathrm{i}})}\right)\cos(k\theta)+\sum_{k=1}^{K}\left(E_{IV,\mathrm{i}}\frac{R_{4,\mathrm{i}}}{k}\frac{U_k(r,R_5)}{Q_k(R_{4,\mathrm{i}},R_5)}+F_{IV,i}\frac{R_5}{k}\frac{U_k(r,R_{4,\mathrm{i}})}{Q_k(R_5,R_{4,\mathrm{i}})}\right)\sin(k\theta) \quad \text{(A-16)}$$

$$A_i^{(III)}(r,\theta)=C_{III,i}+D_{III,i}\ln(r)+\sum_{m=1}^{M}\left(E_{III,i,m}\frac{Q_{f_{m,i}}(r,R_{4,s})}{Q_{f_{m,i}}(R_{3,s},R_{4,s})}-F_{III,i,m}\frac{Q_{f_{m,i}}(r,R_{3,s})}{Q_{f_{m,i}}(R_{3,s},R_{4,s})}\right)\cdot\cos\left(f_{m,i}(\theta-\theta_i)\right) \quad \text{(A-17)}$$

with

$$f_{m,i}=\frac{m\pi}{\beta_i} \quad \text{(A-18)}$$

where m defines the order of harmonics and β_i, θ_i are the opening angle, angular position of the i[th] slot between consecutive pole pieces and s is equal to i or i-1 depending on the matching of pole pieces and slots in the clockwise or anticlockwise directions. The terms $C_{II,\mathrm{i}}$, $D_{II,\mathrm{i}}$, $E_{II,\mathrm{i}}$ and $F_{II,\mathrm{i}}$ are Fourier coefficients.

The boundary conditions at each interface are provided in (A-19) – (A-26).

$$H_\theta^{(I)}\big|_{r=R_2}=H_{\theta,\mathrm{i}}^{(II)}\big|_{r=R_2} \quad \text{(A-19)}$$

$$B_r^{(I)}\big|_{r=R_2}=B_{r,\mathrm{i}}^{(II)}\big|_{r=R_2} \quad \text{(A-20)}$$

$$H_{\theta,i}^{(II)}\big|_{r=R_{3,\mathrm{i}}}=H_\theta^{(III)}\big|_{r=R_{3,\mathrm{i}}} \quad \text{(A-21)}$$

$$A_i^{(II)}\big|_{r=R_{3,\mathrm{i}}}=A_i^{(III)}\big|_{r=R_{3,\mathrm{i}}} \quad \text{(A-22)}$$

$$H_\theta^{(III)}\big|_{r=R_{4,\mathrm{i}}}=H_{\theta,i}^{(IV)}\big|_{r=R_{4,\mathrm{i}}} \quad \text{(A-23)}$$

$$A_i^{(III)}\big|_{r=R_{4,\mathrm{i}}}=A_i^{(IV)}\big|_{r=R_{4,\mathrm{i}}} \quad \text{(A-24)}$$

$$H_{\theta,\mathrm{i}}^{(IV)}\big|_{r=R_5}=H_\theta^{(V)}\big|_{r=R_5} \quad \text{(A-25)}$$

$$B_{r,\mathrm{i}}^{(IV)}\big|_{r=R_5}=B_r^{(V)}\big|_{r=R_5} \quad \text{(A-26)}$$

At the interface (I-II) between the inner rotor PM subdomain and the inner air-gap subdomains the following expressions can be derived (A-27) – (A-30) using (A-7), (A-15) and boundary equations (A-19), (A-20). The Fourier coefficients $\boldsymbol{C_I}, \boldsymbol{E_I}, \boldsymbol{C_{II}}, \boldsymbol{D_{II}}, \boldsymbol{E_{II}}$ and $\boldsymbol{F_{II}}$ are all column vector of length equal to $Q\cdot K$. All constant terms are defined similarly and therefore the definition of only $\boldsymbol{G_1}$ is provided below. Same applies for the magnetization column vectors that are defined as $\boldsymbol{M_{rck}^{(I)}}$ (A-37).

$$\boldsymbol{I_{KQ}C_I+G_1C_{II}+G_2D_{II}}=0 \quad \text{(A-27)}$$

$$\boldsymbol{I_{KQ}E_I+G_1E_{II}+G_2F_{II}}=0 \quad \text{(A-28)}$$

$$\boldsymbol{G_3C_I+I_{KQ}C_{II}=G_{13}\cdot M_{rck}^{(I)}} \quad \text{(A-29)}$$

$$\boldsymbol{G_3E_I+I_{KQ}E_{II}=G_{13}\cdot M_{rsk}^{(I)}} \quad \text{(A-30)}$$

where

$$\boldsymbol{I_{KQ}}=diag(1,1,\dots,1)_{KQ\times KQ} \quad \text{(A-31)}$$

$$\boldsymbol{G_1}=diag(\boldsymbol{g_1}(1),\boldsymbol{g_1}(2),\dots,\boldsymbol{g_1}(\mathrm{Q}))_{QK\times QK} \quad \text{(A-32)}$$

$$\boldsymbol{g_1}(\mathrm{i})=\boldsymbol{I_K}\cdot\left(-\frac{R_2}{k}\frac{U_k(R_2,R_{3,\mathrm{i}})}{Q_k(R_2,R_{3,\mathrm{i}})}\right) \quad \text{(A-33)}$$

$$\boldsymbol{g_2}(\mathrm{i})=\boldsymbol{I_K}\cdot\left(-\frac{R_{3,\mathrm{i}}}{k}\frac{2}{Q_k(R_{3,\mathrm{i}},R_2)}\right) \quad \text{(A-34)}$$

$$\boldsymbol{g_3}(\mathrm{i})=\boldsymbol{I_K}\cdot\left(-\frac{k}{R_2}\frac{Q_k(R_2,R_1)}{U_k(R_2,R_1)}\right) \quad \text{(A-35)}$$

$$\boldsymbol{g_{13}}(\boldsymbol{i})=\boldsymbol{I_K}\left(1-\left(\frac{R_1}{R_2}\right)^{k+1}-\frac{k}{R_2}\frac{Q_k(R_2,R_1)}{U_k(R_2,R_1)}\cdot\left(1+\frac{1}{k}\left(\frac{R_1}{R_2}\right)^{k+1}\right)R_2\right) \quad \text{(A-36)}$$

$$\boldsymbol{M_{rck}^{(I)}}=\left[\boldsymbol{m_{rck}^{(I)}}(1),\boldsymbol{m_{rck}^{(I)}}(2),\dots,\boldsymbol{m_{rck}^{(I)}}(Q)\right]^T \quad \text{(A-37)}$$

$$\boldsymbol{m_{rck}^{(I)}}(\mathrm{i})=\left[m_{rck}^{(I)}(1),m_{rck}^{(I)}(2),\dots,m_{rck}^{(I)}(K)\right] \quad \text{(A-38)}$$

Algebraic manipulation of (A-15), (A-17) and boundary conditions (A-21), (A-22) lead to the following relationships

at the inner air-gap and slot subdomains interface (II-III). The Fourier coefficients $\boldsymbol{E_{III}}, \boldsymbol{F_{III}}$ are column vectors of length $M \cdot Q$ and $\boldsymbol{C_{III}}, \boldsymbol{D_{III}}$ of length equal to Q.

$$-\boldsymbol{I_{Ki\,R3}}\boldsymbol{D_{II}} + \boldsymbol{\delta_i^T}\boldsymbol{D_{III}} + \boldsymbol{\eta_i^T}\boldsymbol{f_m}\boldsymbol{G_4}\boldsymbol{E_{III}} - \boldsymbol{\eta_i^T}\boldsymbol{f_m}\boldsymbol{G_5}\boldsymbol{F_{III}} = 0 \tag{A-39}$$

$$-\boldsymbol{I_{Ki\,R3}}\boldsymbol{F_{II}} + \boldsymbol{\sigma_i^T}\boldsymbol{D_{III}} + \boldsymbol{\xi_i^T}\boldsymbol{f_m}\boldsymbol{G_4}\boldsymbol{E_{III}} - \boldsymbol{\xi_i^T}\boldsymbol{f_m}\boldsymbol{G_5}\boldsymbol{F_{III}} = 0 \tag{A-40}$$

$$\boldsymbol{\delta_{i,\pi}}\boldsymbol{G_6}\boldsymbol{C_{II}} + \boldsymbol{\delta_{i,\pi}}\boldsymbol{G_7}\boldsymbol{D_{II}} + \boldsymbol{\sigma_{i,\pi}}\boldsymbol{G_6}\boldsymbol{E_{II}} + \boldsymbol{\sigma_{i,\pi}}\boldsymbol{G_7}\boldsymbol{F_{II}} - \boldsymbol{I_Q}\boldsymbol{C_{III}} - \boldsymbol{I_Q}\ln\left(R_{3,\mathrm{i}}\right)\boldsymbol{D_{III}} = 0 \tag{A-41}$$

$$\boldsymbol{\eta_{i,\pi}}\boldsymbol{G_6}\boldsymbol{C_{II}} + \boldsymbol{\eta_{i,\pi}}\boldsymbol{G_7}\boldsymbol{D_{II}} + \boldsymbol{\xi_{i,\pi}}\boldsymbol{G_6}\boldsymbol{E_{II}} + \boldsymbol{\xi_{i,\pi}}\boldsymbol{G_7}\boldsymbol{F_{II}} - \boldsymbol{I_{MQ}}\boldsymbol{E_{III}} = 0 \tag{A-42}$$

where

$$\boldsymbol{I_{Ki\,R3}} = diag(R_{3,1}, R_{3,2}, \dots, R_{3,\mathrm{Q}})_{QK\times QK} \tag{A-43}$$

$$\delta(i,k) = \frac{1}{\pi}\int_{\theta_i}^{\theta_i+\beta_i} \cos(k\theta)d\theta \tag{A-44}$$

$$\boldsymbol{\delta_i} = \left(\delta(i,k), \delta(i,k), \dots, \delta(i,k)\right)_{Q\times QK} \tag{A-45}$$

$$\boldsymbol{\delta_{i,\pi}} = diag\left(\frac{\pi}{\beta_i}\delta(1,k), \frac{\pi}{\beta_i}\delta(2,k), \dots, \frac{\pi}{\beta_i}\delta(Q,k)\right)_{Q\times QK} \tag{A-46}$$

$$\sigma(i,k) = \frac{1}{\pi}\int_{\theta_i}^{\theta_i+\beta_i} \sin(k\theta)d\theta \tag{A-47}$$

$$\eta(m,k,i) = \frac{1}{\pi}\int_{\theta_i}^{\theta_i+\beta_i} \cos(k\theta) \cdot \cos\left(f_{m,i}(\theta-\theta_i)\right)d\theta \tag{A-48}$$

$$\boldsymbol{\eta_i} = \begin{bmatrix} \eta(m,k,1) & \cdots & \eta(m,k,1) \\ \vdots & \ddots & \vdots \\ \eta(m,k,Q) & \cdots & \eta(m,k,Q) \end{bmatrix}_{QM\times QK} \tag{A-49}$$

$$\boldsymbol{\eta_{i,\pi}} = diag\left(\frac{2\pi}{\beta_i}\boldsymbol{\eta}(m,k,1), \frac{2\pi}{\beta_i}\boldsymbol{\eta}(m,k,2), \dots, \frac{2\pi}{\beta_i}\boldsymbol{\eta}(m,k,\mathrm{Q})\right)_{QM\times QK} \tag{A-50}$$

$$\xi(m,k,i) = \frac{1}{\pi}\int_{\theta_i}^{\theta_i+\beta_i} \sin(k\theta) \cdot \cos\left(f_{m,i}(\theta-\theta_i)\right)d\theta \tag{A-51}$$

$$\boldsymbol{f_{m,i}} = f_{m,i}\cdot\boldsymbol{I_M} \tag{A-52}$$

$$\boldsymbol{f_m} = diag\left(\boldsymbol{f_{m,i}}(1), \boldsymbol{f_{m,i}}(2), \dots, \boldsymbol{f_{m,i}}(Q)\right) \tag{A-53}$$

$$\boldsymbol{G_4} = diag(\boldsymbol{g_4}(1), \boldsymbol{g_4}(2), \dots, \boldsymbol{g_4}(Q))_{QM\times QM} \tag{A-54}$$

$$\boldsymbol{g_4(i)} = \boldsymbol{I_M}\cdot\left(\frac{U_{f_{m,i}}\left(R_{3,\mathrm{i}}, R_{4,\mathrm{i}}\right)}{Q_{f_{m,i}}\left(R_{3,\mathrm{i}}, R_{4,\mathrm{i}}\right)}\right) \tag{A-55}$$

$$\boldsymbol{g_5(i)} = \boldsymbol{I_M}\cdot\left(\frac{2}{Q_{f_{m,i}}\left(R_{3,\mathrm{i}}, R_{4,\mathrm{i}}\right)}\right) \tag{A-56}$$

$$\boldsymbol{g_6(i)} = \boldsymbol{I_K}\cdot\left(\frac{R_2}{k}\frac{2}{Q_k\left(R_2, R_{3,\mathrm{i}}\right)}\right) \tag{A-57}$$

$$\boldsymbol{g_7(i)} = \boldsymbol{I_K}\cdot\left(\frac{R_{3,\mathrm{i}}}{k}\frac{U_k\left(R_{3,\mathrm{i}}, R_2\right)}{Q_k\left(R_{3,\mathrm{i}}, R_2\right)}\right) \tag{A-58}$$

Similar to the interface with the inner air-gap subdomains, the interface (III-IV) between the outer air-gap and the slot subdomains is described as in (A-59) – (A-62) using (A-16), (A-17) and boundary equations (A-23), (A-24).

$$-\boldsymbol{I_{Ki\,R4}}\boldsymbol{C_{IV}} + \boldsymbol{\delta_i^T}\boldsymbol{D_{III}} + \boldsymbol{\eta_i^T}\boldsymbol{f_m}\boldsymbol{G_5}\boldsymbol{E_{III}} - \boldsymbol{\eta_i^T}\boldsymbol{f_m}\boldsymbol{G_4}\boldsymbol{F_{III}} = 0 \tag{A-59}$$

$$-\boldsymbol{I_{Ki\,R4}}\boldsymbol{E_{IV}} + \boldsymbol{\sigma_i^T}\boldsymbol{D_{III}} + \boldsymbol{\xi_i^T}\boldsymbol{f_m}\boldsymbol{G_5}\boldsymbol{E_{III}} - \boldsymbol{\xi_i^T}\boldsymbol{f_m}\boldsymbol{G_4}\boldsymbol{F_{III}} = 0 \tag{A-60}$$

$$\boldsymbol{\delta_{i,\pi}}\boldsymbol{G_8}\boldsymbol{C_{IV}} + \boldsymbol{\delta_{i,\pi}}\boldsymbol{G_9}\boldsymbol{D_{IV}} + \boldsymbol{\sigma_{i,\pi}}\boldsymbol{G_8}\boldsymbol{E_{IV}} + \boldsymbol{\sigma_{i,\pi}}\boldsymbol{G_9}\boldsymbol{F_{IV}} - \boldsymbol{I_Q}\boldsymbol{C_{III}} - \boldsymbol{I_Q}\ln\left(R_{4,\mathrm{i}}\right)\boldsymbol{D_{III}} = 0 \tag{A-61}$$

$$\boldsymbol{\eta_{i,\pi}}\boldsymbol{G_8}\boldsymbol{C_{IV}} + \boldsymbol{\eta_{i,\pi}}\boldsymbol{G_9}\boldsymbol{D_{IV}} + \boldsymbol{\xi_{i,\pi}}\boldsymbol{G_8}\boldsymbol{E_{IV}} + \boldsymbol{\xi_{i,\pi}}\boldsymbol{G_9}\boldsymbol{F_{IV}} - \boldsymbol{I_{MQ}}\boldsymbol{F_{III}} = 0 \tag{A-62}$$

where

$$\boldsymbol{g_8(i)} = \boldsymbol{I_K}\cdot\left(\frac{R_{4,i}}{k}\frac{U_k\left(R_{4,i}, R_5\right)}{Q_k\left(R_{4,i}, R_5\right)}\right) \tag{A-63}$$

$$\boldsymbol{g_9(i)} = \boldsymbol{I_K} \cdot \left(\frac{R_5}{k} \frac{2}{Q_k(R_5, R_{4,i})} \right) \tag{A-64}$$

The equations at the interface (IV-V) between the outer air-gap subdomains and the outer rotor PM region can be derived adopting the same approach as for the inner rotor using the general solutions (A-8), (A-16) and boundary equations (A-25), (A-26). The Fourier coefficients $\boldsymbol{C_{IV}}, \boldsymbol{D_{IV}}, \boldsymbol{E_{IV}}, \boldsymbol{F_{IV}}, \boldsymbol{C_V}$ and $\boldsymbol{E_V}$ are column vectors of length $Q \cdot K$ and they are described as:

$$\boldsymbol{I_{KQ}C_V} + \boldsymbol{G_{10}C_{IV}} + \boldsymbol{G_{11}D_{IV}} = 0 \tag{A-65}$$

$$\boldsymbol{I_{KQ}E_V} + \boldsymbol{G_{10}E_{IV}} + \boldsymbol{G_{11}F_{IV}} = 0 \tag{A-66}$$

$$\boldsymbol{G_{12}C_V} + \boldsymbol{I_{KQ}C_{IV}} = \boldsymbol{G_{14}} \cdot \boldsymbol{M_{rck}^{(V)}} \tag{A-67}$$

$$\boldsymbol{G_{12}E_V} + \boldsymbol{I_{KQ}E_{IV}} = \boldsymbol{G_{14}} \cdot \boldsymbol{M_{rsk}^{(V)}} \tag{A-68}$$

where

$$\boldsymbol{g_{10}(i)} = \boldsymbol{I_K} \cdot \left(-\frac{R_{4,i}}{k} \frac{2}{Q_k(R_{4,i}, R_5)} \right) \tag{A-69}$$

$$\boldsymbol{g_{11}(i)} = \boldsymbol{I_K} \cdot \left(-\frac{R_5}{k} \frac{U_k(R_5, R_{4,i})}{Q_k(R_5, R_{4,i})} \right) \tag{A-70}$$

$$\boldsymbol{g_{12}(i)} = \boldsymbol{I_K} \cdot \left(-\frac{k}{R_5} \frac{Q_k(R_5, R_6)}{U_k(R_5, R_6)} \right) \tag{A-71}$$

$$\boldsymbol{g_{14}(i)} = \boldsymbol{I_K} \left(1 - \left(\frac{R_6}{R_5} \right)^{k+1} - \frac{k}{R_5} \frac{Q_k(R_5, R_6)}{U_k(R_5, R_6)} \cdot \left(1 + \frac{1}{k} \left(\frac{R_6}{R_5} \right)^{k+1} \right) R_5 \right) \tag{A-72}$$

The torque on each rotor is calculated using the Maxwell's Stress Tensor along a contour in each air-gap (A-73). The accuracy of the torque calculation where large asymmetries exist is maximized by taking an average of the torque calculations for $s = i$ and $s = i\text{-}1$ as per (A-17).

$$T = \frac{L \cdot R_{air-gap}^2}{\mu_0} \int_0^{2\pi} B_r^{(II/IV)}(R_{air-gap}, \theta) \cdot B_\theta^{(II/IV)}(R_{air-gap}, \theta) \cdot d\theta \tag{A-73}$$

Considering the expressions for $B_r^{(II/IV)}$ and $B_\theta^{(II/IV)}$, equation (A-73) can be expanded to the following:

$$T = \frac{L \cdot R_{air-gap}^2}{\mu_0} \left(\sum_{i=1}^{Q} \left(\sum_{k=1}^{2K} \sum_{l=1}^{k} O_{II,i,k} \cdot V_{II,i,j} - \sum_{k=1}^{K} \sum_{l=K+1}^{2K-k+1} O_{II,i,k} \cdot V_{II,i,l} \right) \right) \tag{A-74}$$

where,

$$j = k - l + 1 \tag{A-75}$$

$$\begin{aligned} O_{II,i,k} = -\Bigg(& C_{II,i,k} \frac{R_2}{r} \frac{U_k(r, R_{3,i})}{Q_k(R_2, R_{3,i})} \\ & + D_{II,i,k} \frac{R_{3,i}}{r} \frac{U_k(r, R_2)}{Q_k(R_{3,i}, R_2)} \Bigg) \\ & \cdot \int_{\theta_i}^{\theta_{i+1}} sin(k\theta)\, d\theta \\ & + \Bigg(E_{II,i,k} \frac{R_2}{r} \frac{U_k(r, R_{3,i})}{Q_k(R_2, R_{3,i})} \\ & + F_{II,i,k} \frac{R_{3,i}}{r} \frac{U_k(r, R_2)}{Q_k(R_{3,i}, R_2)} \Bigg) \\ & \cdot \int_{\theta_i}^{\theta_{i+1}} cos(k\theta)\, d\theta \end{aligned} \tag{A-76}$$

$$\begin{aligned} V_{II,i,j} = -\Bigg(& C_{II,i,j} \frac{R_2}{r} \frac{Q_k(r, R_{3,i})}{Q_k(R_2, R_{3,i})} \\ & + D_{II,i,j} \frac{R_{3,i}}{r} \frac{Q_k(r, R_2)}{Q_k(R_{3,i}, R_2)} \Bigg) \\ & \cdot \int_{\theta_i}^{\theta_{i+1}} \cos(j\theta)\, d\theta \\ & + \Bigg(E_{II,i,j} \frac{R_2}{r} \frac{Q_k(r, R_{3,i})}{Q_k(R_2, R_{3,i})} \\ & + F_{II,i,j} \frac{R_{3,i}}{r} \frac{Q_k(r, R_2)}{Q_k(R_{3,i}, R_2)} \Bigg) \\ & \cdot \int_{\theta_i}^{\theta_{i+1}} \sin(j\theta)\, d\theta \end{aligned} \tag{A-77}$$

REFERENCES

[1] K. Atallah and D. Howe, "A novel high-performance magnetic gear," in *IEEE Transactions on Magnetics*, 2001, vol. 37, no. 4 I, pp. 2844–2846.

[2] V. Asnani, J. Scheidler, and T. Tallerico, "Magnetic gearing research at NASA," *Annu. Forum Proc. - AHS Int.*, vol. 2018-May, 2018.

[3] L. Shah, A. Cruden, and B. W. Williams, "A magnetic gear box for application with a contra-rotating tidal turbine," *Proc. Int. Conf. Power Electron. Drive Syst.*, pp. 989–993, 2007.

[4] R. Z. A. Borisavljevic, J. W. Jansen, and E. A. Lomonova, "Modeling , Design and Experimental Validation of a Small-Sized Magnetic Gear," no. 2, pp. 560–565, 2013.

[5] J. X. Shen, H. Y. Li, H. Hao, and M. J. Jin, "A Coaxial Magnetic Gear With Consequent-Pole Rotors," *IEEE Trans. Energy Convers.*, vol. 32, no. 1, pp. 267–275, 2017.

[6] L. Jian, S. Member, K. T. Chau, and S. Member, "A Coaxial Magnetic Gear With Halbach Permanent-Magnet Arrays," *IEEE Trans. Energy Convers.*, vol. 25, no. 2, pp. 319–328, 2010.

[7] X. Yin, P. D. Pfister, and Y. Fang, "A Novel Magnetic Gear: Toward a Higher Torque Density," *IEEE Trans. Magn.*, vol. 51, no. 11, pp. 1–4, 2015.

[8] X. Li, K. T. Chau, M. Cheng, W. Hua, and Y. Du, "An improved coaxial magnetic gear using flux focusing," *2011 Int. Conf. Electr. Mach. Syst. ICEMS 2011*, no. d, pp. 2–5, 2011.

[9] M. Filippini and P. Alotto, "Coaxial magnetic gears design and optimization," *IEEE Trans. Ind. Electron.*, vol. 64, no. 12, pp. 1–1, 2017.

[10] P. O. Rasmussen, T. O. Andersen, F. T. Jørgensen, and O. Nielsen, "Development of a high-performance magnetic gear," *IEEE Trans. Ind. Appl.*, vol. 41, no. 3, pp. 764–770, 2005.

[11] J. Rens, K. Atallah, S. D. Calverley, and D. Howe, "A novel magnetic harmonic gear," *IEEE Trans. Ind. Appl.*, vol. 46, no. 1, pp. 206–212, 2010.

[12] F. T. Jørgensen, T. O. Andersen, and P. O. Rasmussen, "The cycloid permanent magnetic gear," *IEEE Trans. Ind. Appl.*, vol. 44, no. 6, pp. 1659–1665, 2008.

[13] Cheng-Chi Huang, Mi-Ching Tsai, D. G. Dorrell, and Bor-Jeng Lin, "Development of a Magnetic Planetary Gearbox," *IEEE Trans. Magn.*, vol. 44, no. 3, pp. 403–412, 2008.

[14] K. Atallah, S. D. Calverley, and D. Howe, "Design, analysis and realisation of a high-performance magnetic gear," *IEE Proceedings-Electric Power Appl.*, vol. 151, no. 2, pp. 135–143, 2004.

[15] S. Gerber and R. J. Wang, "Analysis of the end-effects in magnetic gears and magnetically geared machines," *Proc. - 2014 Int. Conf. Electr. Mach. ICEM 2014*, pp. 396–402, 2014.

[16] A. Matthee, S. Gerber, and R. Wang, "A high performance concentric magnetic gear," *Proc. - South. African Univ. Power Eng. Conf. 2015*, pp. 203–207, 2015.

[17] A. Matthee, R.-J. Wang, C. J. Agenbach, D. N. J. Els, and M. J. Kamper, "Evaluation of a magnetic gear for air-cooled condenser applications," *IET Electr. Power Appl.*, vol. 12, no. 5, pp. 677–683, 2018.

[18] X. Liu, K. T. Chau, J. Z. Jiang, and C. Yu, "Design and analysis of interior-magnet outer-rotor concentric magnetic gears," *J. Appl. Phys.*, vol. 105, no. 7, pp. 103–106, 2009.

[19] S. Gerber and R. J. Wang, "Evaluation of a prototype magnetic gear," *Proc. IEEE Int. Conf. Ind. Technol.*, pp. 319–324, 2013.

[20] A. Leontaritis, A. Nasseh, and J. M. Yon, "Causes and effects of Geometric Deviation in Magnetic Gears," in *Proc. IEEE Workshop on Electrical Machines Design Control and Diagnosis (WEMDCD 2019)*, 2019, pp. 34–39.

[21] A. Leontaritis, A. Nassehi, and J. M. Yon, "Assessing the Effect of Geometric Error on the Performance of Magnetic Gears," in *Proc. IEEE Int. Electrical Machines & Drives Conf. (IEMDC 19)*, 2019, pp. 1951–1958.

[22] T. Lubin, S. Mezani, and A. Rezzoug, "Analytical computation of the magnetic field distribution in a magnetic gear," *IEEE Trans. Magn.*, vol. 46, no. 7, pp. 2611–2621, 2010.

[23] X. Zhang, X. Liu, Z. Song, and Z. Chen, "Fast calculation of magnetic field distribution in magnetic gear for high torque application," *2016 XXII International Conference on Electrical Machines (ICEM)*. pp. 1742–1748, 2016.

[24] B. Dianati, H. Heydari, and S. A. Afsari, "Analytical Computation of Air-Gap Magnetic Field in a Viable Superconductive Magnetic Gear," *IEEE Trans. Appl. Supercond.*, vol. 26, no. 6, 2016.

[25] A. Penzkofer and K. Atallah, "Scaling of Pseudo Direct Drives for Wind Turbine Application," *IEEE Trans. Magn.*, vol. 52, no. 7, pp. 1–5, 2016.

[26] H. Y. Li, H. Hao, M. J. Jin, and J. X. Shen, "Analytical Calculation of Magnetic Field Distribution in Magnetic Gears with Consequent-Pole Rotors by Subdomain Method," *2016 IEEE Veh. Power Propuls. Conf. VPPC 2016 - Proc.*, pp. 1–6, 2016.

[27] A. Penzkofer and K. Atallah, "Magnetic gears for high torque applications," *IEEE Trans. Magn.*, vol. 50, no. 11, 2014.

[28] A. Pina, S. Paul, R. Islam, and L. Xu, "Analytical Model for Predicting Effects of Manufacturing Variations on Cogging Torque in Surface-Mounted Permanent Magnet Motors," *IEEE Trans. Ind. Appl.*, vol. PP, no. 99, p. 1, 2016.

[29] D. Meeker, "FEMM." 2012.

[30] M. Desvaux, B. Traullé, R. Le Goff Latimier, S. Sire, B. Multon, and H. Ben Ahmed, "Computation Time Analysis of the Magnetic Gear Analytical Model," *IEEE Trans. Magn.*, vol. 53, no. 5, 2017.

[31] K. K. Uppalapati and J. Z. Bird, "An Iterative Magnetomechanical Deflection Model for a Magnetic Gear," *IEEE Trans. Magn.*, vol. 50, no. 2, pp. 4–7, 2014.

[32] M. Desvaux, B. Multon, H. Ben Ahmed, and S. Sire, "Supporting the laminated ferromagnetic pole pieces in a magnetic gear: A structure behaviour analysis from a multibody model," *Mech. Mach. Sci.*, vol. 54, pp. 85–94, 2018.

[33] T. P. Burke, "Kernel Density Estimation Techniques for Monte Carlo Reactor Analysis," 2016.

[34] B. W. Silverman, *Density estimation: For statistics and data analysis*. London: Chapman and Hall, 1986.

[35] The Mathworks Inc., "MATLAB - MathWorks," *www.mathworks.com/products/matlab*, 2016. [Online]. Available: http://www.mathworks.com/products/matlab/.

[36] A. W. Bowman and A. Azzalini, *Applied Smoothing Techniques for Data Analysis*. New York: Oxford University Press Inc., 1997.

[37] V. Epanechnikov, "Nonparametric estimation of a multidimensional probability density," *Theory Probab. Its Appl.*, 1969.

[38] G. J. Hahn, "Sample Sizes for Monte Carlo Simulation.," *IEEE Trans. Syst. Man Cybern.*, vol. SMC-2, no. 5, pp. 678–680, 1972.

[39] A. Hawksworth, "Pole-Piece Structure for a Magnetic Gear," US Patent Number 2017/0005559 A1, 2017.